IJCRT.ORG ISSN : 2320-2882

INTERNATIONAL JOURNAL OF CREATIVE RESEARCH THOUGHTS (IJCRT)

An International Open Access, Peer-reviewed, Refereed Journal

Review On Ligands Containing Phenolic Unit Used As Fluorogenic Chemo-sensors During The Last Decade

Dr. Sanju Das

Assistant Professor of Chemistry

Department of Chemistry, Maulana Azad College, Kolkata 700013, India

Abstract: This review focuses on recent developments arising from studies of fluorescent sensors for different biologically important metal ions and anions, utilizing ligands containing phenolic unit during last decade. Emphasis is given to phenol based ligands owing to their phenol to phenolate conversion with respect to pH and in consequent generation of fluorescence property. A number of chemo-sensors based on phenolic chromophore have recently been introduced in reputed journals.

Index Terms **- Fluorogenic, Chemo-Sensor, Phenol Based Ligand**

I. INTRODUCTION

For the last two decade there has been a significant growth in research related to molecular recognition and molecular signaling. Chemists, environmental scientist and biologists pay incredible strategic attention to design and synthesis of chemical sensor for detecting ionic and neutral species in meaningful way.[1]Chemo-sensing performance based on fluorescence spectroscopy may be considered as primary research tool owing to its simplicity, high sensitivity, rapid responsive ability and obviously non-destructive facility.[2]Such technique is further advantageous not only for ratiometric responses of the analyte but put in extra feather to find out the precise low detection limit of the sensing ion/molecule.[3]Since after rapid modernization, ions and molecules have increasingly been redistributed in the environment with sufficient accumulation in terrestrial and aquatic habitats, that may often invite adverse effects on the human health.[4]On the other hand, some biomolecules in their excessive or acute storage may alter the actual metabolic pathway and in consequent undesirable physiological activities are often observed. Undoubtedly, designing and synthesis of fluorescence chemo-sensor, operable under physiological conditions is a challenging task. In continuation, the fluorescent probes could effectively be utilized to study living cells including living organism using bio-imaging studies.[5]In this short review some phenol based ligands were discussed as fluorogenic chemo sensor mentioned in the existing literature.

1.1 General approaches for designing of fluorescent sensors

An ideal fluorescent chemo-sensor must fulfill three basic requirements – first of all, binding selectivity that is the receptor must have the strongest affinity towards the relevant target. Secondly the signal selectivity that is the fluorescence property should remain unaffected from the environmental interferences such as sensor concentration and photo-bleaching tendency *etc*. Finally, it must be stable under illumination. The fluorescence signal reflected by different pathways like as Photo-induced electron transfer (PET), [6] Photo-induced charge transfer (PCT), [7] Intra and intermolecular charge transfer (ICT), [8] Exited state proton transfer (ESIPT), [9] Fluorescence resonance energy transfer (FRET) [10] etc. Three different approaches are generally employed to construct optical sensors for the detection of different analytes (**Fig. 1**). The most popular strategy involves the chemodosimeter approach which is based on the irreversible binding phenomenon, usually centered on a specific reaction induced by the analyte of interest.[11]The process is associated with significant chemical modification involving both breaking and making of the covalent bonds results the formation of products differing from the starting material concomitantly with optically different properties. Secondly, the strategic use of sensors in which the binding sites and signaling subunits are linked covalently. In this case, interaction of analyte with the binding site makes a change in fluorescence of the signaling subunit. Last but not the least; a coordination complex may be used through displacement approach.[12]In these case, the introduction of analyte leads to decomplexation and regeneration of fluorophoric behavior of the signaling unit. However, the development of fluorescence chemo-sensors for ion/molecule in pure aqueous media is much more advantageous compare to those function only in organic solvents.[13]Among aforesaid strategies, fluorophoric ligand connected coordination complex-based displacement approach is probably the best way to develop chemo-sensor for its simple and straight forward mechanism along with readily operable suitability in physiological condition.[14] Hence, design of fluorescent chemo-sensors is an interesting field towards the chemists, not only because of the potential practical applications in cell physiology and analytical and environmental chemistry, but also as a proving ground for manipulation and/or engineering of various photo-physical processes toward an ultimate goal of selective and sensitive signaling of targeted species.

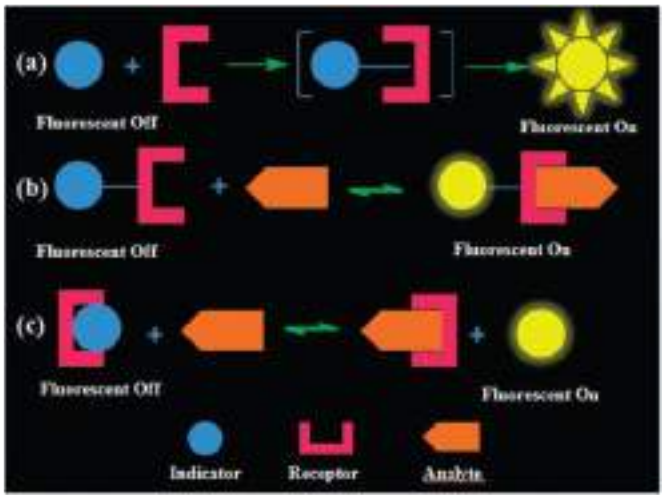

Fig.1. The three main approaches for sensing purpose: (a) chemodosimeter; (b) Binding site-signaling approach; (c) displacement approach.

1.2 Brief review of phenol based ligands for chemo-sensoning

A number of chemo-sensors based on phenolic chromophore have recently been introduced in reputed journals. Some of them are reported as Al^{3+} sensor. Development of simple probes to sense Al^{3+} *in vivo* and *in vitro* in real time is highly desirable since imbalance accumulation of Al^{3+} often correlates with variety of neuro-degenerative diseases. A phenol-based chemo-sensor (**P1**) with dual PET processes by simultaneous introduction of both nitrogen and sulfur donors were synthesized by Y. Lu *et al*. The fluorescence signal of the free chemo-sensor is in its *normal-off* mode due to sulfur and nitrogen donor mediating PET process. Added advantage of the probe is that it may operative over a wide pH range from 3–11. A large fluorescence enhancement was observed for the complexation with Al^{3+} owing to the inhibition of PET processes from both the sulfur and the nitrogen donors of the fluorophore.[15]

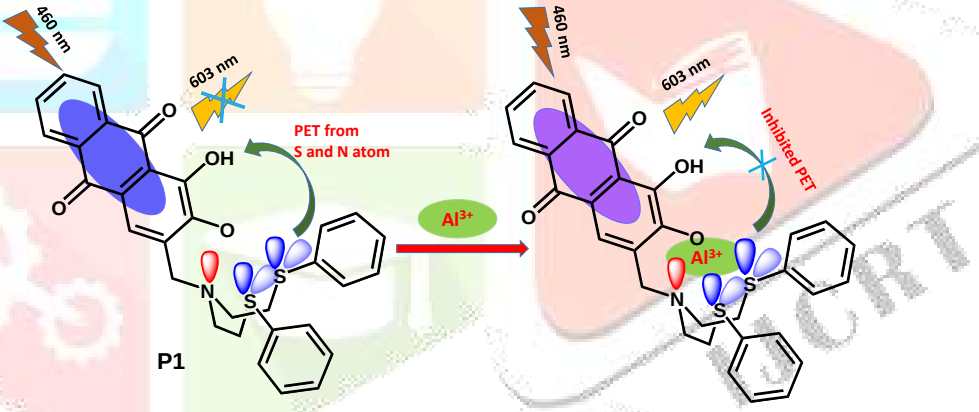

Fig.2. Scheme for Al^{3+} sensing mechanism

Another interesting phenol-based ligand (**P2**) was reported by X. J. Zheng *et al*. as Al^{3+} sensor. Here, inhibition of the ESIPT process by Al^{3+}ion selectively shows fluorescence enhancement.[16]Again, P. Ghosh and co-workers developed an ESIPT based highly sensitive ratiometric fluorescence sensor (**P3**) for selective Al^{3+}detection in acetonitrile as well as in mixed aqueous medium. About 2.3-fold enhancement in emission intensity and lower detection limit ~ 0.5 nM are mentionable features for aforesaid chemo-semsor.[17] Besides, M. Sukwattanasinitt and co-workers have prepared a series of phenolic ligands (**Chart-1**) for *turn-on* Al^{3+} sensors, based on metal chelation-enhanced fluorescence (CHEF) effect that inhibit the non-radiative PET and ESIPT processes.[18] Recently H. Hou and his group synthesized 8-hydroxyquinoline based a fluorescent chemodosimeter (**P4**) for detection of Al^{+3}ion. The probe exhibits *turn-on* fluorescence response to Al^{3+} owing to Al^{3+}promoted hydrolysis of carbon-nitrogen double bond.[19]Another highly sensitive chemo-sensor based on Schiff-base phenolic ligand (**P5**) for Al^{3+} detection in HEPES buffer medium wasre ported by S. Goswami and co-workers.[20] In this connection, organic dye chromone connected phenolic Schiff-based ligand (**P6**) deserves special attention for exhibiting Al^{3+}chemo-sensingin eco-friendly aquatic environment.[21] Another phenol containing Schiff-base ligand (**P7**) acts as Al^{3+} sensor in 100% aqueous media, reported by H. Wu and co-workers, renders novelty for its easy applicability to find out unknownAl^{3+} concentration in river and tap water.[22] Notably, in the contemporary period, anotherAl^{3+}chemo-sensor (**P8**) highlighted in literature for excellent bio-imaging study owing to its excellent cell permeability and low cytotoxicity.[23] In the same Year, D. K. Das *et al*. reported a novel condensation product (**P9**) of 2-hydroxy-1-naphaldehyde and 2-aminophenol to detect Al^{3+}exclusively in aqueous medium. The sensor was well explored for intracellular bio-imaging purpose using live rat L6 myoblasts cells.[24]

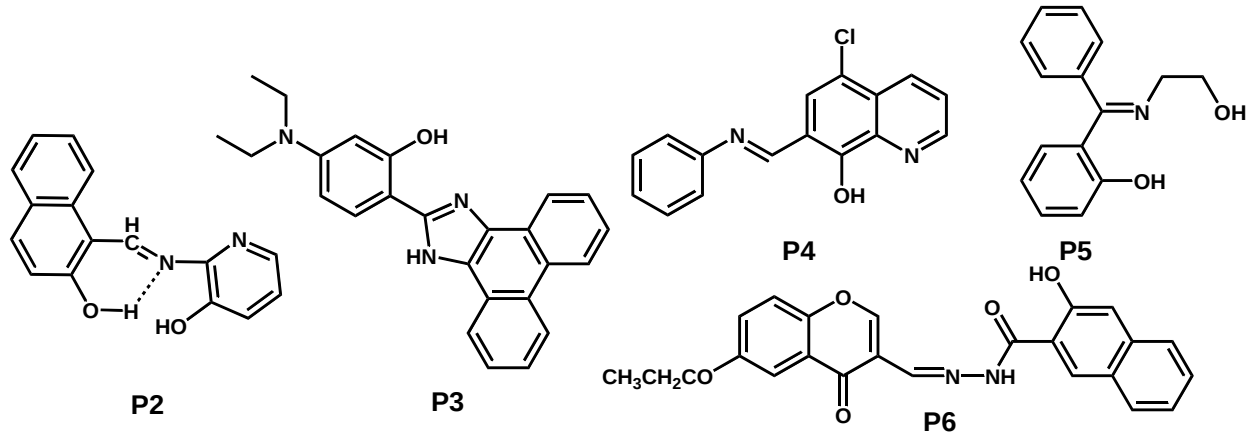

Fig.3. Structural representation of different ligands (P2, P3, P4, P5 and P6)

Phenol-based ligands are also exploited for precise Zn^{2+} detection. M. Ali and co-workers utilized *p*-cresol containing a Schiff-base ligand (**P10**) that was highly selective and sensitive to Zn^{+2} in mixed aqueous medium at physiological pH.[25]A colorimetric and fluorometric dual signaling probe (**P11**) for Mg^{+2} and $Zn^{+2}$was prepared by the same group in 9:1 acetonitrile/water (V/V) medium. The *turn-on* fluorescent enhancement for Mg^{+2} and Zn^{+2} was reported as 40 fold and 53 fold respectively and sensing response was nicely explored *in-vivo* cell imaging.[26] R. G. Harrison *et al.* have synthesized a metal ion sensor (**P12**) containing quinoline and pyridylamino phenolic precursor. It was acted as Zn^{2+}sensor in acetonitrile medium and Cd^{2+} sensor in aqueous medium respectively. The unique combination of pyridine and phenol group appended with quinoline plays the pivotal role for imparting fluoro-sensing selectivity.[27] T. K. Mondal and co-workers reported a coumarin based chemo-sensor (**P13**), in dual switching *turn-on* mode for $Zn^{+2}$and HSO_4^-. Gradual addition of Zn^{+2} to the probe in acetonitrile-water mixture (1:1, V/V) showed an excellent fluorescence emission intensity enhancement ~ 27 fold, whereas that for $HSO_4^-$was 17 fold.[28]

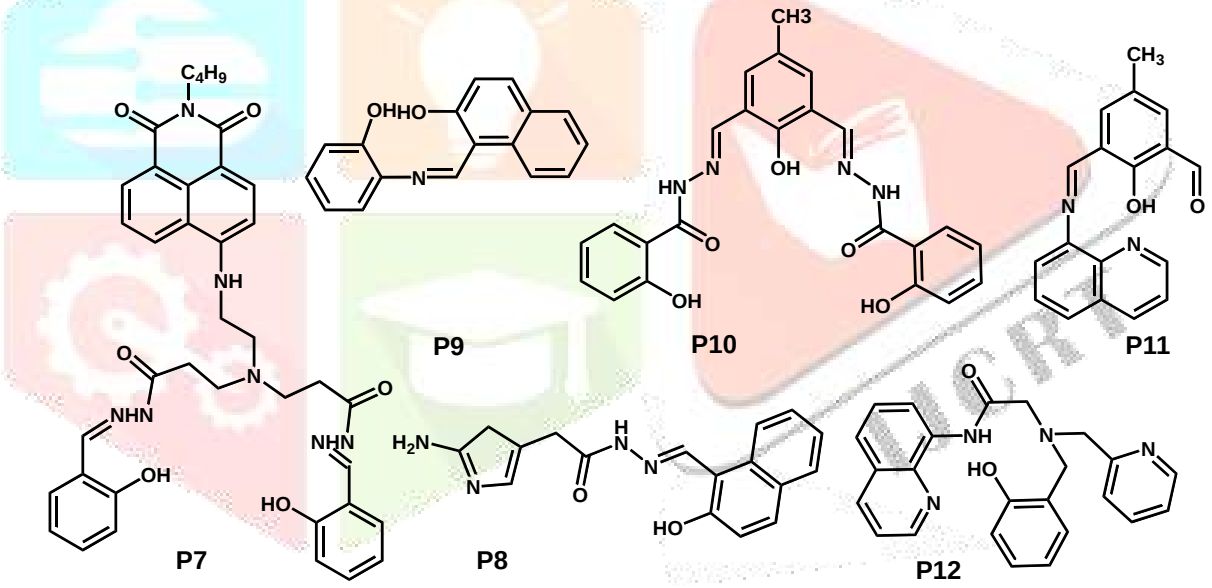

Fig.4. Structural representation of different ligands (P7, P8, P9, P10, P11and P12)

A phenol containing Schiff-base ligand (**P14**) acts as a chemo-sensor for Zn^{+2} over other competitive metals ions in methanol water (4:1) mixture was reported by S. C. Bhattacharya *et al.* using ITC mechanism.[29] In contemporary, M. Hosseini and co-workers have synthesized a water soluble phenol-based ligand (**P15**) for Zn^{+2} sensor at 7.2 pH. Interestingly the sensor was successfully utilized for fluorometric Zn^{+2}determination in water.[30] A physiologically compatible pyridoxal based Zn^{2+} fluorescence chemo-sensor, (**P16**) was reported by S. Goswami and co-workers. It exhibits a *turn-on* fluorescence response for Zn^{2+} in ethanol/water mixture. The combined effect of proton transfer between the prevailing tautomeric forms, C═N isomerization and in consequent metal induced CHEF are responsible for such sensing activity.[31] A water soluble Schiff-base (**P17**), prepared by the same group using salicylaldehyde and 2-amino-1-ethanol, also acts as Zn^{+2} fluorescence sensor at physiological pH.[32] An interesting multi-metal colorimetric and fluorescent sensor (**P18**) based on Schiff base bearing an "O-N-N"-coordination site was developed by S. Jiang and his group. This newly designed sensor is a *turn-on* fluorescence chemo-sensor towards Zn^{2+}. The sensor is also advantageous for cell-imaging. In addition color changes were observed from colorless to yellow, orange and purple respectively for selective binding with Cu^{2+}, $Zn^{2+}$and Ni^{2+} respectively. The corresponding color changes may be utilized for colorimetric determination. The sensor could simultaneously detect and differentiate three transition metal ions through fluorogenic (Zn^{2+}) and chromogenic (Cu^{2+}, $Zn^{2+}$and Ni^{2+}) pathways in aqueous medium.[33]

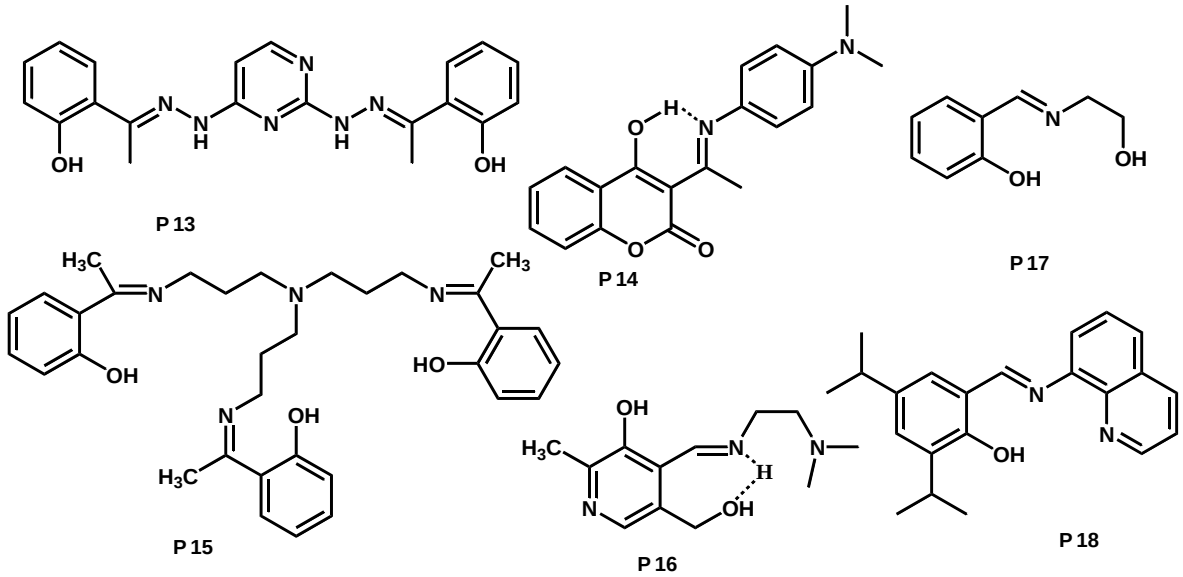

Fig.5. Structural representation of different ligands (P13, P14, P15, P16, P17 and P18)

An amino acid appended Schiff base ligand (**P19**) nicely exhibits its sensing ability for Zn^{+2} was reported by M. A. Neelakantan *et al*. Zn^{+2} ion after complexation in aqueous medium avoids the loss of energy *via* non-radiative transition, resulting fluorescence enhancement.[34] A. Misra and co-workers reported a phenol based new simple and inexpensive fluorescent probe, (**P20**) for Zn^{2+} detection, exploiting its promising CHEF/AIEE features. Sensing ability for Zn^{2+} was observed in dual path way in terms of both colorimetric and fluorometric response in DMF-water (9:1, V/V) medium.[35] P. Rossi *et al*. have synthesized the ligand (**P21**) containing a *bis*-phenolic moiety linked as side arm to an N,N′-dimethylethylenediamine scaffold. The deprotonated form of the ligand selectively coordinates to $Zn^{+2}$and Cd^{+2} ions in 50% ethanol/water medium, resulting sharp increase in emission intensity.[36]

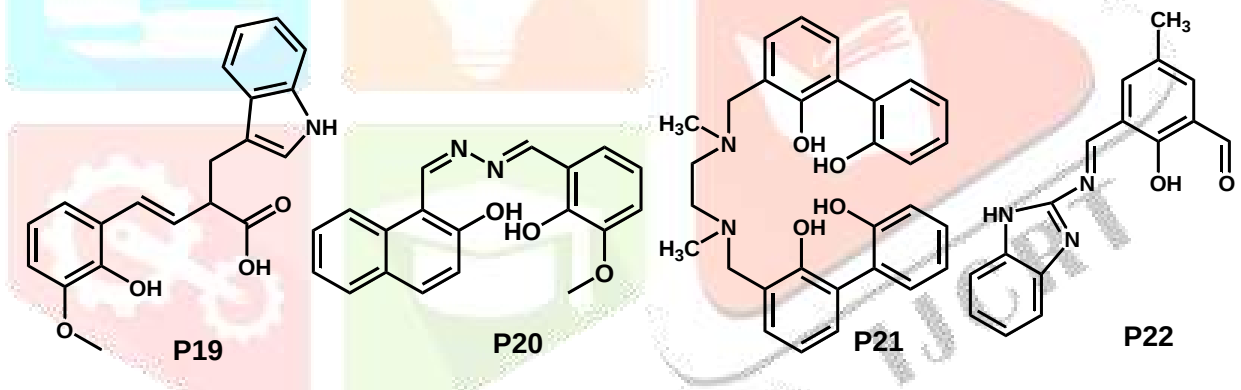

Fig6. Structural representation of different ligands (P19, P20, P21, and P22)

In contemporary, S. Dey and his group have synthesized a novel phenol-based ligand (**P22**), acting as Zn^{2+} sensor by inhibiting the ligand assisted PET in mixed aqueous solvent with very low LOD.[37] M. Shahid and A. Mishra have reported a light stimulated photo-enolization in phenol containing imidazole system by ESPT induced *turn-off-on* fluorescence and ratiometric responses for acetate in mixed aqueous medium.[38] Later, H. Li and co-workers have synthesized a novel cationic fluorescent probe for simultaneous detection of SO_3^{2-}/$HSO_3^-$and HSO_4^-ion with different emission channels. They also reported the fluorescence response in bio-imaging studies for aforesaid ions in HeLa cells.[39] The extracellular pH is often acts as a key factor in many biological processes. In this regard a pioneer work was reported by P. Roy and co-workers.[40] The phenol containing Schiff-base molecule, acts as a pH sensor and exhibits a strong emission band at 464 nm in Britton Robinson buffer solution (pH 2.0) for400 nm excitation. While increasing pH, the intensity at 464 nm decreases gradually and at the same time, a new fluorescence peak emerges at 530 nm and 435 nm in acid and basic region respectively. The probe nicely exploited for unknown pH determination for river water and successfully utilized in bio-imaging studies. It is mentionable that the same group has also designed another Schiff base probe by slight alteration of the mother ligand to monitor the unknown pH both calorimetric *as-well-as* fluorometrically with better sensitivity.[41]

During this period a new 2-(2′-hydroxyphenyl)thiazole-4-carboxaldehyde based fluorescent probe was reported in the literature for sequential detection of Al^{3+} and F^- ions in methanol medium. Al^{3+} was selectively detected through a "*switch on"* response driven by the selective complexation of Al^{3+} ions with ligand by ESIPT and CHEF mechanism followed by F^- ions detected sequentially through a "*switch off"* response.[42] In the same period a new diketopyrrolopyrrole -based dual-responsive colorimetric and fluorescent "turn-on" chemosensor developed for detection of Fe^{3+} ions with high sensitive and selective response based on the inhibition of PET effect and CHEF effect. It also showed a dramatic color change from purple to red with blue shift in absorption maxima and a 9.5-fold fluorescence enhancement response to analyte in water medium.[43] In next year a considerable amount of quality research was published in the literature. Phenyl-ethynyl-phenyl based Schiff base sensor was used to detect Cu^{2+} ions in

water medium with high level of selectivity and sensitivity.[44] A novel terthiophene-derived chemo- sensor was synthesized by a group for colorimetric and fluorescent dual-channel sensing of Fe^{3+} and Cu^{2+} ions with low detection limits.

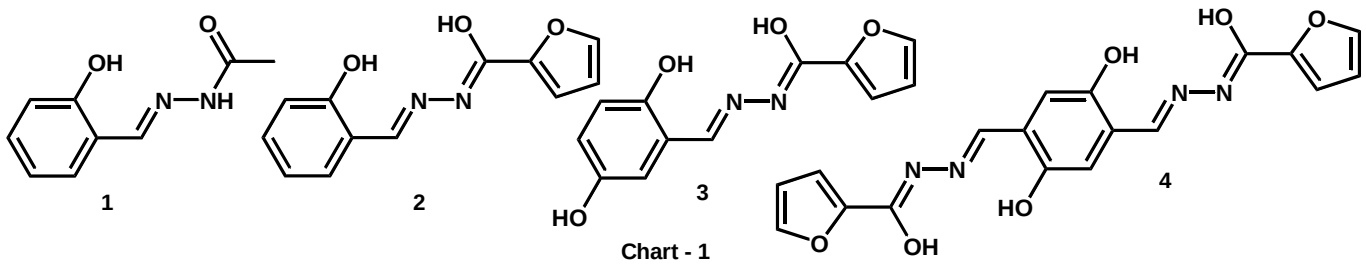

Chart - 1

The chemo-sensor showed a significant fluorescence "turn-on" response to Fe^{3+} and obvious fluorescence turn-off response to Cu^{2+} with high sensitivity, ultrafast response time and high reversibility. They employed the probe to rapidly and visually determine Fe^{3+} and Cu^{2+} in water based on paper test strips and solid silica gel with good results.[45] Based on salicylaldehyde and imidazo[2, 1-b]thiazole a simple Schiff base was exploited to detect Al^{3+} ions through a significant fluorescence enhancement respone via CHEF and inhibition of PET process and then to identify Cu^{2+} selectively through paramagnetic quenching.[46] Two new fluorescence sensors were published by G. Wang and group exploiting benzothiazole moiety identify Fe^{3+} through selective fluorescence quenching response. They employed the probes to monitor the existence of Fe^{3+} ions in living cells.[47] Contemporary a simple sensor was come to the literature to detect various ions and PPi through "turn on-off" response in mixed medium with paper strip test in tap water.[48]

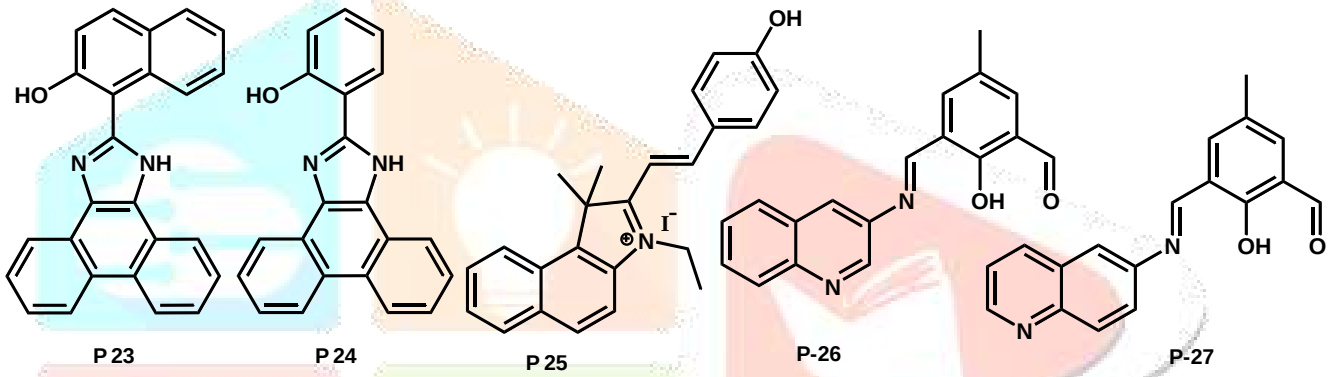

Fig7. Structural representation of different ligands (P23, P24, P25, P26 and P27)

A group of Chinese scientists synthesized a fluorescent chemo-sensor based on a bis(salamo)-like tetraoxime to detect selective metal ions in water medium. It used in double N_2O_2 cavities as sensing elements, which can be combined with specific metal ions to achieve ion recognition. It can detect Cu^{2+} ions by fluorescence quenching response, and a test strip loaded with the sensor is used to quickly and accurately identify Cu^{2+}. Besides, the chemical sensor also can continuously recognize Al^{3+} in the system and realize the interference-free identification effect of other trivalent metal ions on aluminum.[49] Recently, S. K. Chattopadhyay reported a Ni-complex containing phenolic unit to detect most toxic cyanide ion in water medium.[50]

3. Conclusions and Future Outlook

Among many different types of binucleating ligands and more generally polynucleating ligands, the phenol-based ligands and their metal complexes have attracted particularly a great number of researchers. This is due to the key role played by the phenolic group which has many useful electronic and structural characteristics such as: (i) charge as function of pH, spanning from lower pH to higher pH values; (ii) bridging capability, often the phenolic donor atom binds two metal centers in close proximity; (iii) the benzene ring present allows a great synthetic flexibility, (iv) the phenolic chromophore, itself often exhibits fluorescence. Consequently tuning the various characteristic modes to exhibit different physicochemical properties are a great challenge and render special attention. On the other hand, the acid-base properties of the phenol in aqueous solution depends on the ligand topology in which it is inserted, in fact although the phenol loses its acidic proton at pH >10, giving the phenolate anionic species, the process can occur also at lower pH values when the phenol takes part of an amino-phenolic ligand. Often the phenolate oxygen atom takes part to bridge two metal centers. Considering the immense applications in diversified field, phenol containing ligands and their polynuclear complexes demand further exploration. Designing and synthesis of new application oriented phenol based ligands is also a new challenge in this field. Moreover, synthesis of new homo or hetero polynucleating macrocyclic or acyclic metal complexes and isolation of their single crystals not only significant for structural determination that mimick the various metalloenzymes but also important to generate supramolecular motif to understand interesting physicochemical phenomenon.

References

1. P. D. Beer and P. A. Gale, *Angew. Chem. Int. Ed.*, 2001, **40**, 486.
2. J. R. Lakowicz, Principle of fluorescence spectroscopy, *Springer*, New York, 3rdedn, 2006.
3. F. Wang, L. Wang, X. Chen and J. Yoon, *Chem. Soc. Rev.*, 2014, **43**, 4312.
4. *Guidelines for Drinking-water Quality*, Ed. M. Sheffer, World Health Organization, Genva, 1996.
5. Y. L. Pak, K. M. K. Swamy and J. Yoon, *Sensors*, 2015, **15**, 24374.

6. A. Vlcek, *Coord. Chem. Rev*., 2002, **230**, 225.
7. B. Valeur, I. Leray, PCT (Photoinduced Charge Transfer) Fluorescent Molecular Sensors for Cation Recognition, 2001, **vol 1**. Springer, Berlin, Heidelberg.
8. Z. Xu, Y. Xiao, X. Qian, J. Cui and D. Cui, *Org. Lett*., 2005, **7**, 889. (ICT)
9. S. Guha, S. Lohar, A. Sahana, A. Banerjee, D. A. Safin, M. G. Babashikina, M. P. Mitoraj, M. Botle, Y. Garcia, S. K. Mukhopadhyay and D. Das, *Dalton Trans.*, 2013, **42**, 10198.
10. J. M. Serin, D. W. Brousmiche and J. M. J. Frechet, *J. Am. Chem. Soc.*, 2002, **124**, 11848.
11. K. Kaur, R. Saini, A. Kumar, V. Luxmi, N. Kaur, P. Sing and S. Kumar, *Coord. Chem. Rev.*, 2012, **256**, 1992.
12. X. Lou, D. Ou, Q. Li and Z. Li, *Chem. Commun.*, 2012, **48**, 8462.
13. D. Wu, A. C. Sedgwick, T. Gunnlaugsson, E. U. Akkaya, J. Yoon and T. D. James, 2017, **46,** 7105.
14. Z. Xu, X. Chen, H. N. Kim and J. Yoon,*J. Am. Chem. Soc.*, 2010, **39**, 127.
15. Y. Lu, S. Huang, Y. Liu, S. He, L. Zhaoand X. Zeng, *Org. Lett.*, 2011, **13**, 5274.
16. W. H. Ding, W. Cao, X. J. Zheng, D. C. Fang, W. T. Wongand L. P. Jin, *Inorg. Chem.*, 2013, **52**, 7320.
17. S. Sinha, B. Chowdhuryand P. Ghosh, *Inorg. Chem.*, 2016, **55**, 9212.
18. K. Boonkitpatarakul, J. Wang, N. Niamnout, B. Lui, L. Mcdonald, Y. Pangand M. Sukwattanasinitt, *ACS Sens.*,2016**, 1**, 144.
19. J. Wang, Y. Li, K. Li, X. Mengand H. Hou, *Chem. Eur. J.*, 2017, **23**, 5081.
20. B. Naskar, R. Modak, Y. Sikdar, D. K. Maity, A. Bouza, A. Frontera, A. Katarkar, K. Choudhuriand S. Goswami, *Sens. Actuators B*,2017, **239**, 1194.
21. L. Liu and Z. Yang, *Inorganica Chim. Acta*, 2018, **469**, 588.
22. Y. Xu, S. Mao, H. Peng, F. Wang, H. Zhang, S. O. Aderinto and H. Wu, *J. Lumin.*, 2017, **192**, 56.
23. S. R. Gupta, P. Singh, B. Koch and V. P. Singh, *J. Photochem. Photobiol. A*, 2017, **348**, 246.
24. S. Sarma, A. Bhowmik, M. J. Sarma, S. Banu, P. Phukan and D. K. Das, *Inorganica Chim. Acta*, 2018, **469**, 202.
25. R. Alam, T. Misti, A. Katakar, K. Chaudhuri, S. K. Mandal, A. R. Khuda-Bukhsh, K. K. Dasand M. Ali, *Org. Biomol. Chem.*, 2012,**10**,2380.
26. T. Misti, M. Dolai, D. Chakraborty, A. R. Khuda-Bukhsh, K. K. Dasand M. Ali, *Analyst*,2014,**139**,4022.
27. E. J. Song, J. Kang, G. R. You, G, J. Park, Y. Kim, S. J. Kim, C. Kimand R. G. Harrison, *Dalton Trans.*,2013,**42**,15514.
28. D. Sarkar, A. K. Pramanikand T. K. Mondal, *RSC Adv.*, 2014, **4**, 25341.
29. S. S. Mati, S. Chall, S. Konar, S. Rakshit and S. C. Bhattacharya, *Sens. Actuators B*,2014, **201**, 204.
30. M. Hosseini, A. Ghafarloo, M. R. Ganjali, F. Faridbod, P. Norouziand M. S. Niasari, *Sens. Actuators B*,2014, **198**, 411.
31. S. Mandal, Y. Sikdar, D. K. Maiti, G. P. Maiti, S. K. Mandal, J. K. Biswasand S. Goswami, *RSC Adv*., 2015, **5**, 72659.
32. B. Naskar, R. Modak, Y. Sikdar, D. K. Maity, A. Banik, T. K. Dangar, S. Mukhopadhyay, D. Mandaland S. Goswami, *j. Photochem. Photobiol. A*, 2016, **321**, 99.
33. C. Chen, G. Men, W. Bu, C. Liang, H. Sunand S. Jiang, *Sens. Actuators B*, 2015, **220**, 463.
34. L. Subha, C. Balakrishnan, S. Natarajan, M. Theetharappan, B. Subramanianand M. A. Neelakantan, *Spectrochim. Acta A*, 2016,**153**,249.
35. M. Shyamal, P. Mazumder, S. Maity,S. Samanta, G. P. Sahooand A. Misra, *ACS Sens.*, 2016**, 1**, 739.
36. G. Ambrosi, M. Formica, V. Fusi, L. Giorgi, E. Macedi, M. Micheloni, P. Paoliand P. Rossi, *Inorg. Chem.*, 2016, **55**, 7676.
37. S. Dey,A. Roy,G. P. Maiti, S. K. Mandal, P. Banerjee and P. Roy, *New J. Chem.*, 2016, **40**, 1365.
38. M. Shahid and A. Misra, *J. Photochem. Photobiol. A*, 2017, **335**, 190.
39. T. Yu, G. Yin, T. Niu, P. Yin, H. Li, Y. Zhang, H. Chen, Y. Zengand S. Yao, *Talanta*, 2018, **176**, 1.
40. S. Halder, A. Bhattacharjee, A. Roy, S. Chatterjee and P. Roy, *RSC Adv.*, 2016, **6**, 39118.
41. S. Halder, A. Hazra and P. Roy, *J. Lumin.*, 2018, **195**, 326.
42. C. Lim, H. Seo, J. H. Choi, K. S. Kim, A. Helal and H. S. Kim, *J. Photochem. Photobiol. A*, 2018, **356**, 312.
43. S. Zhang, T. Sun, D. Xiao, F. Yuan, T. Li, E. Wang, H. Liu and Q. Niu, *Spectrochim. Acta A*, 2018, **189**, 594.
44. M. Korzec, S. Senkala, R. R. Korzec, S. Kotowicz, E. S. Balcerzak and J. Polanski, *J. Photochem. Photobiol. A*, 2019, **382**, 111893.
45. J. Wang, T. Wei, F. Ma, T. Li and Q. Niu, *J. Photochem. Photobiol. A*, 2019, **383**, 111982.
46. Y. Xu, L. Yang, H. Wang, Y. Zhang, X. Yang, M. Pei and G. Zhang, *J. Photochem. Photobiol. A*, 2019, **391**, 112372.
47. X. Gong, X. Ding, N. Jiang, T. Zhong and G. Wang, *Microchemical Journal*, 2020, **152**,104351.
48. Z. A. Consty, Y. Zhang and Y. Xu, *J. Photochem. Photobiol. A*, 2020, **397**, 112578.
49. R. N. Bian, J. F. Wang, Y. J. Li, Y. Zhang and W. K. Dong, *J. Photochem. Photobiol. A*, 2020, **403**, 111829.
50. A. Mondal and S. K. Chattopadhyay, *ACS Omega*, 2022, 7, **45**, 40941.

IJCSPUB.ORG ISSN : 2250-1770
INTERNATIONAL JOURNAL OF CURRENT SCIENCE (IJCSPUB)
IJCS PUBLICATION (IJCSPUB.ORG) An International Open Access, Peer-reviewed, Refereed Journal

Fluorescence Probing Of Ph Dependent Aggregations And Micellization Of Amphiphilic Block Copolymer At Ultra-Dilute Condition

Subhodip Samanta[a] and Sanju Das[a*]

[a] Department of Chemistry, Maulana Azad College, Kolkata 700013, India

Abstract:

Possible pH dependent aggregation as well as micellization behaviour of amphiphilic block copolymers consisting of poly-(DMA) (DMA= 2-(dimethylamino) ethyl methacrylate) as the hydrophilic block and poly-(MMA) (MMA=methyl methacrylate) is probed by the Coumarin 153 (C-153) as a fluorescent probe molecule. The C-153 molecules are preferentially accommodated in the hydrophobic core region of micelles and aggregates of amphiphilic block copolymers, which is characterized by a strongly non-polar microenvironment of the probe. Steady state and time resolved fluorescence, and dynamic light scattering studies have shown that micellization occurs in presence of ultra dilute polymer concentration range of about 0.001 – 0.005 g/L (32 – 160 nM) in pH 7.0 medium, whereas in pH 9.0 medium micellization takes place at more than three times higher polymer concentration. But on increasing the pH of the medium from 7.0 to 9.0, the aggregation with few numbers of polymer molecules is favored due to the positively charged polymer molecules becomes electrically neutral and hence the intermolecular hydrophobic interaction will work more efficiently at higher pH condition. On the other hand, possible intermolecular H-bonding interaction between protonated hydrogen in the amide moiety of DMA and the carbonyl oxygen of MMA may facilitate the process of micellization at pH 7.0.

Key words: Fluorescent Probe, Micellization, Amphiphilic Block Copolymer, Hydrophobic interaction

1. Introduction

Polymeric micelles derived from block copolymers in an aqueous phase have attracted much attention; because of their unique morphological behavior and a fascinating range of properties.[1-4] Block copolymer micelles have several useful characteristics such as nano size, enormous mechanical and thermodynamic stability etc. Among various polymeric micellar NPs, amphiphilic block copolymeric micelles, which possess significant potential as a carrier for drug delivery,[5-7] have been chosen for present investigation, primarily due to the chemical flexibility of their structure and their outstanding physicochemical and biological properties including biocompatibility[3,4] and various extent of self-assembly property in physiological condition. For instance, the size and shape as well as the different other properties of micelle can be controlled by varying the relative length of hydrophilic part compared to the hydrophobic part.[8]

Block copolymer showing remarkable ability to solubilize low-molecular weight hydrophobic organic guest molecules and transport them efficiently through an aqueous medium.[5-7,9,10] The micellization of block copolymers as a function of temperature and copolymer concentration has been studied using various techniques like thermal analysis,[11] light scattering,[12] surface tension measurement,[13,14] optical absorption,[15] fluorescence spectroscopy,[16-18] etc. Among these, fluorescence spectroscopy has emerged as a powerful technique, since it allows not only the determination of such micellization parameters as critical micellization concentration (CMC) and critical micellization temperature (CMT), but also provides a means to investigate the local environment experienced by the small fluorescent probe molecules at various regions within the micelle.[16-18] This is particularly relevant in the context of the drug-delivery problem, since the nature of the micellar microenvironment is an important factor governing the uptake and release of a small drug molecule by a nano-particulate micelle.[5-7]These micelles are aggregates that have been observed for a variety of block copolymers in water, polar and nonpolar organic solvents, and more recently, in supercritical fluids. For this generality and for the possibility of tuning the aggregate properties by varying either the kind of monomer or the size and proportion of the constituting blocks, these aggregates are able to provide a much wider range of applications involving solubilization of drugs or pollutants, as nanoreactors, as potential DNA carriers, cosmetic industry, templates for inorganic synthesis, protective shells for sensitive enzymes and catalysts, or as confined reaction vessels for performing bio-chemistry even at a single molecule level etc.

In the present work the microenvironment and micellization characteristics of block copolymers having specific hydrophobic and hydrophilic compartment is investigated using coumarin 153 (C-153) as a fluorescent probe molecule. The morphological representations of block copolymers are shown in Fig. 1, along with the molecular formulae of the individual blocks. This copolymer is $DMA_{60}MAA_{60}DMA_{60}$ tri block copolymers with average molecular weight ~ 30,000 D and consist of linear morphology. The hydrophilic part comprises of poly-(DMA) blocks and hydrophobic part comprises of poly-(MMA) blocks, where DMA= 2-(*N*, *N*-dimethyl amino ethyl methacrylate) and MMA = methyl methacrylate, as illustrated in Fig.1.

The above polymers are particularly interesting because aqueous solutions of similar block copolymers are known to form micelles within the size range of nano particles.

The C-153 is chosen as the fluorescence probe due to its fluorescence properties are known to be extremely sensitive to the polarity of its immediate microenvironment.[18-21] In media with low polarity, the fluorescence intensity and lifetime of C-153 increase, while the fluorescence peak-position is blue-shifted, a property that has been used in numerous systems to probe the local microenvironment.

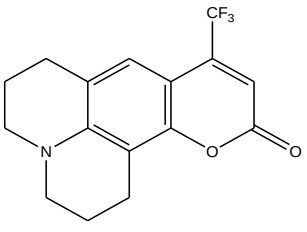

Coumarin 153

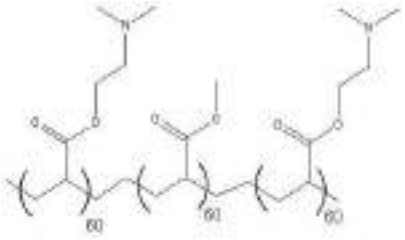

Block copolymer

Scheme 1: Structure of coumarin 153 and copolymer

Recently, Castner and co-workers have shown that the thermally-induced micellization of Pluronic F88 triblock copolymer was reported by three different fluorescent probes in different ways: the most hydrophobic probe, Coumarin 153, showed a sharp response, while the response of the less hydrophobic Coumarin 102 and Coumarin-343 were gradual.[16] They attributed this difference to the fact that C-153 tends to reside predominantly near the

hydrophobic PPO core, while the other two probes partition between the core and the hydrophilic shell. As a result, the former is more sensitive to the dehydration of the core region during micellization.

In this study, we have found that $DMA_{60}MAA_{60}DMA_{60}$ form micelle at extremely diluted condition at ~ 0.005 g/lit (160 nM) at pH 7.0 in sodium phosphate buffer, whereas the micellization occurs at relatively higher concentration when the pH of the medium is higher. To the best of our knowledge, this is the first report of micellization in such a dilute polymer concentration. We have also detected the premicellar aggregates at even lower concentration ~ 0.001 g/L (32 nM) preferably at higher pH condition. We have employed steady state and time resolved fluorescence, and dynamic light scattering methods for the present investigation.

2. Experimental Section

2.1 Material

The $DMA_{60}MAA_{60}DMA_{60}$ triblock copolymer was received as gift and used without further purification. Laser grade C153 was obtained from Exciton, USA, and used as received. $Na_2HPO_4,.H_2O$, NaH_2PO_4,H_2O, Na_2CO_3, $NaHCO_3$ and NaCl were obtained from Aldrich, and used without further purification. Deionized water, having a conductivity of 0.1 μS cm^{-1}, was obtained by passing distilled water through a Millipore Water System and used for the preparation of the different solutions.

Preparation of buffer:

The buffer with pH 7.0 was obtained as follows. 20 mM Na_2HPO_4, H_2O solution was added gradually to 20 mM NaH_2PO_4, H_2O until the pH of solution became 7.0 at 25°C. The buffer solution with pH 9.0 was obtained by appropriate mixing of 20 mM $NaHCO_3$ with 20 mM Na_2CO_3 at 25°C.

Preparation of polymer and C-153 solution:

The stock solution of poly-(DMA-b-MMA-b-DMA) was prepared as follows. About 0.035 g of solid copolymer was taken by accurate weight in 3.0 mL DMF and stirred until the entire solid dissolved in DMF. Then deionized water was added drop wise until the total volume of the solution became 25 mL. The resulting solution was dialyzed overnight to remove DMF from the polymer solution using the dialysis bag (cutoff range 6000 to 8000 Da). After dialysis, the volume of solution was measured accurately and added further water until the concentration of solution became 1.0 g/L. Experiments were performed by diluting the stock solution of 1.0 g/L in the buffer medium. The stock solution of C-135 was prepared in MeOH and the concentration was measured from literature extinction coefficient value by UV-Vis absorbance study. The concentration of C-153 was 5.5×10^{-7} M for all fluorescence experiments. All the solutions were filtered through syringe filter of pore size 0.2 μm.

2.2 Methods

Absorbance spectra were measured with Shimadzu UV-1601PC UV-Vis spectrophotometer. Fluorescence spectra were recorded on a Spex Fluorolog-2 spectrophotometer equipped with DM3000F software. The excitation and emission slits were set at 5 nm (excitation) and 3 nm (emission) respectively. Emission spectra were obtained with excitation wavelengths at 420 nm. All the experiments were done at 25˚ C.

Time-resolved fluorescence measurements were carried out using time-correlated-single photon–counting (TCSPC) techniques. The nanosecond diode (IBH, U. K. nano-LED) as the light source at 450 nm were used as the excitation source and a TBX4 detection module (IBH, U.K.) coupled with a special Hamamastu photomultiplier tube (PMT) was used for the detection of the fluorescence decays. The time resolution achievable with the present setup following deconvolution analysis of the fluorescence decays is about 50 ps. Fluorescence decays were recorded with a vertically polarized excitation beam and fluorescence was collected at the magic angel 54.7˚. Measurements were repeated three times to check the reproducibility.

The hydrodynamic diameter of micelle and aggregates were estimated by Dynamic Light Scattering (DLS) method with DLS-nano ZS90, zeta sizer, nano series, Malvern instrument. In DLS, the monochromatic light beam, e.g. laser, irradiate the particles whose have the diameter much smaller than the incoming wavelength. Then light is scattered by the particles in all directions. The observed scattered light intensity at any instant will be a result of the interference of light scattered by each element. Particles in random Brownian motion show fluctuations in measuring the scattered light intensity. These fluctuations of the scattered light are recorded and then analyzed using the autocorrelation function. It gives a description of the particle's motion in the medium, measuring the diffusion coefficient (D) of the dispersed particles (taken to be spherical) and evaluates the hydrodynamic diameter (d_h) in terms of Stokes–Einstein equation.

3. Result and Discussion

In the present study, we have chosen Coumarin 153 (C-153) as a fluorescent probe for studying the microenvironment of amphiphilic block copolymeric systems (Scheme 1). The polymer contains hydrophilic amide moiety and hydrophobic ester moiety showing amphiphilic behavior in aqueous medium. When this block copolymer forms micelle, the amide groups are oriented towards the bulk water phase and the hydrophobic ester groups form the core structure of the micelle. In a previous study, it has been observed that, at pH lower than 8.0, some amount of positive change is generated in the polymer surface due to the protonation of amide moiety of DMA, whereas the polymer becomes neutral at higher pH[8].

To determine the specific role of the pH induced protonation of DMA-block for the formation of micelles or aggregates, we have investigated the comparative micellization process at the two different pH conditions (pH 7.0 and pH 9.0) of the medium.

3.1 Fluorescence studies

Steady state absorbances of C-153 (not shown here) have been carried out in the presence of different copolymer concentration to investigate possible ground state interaction between polymer and the fluorescent probe molecules. No perceptible changes in the absorbance spectrum as observed indicate that there is no prominent ground state interaction between C-153 and polymeric molecule.

In all the fluorescence measurements, the absorbance maxima at ~425 nm of C-153 in aqueous medium has been selected as the excitation wavelength.

The fluorescence measurements have been performed starting from very diluted polymer concentration ~ 0.001 g/L (about 32 nM) to a concentration of ~ 0.5g/L (about 16 μM) at two different pH (7.0 and 9.0) conditions (Fig. 1 A to D). The fluorescence response of C-153 (with a fixed concentration of 5.5×10^{-7} M in each polymer solution), at both the pH conditions, is found to be a function of the increasing polymer concentration.

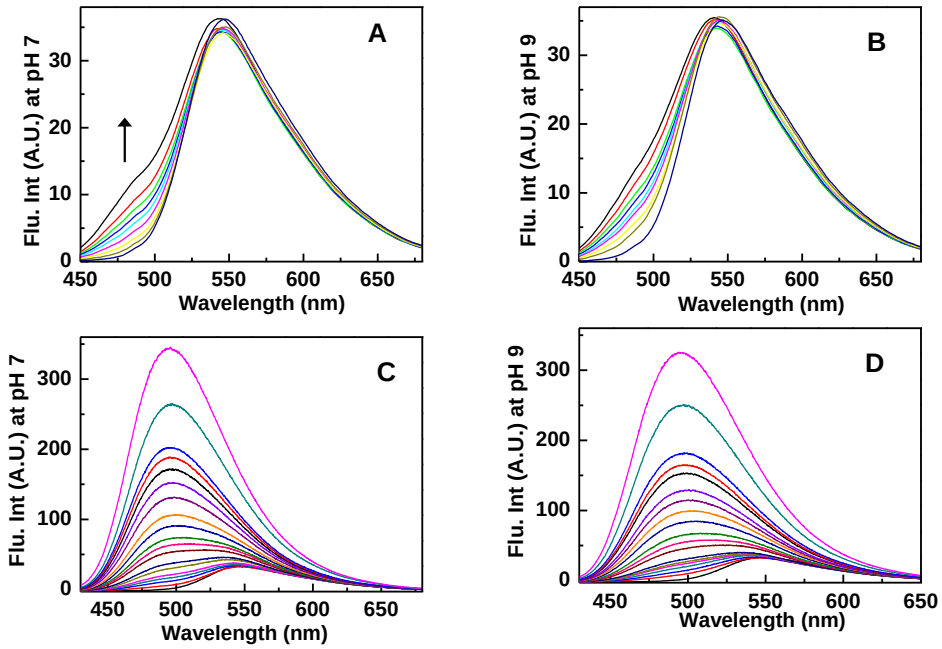

Figure 1: Steady state fluorescence spectra in presence of various polymer concentrations at different pH at 25^{0}C. (A, B) Fluorescence spectra at the lower concentration region (0.0 – 0.005 g/L) and (C, D) Fluorescence spectra at the higher concentration region (0.0 – 0.5 g/L). C-153 concentration was 5.5×10^{-7} M for all measurements. The direction of arrow indicates the fluorescence change in presence of polymer.

In pH 7.0 medium, gradual increase in the concentration of the polymer solution (lower concentration region, 0.0 – 0.005 g/L) results to the generation of a new blue shifted peak at ~ 485 nm apart from the regular peak at ~ 550 nm (Fig-1A). The fluorescence intensity of both the peaks of C-153 (~ 485 nm and ~ 550 nm) increases with increasing concentration of polymer solution. Whereas, at pH 9, similar increase in polymer concentration results almost same magnitude of overall fluorescence enhancement, but without the formation of any new peak (Fig-1B).

The gradual increase in fluorescence intensity may be due to the location of C-153 in the hydrophobic environment produced by the self-aggregation of polymeric molecules. However, the generation of a new peak ~ 485 nm in pH 7.0 medium clearly indicates the formation of specific hydrophobic environment by an appreciable amount and which may suggest that majority of polymeric molecules are aggregated in a specific manner. On the other hand, absence of such new fluorescence peak at pH 9.0 was probably due to the superposition of different fluorescence response from multiple types of aggregated forms without maintaining any specific arrangement.

On further increase of polymer concentration from 0.01 to 0.5 g/L, the fluorescence intensity increases mostly around 500 nm at both the pH conditions (Fig. 1C and D). Although, the magnitude of fluorescence enhancement is similar at both pH conditions, the half width of the emission curve at all polymer concentration is noticeably larger in case of pH 9.0 compared to pH 7.0 (Fig. 1C and D). This result also indicates the presence of greater number of multiple aggregated forms at pH 9.0 relative to that at pH 7.0.

3.2 *Fluorescence lifetime measurement*

Fluorescence lifetime analysis plays critical role for identification of different micro-domains and solvation properties in presence of self-assembling systems. Since C-153 shows large dynamic stroke shift and higher quantum yield and subsequently larger excited state lifetime in the nonpolar medium, the lifetime analysis could be important to understand the nature of micro-environment produced in presence of various of polymeric solutions Emission lifetimes are measured in the presence of different polymer concentration 0.001 – 0.5 g/L at two different emission wavelengths (at 500 and 550 nm) respectively and the fluorescence decay analysis are performed using an iterative convolution method (Fig 2A and B). The reason behind choosing these wavelengths is mainly due to determination of relative amount of aggregation, since fluorescence maxima are shifted from 550 to 500 nm in presence of different amount of polymer solution.

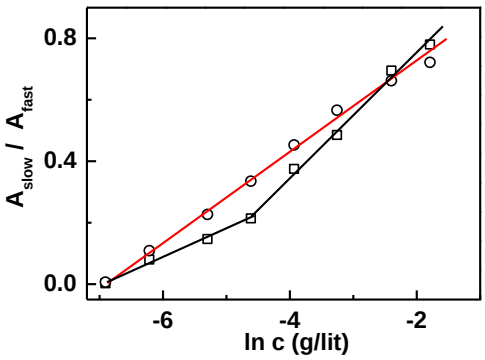

Figure 2: Fluorescence transients of C-153 at (A) pH 7.0 and (B) 9.0 in presence of 0.0 (red), 0.001(blue), 0.005 (pink), 0.040 (dark yellow), and 0.5 (purple) g/L polymer solution. Scattering profile is shown by black curve. The excitation and emission wavelength were 450 and 500 nm respectively.

In absence of polymer, the fluorescence lifetime measurement plot of C-153 best fits to the mono-exponential decay having the same rate constant (~ 1.6 ns) at both the pH. The result suggests that the change in solvent pH from 7.0 to 9.0 does not contribute any change in fluorescence lifetime of C-153 (Fig 2A and B). In presence of very dilute polymer concentration of ~ 0.001 g/L, at both the pH conditions, the mono exponential behavior changes into bi-exponential decay with fluorescence lifetime of ~ 1.6 (fast decay) and ~ 6.0 ns (slow decay), particularly in the 500 nm region. The additional 6.0 ns lifetime even in presence of trace amount of polymer clearly indicates that some aggregated form is generated with nonpolar micro-environment, where the excited state of C-153 is significantly stabilized due to decrease in non-radiative decay rates. The magnitude of slower component with larger fluorescence lifetime gradually increases with increasing polymer concentration due to greater number of aggregated polymers resulting less amount of free dye (Fig. 3).

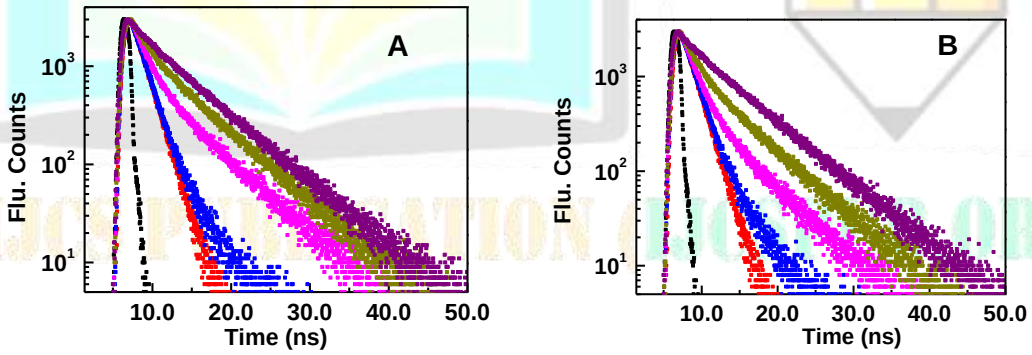

Figure 3: The ratio between slow and fast component obtained from the bi-exponential fitting of fluorescence transients at pH 7.0 (square, black line) and pH 9.0 (circle, red line) in presence of various polymer concentrations. The ratios are plotted with natural logarithmic of concentration.

The unchanged fluorescence lifetime in these two different pH as well as in presence of increasing polymer concentration suggests that the micro-environment of different aggregated forms is similar in nature. However, the plot of the ratio of slow and fast component of the fluorescence lifetime with natural logarithm of the polymer concentration shows single liner correlation at pH 9.0, whereas two different linear behavior with difference in the slop values is observed at pH 7.0 condition (Fig. 3). In the lower polymer concentration (< 0.01 g/L), a smaller number of associated forms may be produced at pH 7.0 compared to pH 9.0, but the amount of association increases more rapidly with increasing amount of polymer concentration beyond 0.01 g/L on lowering the pH of the medium resulting in the two different liner correlation.

3.3 Dynamic Light Scattering measurements

Dynamic Light Scattering (DLS) is a technique that can be used to determine the size distribution profiles of small particles with nm to μm diameter size in suspension or polymers in solution. In the present case, DLS study has been utilized to determine the relative size (hydrodynamic diameter) distribution of the aggregated form of polymer at two different pH (7.0 and 9.0) in presence of different polymer concentrations (Fig. 4).

The formation of nanoparticle with diameter of about 200 nm is detected in presence of 0.005 g/L at pH 7.0, whereas the formation of nanoparticle with average diameter of about 170 nm is observed in presence of three-fold excess polymer amount of about 0.015 g/L at higher pH 9.0 condition. Interestingly, the particle sizes remained the same in presence of all the higher amount of polymer concentrations at both the pH conditions, although the average diameter is smaller by a magnitude of 30 nm in case of pH 9.0. Since the average diameter does not change perceptibly with the polymer concentration, it has presumed that micellization occurs at 0.005 g/L for pH 7.0, whereas threefold higher amount of polymer (0.015 g/L) is needed to form micelle at pH 9.0.

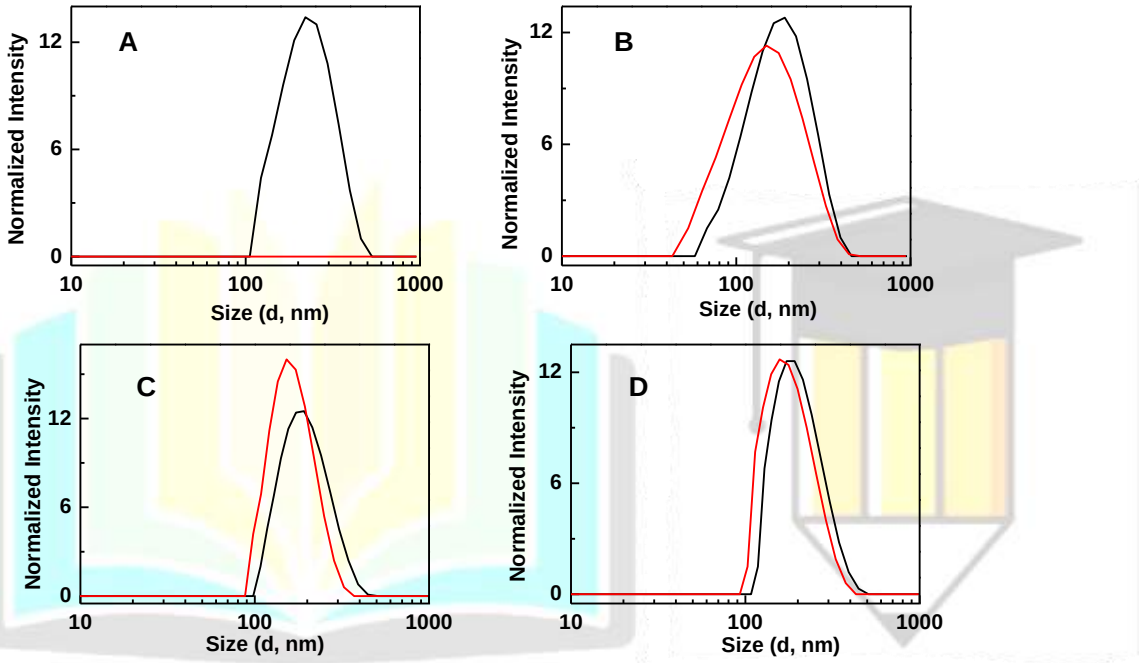

Figure 4: Distribution of average particle size was obtained from dynamic light scattering at pH 7.0 (black curve) and pH 9.0 (red curve) in presence of (A) 0.005, (B) 0.015, (C) 0.040 and (D) 0.500 g/L polymer concentration.

3.4 Effect of salt on polymeric aggregation

To evaluate the possible driving force for the aggregation processes, fluorescence study of diluted polymeric solution (~ 0.002 g/L) at both the pH conditions is performed in the presence of various salt concentrations (Fig. 5). We have chosen diluted polymeric condition, where hardly any micellization occurs at both pH conditions. In case of pH 9.0, the magnitude of fluorescence intensity at ~ 500 nm is increased noticeably in presence of 10 – 50 mM sodium chloride, whereas fluorescence intensity remains almost unaffected for pH 7.0 at the same salt concentration.

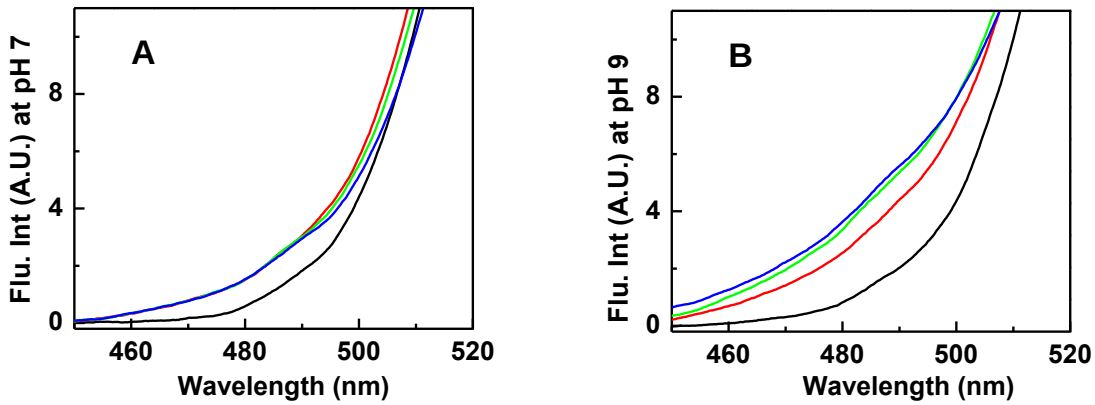

Figure 5: Steady state fluorescence spectra of the solution containing 0.002 g/L polymer in presence of various NaCl solution at (A) pH 7.0 and (B) pH 9.0. Salt concentrations were 0.0 (red), 30 mM (green) and 100 mM (blue). The black curve represented the spectra in absence of polymer.

The result suggests that the hydrophobic interaction among the neutral polymer molecules at pH 9.0 plays crucial role for the aggregation at diluted polymeric condition. Such intermolecular hydrophobic interaction between positively charged polymer molecules is not so operative at pH 7.0 due to same charge repulsion between protonated forms of the polymer molecules and hence the fluorescence intensity ~ 500 nm remain constant.

4. Conclusion

The above results have shown that the block copolymer form different types of aggregations depending on the pH of the medium. The nature of aggregates has been identified by steady state and time resolved fluorescence as well as dynamic light scattering methods. Although similar magnitude of fluorescence enhancement until 0.005 g/L polymer concentration is detected at either pH condition, the shape of the spectra at ~ 500 nm is showing some difference in two pH medium. A clear peak is found at pH 7.0, whereas contentious fluorescence increase is observed at pH 9.0 (Fig. 1A and B). The existence of particle with average diameter of about 200 nm is detected by DLS study only in case of pH 7.0 and we presumed the increase of fluorescence is observed mainly due to formation of this particle (Fig 4). Since the existence of particles are not detected at pH 9.0 by DLS measurement, the fluorescence enhancement occurs probably due to the formation of aggregate with fewer number of polymer molecules which could be difficult to detect by DLS measurement. Moreover, at pH 9.0, the bi-exponential behavior in the fluorescence lifetime analysis also suggests the existence of the aggregates even in presence of 0.001 g/L polymer concentration (Fig. 2B). But higher contribution of the slow component at pH 9.0 compared to pH 7.0 under same polymer concentration indicates that a greater number of dye molecules are associated at pH 9.0, because smaller number of polymer molecules are involved to form single aggregate at pH 9.0 due to its smaller size, whereas larger particle size at pH 7.0 needs a greater number of polymer molecule which results fewer number of particles (Fig. 2 and 3 Table 1). However, the particles with average diameter 170 nm were started to form in presence of three-fold higher polymer concentration (~ 0.015 g/L) at pH 9.0. This result indicates that micelle formation is more favorable at lower pH condition, whereas the formation of aggregates with lower molecular weight becomes easy at pH 9.0.

The higher width of the steady state fluorescence spectra at pH 9.0 compared to pH 7.0 in presence of all the polymer concentrations also suggests the existence of a greater number of different aggregated forms with variable fluorescence properties. Since the amide moiety becomes positively charged at pH 7.0 due protonation, the hydrophobic interaction during aggregation is not energetically favorable due to columbic repulsion, but the possible intermolecular H-bonding interaction between protonated hydrogen in the amide moiety of DMA and the

carbonyl oxygen of MMA may facilitated the process of micellization. The little larger micellar size at pH 7.0 was found due to micellization becomes more favorable at this pH. The enhancement of fluorescence intensity at ~ 500 nm in presence of electrolyte at pH 9.0 also suggests that the aggregation occurs due to the presence of intermolecular hydrophobic interaction (Fig-5).

References

1. M. V. Velasco, A. Munoz, M. R. Jimenez-Castellanos, I. Castellano, I. Goni, M. Gurruchaga, Int J Pharm, 136 (1996) 107.
2. I. Goni, M. C. Ferrero, M. R. Jimenez-Castellanos, M. Gurruchaga, Drug DevInd Pharm 28 (2002) 1101.
3. D. Rutot, E. Duquesne, I. Ydens, P. Degee, P. Dubois 73 (2001) 561.
4. S. Ohya, Y. Nakayama, T. Matsuda Biomacromolecules 2 (2001) 856.
5. I.W. Hamley, Soft Matter 1 458 (2005) 36.
6. J. Ding, G. Liu, J. Phys. Chem. B 102 (1998) 6107.
7. Z. Zhang, G. Liu, S. Bell, Macromolecules 33 (2000) 7877.
8. Y. Sarkar, S. Roy, R. Majumder, S. Das, D.V. Bhalani, S.K. Jewrajka, P.P Parui, Soft Matter 16 (2020) 798.
9. A.V. Kabanov, I.R. Nazarova, I.V. Astafieva, E.V. Batrakova, V.Yu. Alakhov, A.A. Yaroslavov, V.A. Kabanov, Macromolecules 28 (1995) 2303
10. P.K. Sharma, S.R. Bhatia, Int. J. Pharm. 278 (2004) 361
11. G.Wanka, H. Hoffmann,W. Ulbricht, Macromolecules 27 (1994) 4145.
12. C. Booth, D. Atwood, Macromol. Rapid Commun. 21 (2000) 501.
13. U. Chatterjee, S.K. Jewrajka, B.M. Mandal, Polymer 46 (2005) 10699.
14. P. Alexandridis, V. Athanassiou, S. Fukuda, T.A. Hatton, Langmuir 10 (1994) 2604.
15. J.R. Lopes,W. Loh, Langmuir 14 (1998) 750.
16. C.D. Grant, M.R. DeRitter, K.E. Steege, T.A. Fadeeva, E.W. Castner Jr., Langmuir 21 (2005) 1745.
17. S. Jeon, S. Granick, K.W. Kwon, K. Char, J. Polymer. Sci. 40 (2002) 2883.
18. C.D. Grant, K.E. Steege, M.R. Bunagan, E.W. Castner Jr., J. Phys. Chem. B109 (2005) 22273.
19. J.R. Lakowicz, Principles of Fluorescence Spectroscopy, Kluwer Academic/Plenum Publishers, New York, 1999. 506
20. G. Jones II., W.R. Jackson, C.-Y. Choi, W.R. Bergmark, J. Phys. Chem. 89 (1985) 294.
21. H. Shirota, E.W. Castner Jr., J. Chem. Phys. 112 (2000) 511

Materials Today: Proceedings xxx (xxxx) xxx

Contents lists available at ScienceDirect

Materials Today: Proceedings

journal homepage: www.elsevier.com/locate/matpr

Highly sensitive colorimetric and fluorescent pH sensor of physiological interest

Sanju Das

Department of Chemistry, Maulana Azad College, Kolkata 700013, India

ARTICLE INFO

Article history:
Available online xxxx

Keywords:
pH sensor
Colorimetric
Fluorescent
Aqueous medium
DFT

ABSTRACT

Completely water soluble molecule 4-methyl-2,6-diformyl phenol (MFOH) was designed as chemosensor to identify physiological pH. The spectroscopic behaviour of the MFOH and its form in physiological pH was investigated with multi-spectroscopic method like UV–Vis and fluorescence spectroscopy. This sensor exhibited a pH-dependent ratiometric absorption property, along with a reversible color change from colorless to yellow with increasing pH, where as completely non-fluorescent behavior to strong green fluorescence was generated due to such change of pH. Most importantly, a linear fluorescence intensity changes with pH from 6.5 to 7.7 was observed, which may be utilized for ratiometric determination of physiological pH. Detailed DFT-based theoretical calculation was also performed to understand the sensing behavior.

Selection and peer-review under responsibility of the scientific committee of the Fourth International Conference on Recent Advances in Materials and Manufacturing 2022.

1. Introduction

The design and development of pH sensing probe have attracted considerable attention to determining the exact inter-cellular H^+ concentration preliminary because of many fundamental biological processes, such as metabolism, enzyme catalytic, apoptosis, transport of organelles, cell signaling, membrane trafficking, including endo- and *exo*-cytosis, reactions, ion channel formation, and various signaling pathways depend on specific H^+ ion concentration [1–8]. However, intra- or inter-cellular abnormal chemical reactivates may be spotted due to deviation from normal physiological pH conditions [9]. Indeed, the function of different membrane-bound proteins is very sensitive to the environmental pH [10]. Even some proteins manipulate H^+ concentration at the membrane interface, for instance, the enzyme ATP synthase [11]. A minor change in intercellular pH may lead to cellular dysfunction, associated with the disease [12]. Under normal physiological conditions, extracellular H^+ concentration is maintained within very narrow limits. The normal value is about 40 nmol/L at pH 7.4 and varies by about 5 nmol/L in the pH range of 7.35–7.45 [13]. Deviation by 0.10–0.20 units of pH in either direction can cause cardiopulmonary and neurologic problems (e.g. Alzheimer's disease), and more extreme variations can be extremely fatal [9]. Therefore, the precise determination of physiological H^+ concentration or pH of the medium by developing a suitable pH sensing probe is one of the key issues.

Fluorescence and absorption techniques are the two most widely applicable methods owing to their sensitivity and stability for monitoring intercellular pH by selecting suitable pH-sensitive fully water-soluble probe [14–17]. The fluorescence method is very sensitive and often the precise detection of the range of 0.005unit change of pH is possible by selecting a suitable fluorescent probe of high quantum yield, whereas absorption spectroscopy is very useful for the detection of pH from H^+ concentration-dependent change of probe color by naked eye [14]. A limited number of pH-responding fluorescent probes have been developed to monitor diverse physiological and pathological processes. Limitations of the currently available pH probes include low sensitivity and/or excitation profiles in the ultraviolet region [14]. Most importantly, the pH detection range is far beyond from normal physiological pH range, hence the precise determination as well as *in vivo* application with that reported probe shows serious disadvantages.

In this study, I have designed a fully water-soluble small organic fluorescent molecule for sensing the pH of a pure aqueous medium in which the fluorescence quantum yield increase from 0.002 to 0.25 for the variation of pH 5.0 to 8.0 with a detection limit of ~0.01 pH unit. Since the detecting pH range covers the physiological range of interest for most plant and animal species, the present pH-sensitive fluorescent probe is very curtailed for *in vivo* purposes as well as bio-imaging applications. The desired pH-induced fluo-

E-mail address: sanjudasju@gmail.com

https://doi.org/10.1016/j.matpr.2023.03.390
2214-7853/
Selection and peer-review under responsibility of the scientific committee of the Fourth International Conference on Recent Advances in Materials and Manufacturing 2022.

rescence was observed by visible light excitation instead the application of any UV light which may sometime be responsible for undesired cell damage, and hence the present pH-sensing fluorescent probe shows enormous utility for bio-medical application. Moreover, a distinct colorimetric response from colorless to bright yellow on the above similar change of pH is extremely useful for monitoring the pH by the naked eye detection method.

2. Experimental

2.1. Materials

All the chemicals and solvents were purchased from Sigma-Aldrich Chemicals Private Limited (India) and used without further purification. 4-Methyl-2,6-diformyl phenol (MFOH) was prepared as per the reported procedure and purified through recrystallization from spectroscopic grade ethanol and dried repeatedly before use [17]. Mili-Q Milipore®18.2 MΩcm^{-1} water was used for the preparation of Britton-Robinson buffer (0.04 M boric acid, 0.04 M phosphoric acid and 0.04 M acetic acid) solution of different pH throughout all spectroscopic measurements. Britton-Robinson buffer, known as universal buffer, was used for obtaining pH from 2.0 to 12.0 by adding 0.2 M NaOH. The 40 mM Britton-Robinson buffer, with variable pH from 4.0 to 11.0 (experimental conditions) were prepared by the addition of an appropriate amount of NaOH solution by following the standard procedure. The pH of different Britton-Robinson buffer solutions was determined by Systronics digital pH meter (model No.335).

2.2. Methods

2.2.1. UV–Vis absorption, fluorescence and time resolved fluorescence

LAMBDA 25 and LS-55 instruments (Perkin-Elmer, USA) were used to measure UV–Vis absorption fluorescence spectra with a 1 cm quartz cell path length. The excitation wavelength was 440 nm, and slits 8 and 3 were used for excitation and emission, respectively. The time-correlated single photon counting (TCSPC) technique was used to measure time-resolved fluorescence. For the detection of the fluorescence decay, the TBX4 detection module (IBH, U.K.) was used in conjunction with Hamamatsu photomultiplier tubes (PMTs) as the light source at 450 nm. After deconvolution analysis of the fluorescence decays, we achieved a time resolution of 100 ps with the present setup. An optically polarized excitation beam with a magic angle of 54.7° was used to record fluorescence decays.

A minimum of three times of spectroscopic measurements were conducted to check for reproducibility. The temperatures at which all experiments were performed were 25 °C. Spectroscopic measurements were conducted only with freshly prepared solutions.

2.2.2. Determination of fluorescence quantum yield

The fluorescence quantum yield of MFOH was determined using the standard method [18] 9,10-diphenyl anthracene in ethanol was used as reference [19],

$$\phi f^s = \left[\frac{A_r F_s n_s^2}{A_s F_r n_r^2}\right]$$

where, **A** is the absorbance at the excitation wavelength, **F is** the integrated emission area and **n** is the refraction index of the solvents used. Subscripts refer to the reference (r) or sample (s) compound. The MFOH fluorescence spectra were recorded by 440-nm excitation at 25 °C in 40 mM Britton-Robinson buffer, pH 7.3. By using the above equation, ϕ_F = 0.4 (λex = 440 nm) at pH 11.0 was obtained in an aqueous 40 mM Britton-Robinson buffer at pH 7.3. [17].

2.2.3. Theoretical calculation

In the gas phase, Pseudo-empirical density function theories (DFTs) were used to optimize the ground state geometries of MFOH and its corresponding deprotonated species MFO-[20]. In this calculation, a 6-31 G basis set was selected as the basis set for the B3LYP function. All stationary points were found to have positive vibrational frequencies by means of a normal mode analysis. Accordingly, TD-DFT using the optimized geometries of the ground (S_0) states of respective species were used to study low-lying excited states in a water medium [21]. The conductor-polarized continuum model (CPCM) was used to describe the solvent effect in both ground and excited states. Moreover, vertical excitation energies were calculated for the lowest 20 singlet states. The positive vibrational frequencies of all of these species confirmed their global minima. It is also calculated here how much energy is required to excite the lowest 20 singlet states vertically. We computed UV–Vis spectra in a water medium between 250 and 550 nm based on TD-DFT calculations.

3. Results and discussion

3.1. UV–Vis absorption studies

UV–Vis absorption studies of 4-methyl-2,6-diformyl phenol (MFOH) (∼100 μM) were performed in an aqueous 40 mM Britton-Robinson buffer of different pH from 4.0 to 12.0 [17]. At a lower pH-range in an aqueous Britton-Robinson buffer medium, the absorption profile was similar to that of another non-aqueous solvent, where the intensity maxima appeared in the UV region at ∼340 nm with a molar extension coefficient of ∼0.5 × 10^4 M^{-1}cm^{-1} (Table 1). On increasing pH, a new absorption peak in the visible region centered at ∼430 nm was formed with a concomitant decrease of 340 nm peak intensity through an isosbestic wavelength at ∼370 nm until the saturation was observed at ∼pH, 12.0 (Fig. 1A). With increasing pH, the amount of base increase which can be facilitate the phenolic proton abstraction. This formation of phenoxide ion accelerates the resonance of negative charge with phenyl ring as well as two aldehyde groups. This effect was reflected in the spectral change UV–vis by the appearance of peak at 430 nm. These results clearly indicate that with the increase of pH, more amount of deprotonation of phenolate anion (MFO$^-$) are formed from neutral MFOH (Scheme 1).

The plot of normalized 430-nm absorption intensities (each value normalized by 340-nm intensity at pH 5.0) with medium pH was follow typical sigmoidal behavior with a transition midpoint pH of ∼7.2. The unknown pH of an analyte can easily be estimated from the fitted equation by monitoring the 430 nm intensity; where I^{430}_{Normz}, intensity at 430 nm normalized by 340 nm

$$I^{430}_{Normz} = 1.2 - \frac{1.2}{1 + \exp(pH - 7.2)/0.4}$$

Intensity were recorded at pH 5.0 and unknown pH value for the medium (Fig. 1B). It is noteworthy to mention that the transition midpoint pH is very close to the physiological pH, hence small fluctuations of pH for the different physiological mediums can easily be monitored with great accuracy. Therefore, the spectral changes of the compound are rapid with slight changes in the pH of the medium. Most importantly, the colorimetric response from colorless to distinct yellow with increasing pH is highly beneficial for necked eye pH detection (Fig. 1C).

3.2. pH responsive fluorescence studies

The fluorescence method because of its high sensitivity and bio-imaging facility play curtailed role in sensing a very small amount

Table 1
UV–Vis absorption parameters.

	Systems	Transi-tion	λ, (nm)	f_{cal}	$\varepsilon\times10^{-4}$ ($M^{-1}cm^{-1}$)
Calculated	MFOH	$S_0 \rightarrow S_1$	345	0.13	0.53
	MFO^-	$S_0 \rightarrow S_1$	436	0.24	0.96
Observed	MFOH (pH-4.0)	$S_0 \rightarrow S_1$	350		0.52
	MFOH (pH-10.5)	$S_0 \rightarrow S_1$	427		0.69

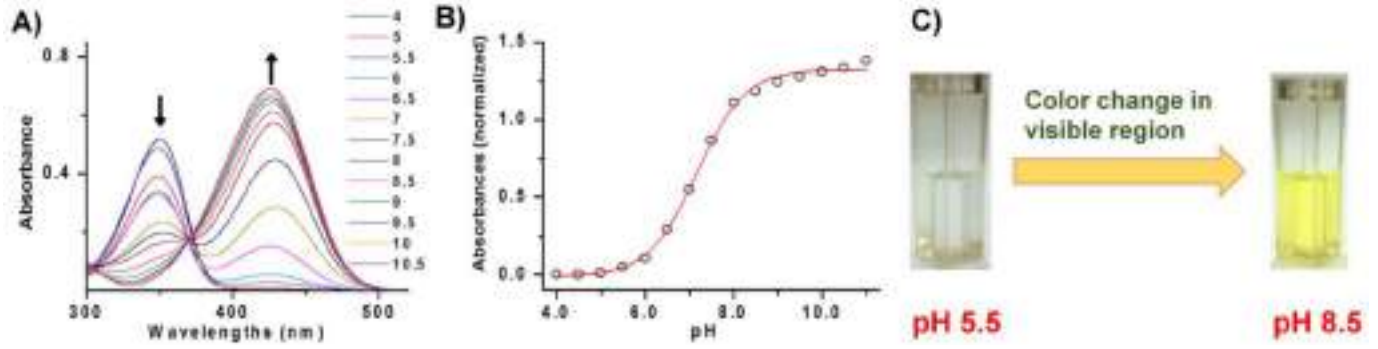

Fig. 1. (A) UV–Vis absorption spectrum profile of MFOH (100 mM) in 40 mM Britton-Robinson buffer medium with increasing pH (4.0–11.0). The increase or decrease in intensities with an increase in pH is indicated by the arrow. (B) The normalized absorbance at 427 nm with different pH of the medium is plotted. The absorbance values at different pH are normalized by dividing absorbance of 340 nm at pH 5.0. The red curve represents the sigmoidal fitting with a transition mid-point of 7.2 ± 0.05. (C) Photograph for the cell containing 1 mM of MFOH at two different pH. (For interpretation of the references to color in this figure legend, the reader is referred to the web version of this article.)

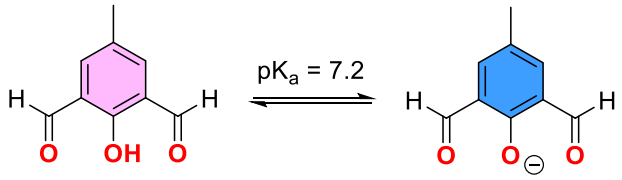

Scheme 1. Acid-base equilibria in aqueous medium.

of essential molecules present in a biological system. It has already been shown that pH-induced fluorescence generation is very useful for the precise estimation of minute cellular pH changes, which is generally not possible by other common electrochemical, conductivity measurements. In the present investigation, we have chosen MFOH as a pH indicator fluorescent probe. However, MFOH did not produce any fluorescence for excitation at 340 nm in aqueous as well another protic (MeOH and EtOH) and aprotic solvent (acetonitrile, THF, etc).On increasing the pH of the Britton-Robinson buffer medium, the fluorescence intensity centered at ~530 nm increases gradually upon excitation at ~440 nm due to the formation of phenolate anion (MFO^-) until the saturation was observed at pH ~ 12.0 (Fig. 2A). Almost 200 times fluorescence quantum yield (ϕ_F) enhancement from 0.002 to 0.4 for changing of pH from 5.0 to 12.0 was detected (Fig. 2B). To remove the probe concentration dependencies for analytical usefulness during the determination of the unknown pH of the medium, the fluorescence intensities at various pH were normalized by diving the intensity

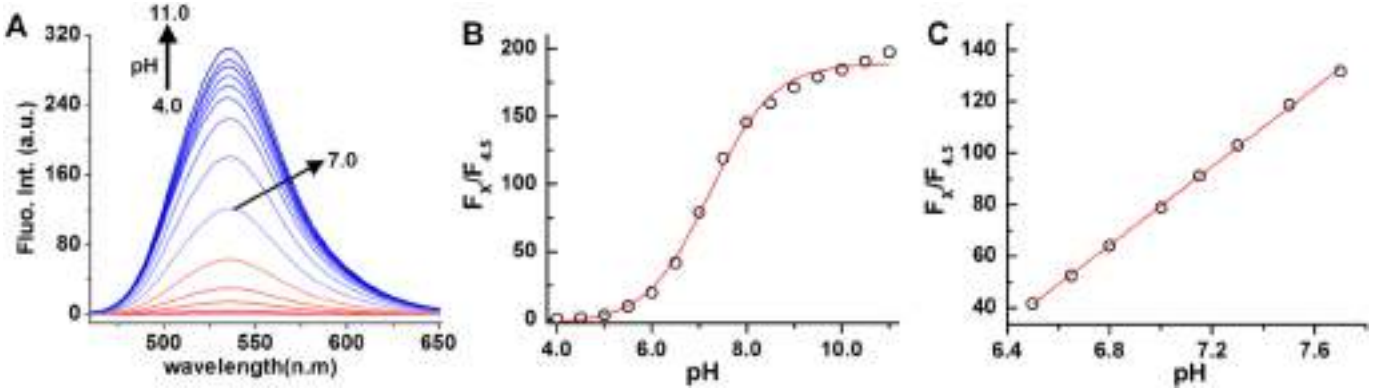

Fig. 2. (A) Fluorescence response of MFOH (25 mM) in 40 mM Britton-Robinson buffer medium with increasing pH (4.0–11.0) (excitation: 440 nm). The increase in intensities with an increase in pH is indicated by the arrow. (B) The normalized fluorescence at 530 nm with different pH of the medium is plotted. The fluorescence values at different pH are normalized by dividing the fluorescence at pH 5.0. The red curve represents the sigmoidal fitting with a transition mid-point of 7.2 ± 0.05. (C) The normalized fluorescence at 530 nm with different pH of the medium is plotted. The red curve represents the linear fitting. (For interpretation of the references to color in this figure legend, the reader is referred to the web version of this article.)

value at pH 5.0, which was then plotted with the pH of the medium (Fig. 2B). The calibration curve was sigmoidal in nature and the transition midpoint was found at ~7.2 (Fig. 2B). The unchanged transition midpoint value between absorption and fluorescence studies clearly suggests that the anionic form of MFOH is solely responsible for the generation of 530-nm fluorescence (Fig. 1B and 2B). Although the typical sigmoidal behavior was grossly followed for the whole pH range from 4.0 to 11.0, a perfect linear correlation was detected near the transition midpoint from 6.5 to 7.7 pH (Fig. 2C), which may be applied for the determination of unknown physiological pH ratio-metrically. Since a large enhancement of emission intensity due to a minute variation of pH between 6.5 and 7.7 was observed, a very small amount of pH change in this range (6.5 to 7.7) may be determined ratiometrically. Indeed, based on the instrumental accuracy and error for linear curve fitting, the limit of certainty ~0.01 for the detection of pH was identified.

Fluorescence lifetime measurements often serve as a sensitive indicator of the local environment of a fluorophore and are responsive to excited-state interactions. This technique provides an efficient way to address and monitor sensitive issues like differential degrees of solvent relaxation around a fluorophore, the presence of more than one chemical entity in a solution, and so forth. Thus in order to achieve a deeper insight into pH-dependent fluorescence changes, excited state lifetime analysis for the 530-nm emission at different pH was performed. The typical decay profile is presented in Fig. 3 with the corresponding fitting parameters calculated. Single exponential behavior for the transient decay at various pH clearly suggests that anionic species is solely responsible for this fluorescence (Fig. 3). The unchanged excited state lifetime of about 4.7 ns also indicates that increasing emission with pH is not due to different excited state species but to more amount of MFO^- formation.

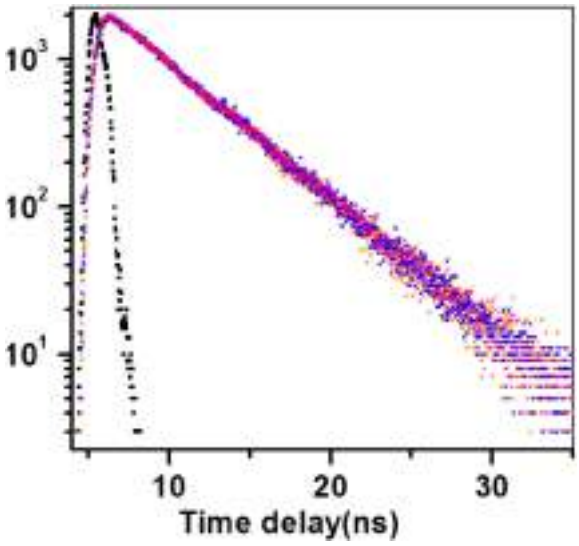

Fig. 3. Fluorescence transient decays of MFOH at different pH: pink, 6.0; yellow, 7.0; blue, 9.0 and black, scatter. (For interpretation of the references to color in this figure legend, the reader is referred to the web version of this article.)

3.3. Theoretical calculations

Density function theories (DFT) were used to optimize the ground state geometry of MFOH in the gas phase in comparison to its corresponding deprotonated species MFO in the gas phase. An H-bonding interaction between the phenolic-H and one of the adjacent formyl-O was detected in the optimized structure for protonated species (MFOH), which exist mainly at acidic pH. Another formyl moiety was located at the position *trans* to phenolic-OH. It has been found, however, that both formyl moieties prefer to position away from phenolate-O at the *trans*-position in the deprotonated molecule (MFO^-), which mostly exists in a basic pH, to prevent electrostatic repulsion between negatively charged phenolate-O and either formyl-O. As a result, TDDFT calculations of UV spectra in an aqueous medium based on ground state geometries matched the experimental spectra nicely (Fig. 4, Table 1). In Table 1, theoretically calculated and experimentally determined UV–Vis absorption parameters are compared. According to Fig. 4B, it can be seen the electronic distribution of both HOMO and LUMO for the $S_0 \rightarrow S_1$ transition. In summary, those results suggest that *trans*-located two formyl moieties generate a colorimetric response as pH sensors.

4. Conclusion

A completely water soluble, suitable pH sensor using 4-Methyl-2,6-diformyl phenol (MFOH) for pH determination in the range of

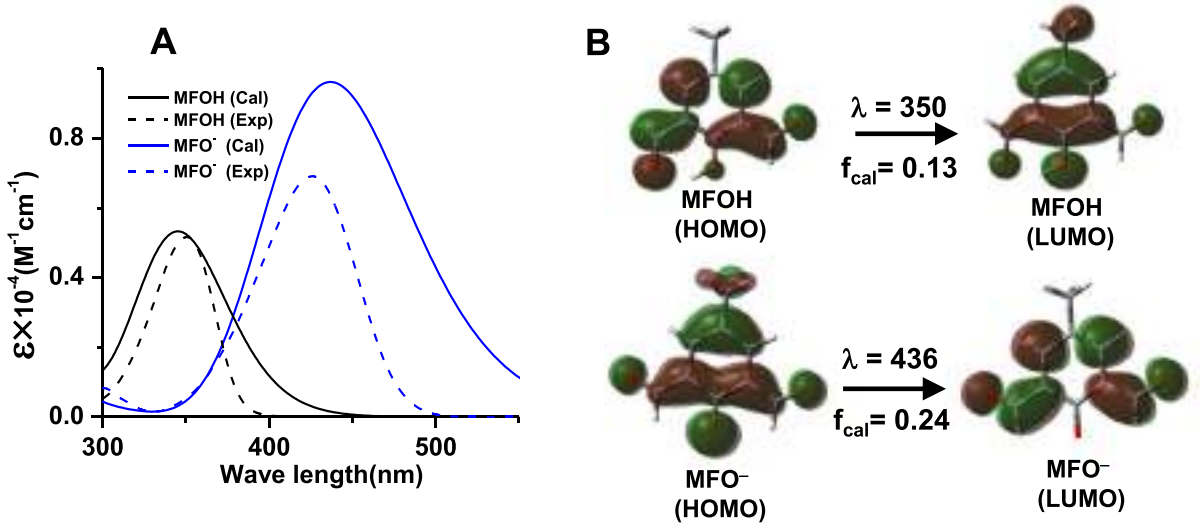

Fig. 4. (A) Calculated absorption spectrum of MFOH and MFO^-. Experimental absorption spectrum at pH 5.0 and 11.0 are depicted for comparison. (B) HOMO and LUMO (for both MFOH and MFO^-) involving for electronic UV–Vis transition with important parameters (λ = wavelength of transition, f_{cal} = oscillator strength) are shown.

5.0–11.0 has been developed by utilizing the pH-dependent colorimetric and fluorometric responses. The generation of bright yellow color from colorless due to the formation of anionic MFO^- at increased pH has been utilized for a colorimetric response, whereas strong green fluorescence at ~530 for this anion responded for fluorescent pH sensor. The obtained pK_a for the $MFOH/MFO^-$ equilibria ~7.2 is very close to physiological pH and hence the present pH sensing probe is highly beneficial for determining *in vivo* pH. Extensive theoretical calculations were performed for evaluating the pH-sensing mechanism.

CRediT authorship contribution statement

Sanju Das: Conceptualization, Data curation, Formal analysis, Funding acquisition, Investigation, Methodology, Project administration, Resources, Software, Supervision, Validation, Visualization, Writing – original draft, Writing – review & editing.

Data availability

Data will be made available on request.

Declaration of Competing Interest

The authors declare that they have no known competing financial interests or personal relationships that could have appeared to influence the work reported in this paper.

References

[1] T. Maeda, The signaling mechanism of ambient pH sensing and adaptation in yeast and fungi, FEBS J. 279 (8) (April 2012) 1407–1413.
[2] R.G. Dickinson, W.D. Hooper, M.J. Eadie, DMD March, 12 (2) (1984) 247–252.
[3] D.F. Babcock, G.A. Rufo, Jr, H.A. Lardy, PNAS March 1, 80(5) (1983) 1327–1331.
[4] Fan Yu, Xiang-Jian Kong, Yun-Yun Zheng, Yan-Ping Ren, La-S. Long, R.B. Huanga, L.S. Zhenga, Dalton Trans. 2009, 9503–9509.
[5] C. Aldridge, P. Cain, C. Robinson, FEBS J. 276 (2009) 1177–1186.
[6] F. Aniento, F. Gu, R.G. Parton, J. Gruenberg, JCB 133(1) 29–41.
[7] K.A. Christensen, J.T. Myers, Joel A. Swanson, February 1, J. Cell Sci. 115(2002) 599–607.
[8] Harvey M. Florman, Robert M. Tombes†, Neal L. First, Donner F. Babcock, Science Direct, 135(1) (1989) 133–146.
[9] S. Balzan, G.S. Johal, N. Carraro, Front Plant Sci. 5 (2014) 393.
[10] A. Mugs, J. M. Gonzalez-Manasll, J. H. Lakeyll, F. Pattusy, W.K. Surewicz, pH-dependent Stability and Membrane Interaction of the Pore-forming Domain of Colicin A. J. Biol. Chem. 268(3) (1993) 1553–1557, 1993.
[11] J.M. Elmore, G. Coaker, Mol. Plant 4 (3) (2011) 416–427.
[12] R.Y. Wang, pH-dependent cocaine-induced cardio toxicity, Am. J. Emerg. Med. 17 (4) (1999) 364–369.
[13] R. Wang, C. Yu, F. Yu, L. Chen, Trends in Analytical Chemistry, 29 (9) (2010).
[14] U.C. Saha, K. Dhara, B. Chattopadhyay, S.K. Mandal, S. Mondal, S. Sen, M. Mukherjee, S. van Smaalen, P. Chattopadhyay, Org. Lett. 13 (17) (2011) 4510–4513.
[15] S. Charier, O. Ruel, J.B. Baudin, D. Alcor, J. Fran Çois Allemand, A. Meglio, L. Jullien, Angew. Chem. Int. Ed. 43 (2004) 4785–4788.
[16] M. Maus, K. Rurack, New J. Chem. 24 (2000) 677–686.
[17] S. Das, Y. Sarkar, S. Mukherjee, J. Bandyopadhyay, S. Samanta, P.P. Parui, A. Ray, Sensor Actuat. Chem. B209 (2015) 545–554.
[18] G.A. Crosby, J.N. Demas, Measurement of photoluminescence quantum yields, Rev. J. Phys. Chem. 75 (1971) 991.
[19] J.V. Morris, M.A. Mahaney, J.R. Huber, J. Phys. Chem. 80 (1976) 969.
[20] M.J. Frisch, et al., Gaussian 09 Rev. A.1, Gaussian Inc., Wallingford CT, 2009.
[21] S. Miertus, E. Scrocco, J. Tomasi, Electrostatic interaction of a solute with a continuum. A direct utilization of ab initio molecular potentials for the previsionof solvent effects, Chem. Phys. 55 (1981) 117–129.

Asian Journal of Chemistry; Vol. 35, No. 2 (2023), 493-498

ASIAN JOURNAL OF CHEMISTRY

https://doi.org/10.14233/ajchem.2023.26944

Fluorometric Detection of Al^{3+} Ion in Mixed Aqueous Solvent Based on Simple Schiff-Base Molecular Prob

SANJU DAS

Department of Chemistry, Maulana Azad College, Kolkata-700013, India

Corresponding author: E-mail: sanjudasju@gmail.com

Received: 22 November 2022; *Accepted*: 17 January 2023; *Published online*: 30 January 2023; AJC-21135

A simple fluorometric detection for Al^{3+} ion in mixed aqueous medium using a simple Schiff-base molecule through PET mechanism is discussed. The di-phenolic Schiff-base molecule (EAMHM) was synthesized by the condensation reaction of multiple phenolic aldehyde molecules with a diamine containing multiple aldehyde-reacting primary amine moieties. The extremely low fluorescence quantum yield for EAMHM is highly useful for the off-mode of fluorescence sensing purposes. Contrary to various other cations Ni^{2+}, Mg^{2+}, Co^{2+}, Cu^{2+}, Zn^{2+}, Cr^{3+}, Cd^{2+}, Fe^{3+}, Ba^{2+}, Hg^{2+}, the selective Al^{3+} ion induced large fluorescence enhancement can be employed to detect Al^{3+} even in the presence other bi- or tri-valent cations. Moreover, linear change in fluorescence intensity with Al^{3+} concentration is highly beneficial for ratiometric detection of unknown Al^{3+} concentrations. As revealed from various spectroscopic and theoretical calculations, EAMHM forms a 1:1 complex with Al^{3+} showing a large increase in fluorescence intensity. It has also been identified that efficient photo-induced electron transfer (PET) in free EAMHM is mainly responsible for its low fluorescence intensity, whereas the removal of such PET process during its complexation with Al^{3+} produces large fluorescence enhancement. The structural and electronic parameters of the free EAMHM and EAMHM-Al^{3+} complex have been analyzed using DFT-based theoretical calculations.

Keywords: Fluorometry, Aluminium ion, Mixed aqueous solvent, Photo-induced electron transfer, Schiff base.

INTRODUCTION

In the lithosphere, aluminium is one of the most available elements, which is widely used in the paper industry, electronic industry, pharmaceutical industry, food processing industry, *etc*. [1-3]. Beyond to the permissible limits, aluminum lead to disorders in people can lead to Alzheimer's, Parkinson's and dialysis encephalopathy, which are neurological diseases [4-6]. Humans are recommended to consume about 7 mg of Al^{3+} per kilogram of body weight per week, according to WHO recommendations [7]. In addition to retarding plant growth, it damages cellular membranes *via* oxidative damage. Although Al has several disadvantages, its mass usage in daily life can accumulate Al^{3+} and cause toxicity to humans and the environment. Aluminum increases the acidity of soil, so it is very fetal for the agricultural production [8]. On account of close relationship between aluminum and human health, there is an urgent need to develop a chemosensor for Al^{3+}.

Fluorescence method is more advantageous than other sophisticated methods as its operational simplicity, sensitivity, high selectivity, easy sample preparation and detection by both visual and instrumental methods and obviously for low cost [9,10]. Due to its weak coordinating abilities, Al^{3+} is more challenging to work with than other metals when it comes to making sensors [11]. As a result, Al^{3+} chemosensors in aqueous media require high selectivity and sensitivity.

Schiff bases are often used as chemosensors because they are easy to make and inexpensive [12-14]. For Al^{3+} chemosensors to work well in aqueous media, they need to be sensitive and selective. Thus, in this work, an attempt is made to construct a novel fluorescent 'turn-on' chemosensor for Al^{3+} ions based on simple Schiff-base molecule through PET mechanism. A diphenolic Schiff base molecule (EAMHM) was synthesized by the condensation reaction of multiple phenolic aldehyde molecules with a diamine containing multiple aldehyde reacting primary amine moieties.

EXPERIMENTAL

Commercially available reagents and solvents were procured from Sigma-Aldrich Chemicals Pvt. Ltd., USA, whereas

the spectroscopic grade solvent was purchased from E. Merck, India. The solvents were purified and dried by distillation procedure and used only after checking their purity fluorimetrically in the interest range of wavelength. Water (Milli-Q Millipore 18.2 MΩ cm^{-1}) was used throughout the study. Solvent mixture MeOH-HEPES buffer (25 mM, pH 7) (1:1 v/v) was used for all the spectroscopic measurements.

Characterization: LAMBDA 25 and LS-55 instruments (Perkin-Elmer, USA) were used for the UV-Vis absorption and fluorescence emission spectra, respectively. Quartz cells with a path length of 10 mm were used for absorption spectrum recording. For all measurements, the excitation wavelength was 365 nm, while the emission wavelength was between 8 and 3 nm. The fluorescence spectra were calibrated with respect to the instrumental response. To check the reproducibility, every spectroscopic measurement was conducted three times. An NMR spectrometer with a Bruker Advance DPX 300 MHz was used to measure ^{1}H NMR spectra in DMSO-d_6 with tetramethylsilane as an internal standard. Also, all the spectroscopic measurements were peformed with freshly made solutions, and the experiments were conducted at 25 ºC.

Synthesis of Schiff-base probe: 2-Hydroxy-3-(hydroxymethyl)-5-methylbenzaldehyde (HHMB) was synthesized from *p*-cresol with yield of 62% by following reported method [15]. To synthesize Schiff-base molecule 6,6′-(1Z,1′Z)-(ethane-1,2-diyl*bis*(azan-1-yl-1-ylidene))*bis*(methan-1-yl-1-ylidene)*bis*(2-(hydroxymethyl)-4-methylphenol) (EAMHM), ethylenediamine (EDA) (0.066 mL, 1 mmol) was added dropwise with constant stirring to a methanolic solution of HHMB (0.322 g, 2 mmol) followed by the addition 3 drops of acetic acid. The reaction mixture was then refluxed for 2.5 h at 45 ºC and finally the crude product was collected under reduced pressure. The product was purified by column chromatography to obtain deep yellow solid product and dried over $CaCl_2$ under vacuum (**Scheme-I**). ^{1}H NMR (DMSO-d_6, 300 MHz) δ ppm: 2.22 (s, 6H, Ar-CH_3), 2.49,3.31 (due to H_20 presence in DMSO-d_6), 3.83 (s, 4H, N-CH_2), 4.45 (s, 4H, CH_2-OH), 4.97 (s, 2H, CH_2-OH), 7.1-7.23 (s, 4H, Ar-H), 8.51 (s, 2H, imine-H), 13.41 (s, 2H, Ar-OH) ppm.

Determination of fluorescence quantum yield: The quantum yield of EAMHM as well as EAMHM-Al^{3+} were determined using standard method [16]. The standard fluorophore used was 9,10-diphenylanthracene in ethanol with emission quantum yield (ϕ_r) = 0.95. Using the following equation, the ϕ_f for the different systems was calculated:

$$\phi_{f_{sample}} = \frac{OD_{standard} \times A_{sample}}{OD_{sample} \times A_{standard}} \times \phi_{f_{standard}}$$

where, A_i is the absorbance at the excitation wavelength, F_i is the integrated emission area and n is the refractive index of solvent used. Subscripts refer to the reference (r) or sample(s) compound. The Schiff base EAMHM as well as EAMHM-Al^{3+} fluorescence spectra were recorded by 365 nm excitation at 25 ºC in 1:1 MeOH-HEPES buffer (v/v). At 450 nm fluorescence intensity band the quantum yield of EAMHM and EAMHM-Al^{3+} were determined 0.02 and 0.2, respectively.

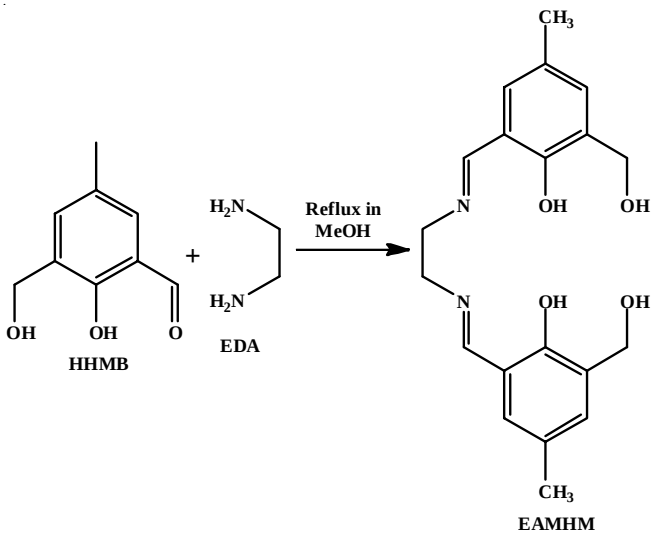

Scheme-I: Synthesis of the Schiff base molecule (EAMHM)

Theoretical calculation: By utilizing Gaussian 09, the ground state geometries of the probe (EAMHM) and its chelate complex with Al^{3+} were fully optimized in the gas phase to study their molecular and electronic structure [17]. The B3LYP functional with standard 6-31G basis set for all atoms had been adopted for this calculation. All of these species' global minima were confirmed using positive vibrational frequencies. The electrochemical properties of singlet excited states were investigated using B3LYP density functional theory (TD-DFT) based on the optimized geometry of their ground states (S_0). A ground state geometry was then evaluated with respect to excitation energies and respective oscillator strengths. Based on TD-DFT calculations, the UV-Vis spectra were calculated in a water medium between 250 and 650 nm. In aqueous medium, the conductor-polarized continuum model (CPCM) was adapted to calculate the fluorescence wavelength for the lowest singlet excited states using TD-DFT. Calculations based on theoretical models were found to reproduce experimentally obtained trends satisfactorily.

RESULTS AND DISCUSSION

UV-Vis studies: The UV-Vis absorption spectrum of the Schiff base ligand (EAMHM) was recorded at 25 ºC in 1:1 aqueous-methanol solution showing two well-defined intensity maxima at ~ 330 and 420 nm, respectively (Fig. 1a). It has been shown that the visible absorption intensity appears due to formation of deprotonated phenolate chromophore due to solvent polarity induced ground state proton transfer reaction from phenolic-OH to adjacent imine-N to generate partially charge separated zwitterionic species [18], while 330 nm intensity indicates that the second phenol-moiety remain as protonated form. The Schiff-base molecule containing multiple N- and O-centers (EAMHM) produces large affinity to interact various metal ions. To monitor the metal ion-induced complexation reaction for EAMHM, the changes in UV-Vis absorption for EAMHM were investigated in presence of various metal ions, such as Al^{3+}, Ni^{2+}, Mg^{2+}, Co^{2+}, Cu^{2+}, Zn^{2+}, Cr^{3+}, Cd^{2+}, Fe^{3+}, Ba^{2+}, Hg^{2+} (Fig. 1b). Interestingly, the absorption intensity profile

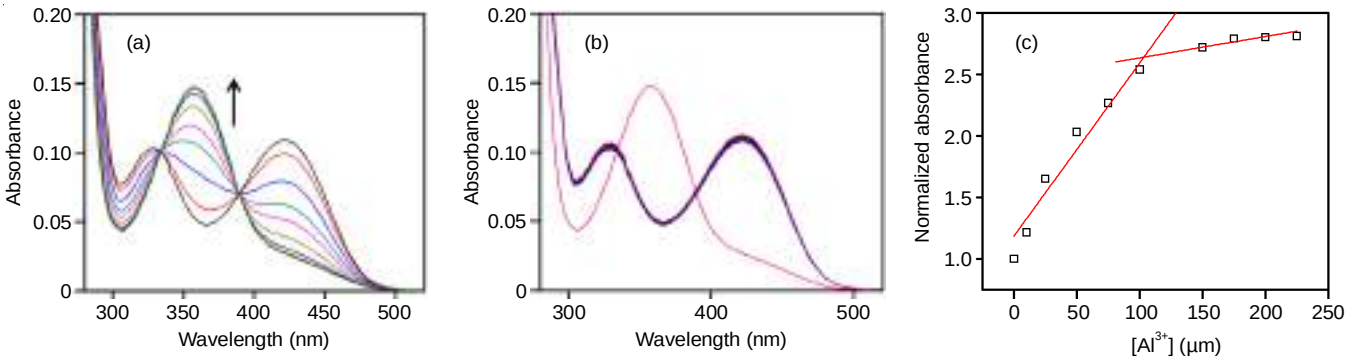

Fig. 1. (a) UV-Vis absorption spectra of EAMHM (25 mM) in 1:1 methanol-HEPES buffer solvent mixture with increasing concentration of Al^{3+} ion (0-225 μM); the changes in absorbance on addition of Al^{3+} is depicted by arrow. (b) The spectra in presence of various metal ions (10 equiv. w.r.t. Al^{3+}) are depicted. Black and pink spectra are for bare ligand EAMHM and in presence of Al^{3+} ion respectively. (c) Plot of normalized absorbance as a function of Al^{3+} ion concentration at 365 nm

of the EAMHM remains almost unchanged in presence of those various individual ions except Al^{3+}. It has been observed that both 330 and 420 nm absorption intensity for EAMHM gradually decreases with concomitant formation of new absorption intensity centered at ~ 365 nm until saturation was observed in presence of 9-equivalents of Al^{3+} ions (Fig. 1a). Most importantly, the appearances of two different isosbestic wavelengths ~ 334 and 390 nm justify a formation of new molecular species between Al^{3+} and EAMHM. Therefore, it has been considered that the Schiff-base molecule involved in complexation only with Al^{3+} ions among those various metal ions and the saturation in the absorption profile originated because of no other free EAMHM molecule present in solution to participate any further complexation reaction. The Al^{3+} ion-induced such change in UV-Vis absorbances of EAMHM may be useful for detection of Al^{3+} in aqueous solution. To observe the sensing applicability, the normalized 365 nm absorption intensities (normalized by 365 nm absorption intensity in absence of Al^{3+}) were plotted with the concentration of Al^{3+} ions and the linear correlation curve upto 4 equiv. of Al^{3+} is highly beneficial for detection of unknown Al^{3+} present in solution (Fig. 1c).

To identify the complex stoichiometry between EAMHM and Al^{3+}, absorbance related with the EAMHM-Al^{3+} complex was plotted against different mole fractions of Al^{3+}, while volume of solution had remained constant according to the Job's plot (Fig. 2) [19]. The maximum amount of complexation at 0.5 mole-fraction of Al^{3+} convincingly suggests the formation of 1:1 complex between EAMHM and Al^{3+} ions.

The influence of different anions to dissociate the EAMHM-Al^{3+} complex was also studied. A 365 nm absorption peak for the complex remains unperturbed in presence of various potential anions, such as Cl^-, BH_4^-, Br^-, NO_3^-, SCN^-, NO_2^-, CN^-, $S_2O_3^{2-}$ (Fig. 3b), which indicates that the complex is highly stable towards those anions. On the other hand, a notable change of absorption was identified in presence of 10 equiv. of S^{2-} (Fig. 3a). More specifically, an identical spectrum between the final absorption spectrum of the complex in presence of saturated S^{2-} ion and EAMHM clearly suggests that Al^{3+} is displaced as insoluble Al_2S_3 from the complex to generate free EAMHM.

Fluorometric detection: The fluorometric studies for EAMHM with or without the presence of various metal ions

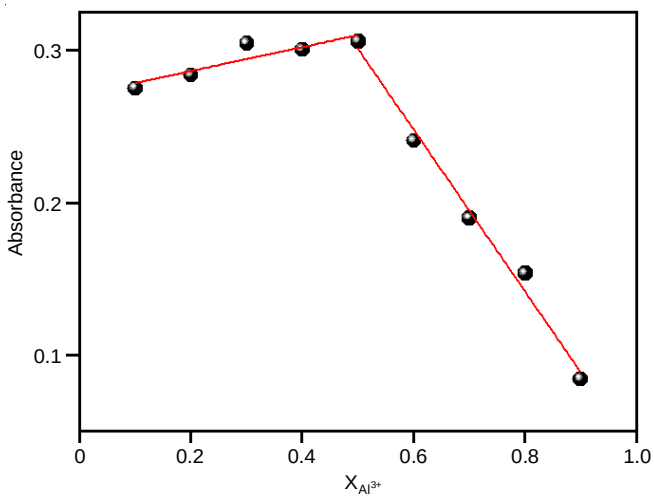

Fig. 2. Job's plot for determining the stoichiometry of the complex between EAMHM and Al^{3+} ion. The difference between the observed and EAMHM absorbance at 365 nm were plotted with mole fraction of Al^{3+} in the mixture of EAMHM and Al^{3+} with various compositions

were performed by maintaining conditions identical to that of absorption studies in 1:1 methanol/buffer mixed solvent medium. The Schiff-base molecule (EAMHM) shows very weak fluorescence intensity centered at ~ 510 nm (relative $\phi_F < 0.01$) for 420 nm excitation (Fig. 4a), whereas the molecule behaves completely non-fluorescent due to excitation by 330 nm light. The results indicates that the zwitterionic residue containing phenolate-conjugated with protonated imine is responsible for weak fluorescence intensity, however, the protonated phenol conjugated with imine moiety in the other half of molecule is completely non-fluorescent in nature. The extremely low fluorescence intensity of EAMHM is highly useful for its application as off-mode of fluorescence sensing. As a fluorescent sensor in aqueous media, EAMHM may be detected by enhancing its fluorescence with a suitable external reagent in its "on" mode.

As the concentration of Al^{3+} was increased in presence of 25 mL of Schiff base (EAMHM), a significant increase of fluorescence centered at 450 nm was observed. It reached saturation at 10 equiv. in 1:1 methanol/buffer (20 mM HEPES) medium (pH 7.0) (Fig. 4a). This indicates that the EAMHM-Al^{3+} complex may be responsible for the large fluorescence enhancement

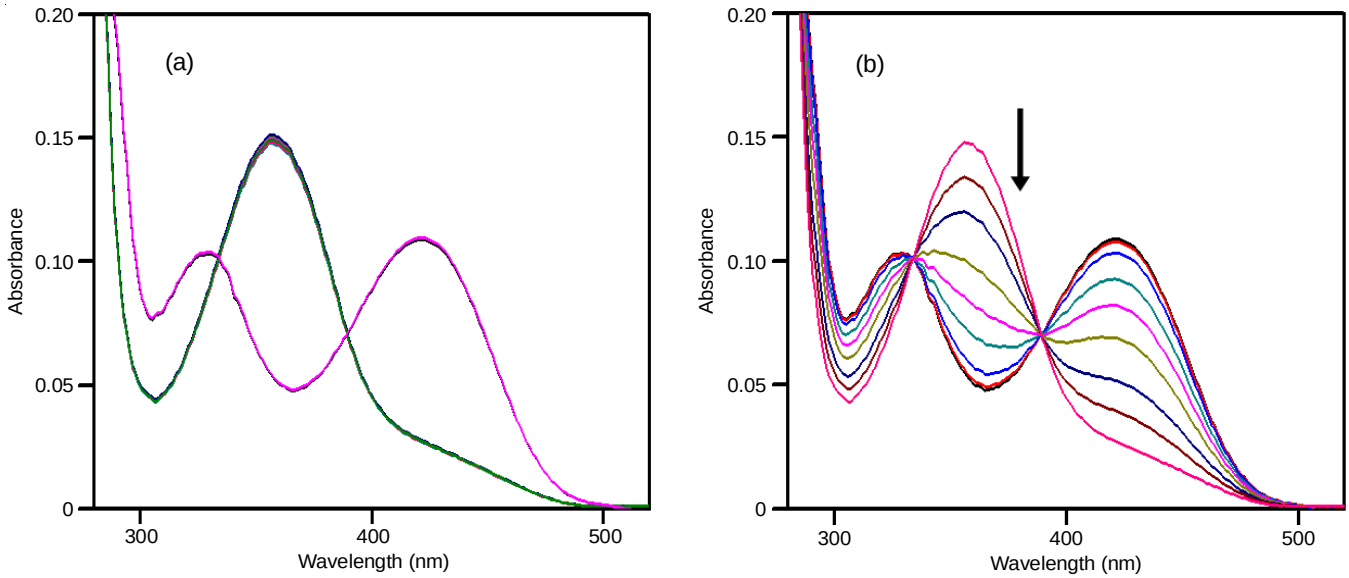

Fig. 3. UV-Vis absorption spectra of EAMHM-Al^{3+} in 1:1 methanol-HEPES buffer solvent mixture (a) with increasing concentration of S^{2-} ion (0-250 mM); the changes in absorbance on addition of S^{2-} is depicted by arrow. (b) In presence of different anions (10 equiv. w.r.t. S^{2-}). Black and magenta spectra are for bare ligand EAMHM and EAMHM-Al^{3+} in presence of S^{2-} respectively

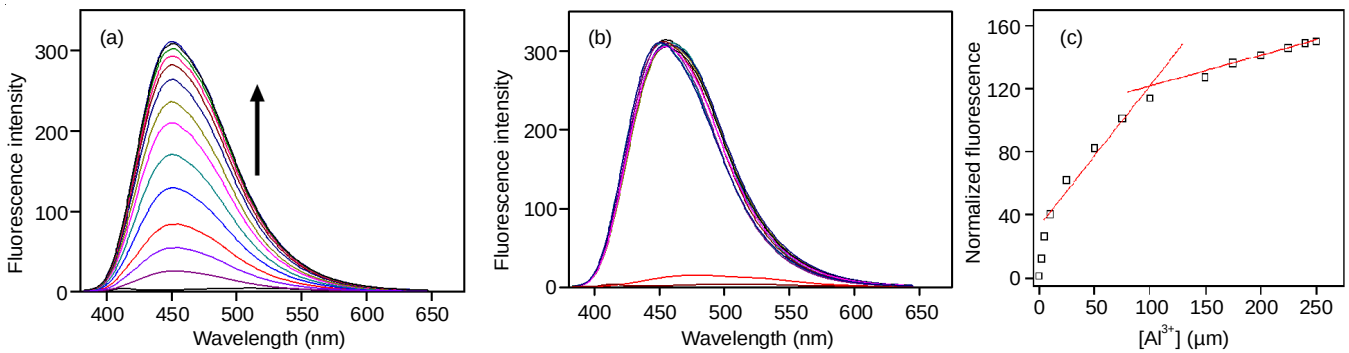

Fig. 4. Changes in the fluorescence spectra of EAMHM (25 μM) in 1:1 HEPES buffer-methanol solvent mixture (a) with increasing concentration of Al^{3+} ion (0-250 μM); the changes in fluorescence intensity on addition of Al^{3+} ion is depicted by arrow. (b) in presence of different anions (10 equiv. w.r.t. S^{2-}): wine, bare ligand EAMHM; red, EAMHM-Al^{3+} in presence of S^{2}. Excitation wavelength was 365 nm. (c) Plot of normalized fluorescence as a function of Al^{3+} ion concentration at 450 nm

since the amount of Al^{3+} required for fluorescence saturation is equal to that required for UV-Vis intensity saturation. When reaching saturation, Al^{3+} generated a 150-fold increase in the fluorescence at 365 nm (Fig. 4a).

Using DFT-based theoretical calculations, the low fluorescence intensity of free ligand (EAMHM) is due to the electron delocalization process (PET) caused by phenoxide oxygen atoms delocalizing electrons to a π-conjugated system of two aromatic rings and imino groups. There is a large increase in fluorescence intensity in the presence of Al^{3+} ions, which is likely due to the PET process being restricted efficiently to the EAMHM. Due to the reduction of electron-accepting abilities of the two aromatic rings and imine groups in the EAMHM-Al^{3+} coordinated complex, the PET process within the ligand would become weak. Additionally, the redshift of the emission wavelength of Schiff base ligand to 450 nm is also peculiar to the intensity of fluorescence emitted by Al^{3+} complexes [20]. A trace amount of Al^{3+} in an analytical medium can be detected by the large fluorescence intensity caused by Al^{3+}.

To verify Al^{3+} selectivity, the fluorescence of EAMHM (25 μM) was monitored individually in presence of different biologically or industrially important cations *viz*. Ni^{2+}, Mg^{2+}, Co^{2+}, Cu^{2+}, Zn^{2+}, Cr^{3+}, Cd^{2+}, Fe^{3+}, Ba^{2+}, Mg^{2+}, Hg^{2+} Na^{+}, Ca^{2+}, K^{+}, Fe^{2+} (~ 10 equivalent each w.r.t. Al^{3+}) in 1:1 methanol/buffer (20 mM HEPES) medium, pH 7.0 (Fig. 5) but failed to generate any noticeably enhanced fluorescence with an exception for the Al^{3+} ion with a very small fluorescence increment for the same cations. Interestingly, Al^{3+} induced fluorescence increment was not disturbed in presence of various other cations under identical solvent composition (Fig. 5). It is also important for Al^{3+} detection in the presence of other cations to have an unperturbed ratiometric response for EAMHM in the presence of large excess of those cations. In addition to limit of detection (LOD) of 1.0 M obtained, it is noteworthy that a trace amount of Al^{3+} can be detected with this LOD.

To determine the binding stoichiometry between Schiff base EAMHM and Al^{3+} as well as the binding constant, Benesi-Hildebrand procedure was adopted [21], where the change in

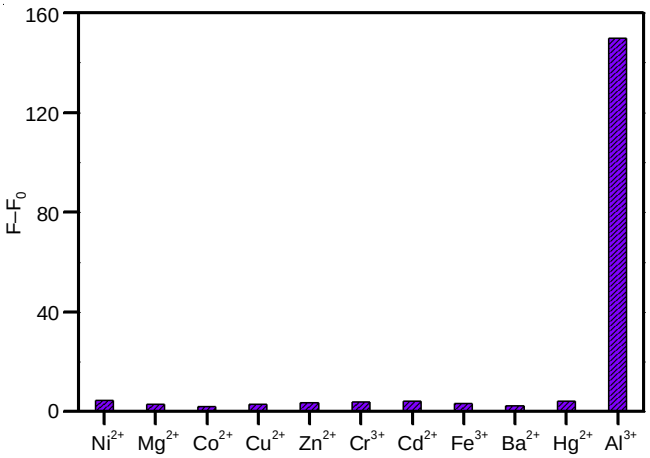

Fig. 5. Bar diagram indicating the Al^{3+} selective fluorescence increase over other metal ions

fluorescence intensity factor $((F_{max}-F_0)/(F_x-F_0))$ shows linear relation with inverse of Al^{3+} concentration indicating 1:1 binding stoichiometry between EAMHM and Al^{3+} (Fig. 6). On the other hand, the binding constant $(k_a) \sim 3.4 \times 10^4\ M^{-1}$ was determined from the slope value ~ 2.99×10^{-5} M.

$$\frac{(F_{max}-F_0)}{(F_x-F_0)} = 1+\left(\frac{1}{K_a[C]^n}\right) \quad (1)$$

where, F_{max}, F_0 and F_x are fluorescence intensities of ligand in the presence of Al^{3+} at saturation, free ligand and any intermediate Al^{3+} concentration at λ_{max} = 450 nm. K_d is the dissociation constant of the EAMHM-Al^{3+}complex and concentration of Al^{3+} is represented by C. The binding constant (k_a) of the complex has been determined using the following relation:

$$k_a = \frac{1}{k_d}$$

As similar to the UV-Vis absorption studies, the quenching of fluorescence intensity due to dissociation of EAMHM-Al^{3+} complex in presence of various anions, such as Cl^-, BH_4^-, Br^-, NO_3^-, SCN^-, NO_2^-, CN^-, $S_2O_3^{2-}$ and S^{2-} was monitored by the fluorescence method (Fig. 4b). Except in presence of S^{2-} anion, almost unchanged fluorescence intensity clearly justifies the complex is highly stable and it can be used as a fluorescence sensor for the detection of Al^{3+} in presence of those anions. Whereas, in case of S^{2-}, almost complete quenching of the fluorescence to a same extent as that of free EAMHM may also indicate that such fluorescence quenching is resulted by the generation of free EAMHM ligand.

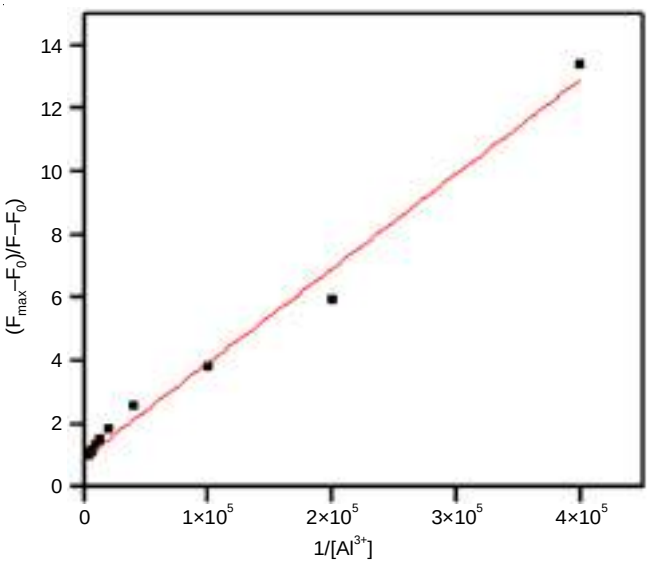

Fig. 6. Benesi-Hildebrand plot of $(F_{max}-F_0)/(F-F_0)$ *vs.* $1/[Al^{3+}]$ (obtained from emission spectra) shows a linear relationship with an intercept of about 0.95 ± 0.1 (close to 1.0) (λ_{ex} = 365 nm)

Notably, the S^{2-} induced selective fluorescence quenching is useful for detection of S^{2-} ion by observing such fluorescence quenching. Moreover, as similar to the UV-Vis absorption studies, the linear correlation of fluorescence intensity increase *vs.* Al^{3+} concentration can be utilized for ratiometric detection of Al^{3+} (Fig. 4c).

Theoretical calculations: Based on evidences, molecular formula of EAMHM-Al^{3+} for 1:1 complex as revealed from Job's plot analysis, the ground state geometry for most probable structure was optimized by DFT method for investigating the absorption to the singlet excited states *via* TD-DFT calculations in solvent MeOH (Fig. 7). In addition, similar calculation was performed for free EAMHM to justify for present consideration for the proposed structural geometry of the EAMHM-Al^{3+} complex. The geometry of complexes possess a distorted tetrahedral arrangement around the central metal ions. The optimized geometry of complex is represented in Fig. 7.

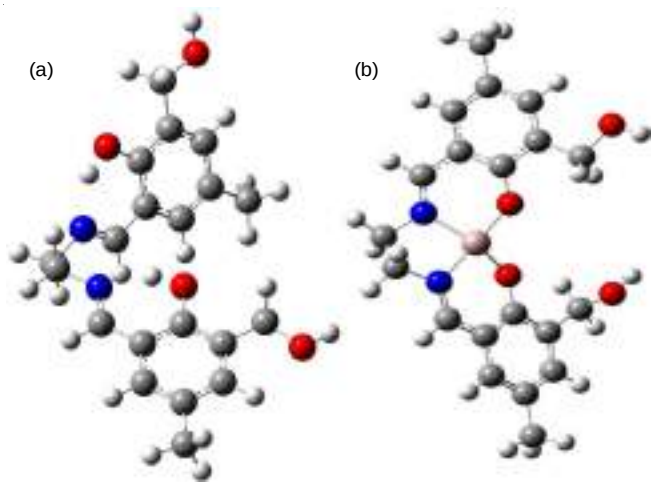

Fig. 7. Optimized ground state geometries of (A) EAMHM and (B) EAMHM-Al^{3+} complex

For EAMHM-Al^{3+} complex, a band around 362 nm is dominated by the HOMO–1(99) → LUMO (101) excitations, while the band around 377 nm for EAMHM is mainly due to HOMO (87) → LUMO (88) transitions. On comparing the experimental UV-Vis spectra for free EAMHM and EAMHM-Al^{3+} complex, it has been observed that the calculated electronic transitions are very close to the experimental electronic bands (Table-1).

Conclusion

In conclusion, a novel fluorescent 'turn-on' chemosensor EAMHM based on a Schiff base molecule containing multiple

TABLE-1
ELECTRONIC EXCITATION WAVELENGTH (nm), OSCILLATOR STRENGTHS (f_{cal}), ABSORPTION MAXIMUM (λ_{max}) AND EXTINCTION COEFFICIENT (ε) OF EAMHM AND EAMHM-Al^{3+} FORMS OBTAINED BY THE TD-DFT/B3LYP/6-31G++(d,p) CALCULATION ON GROUND STATE GEOMETRIES IN VARIOUS SOLVENT WITH CPCM DIELECTRIC SOLVATION MODEL. THE EXPERIMENTALLY OBTAINED UV-VIS ABSORPTION (Obs/Abs) PARAMETERS ARE DEPICTED FOR COMPARISON

	Form	Solvent	λ_{max} (nm)	f_{cal}	$\varepsilon \times 10^{-4}$ (M^{-1} cm^{-1})
TD-DFT	EAMHM	MeOH	377, 303	0.04, 0.21	0.42, 0.39
	EAMHM-Al^{3+}	MeOH	362	0.07	0.55
Obs/Abs	EAMHM	1:1 aqueous methanol	420, 330		0.44, 0.41
	EAMHM-Al^{3+}	1:1 aqueous methanol	365		0.59

phenol-conjugated-imine moieties derived from phenolic aldehyde and diamine molecule is developed . The EAMHM exhibits a high selectivity and sensitivity for the detection of Al^{3+} through significant visible fluorescence enhancement in the wavelength centered at 450 nm with a micromolar detection limit in CH_3OH/HEPES buffer (pH 7.0) binary solution mixture. The unperturbed Al^{3+} induced fluorescence enhancement by addition of different other cations justify that EAMHM molecule can be utilized for the detection of Al^{3+} in the presence of other competing metal ions also.

CONFLICT OF INTEREST

The authors declare that there is no conflict of interests regarding the publication of this article.

REFERENCES

1. S. Goswami, S. Paul and A. Manna, *RSC Adv.*, **3**, 10639 (2013); https://doi.org/10.1039/c3ra40984h
2. R.E. Doherty, *Environ. Forensics*, **1**, 83 (2000); https://doi.org/10.1006/enfo.2000.0011
3. M.S. Golub, J.M. Donald, M.E. Gershwin and C.L. Keen, *Neurotoxicol. Teratol.*, **11**, 231 (1989); https://doi.org/10.1016/0892-0362(89)90064-0
4. N. Fimreite, O.O. Hansen and H.C. Pettersen, *Bull. Environ. Contam. Toxicol.*, **58**, 1 (1997); https://doi.org/10.1007/s001289900292
5. H. Wang, B. Wang, Z. Shi, X. Tang, W. Dou, Q. Han, Y. Zhang and W. Liu, *Biosens. Bioelectron.*, **65**, 91 (2015); https://doi.org/10.1016/j.bios.2014.10.018
6. M. Iniya, D. Jeyanthi, K. Krishnaveni and D. Chellappa, *J. Lumin.*, **157**, 383 (2015); https://doi.org/10.1016/j.jlumin.2014.09.018
7. A. Budimir, *Acta Pharm.*, **61**, 1 (2011); https://doi.org/10.2478/v10007-011-0006-6
8. N.E.W. Alstad, B.M. Kjelsberg, L.A. Vollestad, E. Lydersen and A.B.S. Poleo, *Environ. Pollut.*, **133**, 333 (2005); https://doi.org/10.1016/j.envpol.2004.05.030
9. S. Kim, J.Y. Noh, K.Y. Kim, J.H. Kim, H.K. Kang, S.W. Nam, S.H. Kim, S. Park, C. Kim and J. Kim, *Inorg. Chem.*, **51**, 3597 (2012); https://doi.org/10.1021/ic2024583
10. Y. Lu, S. Huang, Y. Liu, S. He, L. Zhao and X. Zeng, *Org. Lett.*, **13**, 5274 (2011); https://doi.org/10.1021/ol202054v
11. M. Venturini-Soriano and G. Berthon, *J. Inorg. Biochem.*, **85**, 143 (2001); https://doi.org/10.1016/S0162-0134(01)00206-9
12. C. Pan, K. Wang, S. Ji, H. Wang, Z. Li, H. He and Y. Huo, *RSC Adv.*, **7**, 36007 (2017); https://doi.org/10.1039/C7RA05064J
13. S. Muthusamy, K. Rajalakshmi, D. Zhu, W. Zhu, S. Wang, K.-B. Lee H. Xue and L. Zhao, *Sens. Actuators B: Chem.*, **346**, 130534 (2021); https://doi.org/10.1016/j.snb.2021.130534
14. J. Ma, Y. Dong, Z. Yu, Y. Wu and Z. Zhao, *New J. Chem.*, **46**, 3348 (2022); https://doi.org/10.1039/D1NJ05919J
15. E. Lambert, B. Chabut, S. Chardon-Noblat, A. Deronzier, G. Chottard, A. Bousseksou, J.-P. Tuchagues, J. Laugier, M. Bardet and J.-M. Latour, *J. Am. Chem. Soc.*, **119**, 9424 (1997); https://doi.org/10.1021/ja970345q
16. J.V. Morris, M.A. Mahaney and J.R. Huber, *J. Phys. Chem.*, **80**, 969 (1976); https://doi.org/10.1021/j100550a010
17. M.J. Frisch, G.W. Trucks, H.B. Schlegel, G.E. Scuseria, M.A. Robb, J.R. Cheeseman, G. Scalmani, V. Barone, B. Mennucci, G.A. Petersson, H. Nakatsuji, M. Caricato, X. Li, H.P. Hratchian, A.F. Izmaylov, J. Bloino, G. Zheng, J.L. Sonnenberg, M. Hada, M. Ehara, K. Toyota, R. Fukuda, J. Hasegawa, M. Ishida, T. Nakajima, Y. Honda, O. Kitao, H. Nakai, T. Vreven, J.A. Montgomery, Jr., J.E. Peralta, F. Ogliaro, M. Bearpark, J.J. Heyd, E. Brothers, K.N. Kudin, V.N. Staroverov, R. Kobayashi, J. Normand, K. Raghavachari, A. Rendell, J.C. Burant, S.S. Iyengar, J. Tomasi, M. Cossi, N. Rega, J.M. Millam, M. Klene, J.E. Knox, J.B. Cross, V. Bakken, C. Adamo, J. Jaramillo, R. Gomperts, R.E. Stratmann, O. Yazyev, A.J. Austin, C. Pomelli, J.W. Ochterski, R.L. Martin, K. Morokuma, R. Cammi, V.G. Zakrzewski, G.A. Voth, P. Salvador, J.J. Dannenberg, S. Dapprich, A.D. Daniels, Ö. Farkas, J.B. Foresman, J. Cioslowski, J.V. Ortiz and D.J. Fox, Gaussian, Inc., Wallingford CT, , Gaussian 09 Rev. A.1 (2009).
18. Y. Sarkar, S. Das, A. Ray, S.K. Jewrajka, S. Hirota and P.P. Parui, *Analyst*, **141**, 2030 (2016); https://doi.org/10.1039/C5AN02128F
19. S. Biswas, S. Mukherjee, J. Bandyopadhyay, S. Samanta, I. Bhowmick, S. Das, D.K. Hazra, A. Ray and P.P. Parui, *RSC Adv.*, **4**, 9656 (2014); https://doi.org/10.1039/C4RA00069B
20. D. Maity and T. Govindaraju, *Eur. J. Inorg. Chem.*, **2011**, 5479 (2011); https://doi.org/10.1002/ejic.201100772
21. H.A. Benesi and J.H. Hildebrand, *J. Am. Chem. Soc.*, **71**, 2703 (1949); https://doi.org/10.1021/ja01176a030

Monitoring and Assessment of Drinking Water for Chemical Pollutants: A Three-Year Study in Nadia District, West Bengal

A. Mukherji

Department of Chemistry, Maulana Azad College†, 8 Rafi Ahmed Kidwai Road, Kolkata-700013, India
†Formerly, author was in Department of Chemistry, Krishnagar Government College, Krishnagar, Nadia, India

ABSTRACT

A study was undertaken to determine the level of chemical pollutants present in groundwater and water from other sources used for drinking purpose in Nadia district, West Bengal. For this purpose, 76 water samples were collected during the period 2014 - 2016 from the tubewells of the area and municipality sources. The samples were then assessed for eleven parameters - arsenic, fluoride, chloride, residual chlorine, iron, phosphate, nitrate, nitrite, ammonium, total alkalinity and pH. The results clearly indicated high levels of arsenic, low levels of fluoride and phosphate and high levels of nitrate in samples from certain areas. A comparison of the data of those areas with the data from a similar study undertaken two years ago was made to highlight the importance of monitoring process.

KEYWORDS: Chemical pollutants, Groundwater, Drinking water, Monitoring, Assessment.

INTRODUCTION

Water is the most abundant and precious resource of our planet, yet availability of clean, potable water for human use is shrinking day by day. Decades of pollution caused by effluents of industries, use of pesticides in agriculture, rampant withdrawing of groundwater for irrigation, washing purposes and housing have led to the contamination of groundwater with heavy metals like arsenic and toxic anions like fluoride, nitrate and phosphate. Indeed, the Gangetic delta area of West Bengal has been in the spotlight for arsenic contamination since the landmark study by Chakraborti *et al.*[1] The contamination of groundwater by arsenic in districts of Murshidabad, Nadia, 24 Parganas and others, have been the focus of decades of study. Arsenic is highly toxic and long-term use of drinking water with high concentrations can lead to a wide range of health problems in humans.[2-4] The contamination of groundwater by fluoride is another serious hazard[5] and also presence of nitrate in drinking water can cause a potentially fatal disease in infants called methemoglobinemia, or Blue-Baby Syndrome.[6] In this scenario it is, therefore, essential to continuously monitor groundwater wherever it is being consumed for drinking purpose whether it is in rural or urban area.

The World Health Organization (WHO) has defined safe drinking water as "quality of water that is acceptable for lifelong consumption".[7] In its "*Guidelines for drinking water quality*", nearly one hundred chemical contaminants are listed which have significant bearing in the short-term and long-term health of human beings. Also, there are some "acceptable limits" or values of the concentrations of the chemicals which do not result in any significant risk to health over a lifetime of consumption.[8] Hence, for determining the suitability of drinking water in a given area, it is necessary to determine whether the concentration of an ion is within limits given in the *Guidelines*.

In view of the above-mentioned significance of Nadia district, West Bengal in context of arsenic contamination, it was suitable as the area of study. The aim was to determine the quality of drinking water consumed by the students of Krishnagar Government College and their families in Nadia district and to spread awareness in case of high level of contamination found. In the study, water samples were collected by three batches of students of 1st Year Chemistry Honours in 2014, 2015 and 2016 respectively, from their households or neighboring water sources and analysis of those water samples was carried out in the department of chemistry, Krishnagar Government College. Since the occurrence of 1st Year Honours students in a college is a random choice, the study may be considered as a random study of the quality of drinking water of the households in Nadia district, West Bengal.

EXPERIMENTAL

Material and Methods: Commercially available water-testing kits, which are a low-cost, easily available, easy-to-use and rapid means to detect inorganic ions, were used to analyse the water samples. Their usefulness and limitations are given in the *Guidelines*.[9] Water-testing kits were purchased from NICE Chemicals Pvt. Ltd., Kochi, Kerala. Five different types of kits, either for a single ion or for more than one ion (combination kit) were used, viz., one kit for Total Alkalinity and pH, one for Arsenic, one for Iron and Phosphate, one for Fluoride, Chloride and Residual Chlorine and one for Nitrate, Nitrite and Ammonium.

General procedure: Approx. 200 mL of water sample was collected, either from a tubewell, house reservoir or municipality tap, in 250 mL of a standard plastic bottle and analysed as such within 2-3 days of collection. Each sample was given a unique sample number and the source of water in each case was noted. The samples were analysed following strictly the procedure given in each testing kit and reagents provided in the kit.

Detection Method: The chemical reaction by the reagents in a given water sample produced some observable change, either different colours (e.g. in case of pH) or different intensities of a particular colour (e.g. yellow in case of arsenic). The produced colour or intensity of colour was then matched with the range of concentration of that particular ion given in the chart in the kit. In order to determine whether a water sample contains harmful ions in "unsafe range", it is not necessary to know the absolute value of concentration but rather whether the concentration is above the "acceptable limit" or not. This can be easily detected by the water-testing kit.

RESULTS AND DISCUSSION

The WHO and the Bureau of Indian Standards (BIS) have established some acceptable limits of concentrations ions in drinking water.[7,10] These are given in Table 1.

In 2014, water samples were collected from 21 households in Nadia district, their addresses identified by the Post Office (P.O.) and the Police Station (P.S.) for simplicity and analyzed for 10 parameters. These households have been grouped into 7 different localities according to the corresponding Police Stations. Further, the results have been grouped into two categories – **Table 2** shows the parameters which were within acceptable limits and **Table 3** shows the water source of the samples and the parameters which exceeded the acceptable limits in these areas.

From an analysis of the results obtained in Table 2, it can be seen that although strictly within acceptable limit, 48% (sample Nos. **1-3**, **8**, **11**, **13-15**, **18**, **20**) of the samples showed fluoride to be in borderline concentration (0-1 mg/L). An analysis of the results obtained in Table 3 showed that 11 samples had high pH and 8 samples had borderline or high iron content. However, more alarmingly, 52% samples (Nos. **1**, **3**, **4**, **6**, **8**, **9**, **11**, **13**, **15**, **16**, **21**) showed the presence of nitrate while 29% samples (Nos. **6**, **8**, **9**, **10**, **13**, **16**) tested positive for nitrite ions.

In 2015, water samples were collected from 28 households, identified by their P.O. and P.S. and analyzed for 11 parameters. These households have also been grouped into 11 localities according to the corresponding P.S. As before, the results have been grouped into two categories – **Table 4** shows the parameters which were within acceptable limits and **Table 5** shows the water source of the samples and the parameters which exceeded the acceptable limits in these areas.

From the results obtained in Table 4, it can be seen although within acceptable limits, 46% samples had fluoride (Nos. **2-4**, **6**, **7**, **9**, **13-15**, **19**, **26-28**) in borderline concentration (0-1 mg/L) while 21% samples (Nos. **2**, **7**, **13**, **18**, **22**, **23**) tested positive for nitrite ions. However, from Table 5, it can be seen that two of the samples (Nos. **13**, **27**) had very high values of Total alkalinity, one sample (No. **7**) had very high pH, two samples (Nos. **8**, **15**) had very high value of arsenic and one sample (No. **6**) had very high value of nitrate. Overall, 39% and 25% of the samples tested positive for arsenic and nitrate, respectively.

In 2016 also, water samples were collected from 27 households in Nadia district, identified by the respective P.O. and P.S. and analyzed for 11 parameters. The said households have been grouped into 9 localities according to the Police Stations. The results for which parameters were within acceptable limit are shown in **Table 6** and those for which the parameters exceeded the acceptable limits are shown in **Table 7**.

From Table 6, it can be seen that the concentration of arsenic was found to be borderline in 44% of samples (Nos. **3**, **5**, **6**, **10**, **11**, **14**, **16**, **17**, **21-23**, **26**) while 37% of the samples (Nos. **2**, **4**, **6**, **9**, **13**, **18**, **23**, **25-27**) showed

the presence of nitrite ion. Form Table 7, it can be seen that two of the samples (Nos. **25**, **27**) had very high value of total alkalinity, 14 of the samples had high values of iron content and two samples (Nos. **25**, **27**) had very high value of nitrate. Overall, 26% of the samples (Nos. **9**, **13**, **20**, **23**, **25-27**) tested positive for nitrate.

In order to further assess the status of chemical pollutants in drinking water in Nadia district, the contaminants arsenic, fluoride and nitrate were chosen since these three have significant health impacts in the population. Percentage of samples which produced a positive result for presence of these three ions, that is, were present at least in the minimum concentration range, was compared over a period of 4 years (in case of Arsenic) and over a period of 5 years (in case of Fluoride and Nitrate) from a few chosen localities, namely, Nabadwip, Dhubulia, Nakashipara and Kotwali since data was available from these localities for all 4/5 years. The data for 2012 and 2013 were obtained from a previous study by the present author.[11] The detection trends for these three ions are shown in **Figure 1**, **Figure 2** and **Figure 3**, respectively.

From Figure 1, it can be seen that although percentage of samples containing arsenic has decreased over the years, more localities in Nadia district are affected by arsenic.

From Figure 2, it can be seen that percentage of samples containing fluoride exhibits a downward trend. From Figure 3, it can be concluded that on an average, the percentage of samples containing nitrate exhibits a downward trend.

CONCLUSION

In the present study, 76 water samples were collected from 76 different households in Nadia district, West Bengal over a period of three years in three batches and were analyzed each year by water testing kits for 11 selected parameters of chemical pollutants. The comprehensive results of the analysis have been presented which helped to successfully monitor the the status of drinking water of the corresponding localities of Nadia district. Further, to assess the trends of arsenic, fluoride and nitrate contamination, the percentage of samples which produced a positive result for these ions or positivity percentage data for 2014-2016 was compared with data for 2012-2013 for certain chosen localitites. This showed upward trends for presence of Arsenic in more localities and downward trends for presence of Fluoride and Nitrate ions. This study re-iterates the need to routinely monitor the water from a particular areas, since the concentration of ions could change with time.

ACKNOWLEDGEMENTS

The author would like to thank the Principal and Department of Chemistry, Krishnagar Government College for laboratory facilities and the students of First Year Chemistry Honours batches of 2014, 2015 and 2016, respectively, for sample collection and their active participation in the study. The Water Testing Kits were purchased from UGC-CPE XII Plan Grant of Krishnagar Government College.

REFERENCES

1. B.K. Mandal, T. Roy Chowdhury, G. Samanta, G.K. Basu, P.P. Chowdhury, C.R. Chanda, D. Lodh, N.K. Karan, R.K. Dhar, D.K. Tamili, D. Das, K.C. Saha and D. Chakraborti, *Curr. Sci.*, **70**, 976 (1996).
2. D. Chakraborti, B. Das, M.M. Rahman, U.K. Chowdhury, B. Biswas, A.B. Goswami, B. Nayak, A. Pal, M.K. Sengupta, S. Ahamed, A. Hossain, G. Basu, T. Roychowdhury and D. Das, *Mol. Nutr. Food Res.*., **53**, 542 (2009) and the references cited therein.
3. D.N. Guha Mazumder, A. Ghosh, K.K. Majumdar, N. Ghosh, C. Saha and R.N. Guha Mazumder, *Indian J. Community Med.*, **35**, 331 (2010).
4. P. Bhattacharya, A.C. Samal, J. Majumdar and S.C. Santra, *Water Air Soil Pollut.*, **213**, 3 (2010).
5. H.N. Bhattacharya and S. Chakrabarti, *Curr. Sci.*, **101**, 152 (2011).
6. World Health Organization: Nitrate and Nitrite in Drinking-water, Background document for development of WHO Guidelines for Drinking water Quality, 2011.
7. World Health Organization: Guidelines for Drinking-water Quality, 3rd Edition, incorporating the 1st and 2nd Addenda, Vol. 1, Recommendations, Geneva, 2008, ISBN 978-92-4-154761-1 (Web), p.1.
8. World Health Organization: Chemical Aspects, Guidelines for Drinking-water Quality, Chapter 8, 3rd Edition, 2008, p. 145.
9. World Health Organization: Guidelines for Drinking-water Quality, 4th Edition, 2011, ISBN 978-92-4-154761-1 (Web), p.170.
10. Bureau of Indian Standards (BIS): Drinking Water Specification (Second Revision), 2012, New Delhi.
11. A. Mukherji, *Int. J. Ecosyst.*, **5**, 18 (2015).

Table 1 Acceptable Limits (in mg/L or ppm) of Ions in Drinking Water

Chemical	WHO	BIS
Total Alkalinity (TA) (in terms of $CaCO_3$)	--	200/**600**[a]
pH	--	6.5-8.5
Arsenic (As)	0.01	0.01/**0.05**[a]
Fluoride (F^-)	1.5	1.0/**1.5**[a]
Chloride (Cl^-)	[b]	250/**1000**[a]
Residual Chlorine (Res. Cl_2) (used for disinfection)	0.2	0.2/**1.0**[a]
Iron (Fe)	[b]	0.3
Phosphate (PO_4^{3-})	[b]	5
Nitrate (NO_3^-)	50	45
Nitrite (NO_2^-)	3	3
Ammonium (NH_4^+)	[b]	5

a. Permissible limit in absence of alternate source.
b. Not of health concern at levels found in drinking water.

Table 2 Parameters[††] within Acceptable Limits in Water Samples of 2014

Sample No.	P.O.	P.S.	TA	F^-	Cl^-	Res Cl_2	PO_4^{3-}	NH_4^+
1	Habibpur	Ranaghat	450	1	290	0	0	0
2	Ranaghat	Ranaghat	400	0-1	60	0	0	0
3	Nazirpur	Tehatta	310	0-1	100	0	0-0.5	0
4	Betai	Tehatta	445	0	180	0	0-0.5	0
5	Bagula	Hanskhali	390	0	120	0	0-0.5	0
6	Bagula	Hanskhali	470	0	250	0.5	0-0.5	0-0.5
7	Bagula	Hanskhali	390	0	120	0	0-0.5	0
8	Bethuadahari	Nakashipara	450	0-1	100	0	0	0
9	Bethuadahari	Nakashipara	420	0	120	0	0	0
10	Bethuadahari	Nakashipara	285	0	70	0	0	0
11	Gachha	Nakashipara	290	0-1	100	0-0.2	0-0.5	0-0.5
12	Duttapulia	Dhantala	250	0	30	0	0	0-0.5
13	Natna Pattabuka	Karimpur	520	0-1	250	0-0.2	0	0
14	Krishnagar	Kotwali	400	0-1	50	0	0-0.5	0
15	Krishnagar	Kotwali	455	0-1	100	0	0-0.5	0
16	Krishnagar	Kotwali	495	0	160	0	0	0
17	Krishnagar	Kotwali	390	0	80	0	0	0
18	Krishnagar	Kotwali	360	0-1	70	0	0	0
19	Krishnagar	Kotwali	275	0	30	0	0	0
20	Krishnagar	Kotwali	400	1	80	0	0-0.5	0
21	Saktinagar	Kotwali	430	0	100	0	0-0.5	0

[††] Measured in mg/L or ppm

Table 3 Parameters[††] exceeding Acceptable Limits in Water Samples of 2014

Sample No.	P.S.	Water Source	pH	Fe	NO_3^-	NO_2^-
1	Ranaghat	Tubewell (house)	8-9	0.3	5	0
2	Ranaghat	Filter (house)	8-9	0	0	0
3	Tehatta	Municipality	7-8	0-0.3	0-5	0
4	Tehatta	Tubewell	8	0	20-30	0

5	Hanskhali	Filter (house)	8-9	0	0	0
6	Hanskhali	Tubewell (house)	8	**0.3-1**	**50**	**5**
7	Hanskhali	Filter (house)	8-9	0-0.3	0	0
8	Nakashipara	Tubewell (house)	8	0	**30-50**	0-0.5
9	Nakashipara	Tubewell (house)	8	0	**30-50**	0-0.5
10	Nakashipara	Tapwater (outside)	8-9	0	0	0-0.5
11	Nakashipara	Tubewell (house)	7-8	0-0.3	20-30	0
12	Dhantala	Tubewell	7-8	**0.3-1**	0	0
13	Karimpur	Tubewell	7-8	0	**30-50**	**3-5**
14	Kotwali	Supplied water	7-8	0	0	0
15	Kotwali	House Reservoir	7-8	0	0-5	0
16	Kotwali	House Reservoir	8-9	0	5-10	0-0.5
17	Kotwali	Supplied water	8-9	0	0	0
18	Kotwali	Tapwater (house)	9	0	0	0
19	Kotwali	Tubewell (house)	9	0	0	0
20	Kotwali	House Reservoir	8-9	0-0.3	0	0
21	Kotwali	Krishnagar Municipality	8-9	0.3	0-5	0

[††]Measured in mg/L or ppm

Table 4 Parameters[††] within Acceptable Limits in Water Samples of 2015

Sample No.	P.O.	P.S.	Fe	F^-	Cl^-	Res Cl_2	PO_4^{3-}	NH_4^+	NO_2^-
1	Idrakpur	Nabadwip	0-0.3	0	40	0	0	0.5	0
2	Aranghata	Dhantala	0	1	70	0	0-0.5	0	0-0.5
3	Duttapulia	Dhantala	0	0-1	30	0	0-0.5	0	0
4	Panditpur	Dhubulia	0	0-1	130	0	0-0.5	0	0
5	Anandanagar	Dhubulia	0	0	60	0	0-0.5	0	0
6	Mayakol	Dhubulia	0	0-1	120	0	0.5	0	0
7	Bethuadahari	Nakashipara	0	0-1	40	0-0.2	0	0	0-0.5
8	Chandanpur	Nakashipara	0-0.3	0	50	0	0	0	0
9	Dharmatala	Nakashipara	0	0-1	40	0	0-0.5	0	0
10	Bethuadahari	Nakashipara	0.3	0	60	0	0	0	0
11	Dharmada	Nakashipara	0	0	40	0	0-0.5	0	0
12	Santipur	Santipur	0	0	70	0	0	0	0
13	Babla Gobindapur	Santipur	0	0-1	110	0	0-0.5	0	0-0.5
14	Babla Gobindapur	Santipur	0	0-1	40	0	0-0.5	0	0
15	Chakdaha	Chakdaha	0-0.3	0-1	40	0	0-0.5	0-0.5	0
16	Chakdaha	Chakdaha	0-0.3	0	40	0	0-0.5	0	0
17	Bangaljhi	Chapra	0	0	30	0	0-0.5	0	0
18	Bangaljhi	Chapra	0-0.3	0	40	0	0-0.5	0	0-0.5
19	Ramnagar	Hogalbaria	0	0-1	40	0	0	0	0
20	Bagula	Hanskhuli	0.3	0	60	0	0.5	0	0
21	Hanspukuria	Tehatta	0-0.3	0	80	0	0	0	0
22	Krishnagar	Kotwali	0	0	70	0	0	0	0-0.5
23	Krishnagar	Kotwali	0	0	150	0	0	0	0-0.5
24	Krishnagar	Kotwali	0	0	20	0	0	0	0

25	Krishnagar	Kotwali	0	0	110	0	0	0	0
26	Krishnagar	Kotwali	0	0-1	20	0	0	0	0
27	Krishnagar	Kotwali	0	0-1	130	0	0-0.5	0	0
28	Krishnagar	Kotwali	0	0-1	80	0	0-0.5	0	0

[††] Measured in mg/L or ppm

Table 5 Parameters[††] exceeding Acceptable Limits in Water Samples of 2015

Sample	P.S.	Water Source	TA	pH	As	NO_3^-
1	Nabadwip	Tap water	60	7	0	0
2	Dhantala	Tubewell	385	8-9	0	0-5
3	Dhantala	Tubewell	445	7-8	0-0.05	0
4	Dhubulia	Tap water	780	7-8	0.05	5
5	Dhubulia	Tap water	185	8-9	0-0.05	0
6	Dhubulia	Tubewell	535	8	0	**50**
7	Nakashipara	Tap water	160	**9-10**	0	0
8	Nakashipara	Tap water	435	8-9	**0.5**	0
9	Nakashipara	Tap water	180	8-9	0	0
10	Nakashipara	Tubewell	420	9	0-0.05	0
11	Nakashipara	Tap water	185	9	0	0
12	Santipur	Tap water	320	9	0	30
13	Santipur	Tubewell	**695**	8	0	10
14	Santipur	Water Filter	300	7-8	0	0
15	Chakdaha	Municipality	565	7	**0.1-0.5**	0
16	Chakdaha	Municipality	580	8-9	0	0
17	Chapra	Tubewell	500	8-9	0.05	0
18	Chapra	Tubewell	405	8-9	0.05	0
19	Hogalbaria	Water Filter	45	**5-6**	0	0
20	Hanskhuli	Tap water	390	9	0-0.05	0
21	Tehatta	Tubewell	325	8	0.05	0
22	Kotwali	Water Filter	315	8	0	0
23	Kotwali	Tubewell	410	9	0.05	20-30
24	Kotwali	Water Filter	95	7	0	0
25	Kotwali	Water Filter	320	8-9	0	0
26	Kotwali	Water Filter	100	**6**	0	0
27	Kotwali	Tubewell	**600**	8	0	5
28	Kotwali	Water Filter	545	8	0	0

[†] Measured in mg/L or ppm

Table 6 Parameters[††] within Acceptable Limits in Water Samples of 2016

Sample	P.O.	P.S.	As	F^-	Cl^-	Res Cl_2	PO_4^{3-}	NH_4^+	NO_2^-
1	Nabadwip	Nabadwip	0	0	40	0	0	0	0
2	Nabadwip	Nabadwip	0	0	60	0	0.5	0	0.5
3	Charbrahmanagar	Nabadwip	0-0.05	0	30	0	0	0.5	0
4	Nabadwip	Nabadwip	0	0	40	0	0	0-0.5	0.5
5	Charbrahmanagar	Nabadwip	0-0.05	0	30	0	0	0-0.5	0
6	Dhubulia	Dhubulia	0-0.05	0	30	0	0.5	0	0.5

7	Ghateswar	Dhubulia	0	0	70	0	0	0.5	0
8	Bethuadahari	Nakashipara	0	0	230	0	0	**1-3**	0
9	Bethuadahari	Nakashipara	0	0	120	0	0	0	0.5
10	Matchpota	Nakashipara	0-0.05	0	120	0	0	0-0.5	0
11	Bethuadahari	Nakashipara	0.05	0	80	0	0	0	0
12	Bethuadahari	Nakashipara	0	0	80	0	0	0	0
13	Bethuadahari	Nakashipara	0	0	120	0	0	0	0-0.5
14	Fulia Colony	Santipur	0-0.05	0	60	0	0	0-0.5	0
15	Subarnapur	Haringhata	0	0	60	0	0	0-0.5	0
16	Majdia	Krishnaganj	0.05	0	60	0	0	0.5	0
17	Debagram	Kaliganj	0-0.05	0	80	0	0	0.5	0
18	Jitpur	Tehatta	0	0	80	0	0	0	0.5
19	Ghurni	Kotwali	0	0	70	0	0	0	0
20	Krishnagar	Kotwali	0	0	50	0	0	0	0
21	Ghurni	Kotwali	0.05	0	50	0	0	0	0
22	Krishnagar	Kotwali	0-0.05	0	80	0	0	0	0
23	Krishnagar	Kotwali	0.05	0	60	0	0.5	0.5	0.5
24	Krishnagar	Kotwali	0	0	160	0	0	0	0
25	Krishnagar	Kotwali	0	0	150	0	0	0	0-0.5
26	Krishnagar	Kotwali	0.05	0	90	0	0	0	0.5
27	Krishnagar	Kotwali	0	0	170	0	0	0	0-0.5

† Measured in mg/L or ppm

Table 7 Parameters†† exceeding Acceptable Limits in Water Samples of 2016

Sample	P.S.	TA	pH	Fe	NO_3^-
1	Nabadwip	405	8	0-0.3	0
2	Nabadwip	345	9	0	0
3	Nabadwip	510	8	0-0.3	0
4	Nabadwip	435	8-9	0.3	0
5	Nabadwip	560	9	**3-5**	0
6	Dhubulia	360	8-9	**1**	0
7	Dhubulia	425	8	**1**	0
8	Nakashipara	505	9	**1**	0
9	Nakashipara	445	8-9	0.3	20
10	Nakashipara	360	8-9	**0.3-1**	0
11	Nakashipara	370	8	**1**	0
12	Nakashipara	300	8-9	0-0.3	0
13	Nakashipara	400	8	0.3	5-10
14	Santipur	300	9	**1**	0
15	Haringhata	365	9	0	0
16	Krishnaganj	350	7-8	**3**	0
17	Kaliganj	450	9	**3-5**	0
18	Tehatta	365	8-9	**1**	0
19	Kotwali	440	9	**1-3**	0
20	Kotwali	445	8	0-0.3	5
21	Kotwali	495	8	**1-3**	0

22	Kotwali	380	8	**3-5**	0
23	Kotwali	405	8-9	0.3	5
24	Kotwali	550	7	0-0.3	0
25	Kotwali	**605**	8-9	0-0.3	**30-50**
26	Kotwali	450	8	**1**	5
27	Kotwali	**650**	8-9	0	**30-50**

[††] Measured in mg/L or ppm

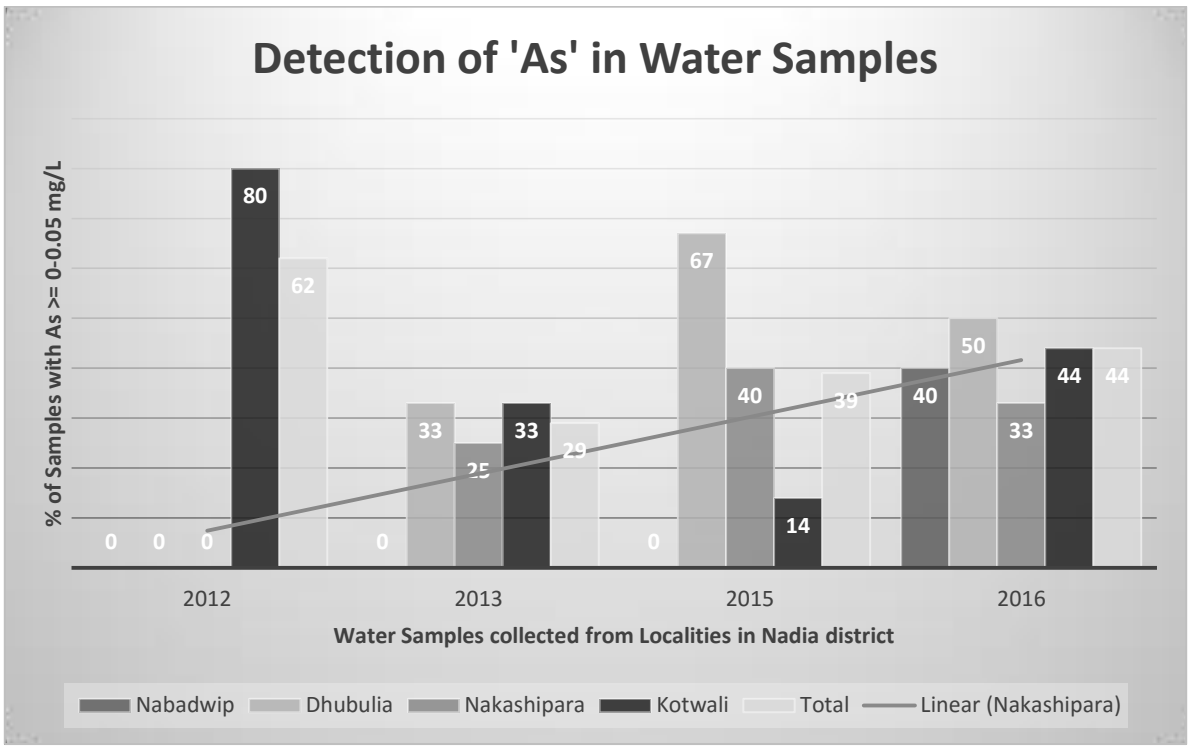

Fig. 1 Detection Trend of Arsenic in water samples over 4 years (2012, ’13, ’15, ’16)

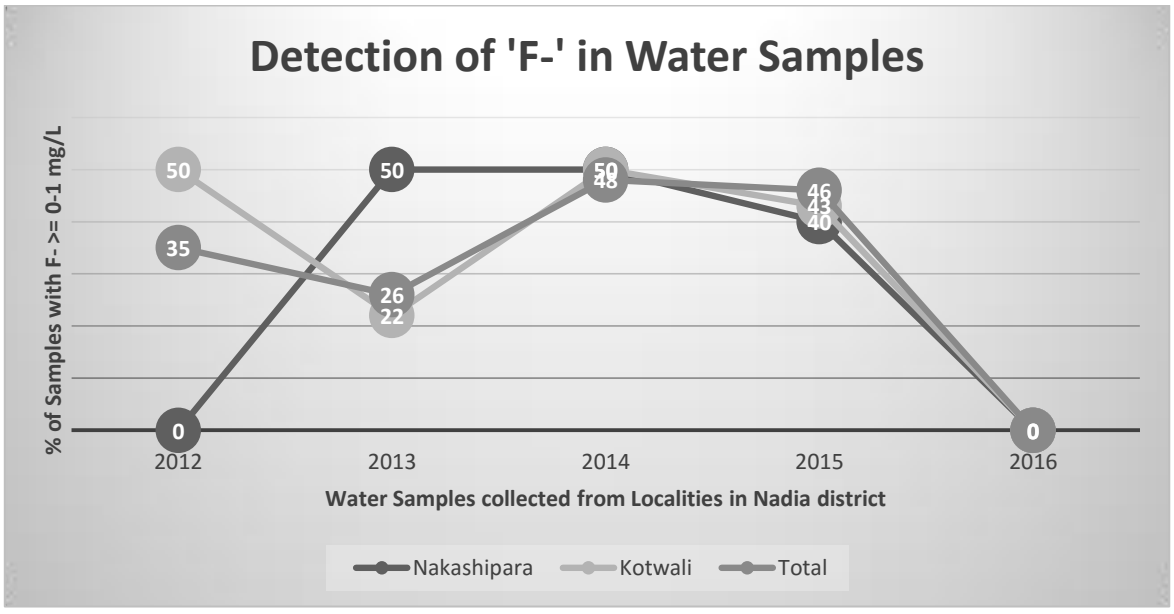

Fig. 2 Detection Trend of Fluoride in water samples over 5 years (2012 - 2016)

ISSN Online: 2456-8937
UGC CARE APPROVED JOURNAL

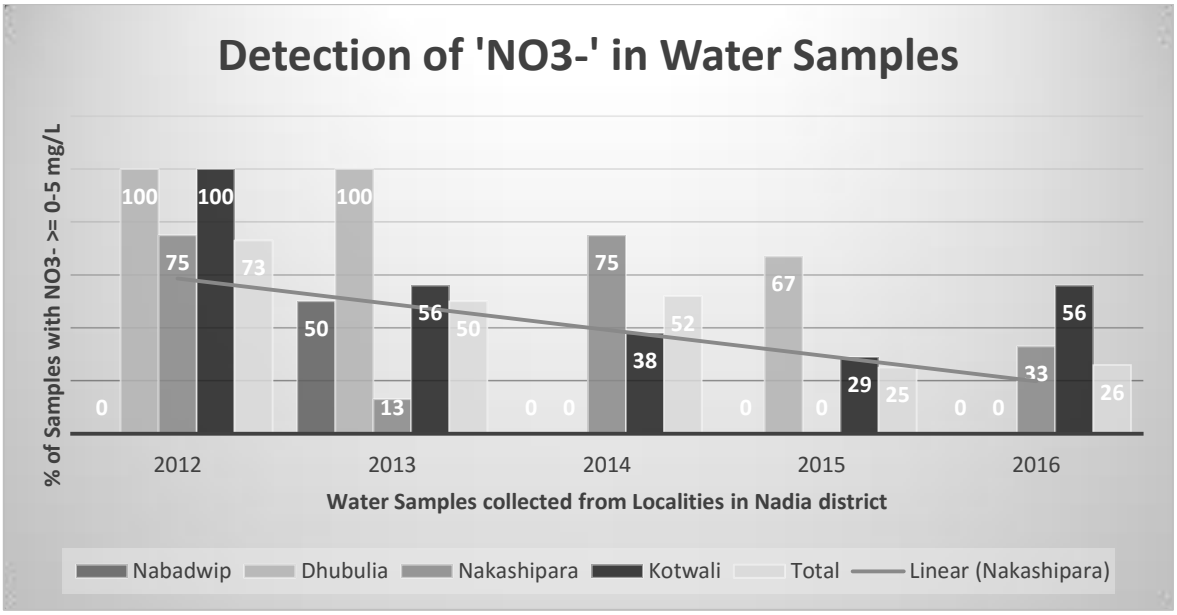

Fig. 3 Detection Trend of Nitrate in water samples over 5 years (2012 - 2016)

RSC Advances

PAPER

View Article Online
View Journal | View Issue

Cite this: *RSC Adv.*, 2021, **11**, 30093

Fluorometric trace methanol detection in ethanol and isopropanol in a water medium for application in alcoholic beverages and hand sanitizers†

Snigdha Roy,[a] Sanju Das,[b] Ambarish Ray*[c] and Partha Pratim Parui *[a]

Detection of methanol (MeOH) in an ethanol (EtOH)/isopropanol (^{i}PrOH) medium containing water is crucial to recognize MeOH poisoning in alcoholic beverages and hand sanitizers. Although chemical sensing methods are very sensitive and easy to perform, the chemical similarities between the alcohols make MeOH detection very challenging particularly in the presence of water. Herein, the fluorometric detection of a trace amount of MeOH in EtOH/^{i}PrOH in the presence of water using alcohol coordinated Al(III)-complexes of an aldehydic phenol ligand containing a dangling pyrazole unit is described. The presence of MeOH in the EtOH/^{i}PrOH causes a change of the complex geometry from tetrahedral (Td) to octahedral (Oh) due to the replacement of the coordinated EtOH/^{i}PrOH by MeOH molecules. The Td-complex exhibited fluorescence but the Oh-species did not, because of the intramolecular photo-induced electron transfer (PET). By interacting the Oh species with water, its one MeOH coordination is replaced by a water molecule followed by the proton transfer from the water to pyrazole-N which generates strong fluorescence by inhibiting the PET. In contrast, the water interaction dissociates the Td-complex to exhibit fluorescence quenching. The water induced reversal of the fluorescence response from the decrease to increase between the absence and presence of MeOH is utilized to detect MeOH in an EtOH/^{i}PrOH medium containing water with a sensitivity of ~0.03–0.06% (v/v). The presence of water effected the MeOH detection and allows the estimation of the MeOH contamination in alcoholic beverages and hand sanitizers containing large amounts of water.

Received 6th July 2021
Accepted 25th August 2021

DOI: 10.1039/d1ra05201b

rsc.li/rsc-advances

Introduction

Worldwide, hundreds of economically constrained people are dying every year because of consumption of methanol (MeOH) contaminated illicit liquors.[1–3] In the countryside, use of crude fermentation methods and improper distillation are the main culprits for the MeOH contamination in ethanol (EtOH). In some cases, unavoidable MeOH formation during standard fermentation processes is also a major concern.[4] Consumption of MeOH beyond a certain permissible limit (1–2 mL per kg body mass) directly affects the central nervous system, by inhibiting the activity of cytochrome c oxidase, causing hypoxia, acidosis or even a painful death.[5–9] Even a minute amount of MeOH ingestion, approximately 10 mL of dietary intake, is potent enough to cause some adverse effects.[10,11] The use of much less expensive MeOH is a very common illegal practice used to alter the EtOH strength in alcoholic beverages to give a higher profit. Nevertheless, in recent times during the COVID-19 pandemic, a large number of poisonous MeOH containing hand sanitizers were seized worldwide, even after repeated warnings from the FDA.[12] Because the use of costly EtOH and isopropanol (^{i}PrOH) based hand sanitizers has significantly increased to help combat the COVID-19 pandemic, indiscriminate commercial production inevitably increases the chance of using MeOH containing cheaper hand sanitizers.[12]

The MeOH, EtOH and ^{i}PrOH are all chemically similar in nature.[13–15] Thus, using a reaction based chemical sensor, MeOH detection in commercial alcoholic beverages and hand sanitizers containing a large amount of EtOH/^{i}PrOH as well as water is an extremely challenging task.[16–18] In the search for an alternative method of detection, researchers focused on various other analytical procedures, such as different types of mass spectrometry (MS),[19–21] gas chromatography,[22–24] cyclic voltammetry,[25] capillary electrophoresis,[26] quartz crystal microbalances (QCMs) and so on.[27] However, costly sophisticated instrumentation, the requirement of skilled technicians or tedious standardizations for the previous methods are major disadvantages for using them in routine analysis. In view of their cost-effectiveness and easy detection protocol, the reaction

[a]*Department of Chemistry, Jadavpur University, Kolkata 700032, India. E-mail: parthaparui@yahoo.com; Fax: +91-33-24146223; Tel: +91-9433490492*
[b]*Department of Chemistry, Maulana Azad College, Kolkata 700013, India*
[c]*Department of Chemistry, Barasat Govt. College, Kolkata 700124, India. E-mail: r_ambarish@yahoo.co.in; Tel: +91-9836650180*

† Electronic supplementary information (ESI) available. See DOI: 10.1039/d1ra05201b

based chemical sensing methods are far superior detection techniques.

Fluorometric chemical sensing because of its ultra-high sensitivity is considered to be one of the most effective methods. Despite this, few organic fluorescent probes for MeOH are reported in the literature and those that are have certain limitations.[17,28–30] Different materials have also been used as MeOH fluorosensors such as a supramolecular ionic material by Zhang *et al.*,[31] a bimetallic lanthanide-organic framework by Du and co-workers,[32] and nitrogen-doped oxidized carbon dots by Latha *et al.*[33] In most of the cases MeOH is differentiated only from EtOH but not from ^{i}PrOH. The detection is based on either an increase or decrease of the relative intensity changes between MeOH and EtOH but never in the opposite direction, that is an increase for one and a decrease for the other. In addition, the effect of a large amount of water in the sample being analyzed for MeOH, although useful in the preparation of alcoholic beverages and hand sanitizers, has not been thoroughly investigated. Thus, it is proposed that the MeOH detection based on water induced a reverse fluorescence response for the probe such as an increase in intensity in the presence of MeOH but a decrease in intensity in its absence for a EtOH/^{i}PrOH medium.

The aldehydic phenol ligand (PPY) and its alcohol coordinated Al(III)-complexes were strategically synthesized, and they exhibited a water mediated MeOH selective fluorometric response. The presence of MeOH in EtOH/^{i}PrOH induces a change in the complex geometry from a fluorescent tetrahedral (Td) form to a weakly fluorescent octahedral (Oh) form, which is due to the exchange of coordinated EtOH/^{i}PrOH by MeOH. The interaction of water with the Oh-species exhibited a strong fluorescence intensity because of the exchange of its one coordinated MeOH with a water molecule followed by an intramolecular proton transfer from the coordinated water to the ligand moiety. However, the less stable Td-complex in the absence of MeOH is dissociated by the water interaction to exhibit an intensity decrease. Such water induced opposite intensity changes between the absence and presence of MeOH are utilized to detect MeOH in EtOH/^{i}PrOH and in alcoholic beverages/hand sanitizers in a water medium.

Experimental

The general experimental procedures and materials are described on page S2 of the ESI.†

Synthesis of PPY

Firstly, 3,5-dimethylpyrazole (**1**) and 2-hydroxy-3-(hydroxymethyl)-5-methylbenzaldehyde (**2**) were synthesized according to published procedures.[34,35] To synthesize 3-(chloromethyl)-2-hydroxy-5-methylbenzaldehyde (**3**), **2** (0.5 mol) was taken in 2 mL of dichloromethane (DCM, CH_2Cl_2) and the suspension obtained was stirred. Freshly distilled $SOCl_2$ in DCM was added drop wise (final ratio of $SOCl_2$: DCM = 1 : 1) under constant stirring. The yellow colored solution obtained was then stirred for another hour. Then the unreacted $SOCl_2$ was removed. The solid residue was dissolved in 1 mL of DCM and the solution was further diluted in 1 mL of hexane. The diluted solution was then kept until it had evaporated to dryness, which produced white colored crystals. Next, 1.84 g (10 mmol) of **3** was dissolved in 5 mL of dry THF. Then, 0.96 g (10 mmol) of **1** was taken in 20 mM of TEA. The solution of **1** was added drop wise into the solution of **3**, and the mixture was stirred for 24 h. The solution was extracted with brine solution and activated by Na_2SO_4 to obtain the desired product (PPY), which was further purified using column chromatography. ^{1}H-NMR (DMSO-d_6, 400 MHz): 2.08 (s, 3H, ArC$\underline{H}_3$), 2.23 (s, 6H, Py-2C$\underline{H}_3$), 2.51 (solvent residual peak), 3.33 (due to trace H_2O), 5.14 (s, 2H, C$\underline{H}_2$-Ar), 5.86 (s,1H, Py-C=CH), 6.98 (s,1H, ArH), 7.49 (s,1H, ArH), 10.08 (s, 1H, CH=O), 11.12 (s,1H, ArOH) ppm. ^{13}C-NMR (DMSO-d_6, 75 MHz): 10.96, 13.82, 20.51, 39.51–40.90 (solvent residual peak), 46.51, 105.44, 121.82, 126.43, 129.27, 131.85, 136.95, 139.96, 139.79, 146.99, 156.36, 196.19 (Fig. S1 and S2, ESI†). ESI-MS$^+$ for PPY in methanol: m/z calc. for [PPY + H]$^+$: 245.281, found: 245.221 (Fig. S3A, ESI†).

Generation of PPY/Al^{3+} *in situ* complex and its reaction with water

For preparation of a stock solution of $AlCl_3$ (1 mM), appropriate amounts of anhydrous $AlCl_3$ were taken in different alcohol mediums and the mixture was vortexed until completely solubilized. Stock solutions of PPY (1 mM) in each alcohol medium were prepared separately. The alcohol medium was kept the same for the preparation of stock solutions and reaction medium. A portion (10 μL or 4 μL) of the stock solution of PPY (final concentration: 10 μM or 2 μM) was added to each reaction medium (final volume 2 mL) containing various amounts of $AlCl_3$ (5–200 μM) in the absence or presence of water and/or MeOH in alcohol mediums under constant stirring, and the time-dependent PPY/Al^{3+} complex formation kinetics were monitored using UV-vis absorption and fluorescence studies at 25 °C. A diluted solution of PPY/Al^{3+} (0.1 μM PPY + 5 μM $AlCl_3$) was used for the limit of detection (LOD) studies.

UV-vis absorption and fluorescence studies

The UV-vis absorption and fluorescence studies were carried out in a double beam spectrophotometer (TCC-240A, Shimadzu, Japan) and spectrofluorometer (LS 55, PerkinElmer). The fluorescence spectra were obtained upon excitation at 402 nm (excitation band-pass: 10 or 8, and emission band pass: 2 or 8). Time-dependent fluorescence intensities at 505 nm were monitored for up to 60 min upon excitation at 405 nm while maintaining the same excitation and emission band-pass. The measuring solutions were filtered using a 0.45 mm filter (Millex, Millipore). The data reproducibility was checked using multiple measurements.

The LOD for MeOH was obtained as:[36]

$$\text{Detection limit (LOD)} = 3\sigma/k,$$

where σ, and k represent the experimental standard deviation and slope value of the linear fitting, respectively.

The fluorescence quantum yields were measured according to a procedure described earlier.[37]

Theoretical calculations

For structural optimization, density function theory (DFT) calculations were performed with the Gaussian 09 Program.[38] Time-dependent DFT (TD-DFT) calculations were performed to obtain UV-vis absorption parameters of different species. The structural optimizations were carried out by considering the B3LYP exchange-correlation functional and the 6-31G basis function.

Results and discussion

Probe design for MeOH detection

The synthesis route of the Al^{3+} binding aldehydic phenol ligand consisting of a dangling pyrazole unit (PPY) is shown in Scheme 1. It has recently been reported that the Al^{3+} ion exhibits a strong complex formation affinity with phenolic Schiff-base molecules by binding to phenolic-O and imine-N in alcohol solvents, and the rest of the Al(III)-coordination sites were filled by alcohol molecules.[39] In this research, the aldehydic moiety was deliberately not converted into the corresponding imine functionality of PPY, in order to achieve a reduced complex formation affinity due to the weaker interaction ability of aldehydic-O than that of the imine-N. Thus, upon the addition of a trace amount of the MeOH in the EtOH/^{i}PrOH medium, a spontaneous conversion from a structurally fragile Td geometry to a relatively stable Oh symmetrical PPY/Al^{3+} complex is possible due to the exchange of coordinated EtOH/^{i}PrOH by MeOH molecules. The reaction of water with PPY/Al^{3+} induces a fluorescence increase for the Oh species, but an intensity decrease for the Td complex. The MeOH induced the reversal of the fluorescence intensity change due to the change of the Al(III) geometry which was utilized for the detection of trace MeOH in EtOH/^{i}PrOH.

The PPY/Al^{3+} complex formation and its interaction with water

In the presence of anhydrous $AlCl_3$ (200 μM), the UV-vis absorption intensity at ~340 nm for PPY (10 μM) in alcohol solvents decreased gradually with time (up to 60 min), upon the formation of a new intensity at 405−410 nm through an isosbestic point at ~378 nm (Fig. 1 and S4, ESI†), indicating that PPY was involved in a complex formation reaction with the Al^{3+} ion by a kinetically slow process. The amount of complex formation was evaluated directly by judging the relative intensity changeover from ~340 nm to the 405–410 nm absorption band, because both intensities are not overlapped by each other (Fig. 1). However, to estimate the equilibrium between PPY and its Al(III)-complex in the presence of various amount of $AlCl_3$ (20–200 μM), the intensity values when the reaction attained equilibrium in nearly in 60 min were evaluated (Fig. 1 and S5, ESI†). It should be noted that a large amount of Al^{3+} (~200 μM, 20 equiv.) was required to react all the PPY with Al^{3+} in an MeOH medium (Fig. 1 and S5, ESI†), which suggested that the interaction of PPY with the Al^{3+} ions was not only kinetically slow but also thermodynamically weak in nature. However, large fractions of unreacted PPY ~60% in EtOH and ~50% in ^{i}PrOH medium were identified in the presence of the same concentration of Al^{3+} (20 equiv.) (Fig. 1). This result indicates that the complex formation affinity was reduced even more in the EtOH/^{i}PrOH than in the MeOH medium.

In spite of inadequate complex formation in the EtOH or ^{i}PrOH solvents, the intensity at ~405 nm for the PPY/Al^{3+} complex was ~3-fold larger, *i.e.*, there was a 6–7 times higher molar extinction coefficient (ε) value (~1.1 × 10^4 M^{-1} cm^{-1}), than that observed in MeOH (~0.17 × 10^4 M^{-1} cm^{-1}) (Fig. 1). Although phenolate-O and Al^{3+} bond formation was quite obvious, the formation of aldehydic-O with the Al^{3+} bond was

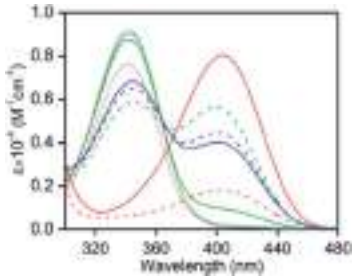

Fig. 1 The UV-vis absorption spectra of PPY (10 μM) in the presence (solid lines) and absence (broken lines) of 2.5% (v/v) water containing anhydrous $AlCl_3$ (200 μM) at 25 °C: red, MeOH; blue, EtOH and green, ^{i}PrOH. The spectra were collected during the 60 min of $AlCl_3$ addition. The spectra of PPY in the absence of $AlCl_3$ and water are depicted in their respective light colors for comparison.

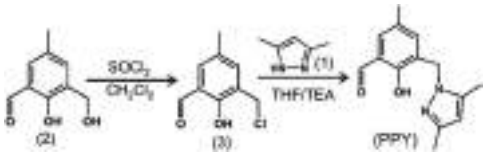

Scheme 1 Synthesis route of PPY.

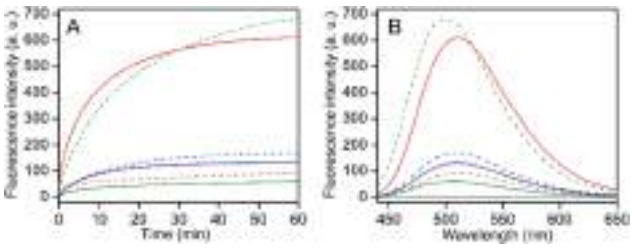

Fig. 2 (A) Time-dependent fluorescence intensity changes at 505 nm upon the addition of anhydrous $AlCl_3$ addition (50 μM), and (B) fluorescence spectra in 60 min of $AlCl_3$ addition in various alcohol solvents in the presence (solid line) and absence (broken line) of 2.5% (v/v) water containing PPY (2 μM) at 25 °C: red, MeOH; blue, EtOH and green, ^{i}PrOH. The spectrum in the absence of PPY is shown in grey (B). The excitation wavelengths were 405 nm in both (A and B).

assured by an up-field ^{1}H-NMR chemical shift from ~9.91 to 9.53 ppm, which was presumably due to an Al^{3+} binding induced, increased negative charge density at the aldehydic-O (Fig. S6 and S7 ESI,† compare with the theoretical calculation section). Furthermore, a 1 : 1 PPY to Al^{3+} binding with a reflection of coordinated alcohol molecules (maximum up to four MeOH molecules (*m*/*z* calc. for $[PPY + 4MeOH + Al + Cl]^+$: 433.873, found: 433.912) and two EtOH molecules (*m*/*z* calc. for $[PPY + 2EtOH + Al + Cl]^+$: 397.854, found: 397.823)) were recognized in the ESI-MS$^+$ studies (Fig. S3B and D ESI†)). The results indicated that the saturation of the Al(III)-coordination was effected by the solvent alcohol molecules. The reaction of MeOH (1–20% (v/v) with the solvent coordinated PPY/Al^{3+} in the presence of unreacted PPY in EtOH/^{i}PrOH showed a gradual decrease of both UV-vis intensities at ~340 nm of unreacted PPY and at ~403 nm of the PPY/Al^{3+} complex due to newly formed MeOH coordinated complexes and a replacement of coordinated EtOH/^{i}PrOH by MeOH molecules in the solvent coordinated PPY/Al^{3+}, respectively, (Fig. S8, ESI†). The results justified the proposition that the stability or formation affinity was higher for MeOH coordinated PPY/Al^{3+} than for the EtOH/^{i}PrOH coordinated one.

The interaction of the PPY/Al^{3+} complex with water molecules in EtOH/^{i}PrOH medium showed an increase of absorption intensity at ~340 nm whereas a decrease in intensity at ~405 nm indicated the dissociation of the complex (Fig. S9, ESI†). However, a similar water interaction in the MeOH medium caused a large increase of absorption intensity (~4-fold) at 405 nm without generating any absorption band at ~340 nm for free PPY (Fig. 1). This result shows that water reacted with the Al(III) center in the MeOH coordinated PPY/Al^{3+} complex without disturbing the PPY and Al(III) interaction. Because of the greater stabilities of MeOH coordinated species, an incorporation of a water molecule in the Al(III) coordination site may occur by it replacing one coordinated MeOH molecule, and this phenomenon was verified from the ESI-MS$^+$ measurements (*m*/*z* calc. for $[PPY + 3MeOH + H_2O + Al + Cl]^+$: 419.842, found: 419.762) (Fig. S3C, ESI†).

Solvent alcohol/water induced fluorescence response for PPY/Al^{3+}

The PPY exhibited no fluorescence intensity. With an addition of $AlCl_3$ (50 μM, 25 equiv.) in separate different alcohol mediums (MeOH, EtOH or ^{i}PrOH) containing PPY (2 μM), the fluorescence intensity at ~510 nm was enhanced gradually with time until the intensity was nearly saturated in ~60 min of Al^{3+} addition (Fig. 2A). However, the saturated intensity value varied widely depending on the alcohol medium. Compared to MeOH, ~8- and 2-fold larger intensities were detected in ^{i}PrOH and EtOH, respectively, (ϕ_F ~ 0.013 for MeOH, ~0.025 for EtOH, and ~0.102 for ^{i}PrOH) (Fig. 2). Interestingly, the interaction of water with the PPY/Al^{3+} complex exhibited an increase of intensity in the MeOH medium but an intensity decrease in the EtOH/^{i}PrOH medium (Fig. 2). An intensity increase of about 6-fold was observed in the MeOH medium containing ~1.2% (v/v) water, whereas the intensity increased maximally up to ~6.7-fold (ϕ_F ~ 0.09) in the presence of ~2.5% water (Fig. 3). In contrast, intensity quenching, almost completely in ^{i}PrOH and ~20% in EtOH solvents was detected by the addition of 5% water (Fig. 3). Similarly to the EtOH/^{i}PrOH solvent, the water induced fluorescence decrease was noticed for other alcohols (*n*-PrOH, ^{t}BuOH, *n*-hexanol) (Fig. S10, ESI†). Therefore, MeOH is a unique alcohol to use to show the water induced fluorescence increase.

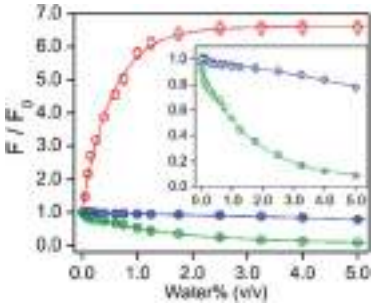

Fig. 3 The ratio of fluorescence intensities at 505 nm for the PPY/Al^{3+} complex in the presence of various amounts of water% and its absence are plotted with the value of water% (v/v) in different alcohol mediums at 25 °C: red, MeOH; blue, EtOH and green, ^{i}PrOH. The intensity values in the absence and presence of different water% are collected in 60 min of anhydrous $AlCl_3$ (50 μM) addition in the medium containing PPY (2 μM). Inset: the *Y*-axis expanded plots for EtOH and ^{i}PrOH medium are shown for clarity. Excitation and emission wavelength were 405 and 505 nm, respectively. The data points for each alcohol solvent are fitted using a single exponentially-fitted method. The average value for each data point is obtained from triplicate measurements ($n = 3$).

DFT theoretical calculations: complex structure *vs.* optical response

The Al(III) can exist as both Oh and Td geometric forms,[40–42] where the Oh symmetry is more preferred than the Td symmetry.[41,42] According to the results of the ESI-MS$^+$ studies, coordination of four MeOH and two EtOH molecules in the respective solvents were identified (Fig. S3, ESI†). Because PPY was acting as 1 : 1 bi-dentate ligand for Al^{3+}, the coordination of the four MeOH molecules was related to the Oh geometry of Al(III). However, the same number of alcohol molecules binding for bigger EtOH or ^{i}PrOH or any other alcohol molecules may not be a steric fit around the Al(III) coordination sphere, thus a less stable Td structure which would allow two EtOH/^{i}PrOH molecules was the most likely to occur (Scheme 2).

Using a DFT based theoretical calculation, it was identified that a possible Oh to Td structural interconversion for PPY/Al^{3+} was responsible for the alcoholic solvent dependent changes in UV-vis absorption and fluorescence properties, both in the presence and absence of water. The ground state geometries of four MeOH and two EtOH/^{i}PrOH molecules coordinated Oh and Td complexes, respectively, with common phenolic-O and aldehydic-O coordination were optimized using B3LYP density function and a 6-31G basis set. The UV-vis absorption properties for the Oh and Td structures were evaluated using the TD-DFT calculations on the optimized ground state structures. The calculated HOMO to LUMO electronic transitions at ~409 nm

for both Oh and Td structures corresponded well with the respective experimental absorption wavelengths (Fig. 1, 4 and Scheme 2). In a similar way to the experimentally observed UV-vis intensity increase at ~405 nm obtained by changing the solvent medium from MeOH to EtOH/^{i}PrOH, the HOMO → LUMO oscillator strength (f_{cal}) for the MeOH coordinated Oh geometry (~0.04) was found to be significantly lower than that detected for the EtOH/^{i}PrOH coordinated Td geometry (~0.07) (Fig. 4). When one coordinated MeOH close to the pyrazole-N was replaced by a water molecule, the optimized structure showed a proton transfer reaction from the coordinated water molecule to pyrazole-N, and a large increase of f_{cal} from ~0.04 to 0.09 was detected (Fig. 4 and Scheme 2). The increase of f_{cal} agreed well with the experimentally observed water induced large increase of UV-vis intensity in the MeOH medium (Fig. 1).

The efficient PET process from the pyrazole unit to the aldehydic phenol chromophore moiety made the PPY non-fluorescent (Fig. S11, ESI†). For the MeOH coordinated Oh structure, the PET process did not disturb it significantly, and thus a weak fluorescence intensity was observed experimentally (Fig. 2 and 4). However, the electron distribution in both HOMO and LUMO for EtOH or ^{i}PrOH coordinated Td-species centered mostly at the aldehydic phenol chromophore, and the resultant suppression of the PET process made the Td complex highly fluorescent (Fig. 2, **4** and Scheme 2). Most interestingly, the calculations also identified that the PET process in the water substituted Oh species was eliminated, which clarified the probable reason for the water induced large increase of fluorescence intensity in the MeOH medium. All these studies suggested that the change of Al(III) geometry from Oh to Td may be responsible for the alcohol solvent dependent change in optical response for the PPY/Al^{3+} complex.

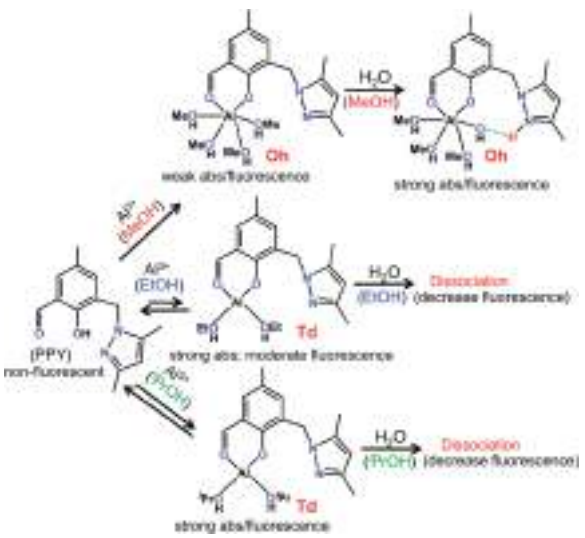

Scheme 2 Mechanistic view of alcoholic solvent selective formation of geometrically different PPY/Al^{3+} complexes and their reaction with water molecules. The Al(III) coordination saturation for the octahedral (Oh) geometry in MeOH and the tetrahedral (Td) geometry in EtOH/^{i}PrOH medium are achieved by the coordination of four MeOH and two EtOH/^{i}PrOH molecules, respectively. The coordination geometry dependent relative UV-vis absorption (abs), and the emission parameters of the PPY/Al^{3+} complex are shown.

Detection of MeOH in EtOH or ^{i}PrOH in the presence of water

It was found that the addition of water induced a fluorescence increase for MeOH coordinated Oh PPY/Al^{3+}, whereas the intensity decreased for the EtOH/^{i}PrOH coordinated Td complex (Fig. 3). An intensity increase of about 6.7-fold was found in MeOH/water mixed medium, which remained unaffected within a water% of ~2.5%–11.0% (v/v), although the intensity decreased gradually as the water% was further increased (Fig. 3 and S12, ESI†). However, for the water% amount above ~75%, the intensity value was found to be less in comparison to that observed in the absence of water (Fig. S12, ESI†). It was also observed that the coordinated solvent in the PPY/Al^{3+} complex were replaced by MeOH from the EtOH/^{i}PrOH molecules with a subsequent change of complex geometry from Td to Oh by the addition of MeOH in EtOH/^{i}PrOH (Fig. 2, Scheme 2, and Fig. S8, ESI†). Additionally, the residual unreacted PPY existed after the completion of a complex formation in EtOH/^{i}PrOH medium reacted further with Al^{3+} to form MeOH coordinated PPY/Al^{3+} in the presence of MeOH (Fig. S8, ESI†). Moreover, the presence of 10% MeOH in the solution with various EtOH/^{i}PrOH to water ratios showed that the presence of water effected different extents of intensity increase up to 70% water (Fig. S13, ESI†). All these results strongly suggest that the relative percentage of MeOH

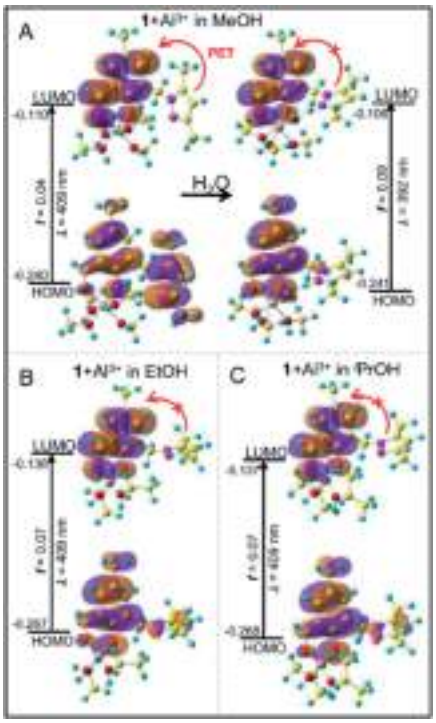

Fig. 4 Frontier molecular orbital (FMO) profiles including different calculated UV-vis absorption parameters of MeOH (A: left upper panel) and MeOH/H_2O (A: right upper panel) coordinated Oh. The EtOH (B: left lower panel) and ^{i}PrOH (C: right lower panel) coordinated Td complexes based on DFT and TD-DFT (B3LYP/6-31G) calculations.

coordinated Oh complex with respect to the EtOH/^{i}PrOH coordinated Td species should be much higher even in the presence of a low amount of MeOH in EtOH/^{i}PrOH. The water effected fluorescence intensity increased in the presence of various MeOH amounts was investigated for its potential use in the analytical detection of MeOH in EtOH/^{i}PrOH.

In the EtOH/^{i}PrOH medium containing water, the intensity ratios between the presence and absence of MeOH increased gradually with the increase of MeOH% (0.5–10% (v/v)) when the amount of any fixed water% value was within 2.5–55% (Fig. 5 and S14, ESI†). The relative intensity enhancements depended on the water%. For a solution containing 10% MeOH, the relative intensity increments were ~2.0-, 3.1-, 2.5- and 1.5-fold for the EtOH system or ~1.8-, 3.7-, 3.5- and 2.2-fold for the ^{i}PrOH system in the presence of 2.5%, 10%, 25%, and 55% (v/v) of water, respectively (Fig. 5). The extent of the relative intensity increase with increasing MeOH% under various water% (2.5–55%) values followed a fairly good linear correlation (residual of fitting $\chi^2 \sim 0.99$) for both the EtOH and ^{i}PrOH systems, where the water% dependent slope values were estimated to be ~0.10, 0.21, 0.15 and 0.08 for EtOH or ~0.08, 0.26, 0.25 and 0.12 for ^{i}PrOH in the presence of 2.5%, 10%, 25% and 55% water, respectively (Fig. 5). Using the linear calibration curve, the unknown amount of MeOH in the EtOH/^{i}PrOH solvent containing various water% can be evaluated ratiometrically. It was evident that the water amount present in the solution played the most critical role for the MeOH detection sensitivity, in which the sensitivity was at maximum at a water amount of ~10% (v/v) for both EtOH and ^{i}PrOH. Notably, the MeOH (10% v/v) also induced an appreciable amount of increased fluorescence intensity for PPY/Al^{3+} and this was also observed in other alcohol mediums (*n*-PrOH, ^{t}BuOH and *n*-hexanol) containing 5% water (Fig. S15, ESI†), which indicated that the MeOH detection selectivity of the PPY/Al^{3+} complex did not alter with the change of alcohol systems. However, to detect a low amount of MeOH or low LOD values, fluorescence studies were conducted in the presence of very low PPY/Al^{3+} concentrations (0.1 μM PPY and 4 μM Al^{3+}) so that an appreciable fluorescence response can be observed even in the presence of much lower amount of MeOH. The fluorescence intensity changes in the presence of much lower amounts of MeOH (0.05–0.30%) are shown in Fig. S16 (ESI†). The LOD was evaluated using the equation: LOD = $3\sigma/k$ (see Experimental section). The LOD values for MeOH detection were estimated to be ~0.03%–0.06% depending on the solvent compositions.

The water% dependency variation of the fluorescence response for MeOH was interpreted by combining the water% dependent various extent of intensity increase for MeOH medium in the absence of EtOH/^{i}PrOH and the intensity decrease for EtOH/^{i}PrOH in the absence of MeOH (Fig. 3 and S12, ESI†). The presence of a small amount of MeOH in the EtOH/^{i}PrOH medium replaced coordinated EtOH/^{i}PrOH with MeOH molecules in PPY/Al^{3+} to obtain a Td to Oh structural change. However, the existence of an EtOH/^{i}PrOH coordinated Td complex and its water interaction induced intensity decrease cannot be neglected entirely in the interpretation of the fluorescence response values in the presence of various amounts of MeOH and water. The presence of a water induced ~6.7-fold intensity increase remains unchanged between 2.5% and 10% of water for MeOH in the absence of EtOH/^{i}PrOH (Fig. 3 and S12, ESI†) and the observed intensity was decreased by increasing the water% (2.5% to 10%) for EtOH/^{i}PrOH in the absence of MeOH, which effects the enlargement of the MeOH detection slope value (~0.10 to 0.21 for EtOH and ~0.08 to 0.26 for ^{i}PrOH) by the increase of water%. Significantly higher slope changes for ^{i}PrOH medium: ~3.7-fold compared to ~2.1-fold for EtOH medium due to the increase of water% (2.5% to 10%) was rationalized by the increased water amount which induced a greater amount of intensity quenching for ^{i}PrOH (~90%) than the EtOH medium (45%) in the absence of MeOH (Fig. 5 and S12, ESI†). However, any further increase of water% from 10% to 55% produced a larger intensity decrease for MeOH in the absence of EtOH/^{i}PrOH than for EtOH/^{i}PrOH in the absence of MeOH (Fig. S12, ESI†), and thus a gradual decrease of the MeOH detection slope value from ~0.21 to 0.08 for EtOH and ~0.26 to 0.12 for ^{i}PrOH was observed.

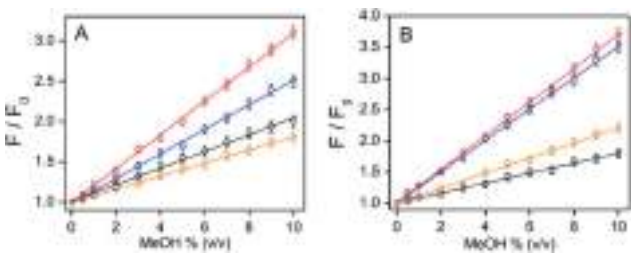

Fig. 5 Relative fluorescence intensity changes between the presence and absence of MeOH for PPY/Al^{3+} are plotted with MeOH% (v/v) in (A) EtOH/water and (B) ^{i}PrOH/water mixed medium containing various amounts of water% (v/v): black, 2.5%; red, 10%; blue, 25%; orange, 55%. The identical value of water% before and after the MeOH spike was maintained by an addition of an appropriate amount of water in the spiked sample. The intensity values in the absence and presence of various MeOH% were collected during the addition of $AlCl_3$ (50 μM), over 60 min, to the medium containing PPY (2 μM). The data points for each solvent system are fitted with a linear equation. Excitation and emission wavelengths were 405 nm and 505 nm. The average value for each data point is obtained from triplicate measurements ($n = 3$).

The MeOH detection in alcoholic samples and sanitizers

The EtOH% in alcoholic beverages are dependent (5–70% (v/v)) on their classifications, and usually water is the rest of the liquid volume. However, according to WHO guidelines, the composition of hand sanitizers should be ~80% EtOH (v/v) or 75% ^{i}PrOH (v/v), glycerol (1.45% (v/v)), and H_2O_2 (0.125% (v/v)).[43] Spiked MeOH% in high and low EtOH% containing vodkas (~45% (v/v)) and wine (~15% (v/v)) samples, respectively, were estimated. As the MeOH detection sensitivity at above 55% (v/v) of water was comparatively low (Fig. S12 and S13, ESI†), an external EtOH addition is required for the detection of MeOH in the wine samples. In addition, spiked MeOH was estimated both in the presence and absence of externally added EtOH to show the applicability of the method for alcoholic beverages containing higher EtOH%. However, the

spiked MeOH amounts were estimated in EtOH- and ^{i}PrOH-based hand sanitizers without any further addition of external EtOH/^{i}PrOH.

To observe the MeOH induced fluorescence intensity increase, the water% before and after MeOH spikes in the hand sanitizer samples were maintained by addition of an appropriate amount of water in the spiked MeOH sample. With the increase of MeOH spikes from 0.5% to 10% in the vodka sample in the presence and absence of externally added 30% EtOH (total water ~25%), the relative fluorescence intensity between the presence and absence of MeOH was found to increase linearly from 1.04- to 1.77-fold and 1.08- to 2.45-fold, respectively (Fig. 6A–C). For a wine sample with the externally added 30% EtOH, the relative intensity also increased linearly from 1.05- to 1.78-fold (Fig. S17, ESI†), where the slope value of the linear plots ~0.08 was found to be similar to that obtained for a known EtOH/water mixed medium (45% EtOH) or vodka (45% EtOH) sample (Fig. 5A). In addition, the slope values for vodka samples with 30% EtOH added externally (total EtOH, 75%) were also similar to the results obtained for the known 75% EtOH medium (Fig. 5A, 6B and C). All these results clearly showed that the presence of other chemicals in alcoholic beverages did not disturb the detection ability of the MeOH. Even without knowing the accurate water% value in the test sample, the estimation of MeOH contamination was possible from the correlation of fluorescence response of the test sample with the linear calibration plots for the corresponding MeOH free alcoholic beverages (Fig. 6C).

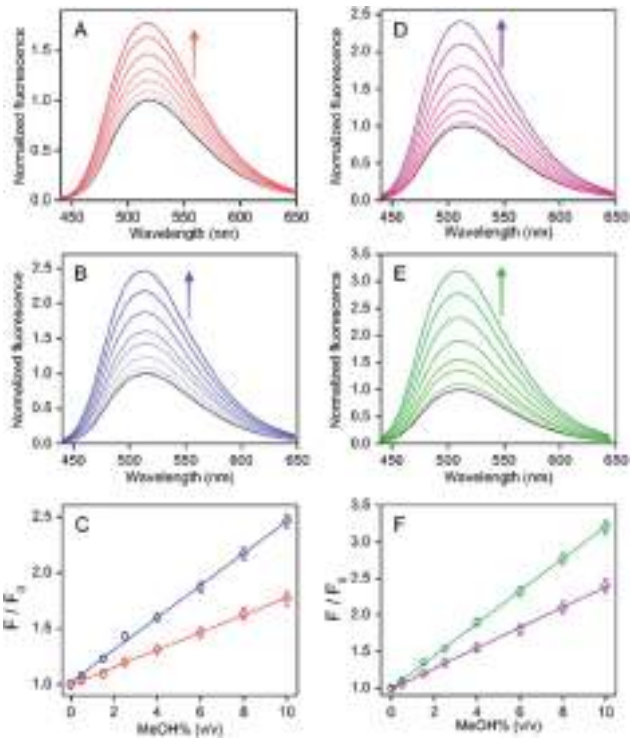

Fig. 6 The relative fluorescence spectral changes between the presence and absence of MeOH for PPY/Al^{3+} with various MeOH spikes (0.5–10% (v/v)) in an alcoholic beverage (vodka: labelled EtOH% ~ 45% (v/v)) in (A) the absence and (B) the presence of externally added 30% EtOH, and (D) EtOH or (E) ^{i}PrOH-based hand sanitizers (labelled ^{i}PrOH ~75% and EtOH ~80%) at 25 °C. The spectra in the absence of MeOH spikes are shown in black. The maximum intensity values for alcoholic beverages (C) and hand sanitizer (F) samples are plotted against the amount of the MeOH spikes. (A–C) Blue and red correspond to the presence and absence of externally added 30% EtOH, respectively. (D–F) Purple and green correspond to EtOH- and ^{i}PrOH-based hand sanitizer, respectively. (A–F) The identical value of water% before and after of MeOH spike was maintained by using an appropriate amount of water addition in the spiked sample. The intensity increases with the increase of MeOH% are shown by arrows. The excitation wavelength was 405 nm. The average value for each data point is obtained from triplicate measurements ($n = 3$).

The fluorescence spectra for PPY/Al^{3+} in EtOH (80%) or ^{i}PrOH (75%) and a water mixed medium remain unchanged by the addition of glycerol (1.45% (v/v)) or H_2O_2 (0.125% (v/v)), both in the presence and absence of MeOH (Fig. S18, ESI†), showing that the presence of glycerol and H_2O_2 in hand sanitizers did not affect the performance of the probe. The intensity increased linearly from ~1.05 to 2.38 for EtOH-based sanitizer or from ~1.08 to 3.22 for the ^{i}PrOH-based sanitizer because of the increase of the amount of MeOH spiking from 0.5% to 10% under the identical water% condition. The observed slope value of ~0.22 for the ^{i}PrOH-based sanitizer and of ~0.14 for the EtOH-based sanitizer were similar to that detected for the known 80% EtOH and 75% ^{i}PrOH medium, respectively (Fig. 5 and 6D–F). Therefore, an unknown amount of MeOH contamination in hand sanitizers could be estimated by correlating the intensity value of the test sample with the known linear calibration line obtained for the EtOH (or ^{i}PrOH) containing water or MeOH free standard for the EtOH (or ^{i}PrOH)-based hand sanitizer.

As in the procedure described previously, a low level of MeOH contamination in alcoholic beverages and sanitizer could be estimated using a low probe concentration (0.1 μM PPY and 4 μM Al^{3+}). The MeOH induced fluorescence spectral changes in the presence of a lower amount of MeOH spikes (0.06–0.18% for a vodka sample and 0.03–0.10% for the ^{i}PrOH hand sanitizer) revealed that even a MeOH contamination of below 0.1 μM in alcoholic beverages and sanitizer can be estimated accurately by the present protocols (Fig. S19, ESI†). The efficiency of probe recovery was also verified by conducting EDTA induced fluorescence intensity quenching studies in vodka and EtOH-based hand sanitizers. For both samples, MeOH induced ~90% of the increased intensity for PPY/Al^{3+} which was found to be quenched by the addition of EDTA, whereas the intensity recovered again upon further addition of Al^{3+} (Fig. S20, ESI†). The EDTA induced displacement of PPY from the PPY/Al^{3+} complex again participated in complexation with the freshly added Al^{3+} to regain the fluorescence intensity by the reaction with MeOH present in solution. Thus, the probe can be reused on several occasions.

Conclusions

A sensitive fluorometric MeOH detection method was demonstrated in EtOH/^{i}PrOH in a water medium using a 1 : 1 Al(III)-complex of an aldehydic phenol ligand containing a pyrazole

unit (PPY). The complex adopted the MeOH coordinated weakly fluorescent octahedral (Oh) geometry from the fluorescent tetrahedral (Td) structure by an addition of MeOH in the EtOH/^{i}PrOH. The interaction of water with the Oh species causes a large fluorescence intensity increase due to the exchange of one coordinated MeOH by a water molecule, whereas a similar water interaction for the Td complex resulted in an intensity decrease due to its dissociation. The water mediated fluorescence intensity reversal due to the change in complex geometries by the addition of MeOH was utilized to detect MeOH in EtOH/^{i}PrOH and various alcoholic beverages/hand sanitizers. Such water induced MeOH detection could be very useful industrially.

Author contributions

Snigdha Roy: experimental, analysis and review and editing. Sanju Das: synthesis. Ambarish Ray: conceptualization, supervision, editing. Partha Pratim Parui: experimental, conceptualization, writing – original draft, supervision.

Conflicts of interest

There are no conflicts of interest to declare.

Acknowledgements

This study is partially supported by UGC and the Government of West Bengal for financial support under the RUSA 2.0 scheme (PPP; No: 5400-F(Y)). SR wishes to acknowledge the UGC for the SRF fellowship. The authors also acknowledge Jadavpur University for use of their departmental facilities.

Notes and references

1 S. B. Jarwani, P. D. Motiani and S. Sachdev, *J. Emerg. Trauma Shock*, 2016, **6**, 73.
2 G. A. Beauchamp and M. Valento, *Emerg. Med. Pract.*, 2016, **18**, 1.
3 R. Paasma, K. E. Hovda, A. Tikkerberi and D. Jacobsen, *Clin. Toxicol.*, 2007, **45**, 152.
4 F. Bindler, E. Voges and P. laugel, *Food Addit. Contam.*, 1988, **5**, 343.
5 P. E. Hantson, *Bull Mem Acad R Med Belg*, 2006, **161**, 425.
6 D. G. Barceloux, G. R. Bond, E. P. Krenzelok, H. Cooper and J. A. Vale, *J. Toxicol. Clin. Toxicol.*, 2002, **40**, 415.
7 J. J. Liu, M. R. Daya and N. C. Mann, *J. Toxicol., Clin. Toxicol.*, 1999, **37**, 69.
8 F. Onder, S. Ilker, T. Kansu, T. Tatar and G. Kural, *Int. Ophthalmol.*, 1998, **22**, 81.
9 J. A. Kruse, *Crit. Care Clin.*, 2012, **28**, 661.
10 C. S. Moon, *Ann Occup Environ Med*, 2017, **29**, 44.
11 D. Jacobsen and K. E. McMartin, *Med. Toxicol.*, 1986, **1**, 309.
12 L. Welle, A. Medoro and B. Warrick, *Ann. Emerg. Med.*, 2021, **77**, 131.
13 P. F. Pereira, R. M. F. Sousa, R. A. A. Munoz and E. M. Richter, *Fuel*, 2013, **103**, 725.
14 Methanol: colorless, mp = −97.0 °C, bp = 64.7 °C, d = 0.79 g dm^3, n_D (at 20 °C) = 1.33, dipole moment = 1.70 D, dielectric constant = 33, pK_a = 15.5.
15 Ethanol: colorless, mp = −114.3 °C, bp = 78.4 °C, d = 0.799 g dm^3, n_D (at 20 °C) = 1.36, dipole moment = 1.69 D, dielectric constant = 24.6, pK_a = 15.9.
16 G. J. Mohr, F. Lehmann, U. W. Grummt and U. E. Spichiger-Keller, *Anal. Chim. Acta*, 1997, **344**, 215.
17 S. H. Lim, L. Feng, J. W. Kemling, C. J. Musto and K. S. S. Suslick, *Nat. Chem.*, 2009, **1**, 562.
18 T. Qin, B. Liu, Y. Huang, K. Yang, K. Zhu, Z. Luo, C. Pan and L. Wang, *Sens. Actuators, B*, 2018, **277**, 484.
19 L. R. Cordell, H. Pandya, M. Hubbard, A. M. Turner and S. P. Monks, *Anal. Bioanal. Chem.*, 2013, **405**, 4139.
20 T. M. Allen, T. M. Falconer, M. E. Cisper, A. J. Borgerding and C. W. Wilkerson, *Anal. Chem.*, 2001, **73**, 4830.
21 V. Shestivska, V. Kolivoska, J. Kubista, D. Smith and P. Spanel, *Rapid Commun. Mass Spectrom.*, 2020, **34**, 1.
22 M. L. Wang, Y. M. Choong, N. W. Su and M. H. Lee, *J Food Drug Anal*, 2003, **11**, 133.
23 M. Bursova, T. Hlozek and R. Cabala, *J. Anal. Toxicol.*, 2015, **39**, 741.
24 J. V. D. Broek, S. Abegg, S. E. Prastsinis and A. T. Guntner, *Nat. Commun.*, 2019, **10**, 1.
25 D. S. Park, M. S. Won, R. N. Goyal and Y. B. Shim, *Sens. Actuators, B*, 2012, **174**, 45.
26 M. S. F. Santos, E. T. D. Costa, I. G. R. Gutz and C. D. Garcia, *Anal. Chem.*, 2017, **89**, 1362.
27 C. Wang, F. Chen, X. W. He, S. Z. Kang, C. C. You and Y. Liu, *Analyst*, 2001, **126**, 1716.
28 V. Kumar, A. Kumar, U. Diwan, M. K. Singh and K. K. Upadhyay, *Org. Biomol. Chem.*, 2015, **13**, 8822.
29 Z. Wu, X. Fu and Y. Wang, *Sens. Actuators, B*, 2017, **245**, 406.
30 M. Zhao, Y. Yue, C. Liu, P. Hui, S. He, L. Zhao and X. Zheng, *Chem. Commun.*, 2018, **54**, 8339.
31 L. Zhang, H. Qi, Y. Wang, L. Yang, P. Yu and L. Mao, *Anal. Chem.*, 2014, **86**, 7280.
32 D. M. Chen, C. X. Sun, Y. Peng, N. N. Zhang, H. H. Si, C. S. Liu and M. Du, *Sens. Actuators B*, 2018, **265**, 104.
33 M. Latha, R. A. Devi, N. K. R. Bogireddy, S. E. S. Rios, W. L. Mochan, J. C. Uribe and V. Agarwal, *RSC Adv.*, 2020, **10**, 22522.
34 R. H. Wiley and P. E. Hexner, *Org. Synth.*, 1951, **31**, 43.
35 R. R. Gagne, C. L. Spiro, T. J. Smith, C. A. Hamann, W. R. Thies and A. K. Schiemke, *J. Am. Chem. Soc.*, 1981, **103**, 4073.
36 *International Conference on Harmonization (ICH) of Technical Requirements for Registration of Pharmaceuticals for Human Use, Topic Q2 (R1): Validation of Analytical Procedures: Text and Methodology*, 2005, http://www.ich.org.

37 J. V. Morris, M. A. Mahaney and J. R. Huber, *J. Phys. Chem.*, 1976, **80**, 969.
38 M. J. Frisch, *et al.*, *Gaussian 09 Rev. A.1*, Gaussian Inc., Wallingford CT, 2009.
39 S. Roy, S. Das, R. Majumder, A. Ray and P. P. Parui, *RSC Adv.*, 2020, **10**, 23245.
40 J.-J. Delpuech, M. R. Khaddar, A. A. Peguy and P. R. Rubini, *J. Am. Chem. Soc.*, 1975, **97**(12), 3373.
41 E. Furia, A. Beneduci, N. Russo and T. Marino, *New J. Chem.*, 2018, **42**, 11006.
42 L. Malacaria, G. A. Corrente, A. Beneduci, E. Furia, T. Marino and G. Mazzone, *Molecules*, 2021, **26**, 2603.
43 *Guide to Local Production: WHO-recommended handrub formulations (PDF)*, World Health Organization, WHO/IER/PSP/2010.5, WHO April, 2010.

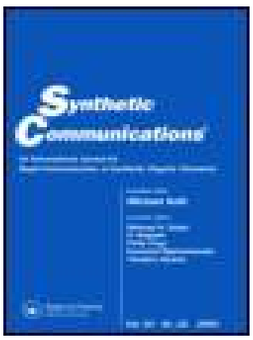

Synthetic Communications

An International Journal for Rapid Communication of Synthetic Organic Chemistry

ISSN: (Print) (Online) Journal homepage: https://www.tandfonline.com/loi/lsyc20

A facile potassium 18-crown ether catalysed synthesis of 2,6-dicyanoaniline and 3-amino-9,10-dihydrophenanthrene-2,4 dicarbonitrile and their *in vitro* intercalation study on calf thymus DNA

Arijit Kundu

To cite this article: Arijit Kundu (2021): A facile potassium 18-crown ether catalysed synthesis of 2,6-dicyanoaniline and 3-amino-9,10-dihydrophenanthrene-2,4 dicarbonitrile and their *in vitro* intercalation study on calf thymus DNA, Synthetic Communications, DOI: 10.1080/00397911.2021.1980807

To link to this article: https://doi.org/10.1080/00397911.2021.1980807

SYNTHETIC COMMUNICATIONS®
https://doi.org/10.1080/00397911.2021.1980807

Taylor & Francis
Taylor & Francis Group

A facile potassium 18-crown ether catalysed synthesis of 2,6-dicyanoaniline and 3-amino-9,10-dihydrophenanthrene-2,4 dicarbonitrile and their *in vitro* intercalation study on calf thymus DNA

Arijit Kundu

Department of Chemistry, Maulana Azad College, Kolkata, India

ABSTRACT

An efficient two-component domino reaction strategy has been developed for the synthesis of 2,6-dicyanoaniline and 3-amino-9,10-dihydrophenanthrene-2,4-dicarbonitrile derivatives in moderate to good yield by the reaction between malononitrile and β-chloro-α,β-unsaturated aldehydes catalyzed by potassium hydroxide-18-crown-6 in methanol. *In-vitro* intercalation studies of 3-amino-9,10-dihydrophenanthrene-2,4-dicarbonitriles with Calf-Thymus DNA have been carried out which reveal that the moiety interacts with an affinity greater than that of ethidium bromide (EtBr).

ARTICLE HISTORY
Received 24 June 2021

KEYWORDS
ADA molecule; DNA intercalation; potassium-18-crown 6

Introduction

Aromatic compounds substituted with acceptor-donor-acceptor (A-D-A) moieties such as 2,6-dicyanoaniline derivatives are of significant interest not only for mechanistic organic chemistry but for material science also. They are key structural features of various types of bioactive compounds, both naturally occurring and synthetically prepared,[1] and also versatile synthons for the wide-ranging nature of asymmetric compounds.[2] Varieties of molecules bearing A-D-A architectures have exhibited promise for use as molecular electronic devices[3] and nonlinear optical materials.[4] Hence, there is an enduring effort to explore an efficient methodology for the synthesis of A-D-A functionalized molecules starting from simple substrates and numerous protocols have been developed.[5] Domino reaction is a highly effective pathway in the sustainable and diversity-oriented synthesis involving the required number of starting materials using a one-pot reaction strategy, thus fulfilling the criteria of cost-effectiveness and less reaction time. With this idea in view, we have developed a two-component reaction for the synthesis of 2,6-dicyanoaniline and 3-Amino-9,10-dihydrophenanthrene-2,4-dicarbonitrile derivatives. Utilizing the benefit of the structural motif of β-chloro-α,β-unsaturated aldehydes, we optimize our strategy on the reaction between malononitrile and β-chloro-α,β-unsaturated aldehydes catalyzed by potassium hydroxide-18-crown-6 in methanol. To the best of our knowledge, this is the first report

CONTACT Arijit Kundu kunduarijit85@gmail.com Department of Chemistry, Maulana Azad College, 8, Rafi Ahmed Kidwai Road, Kolkata 700013, India.

Supplemental data for this article can be accessed on the publisher's website

Table 1. Optimization study using **1c** and **2**.

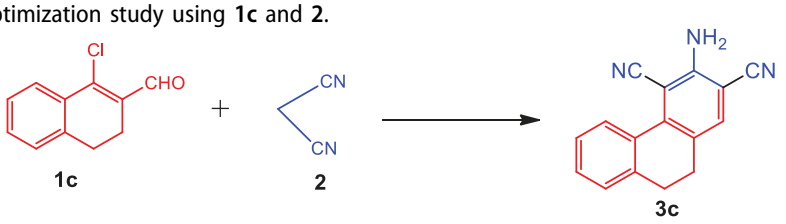

Sl. No.	Base[a]	Solvent[b]	Time (h)	Temp (°C)	Yield (%)[c,d]
1.	K_2CO_3	Water	3.5	100	15
2.	K_2CO_3	Water:EtOH (1:1)	3	100	20
3.	K_2CO_3	Water:EtOH (1:1)	2.5	80	25
4.	K_2CO_3	Water:EtOH (1:1)	3.5	60	15
5.	Triethyl amine	Water	3	100	20
6.	Triethyl amine	Water:EtOH (1:1)	3	100	35
7.	Triethyl amine	Acetonitrile	3.5	100	15
8.	Pyridine	Water	4	100	–
9.	Pyridine	Acetonitrile	4	100	–
10.	γ-Picoline	Water	4	100	10
11.	γ-Picoline	Acetonitrile	4	100	–
12.	Piperidine	Water	4.5	100	35
13.	Piperidine	Water:EtOH (1:1)	4	100	40
14.	Piperidine	Water:EtOH (1:1)	3.5	80	45
15.	Potassium hydroxide-18-crown-6	Water	1	100	70
16.	Potassium hydroxide-18-crown-6	Methanol	40 min	65	80
17.	**Potassium hydroxide-18-crown-6**	**Methanol**	**30 min**	**65**	**97**
18.	Potassium hydroxide-18-crown-6	Methanol	45 min	50	90

[a]All the reactions were carried out with 3 mmol base; [b]15 ml of solvent was used in each case; [c]All the reactions were carried out with 1-chloro-3,4-dihydronaphthalene-2-carbaldehyde (1.0 mmol) and malononitrile (2.0 mmol); [d]Yield of isolated product.

of the syntheses of 2,6-dicyanoanilines and 3-Amino-9,10-dihydrophenanthrene-2,4-dicarbonitriles from β-chloro-α,β-unsaturated aldehydes as masked β-dicarbonyl.

As nucleic acids have been chosen as drug targets for several types of ailments, studies on the nature of binding DNA by small molecules become highly important for drug designing.[6] DNA-binding via intercalation occurs by introducing a planar aromatic/heteroaromatic motif between adjacent DNA base pairs resulting in a substantial change in DNA structure with lengthening, stiffening, and unwinding of DNA helix.[7] Literature survey of the intercalators, which included highly potent drugs and also some carcinogens,[8] revealed that they encompass phenanthridines, quinolones, acridines, anthraquinones, anthracenes, phenazines, phenanthrolines, pyrenes derivatives. In the recent era, attention toward the designing and synthesis of new and efficient DNA-targeted intercalators acting as antitumor agents had grown.[9] In this perspective, we undertake *in vitro* binding studies of the synthesized A-D-A moieties bearing 9,10-dihydrophenanthrene structures with DNA. We have demonstrated that one 3-amino-9,10-dihydrophenanthrene-2,4-dicarbonitrile derivative interacts with Calf-Thymus DNA with an affinity greater than that of ethidium bromide (EtBr).

Results and discussion

We have established the optimum reaction condition for the synthesis of 2,6-dicyanoaniline derivatives viz. 3-amino-9,10-dihydro-phenanthrene-2,4-dicarbonitrile derivatives

Table 2. Potassium hydroxide-18-crown-6 catalysed synthesis of dicyanoaniline derivatives from β-chloro-α,β-unsaturated aldehydes.

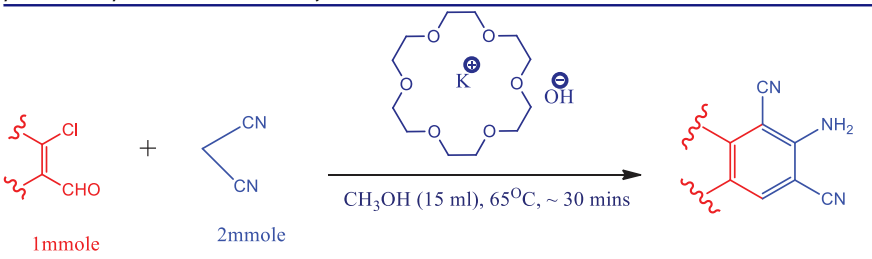

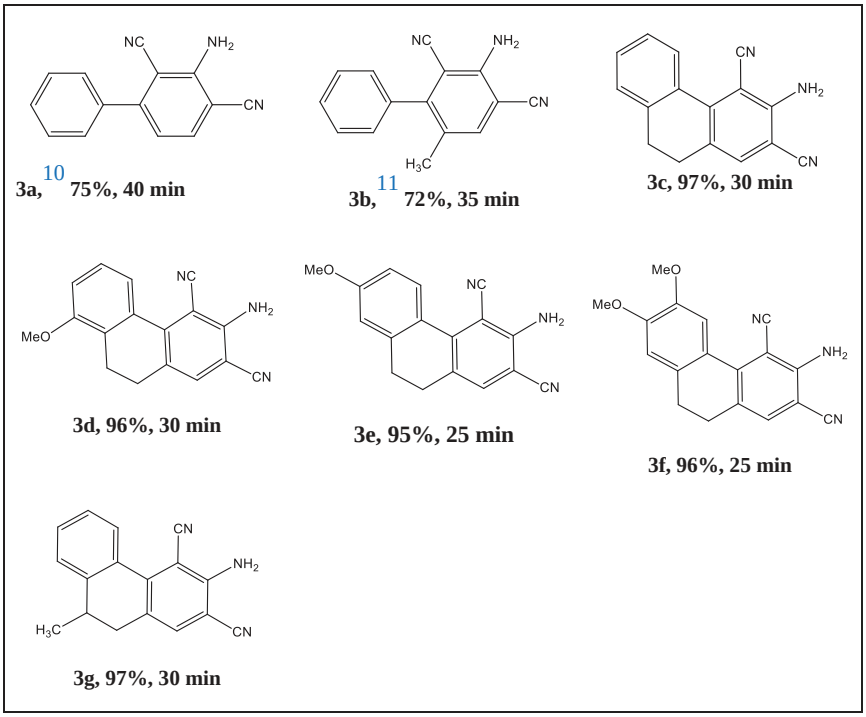

by carrying out extensive screening of a representative reaction between 1-chloro-3,4-dihydronaphthalene-2-carbaldehyde (**1c**) (1 mmol) and malononitrile (**2**) (2 mmol) in presence of different solvents and bases. The reaction parameters such as temperature, reaction time, etc. were also investigated and the results have been summarized in Table 1.

Initially, the reaction was carried out in the water by using potassium carbonate as a base which gave a low yield of the desired product after 3.5 h at 100 °C (Table 1, entry 1). The reaction was further carried out with the same base in water-ethanol (1:1) solvent at varying temperatures (Table 1, entries 2, 3, and 4) which resulted in a slight increase of product formation at the temperature 80 °C. The reaction was again tried in presence of triethylamine as a base in different solvents (Table 1, entries 5, 6, and 7) when no perceptible development

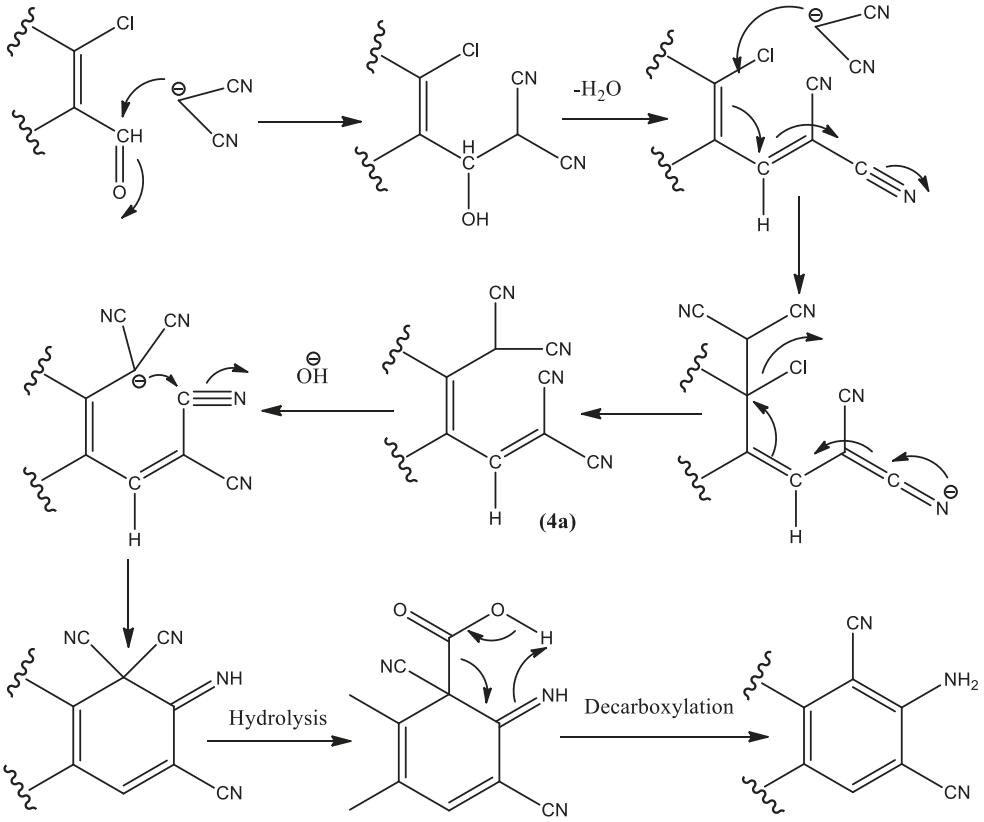

Figure 1. Plausible mechanism for the synthesis of dicyanoaniline derivatives from *β*-chloro-*α,β*-unsaturated aldehydes.

in the yield of product formation was observed. Henceforth, more screening tests were done by varying the bases, solvents, and temperatures (Table 1, entries 8, 9, 10, 11, 12, 13, 14, and 15) which showed a moderate yield of the desired product when potassium hydroxide-18-crown-6 was used in water at 100 °C within 1 h. Eventually, to identify the optimum condition, the reaction was carried out in methanol by varying temperatures in presence of potassium hydroxide-18-crown-6 (Table 1, entries 16, 17, and 18) and it was observed that heating the substrates in methanol at 65 °C using potassium hydroxide-18-crown-6 as base provided 97% yield of the product within 30 mins (Table 1, entry 17). Even slight alteration of reaction temperature caused a lower yield of the product formation (Table 1, entries 16 and 18). On the basis of the above results, we further studied the new methodology using different acyclic β-chloro-α,β-unsaturated aldehydes, and cyclic β-chloro-α,β-unsaturated aldehydes to demonstrate the versatility of the reaction (Table 2). In all the cases reaction proceeded efficiently with good to an excellent yield of the products.

The reaction was also scaled up with 10 mmoles of (**1c**) and 20 mmoles of (**2**) when the percentage yield of the product remained the same. The methodology yielded five new compounds (**3c–3g**) bearing 3-amino-9,10-dihydro-phenanthrene-2,4-dicarbonitrile structural features.

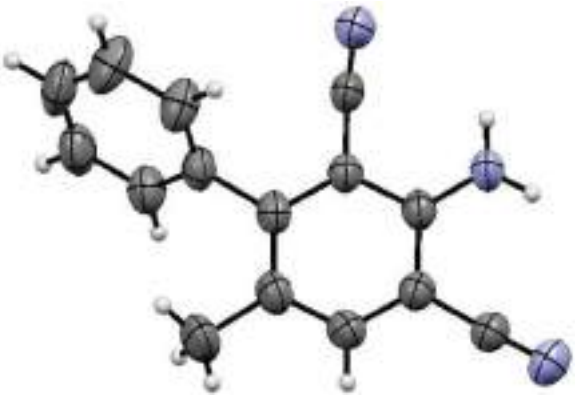

Figure 2. X-ray crystallographic structure of compound **3b**.

A plausible mechanistic pathway is proposed to explain the formation of 3-phenyl-2,6-dicyanoaniline derivatives and 3-amino-9,10-dihydro-phenanthrene-2,4-dicarbonitrile derivatives from β-chloro-α,β-unsaturated aldehydes (Fig. 1). Initially β-chloro-α,β-unsaturated aldehyde undergoes condensation with malononitrile in presence of potassium hydroxide-18-crown-6. Consequently the second molecule of malononitrile replaces the vinylic chlorine atom of β-chloro-α,β-unsaturated aldehyde to form **4a**. The in-situ formed **4a** undergoes hydrolysis followed by decarboxylation in methanol at 65 °C and ring closure yielding the desired dicyanoaniline derivatives.

The structures of all seven products were well characterized by using spectral (IR, ^{1}H, and ^{13}C NMR) and elemental analyses data. The structural motif was fully established by X-ray crystallographic analysis of one signified compound **3b** (CCDC 1543187) (Fig. 2). We could not obtain well- defined single crystal of any of the new compounds **3c–3g**.

Role of potassium hydroxide-18-crown-6

Potassium hydroxide-18-crown-6 plays an important role in the formation of dicyanoamines from β-chloro-α,β-unsaturated aldehyde. Essentially it acts as a base to abstract proton from malononitrile and initiates Knovenagel reaction. It is also evident from the mechanism that the hydrolysis of the aliphatic cyanide group in the proposed intermediate **4a** requires a very strong base. The naked hydroxyl ions from potassium hydroxide 18-crown-6 fulfill the criterion and accelerate the reaction to completion.

In vitro intercalation study on calf thymus DNA

Interaction of compound 3c with DNA

Absorption spectroscopic studies of the compound in presence of CT DNA

The interaction of the 3-amino-9,10-dihydrophenanthrene-2,4-dicarbonitrile derivatives with chromosomal CT DNA was investigated by the spectrophotometric method. From the spectral data it has been observed that, among the five synthesized 3-amino-9,10-dihydro-phenanthrene-2,4-dicarbonitrile derivatives, only compound **3c** interact with CT DNA

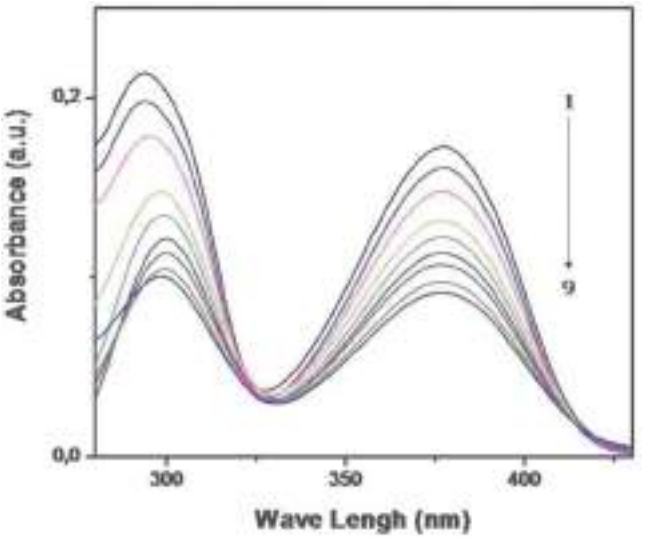

Figure 3. Absorption spectroscopic study of 50 μM of **3c** with increasing concentrations of CT DNA (0, 2, 4, 6, 8, 10, 12, 14, and 16 μg/ml, respectively) (**1–9**).

(**3a** and **3b** also show no interaction with DNA). So the investigation regarding DNA interaction was scheduled with compound **3c** only. This is probably due to a more planer structure of **3c**. When CT DNA was added with increasing concentrations to a fixed concentration of **3c** (50 µM), the absorption gradually decreased at λ_{max} of the compound (377 nm) with the generation of an isosbestic point (Fig. 3) while the addition of **3c** to a fixed concentration of DNA solution (50 µg/ml) showed an increase in absorption of the DNA band again with the generation of an isosbestic point (Fig. 4). These different types of absorption characteristics, under specified conditions mentioned above, may be due to some specific type of interaction between compound **3c** and DNA molecules resulting in a more relaxed structure of the compound and conversely enhanced rigidity within base pairs of DNA. At the absorption maximum of DNA, the binding constant between compound **3c** and DNA was calculated by using a modified Benesi–Hildebrand (BH) plot (Fig. 5). It was found out from the calculation that the value of the binding constant is 1.7×10^4 M^{-1}, which indicates a strong interaction between the moieties.

Fluorescence spectroscopic studies of the compound 3c with ethidium bromide (EB) bound DNA

Fluorescence spectroscopic studies have been carried out to find the interaction of DNA with compound **3c**. As evidenced from absorption spectral studies, that compound **3c** interacts with DNA molecules, it is important to know whether compound **3c** is able to replace ethidium bromide (EB) from DNA, which has an association constant value of 3.4×10^3 M^{-1} against any double-stranded DNA.[12] As, either DNA or EB or even compound **3c** do not show fluorescence property individually at 510 nm excitation wavelength, we have used the fluorescence property of EB bound DNA for comparing the ability of DNA binding of compound **3c**. When the solution of **3c** was added to EB saturated DNA (Fig. 6a) the compound partially replaces EB from DNA (Fig. 6b) which

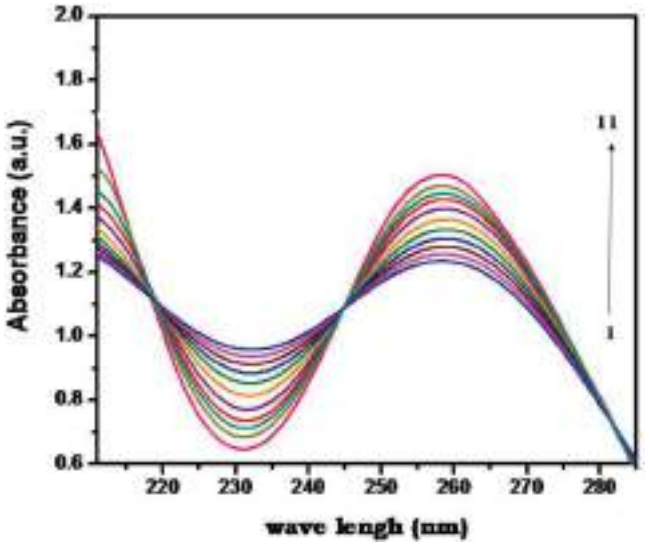

Figure 4. Absorption spectroscopic study of CT DNA (50 μg/ml) with increasing concentrations of **3c** (0, 2, 4, 6, 8, 10, 12, 14, 16, 18, and 20 μM, respectively).

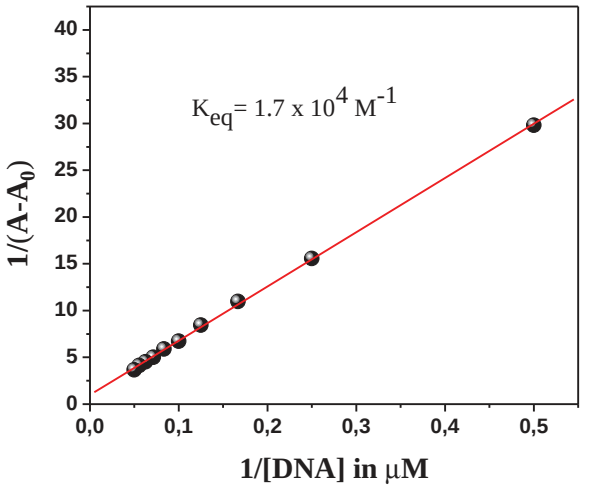

Figure 5. Modified Benesi–Hildebrand plot for the determination of ground state binding constant between CT DNA and **3c**.

is indicated from the change in fluorescence intensity. EB–DNA association constant is 3.4×10^3 M^{-1}[13]

However, it is not necessary to be an intercalator which would reduce the fluorescence intensity of the EB bound DNA. Alternatively, the compound might bind DNA molecules in such a way (possibly slight unwinding of the DNA backbone) that affects structural variation in the DNA leading to partial replacement of EB from DNA. The compound **3c** also has low-lying energy states that might quench the emission of EB by means of energy transfer when both molecules are bound to DNA in close proximity.

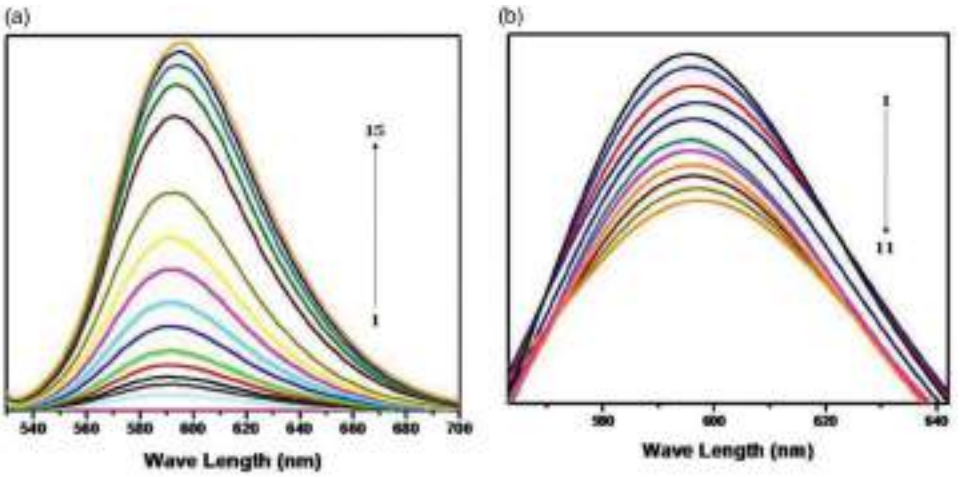

Figure 6. Comparative fluorescence spectroscopic study of **3c** with EB bound CT DNA. Excitation wavelength was 510 nm and the emission spectra were scanned from 520 to700 nm in each case. (a) The mode of EB saturation in CT DNA (50 μg/ml). The maximum fluorescence intensity of EB bound DNA complex was observed at 10.45 μM of EB concentration. At this point of saturation, **3c** was added gradually up to 42 μM till its saturation level, which is represented in (b).

Reaction procedure

2 mmol of malononitrile and 1 mmol of β-chloro-α,β-unsaturated aldehydes were heated with potassium hydroxide-18-crown-6 in 15 ml methanol solvent at 65 °C for 25–40 min. In the case of 2,6-dicyanoaniline derivatives the reaction mixture was poured into the water and extracted with ethyl acetate. Ethyl acetate part was washed with brine solution thrice and evaporated under vacuum. Column chromatographic separation was done on silica gel using different proportions of pet-ether: ethyl acetate mixture. The product was obtained from a 20% ethyl acetate pet-ether mixture. In the case of 3-Amino-9,10-dihydro-phenanthrene-2,4 dicarbonitrile derivatives, the products precipitated out from the reaction mixture and were filtered and crystallized from chloroform- pet-ether solvent. The products were characterized by IR, ^{1}H- and^{13}C-NMR, elemental analyses, and an X-ray crystallographic study.

Conclusion

An atom economic straightforward methodology has been developed for the synthesis of 2,6-dicyanoaniline and 3-Amino-9,10-dihydro-phenanthrene-2,4-dicarbonitrile derivatives from β-chloro-α,β-unsaturated aldehydes, and malononitrile using potassium hydroxide-18-crown-6 with good to the excellent yield of the product. One 3-amino-9,10-dihydrophenanthrene-2,4-dicarbonitrile compound induces important structural changes in Calf-Thymus DNA as indicated from spectroscopic evidence.

It contains full experimental details and ^{1}H and ^{13}C NMR spectra. This material can be found via the "Supplementary Content" section of this article's webpage.

Acknowledgments

The authors gratefully acknowledge the Department of Chemistry, the University of Calcutta for Crystallographic and NMR studies. The author also thanks Maulana Azad College, Kolkata for use of the departmental facilities.

ORCID

Arijit Kundu http://orcid.org/0000-0002-9065-0001

References

[1] (a) Müller, T. J. J.; Bunz, U. H. F., Eds. *Functional Organic Materials, Synthesis, Strategies and Applications*; Wiley-VCH: Weinheim, Germany, 2007. (b) Thomson, R. H. *The Chemistry of Natural Products*; Blackie and Son: Glasgow, UK, 1985. (c) Singh, F. V.; Vatsyayan, R.; Roy, U.; Goel, A. *Bioorg. Med. Chem. Lett.* **2006**, *16*, 2734. DOI: 10.1016/j.bmcl.2006.02.012.

[2] (a) Maitraie, D.; Reddy, G. V.; Rao, V. V. V. N. S. R.; Ravikanth, S.; Narsaiah, B.; Rao, P. S.; Ravikumar, K.; Sridhar, B. *Tetrahedron* **2005**, *61*, 3999. DOI: 10.1016/j.tet.2005.02.046. (b) Andersen, N. G.; Maddaford, S. P.; Keay, B. A. *J. Org. Chem.* **1996**, *61*, 9556. DOI: 10.1021/jo9617880.

[3] (a) Carroll, R. L.; Gorman, C. B. *Angew. Chem., Int. Ed.* **2002**, *41*, 4378. DOI: 10.1002/1521-3773(20021202)41:23<4378::AID-ANIE4378>3.0.CO;2-A. (b) van Mullekom, H. A. M.; Vekemans, J. A. J. M.; Meijer, E. W. *Chem. Eur. J.* **1998**, *4*, 1235. DOI: 10.1002/(SICI)1521-3765(19980710)4:7<1235::AID-CHEM1235>3.0.CO;2-4. (c) Bendikov, M.; Wudl, F.; Perepichka, D. F. *Chem. Rev.* **2004**, *104*, 4891. DOI: 10.1021/cr030666m.

[4] (a) Cardozo, T. M.; Nascimento, M. A. C. *J. Mater. Sci.* **2005**, *40*, 3549. DOI: 10.1007/s10853-005-2883-x. (b) Kanis, D. R.; Ratner, M. A.; Marks, T. *J. Chem. Rev.* **1994**, *94*, 195. DOI: 10.1021/cr00025a007. (c) Murugan, P.; Shanmugasundaram, P.; Ramakrishnan, V. T. ; Srividya, N.; Ramamurthy, P. *Indian J. Chem.* **1998**, *37B*, 737.

[5] Schwander, H. *Chem. Abstr.* **1988**, *108*, 23345. (b) Ito, N.; Mikota, T.; Aiga, H. *Chem. Abstr.*, **1987**, *107*, 226081. (c) Bello, K. A.; Yakubu, M. K. *Colourage* **1997**, *44*, 49. (d) Johri, S.; Varshney, A. *Acta Cienc. Indica, Chem.* **1997**, *23*, 113. (e) Yi, C.; Blum, C.; Liu, S.-X.; Ran, Y.-F.; Frei, G.; Neels, A.; Stoeckli-Evans, H.; Calzaferri, G.; Leutwyler, S.; Decurtins, S. *Cryst. Growth Des.* **2008**, *8*, 3004. DOI: 10.1021/cg800122v. (f) Petermann, R. ; Suppiger C.; Lauk, U. *Chem. Abstr.* **2010**, *152*, 503450. (g) Hassan, J.; Sévignon, M.; Gozzi, C.; Schulz, E.; Lemaire, M. *Chem. Rev.* **2002**, *102*, 1359. DOI: 10.1021/cr000664r. (h) Snieckus, V. *Chem. Rev.* **1990**, *90*, 879. DOI: 10.1021/cr00104a001. (i) Wang, H.; Huang, J.; Wulff, W. D.; Rheingold, A. L. *J. Am. Chem. Soc.* **2003**, *125*, 8980. DOI: 10.1021/ja035428n. (j) Xi, Z.; Sato, K.; Gao, Y.; Lu, J.; Takahashi, T. *J. Am. Chem. Soc.* **2003**, *125*, 9568. DOI: 10.1021/ja027234y. (k) Asao, N., Aikawa, H.; Yamamoto, Y. *J. Am. Chem. Soc.* **2004**, 126, 7458. (l) Ballini, R.; Barboni, L.; Fiorini, D.; Giarlo, G.; Palmieri, A. *Chem. Commun.* **2005**, 20, 2633. DOI: 10.1039/b500846h. (m) Lee, M. J.; Lee, K. Y.; Gowrisankar, S.; Kim, J. N. *Tetrahedron Lett.* **2006**, *47*, 1355. DOI: 10.1016/j.tetlet.2005.12.032. (n) Bonaga, L. V. R; Zhang, H.-C.; Moretto, A. F.; Ye, H.; Gauthier, D. A.; Li, J.; Leo, G. C.; Maryanoff, B. E. *J. Am. Chem. Soc.* **2005**, *127*, 3473. DOI: 10.1021/ja045001w. (o) Odedra, A.; Wu, C.-J.; Pratap, T. B.; Huang, C.-W.; Ran, Y.-F.; Liu, R.-S. *J. Am. Chem. Soc.* **2005**, *127*, 3406. DOI: 10.1021/ja043047j. (p) Agarwal, N.; Saxena, A. S.; Farhanullah, A.; Goel, V.; Ram, J. *Tetrahedron* **2002**, *58*, 8793. DOI: 10.1016/S0040-4020(02)01066-9. (q) Veverková, E.; Noskov, M.; Toma, Š. *Synth. Commun.* **2002**, *32*, 2903. DOI: 10.1081/SCC-120006476. (r) Xin, X.; Wang, Y.; Xu, W.; Lin, Y.; Duan, H.; Dong, D. *Green Chem.* **2010**, *12*, 893. DOI: 10.1039/b921390b. (s) Das, P.; Butcher, R. J.; Mukhopadhyay, C. *Green Chem.* **2012**, *14*, 1376. DOI: 10.1039/c2gc16641k. (t) Borate, H. B.; Kudale, A. S.;

Agalave, S. G. *Org. Prep. Proced. Int.* **2012**, *44*, 467. DOI: 10.1080/00304948.2012.715055. (u) Kalita, E. V.; Kim, D. G. *Russ. J. Org. Chem.* **2018**, *54*, 1565. DOI: 10.1134/S1070428018100214. (v) Mohammadi, B.; Kazemi, H.; Shafieey, M. *Monatsh. Chem.* **2014**, *145*, 1649. DOI: 10.1007/s00706-014-1229-2. (w) Sunke, R.; Kalyani, A.; Swamy, K. C. K. *J. Org. Chem.* **2020**, *85*, 1073. DOI: 10.1021/acs.joc.9b02991. (x) Tietze, L. F.; Brasche, G.; Gericke, K. M. *Domino Reactions in Organic Synthesis*; Vydal Wiley-VCH: Weinheim, Germany; 2006.

[6] Zuber, G.; Quada, J. C. Jr.; Hecht, S. M. *J. Am. Chem. Soc.* **1998**, *120*, 9368–9369. DOI: 10.1021/ja981937r.

[7] Torigoe, H.; Sato, S.; Yamashita, K.; Obika, S.; Imanishi, T.; Takenaka, S. *Nucl. Acids Res.* **2002**, *2*, 55–56. DOI: 10.1093/nass/2.1.55.

[8] Hendry, L. B.; Mahesh, V. B.; Bransome, E. D.; Ewing, D. E. *Mutat. Res.* **2007**, *623*, 53–71. DOI: 10.1016/j.mrfmmm.2007.03.009.

[9] Rescifina, A.; Zagni, C.; Varrica, M. G.; Pistarà, V.; Corsaro, A. *Eur. J. Med. Chem.* **2014**, *74*, 95–115. DOI: 10.1016/j.ejmech.2013.11.029.

[10] (a) Yu, Z.; Velasco, D. *Tetrahedron Lett.* **1999**, *40*, 3229. DOI: 10.1016/S0040-4039(99)00370-6. (b) Murugan, P.; Shanmugasundaram, P.; Ramakrishnan, V. T.; Srividya, N.; Ramamurthy, P. *Indian J. Chem.* **1998**, *37B*, 737. (c) Victory, P.; Borrell, J. I.; Vidal-Ferran, A.; Montenegro, E.; Jimeno, M. L. *Heterocycles*, **1993**, *36*, 2273. DOI: 10.3987/COM-93-6412.

[11] Singh Khaidem, I.; Singh, S. L.; Singh, L. R.; Khan, M. Z. R. *Indian J. Chem.* **1996**, *35B*, 911.

[12] (a) Ziolo, R. F.; Allen, M.; Titus, O. D.; Gray, H. B.; Dori, Z. *Inorg. Chem.* **1972**, *11*, 3044. DOI: 10.1021/ic50118a034. (b) Scaria, P. V.; Shafer, R. H. *J. Biol. Chem*. **1991**, *266*, 5417. DOI: 10.1016/S0021-9258(19)67611-8.

[13] Saha, B.; Mukherjee, A.; Santra, C. R.; Chattopadhyay, A.; Ghosh, A. N.; Choudhuri, U.; Karmakar, P. *J. Biomol. Struct. Dyn.* **2009**, *26*, 421–429. DOI: 10.1080/07391102.2009.10507257.

NJC

ROYAL SOCIETY OF CHEMISTRY

PAPER

View Article Online
View Journal | View Issue

Cite this: *New J. Chem.*, 2021, **45**, 4574

An inquisitive fluorescence method for the real-time detection of trace moisture in polar aprotic solvents with the application of water rancidity in foodstuffs†

Snigdha Roy,[a] Sanju Das,[b] Ambarish Ray[c] and Partha Pratim Parui *[a]

A simple analytical technique for detection of trace water in organic solvents is indispensable for moisture-free organic synthesis, environmental research, and food monitoring industry. Using a simple 4-methyl-2,6-diformyl phenol molecule (AH), we report the convenient fluorometric detection of trace water in various polar aprotic organic solvents having detection limits within 0.01–0.04% (v/v). Phenolate-oxygen of deprotonated AH (A^-) forms an H-bond with a water molecule to exhibit a large spectral blue-shift from ~485 to 440 nm in the UV-vis absorption or fluorescence excitation spectra, while unchanged emission characteristics were detected apparently due to dissociation of the H-bond in the excited state. The gradual blue-shift of the excitation band with the increase in water% (v/v) in the solution affects an opposite emission intensity changing behavior, from an increasing to a decreasing trend, due to the change in the excitation wavelength from 440 to 485 nm. Emission intensity changes of free A^- and A^-/H_2O H-bonded species for each water addition are combined together for the spectral normalization to achieve water% induced a highly manifested linear emission response. The improved sensitivity allows us to quantify real-time atmospheric moisture incorporations in various polar aprotic solvents. The normalized emission intensity does not depend on AH concentration, and thus the water detection process is very effective for the estimation of water% in the solution with heterogeneous probe distributions. With this advantage, we succeed to estimate water% in various moisture-sensitive edible oils and dairy foods produced from water-rich raw materials. Therefore, the method can be applied to prevent water rancidity in foods with greater than its permissible limits *via* identifying higher moisture contamination.

Received 11th December 2020,
Accepted 2nd February 2021

DOI: 10.1039/d0nj06046a

rsc.li/njc

Introduction

An effective analytical procedure for the estimation of trace water in organic solvents displays a direct impact in chemical research, industry and food inspection.[1–5] For organic synthesis, in particular the synthesis of organometallic compounds, moisture-free solvents are essential to obtain the optimum product yield.[6,7] Carboxylic ester and imine functional compounds are highly susceptible to hydrolysis even in the presence of trace amounts of moisture during their storage in organic solvents.[8] The moisture contamination in oil can be a major problem in the petroleum industry due to emulsification and phase separation processes,[9,10] resulting in the blockage of fuel pipe, and subsequent engine damage or failure.[11,12] Furthermore, the estimation of water in food samples is very important for various reasons:[13–17] (a) optimum moisture level in foods is essential for to sustain an appropriate test, texture and appearance, and most vital nutritional values; (b) food manufacturers often incorporate inexpensive water ingredients illegally as much as possible in foods for their profit; (c) trace water affects microbial food degradation or water rancidity, especially for pure oil-based food materials;[15–17] (d) food processing operations such as transferring through pipes, packaging and mixing also affect the estimation.

The Karl Fischer titration is one of the best known methods for the estimation of moisture in organic solvents.[18] Gas chromatography is another well-acquainted classic option.[19,20] However, certain limitations in those methods such as time consumption, inability for real-time analysis, specialized equipment design requirement, difficulties in sample preparation, and rigorous data handling are major concerns for easy and cost-effective moisture

[a] *Department of Chemistry, Jadavpur University, Kolkata 700032, India. E-mail: parthaparui@yahoo.com; Fax: +91-33-24146223; Tel: +91-9433490492*
[b] *Department of Chemistry, Maulana Azad College, Kolkata 700013, India*
[c] *Department of Chemistry, Barasat Govt. College, Kolkata 700124, India*

† Electronic supplementary information (ESI) available. See DOI: 10.1039/d0nj06046a

detection for applied analytical samples.[21,22] Fluorescence technique may opt as a better alternative owing to its simplicity and rapid response, and non-destructive fabrication and most importantly its high sensitivity.[23–25] Consequently, a number of research groups currently switch their focus to various kinds of commercially viable fluorescence-based water sensing procedures. Up to now, a number of fluorosensing mechanisms, such as intramolecular charge transfer (ICT),[26,27] photo-induced electron transfer (PET),[1,28] excited-state intramolecular proton transfer (ESIPT),[29,30] hydrogen-bonding interaction,[5,31,32] aggregation-induced emission (AIE)[33–35] or Förster resonance energy transfer (FRET),[36,37] have been reported to detect trace water in organic solvents. Water fluorosensors based on chemical rearrangements such as ring-opening of cyclic rhodamine derivatives,[38] hydrolytic cleavage of Schiff bases[39,40] and hydration of aldehyde functionality[41] have also been reported. In addition, researchers constructed various metal/ligand complexes or metal organic frameworks (MOFs)[42,43] as water fluorosensors.

Among the various water sensing fluorescent probe molecules reported in the literature, some exhibit very high detection sensitivity (~0.001% or even below), although often the high detection accuracy is restricted to specific solvent systems.[14,44–46] However, the requirement of multi-step complex synthesis procedures for the preparation of probe molecules makes the overall moisture detection procedure inconvenient for routine analytical purpose.[34,37,41–43] In most cases, the detection methodologies are relying only upon a single emission/excitation band originated by the association/interaction of water with the recognition site of a probe molecule.[26–32,34–38,41,42] Therefore, it is not always straightforward to recognize the actual cause for the observed fluorescence response between the inhomogeneous probe distribution in the solution due to sample micro-heterogeneity and any moisture affected changes. In addition, photobleaching of the probe molecule and instrumental parameters[44] are often troublesome to assess the actual fluorosensing response induced by water incorporation.

In this study, a simple 4-methyl-2,6-diformyl phenol fluorescent probe (AH) was exploited to detect trace water in several polar aprotic organic solvents with high precision (detection limit ~0.01–0.04% (v/v)). The phenolate form of the probe molecule (A^-) exhibits a water-induced spectral blue-shift to various extents in the UV-vis absorption and fluorescence excitation spectra from ~470–490 nm to 440–450 nm depending on various polar aprotic organic solvents due to the formation of an A^-/H_2O H-bonded complex. Although both A^-/H_2O and free A^- show identical fluorescence emission characteristics, an opposite emission intensity changing pattern, from a gradually increasing to a decreasing trend with the increase in water%, was detected upon switching the excitation wavelength from 440 to 485 nm. Water induced emission intensity changes of A^- and A^-/H_2O species for each water% value were combined together to obtain a normalized single spectral profile, and thus the water% induced emission increase manifested considerably with eliminating the probe concentration dependency on the intensity response. Moreover, such normalization eventually produces linear intensity changes dependent on water%, which are effective to estimate water% ratiometrically. In addition, a large spectral blue-shift of ~25 nm in the excitation spectra induced by only a small quantity of water (2–5% v/v) can also be suitably tuned for its detection purpose. The water detection procedure was applied to monitor real-time atmospheric moisture incorporation in common polar aprotic solvents and moisture analysis studies in various food samples useful for water rancidity.

Experimental

Chemicals and general methods

Chemicals of analytical grade were purchased from different commercial sources. The chemical 4-methyl-2,6-diformyl phenol (AH) was synthesized according to a published procedure starting from *p*-cresol[47] (Sigma Aldrich (USA)), and the purity was checked by ^{1}H-NMR studies (Fig. S1, ESI†). Different commercially available food samples (butter, cheese, ghee and coconut oil) were collected from different local market sources. Molecular sieves of 3 Å pore size were obtained from Sigma-Aldrich (USA). HPLC-grade solvents (methanol, ethanol, acetone, MeCN, DMF and DMSO) and triethyl amine (TEA) were purchased from Sigma-Aldrich (USA), and the solvents were further dried over the 3 Å molecular sieves.[21] The solvents were stored in a dry nitrogen atmosphere in the presence of the molecular sieves. Throughout all experimental studies, Milli-Q water (Millipore) of conductivity 18.2 MΩ cm was used. ^{1}H-NMR studies were performed in DMSO-d_6 using a Bruker 300 MHz NMR spectrophotometer considering tetramethylsilane (0 ppm) as an internal standard.

UV-vis absorption and fluorescence studies

UV-vis absorption spectra were monitored using a 1 cm path-length quartz cell with a double-beam spectrophotometer (Shimadzu, Japan; model TCC-240A) equipped with a thermostatted cell holder. Steady-state fluorescence studies were carried out using a Perkin-Elmer LS-55 spectro-fluorimeter (PerkinElmer, USA) using a 1 cm path-length quartz cell. Fluorescence excitation and emission spectra were recorded for the fixed emission at 525 nm and excitation at 440 or 485 nm, respectively (excitation band pass: 11; emission band pass: 4). The measuring solutions were filtered using a 0.45 mm filter (Millex, Millipore). The spectral reproducibility was checked by measurements in triplicat.

The phenolic-OH deprotonated form of AH (A^-) acting as the actual water sensing probe was generated by addition of base (KOH or TEA) in different solvents. For the detection of water in polar aprotic solvents (acetone, MeCN, DMF and DMSO), the fluorescence spectral studies for A^- were monitored in the absence and presence of various water% (v/v) values.

The fluorometric limit of detection (LOD) for water was obtained using the following equation:[48]

$$\text{Detection limit (LOD)} = 3\sigma/k,$$

where σ and k represent the experimental standard deviation and slope value of the linear fitting curve, respectively.

The fluorescence quantum yield for the A^- form of AH (AH (0.5 μM + KOH (10 μM))) was evaluated according to the

procedure described earlier.[49] In brief, 9,10-diphenylanthracene in an ethanol medium was used as the reference fluorophore with an emission quantum yield (Φ_F^r) = 0.95. The Φ_F was estimated using the following equation:

$$\Phi_F^s = [A_r F_s n_s^2 / A_s F_r n_r^2]\Phi_F{}^r$$

where A represents the absorbance at the excitation wavelength, and the integrated emission area is designated by F. n is the refractive index of the medium. Subscripts refer to the reference (r) or sample (s) molecule.

Fluorescence transient decays were monitored by the time-correlated single-photon counting (TCSPC) method. Two separate nano-second diodes with excitation at ~450 and 490 nm respectively (nano-LED; IBH, UK) were used as the light source. Fluorescence decays were monitored using a special Hamamastu photomultiplier tube (PMT) coupled with TBX4 detection module (IBH, UK). The solutions for analysis were passed through a 0.45 μm filter (Millex, Millipore) before all the experiments. All measurements were repeated at least three times to check the reproducibility. The decays were analyzed using the in-built software.

Theoretical calculations

To identify the solution structure of the hydrogen-bonded A^-/H_2O complex, density function theoretical (DFT) calculations were performed using the Gaussian 09 Program.[50] Furthermore, time-dependent DFT (TD-DFT) calculations were carried out to obtain UV-vis absorption parameters. The structural optimization was carried out by considering the B3LYP exchange–correlation functional. The 6-31G++(3d,3p) basis was set and the geometries were optimized in the solvent phase. The global minima of all these species were confirmed by the positive vibrational frequencies. The TD-DFT calculation in different solvents with the CPCM solvent model was performed to obtain the electronic properties of the singlet excited state using optimized geometries of the ground states (S_0) of the relevant species, along with the determination of vertical excitation energy and oscillator strength of the respective ground-state geometry.

Atmospheric moisture incorporation studies

First, 40 mL of dry acetone, MeCN, DMF and DMSO were taken separately in a 100 mL dry beaker with a diameter of ~5 cm. Each solvent was incubated under open laboratory conditions with 75% (±5%) relative humidity at 25 °C (±1 °C) for different time intervals (12 to 120 min). To estimate atmospheric moisture incorporation in the medium, steady-state fluorescence emission and excitation spectra were monitored by addition of AH (0.5 μM) with KOH (10 μM) in the laboratory-exposed solvents at different intervals of time (12 to 120 min). For acetone and MeCN solvents, the effects of small amounts of solvent evaporation during the exposure in the open atmosphere on the moisture incorporation values evaluated from the fluorescence response at different time intervals were included to find the time-dependent actual moisture incorporation values.

Moisture detection in food samples

All the food samples (butter, cheese, ghee and coconut oil) were collected from local markets. The food samples were stored at 4 °C in the same commercial seal container until use for the moisture analysis studies. To extract free moisture present in food samples, various amounts of different food samples were mixed separately with 100 mL DMSO in a stoppered container under dry nitrogen conditions at room temperature (25 °C). Then, each mixture was heated at 60–70 °C to completely liquefy the food samples, followed by vigorous vortexing at the same temperature for 10 min to relocate all the free water from the food sample to the DMSO medium. Then, the solution was settled until complete separation of the DMSO phase from the rest of the solution. The DMSO phase was separated using a separating funnel, and the fluorescence studies were conducted in the DMSO phase by addition of AH (0.5 μM) and KOH (10 μM).

Results and discussion

Solvent-induced spectral shifts of the phenolate form of AH

AH deprotonated partially around neutral pH (pK_a ~ 7.1) in an aqueous buffer according to the pH-dependent changeover of UV-vis absorption intensities between ~350 nm for the phenol form (AH) and ~440 nm for the phenolate form (A^-) (Fig. S2, ESI†). A^- exhibited a strong fluorescence intensity (quantum yield (Φ) ~ 0.4) (*cf.* Experimental section), but AH did not (Fig. S3, ESI†).[51] Consistent with the earlier reports, an additional absorption intensity at ~485 nm with appreciable quenching of the intensity at ~350 nm for AH (6 μM) was identified in the DMF or DMSO medium even in the absence of the base[52,53] (Fig. S4A, ESI†). The appearance of band at ~485 nm is mainly due to partial deprotonation of AH induced by the basic solvent character,[54] since the spectral shape and position did not change except a large increase in its intensity by an addition of base (KOH, 15 μM) in DMF or DMSO (Fig. S4B, ESI†). This proposition is further supported by the base-induced similar spectral shift from ~350 nm to 470–480 nm for other non-basic aprotic solvents (acetone, MeCN) (Fig. S4B, ESI†). However, similar to the aqueous medium, a large blue-shifting of absorption band from 470–485 nm to 440–435 nm for the phenolate form (A^-) was detected by changing the medium from aprotic to protic methanol or ethanol (Fig. S5, ESI†). Previously, the solvent-induced large spectral blue-shift has been justified with presuming higher dipole moment of DMSO/DMF than the water molecule.[53] However, since the solvent-dependent absorption spectral shift is usually very nominal, the large spectral blue-shift is attributed to a specific A^-/solvent interaction (Fig. 1 and Fig. S5, ESI†).

Formation of A^-/H_2O complexes in aprotic solvents

The phenolic-OH deprotonated form of AH (A^-) was confirmed with forming UV-vis intensity at 470–485 nm by addition of any base (KOH or TEA) to polar aprotic solvents (Fig. 1). However, TEA (THF-solubilized base) induced no spectral change in a relatively nonpolar THF medium, suggesting no such deprotonation

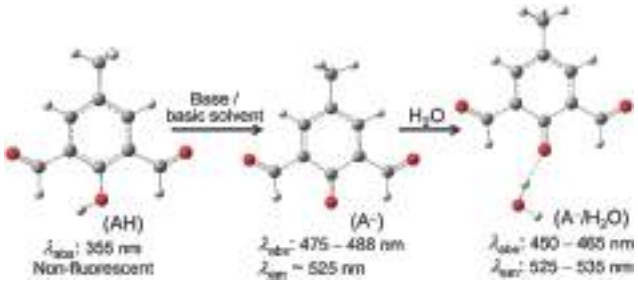

Fig. 1 Schematic of base or basic solvent (DMSO/DMF)-induced complete/partial deprotonation of AH (A^-) and its H-bonding interaction with water. The DFT-optimized structures are shown (color index: C, gray; O, red; and H, white). The experimental UV-vis absorption (λ_{abs}) and emission (λ_{em}) wavelengths for different species are depicted in the lower panel. (*cf.*) The calculated absorption parameters are shown in Table 1.

reaction of AH (Fig. S6, ESI†), presumably due to poor solvation of the negatively charged A^- species. The water-induced large blue-shift of the absorption band for A^- shows the interaction of A^- with the water molecule (Fig. 2). A similar UV-vis spectral blue-shift by water interaction was reported by C. Pinheiro *et al.*[6] Instead, the presence of water causes no spectral changes for the protonated AH form (Fig. S7, ESI†), which excludes the possibility of water/AH interaction. Most probably, the large negative charge density at phenolate-O in A^- may induce efficient H-bonding affinity with the water molecule to form an A^-/H_2O complex.

To avoid any significant change of general solvent properties, UV-vis absorption spectral changes of A^- (AH (6 μM) + KOH (15 μM)) in different polar aprotic solvents (acetone, MeCN, DMF and DMSO) were monitored in the presence of low amounts of water up to ~6–12% (v/v). With the increase in water% in solvents (0.1–6.0% for acetone, 0.1–8% for MeCN, 0.1–12% for DMF and 0.3–12% DMSO), the absorption band of A^- gradually

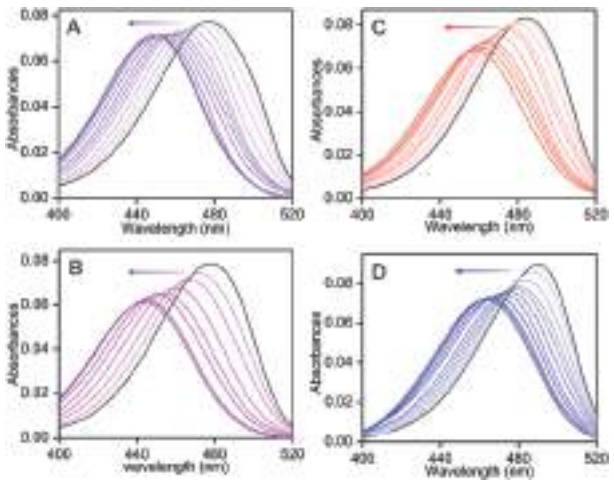

Fig. 2 UV-vis absorption spectra of AH (6 μM) in the presence of KOH (15 μM) and various water% (v/v) in different solvents: (A) acetone (water%: 0.1, 0.3, 0.6, 1.0, 1.5, 2.0, 3.5, 6.0, 8.5 and 11.0); (B) MeCN (water%: 0.1, 0.3, 0.6, 1.5, 2.5, 6.5 and 9.0); (C) DMF (water%: 0.1, 0.4, 1.0, 1.5, 2.7, 4.8, 6.5, 8.5 and 10.0) and (D) DMSO (water%: 0.3, 0.9, 1.4, 2.0, 3.2, 5.1, 6.3, 8.5, 6.3, 10.0 and 12.3). (A–D) The gradual spectral blue-shift with the increase in water% is depicted by arrows. The spectra in the absence of water are shown in black.

blue-shifted from 475 to 488 nm maximally up to ~445–450 nm (Fig. 2). The spectrum at the highest water% for each aprotic solvent was found to be closely similar to that obtained in a pure aqueous medium (Fig. 2 and Fig. S5, ESI†). Upon reverse solvent addition, *i.e.*, each aprotic solvent (~10% (v/v)) in an aqueous medium causes an insignificantly small spectral wavelength shift (Fig. S8, ESI†), indicating that A^- involves a specific interaction with water in the aprotic solvents. Notably, the observed small spectral changes between the aprotic medium in the presence of the highest water% and in pure water can be explained by their general solvent properties, even though the same species, namely, A^-/H_2O complex, can be expected in both types of solvents (Fig. 2 and Fig. S8, ESI†). However, the replacement of water with other protic solvents such as methanol or ethanol, in the aprotic solvents showed a similar spectral blue-shift up to ~435 nm (Fig. S9, ESI†), while the blue-shift requires much higher alcohol% (~23–25% (v/v)) than water% (6–12%) presumably due to weaker interaction ability of A^- with the alcohol molecules. Most probably, A^- participates in the H-bonding interaction with water molecules, which may increase the $S_0 \rightarrow S_1$ transition energy for the phenolate chromophore moiety to attribute for the 30–50 nm spectral blue-shift (Fig. 1). Since the water molecule itself participates in the H-bonding interaction with large affinity in the aprotic solvents, the fraction of H-bonded A^- was found to be enhanced with the increase in water% due to the formation of more number of A^-/H_2O H-bonded complexes than its dissociation affected by the increased ratio of the water amount in the solvent composition.

The H-bonding interaction of A^- with water molecules was also examined by steady-state and time-resolved fluorescence methods. The deprotonated A^- species exhibited a strong emission intensity at 525–535 nm in different solvents (acetone, MeCN, DMF, DMSO and water) (Fig. S10, ESI†). The excitation spectra of deprotonated A^- for the emission at 525 nm showed an intensity at 470–490 nm for different aprotic solvents, whereas in the water medium the peak shifted to ~440 nm (Fig. S11, ESI†), which is consistent with the observed absorption wavelength shift by changing an aprotic to water medium (Fig. 2 and Fig. S5, ESI†). Similar to the absorption studies, the fluorescence excitation band gradually blue-shifted up to ~445–450 nm by a gradual increase in water% up to 6–12% (v/v) in different aprotic solvents (Fig. 2 and Fig. S12, ESI†). These results corresponded well with that interpreted from the absorption studies for the formation of the H-bond in the A^-/H_2O complex (Fig. 1). However, no emission wavelength shift under a particular water% value in the aprotic media was detected by the change in the excitation wavelength from 440 to 485 nm (Fig. S13, ESI†). The result indicates that the emissive properties are similar between free A^- and A^-/H_2O H-bonded complexes.

Different water%-dependent fluorescence transient decays for A^- in the aprotic solvents were monitored at 530 nm for excitations at ~450 nm and ~490 nm. For either excitation, a mono-exponential decay with unchanged fluorescence lifetime (τ) values was noticed at each water% value (Fig. 3 and Fig. S14, ESI†), where the τ value was found to increase gradually with

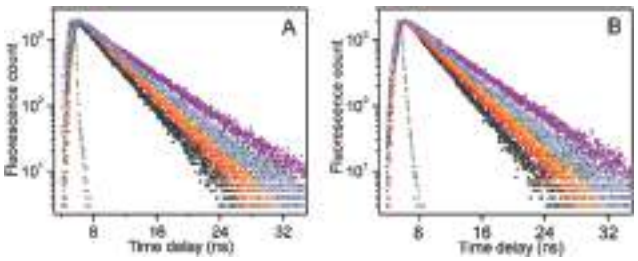

Fig. 3 Excitation wavelength-dependent fluorescence transients of AH (6 μM) in the presence of KOH (15 μM) in acetone under various water% (v/v) values (water%: red, 1.0%; orange, 2%; green, 4%; purple, 8%). Excitation wavelengths were (A) 450 nm and (B) 490 nm. (A and B) The transient decay in pure water and acetone media is shown in blue and black, respectively, for comparison. The emission collected at 525 nm both excitation wavelengths. The scattering profile is shown in grey.

the increase in water% from 0 up to 8%; from ~3.3 to 5.7 ns for acetone, ~3.8 to 5.7 ns for MeCN, ~3.8 to 5.9 ns for DMF and 4.1 to 5.9 ns for DMSO (Table 1). The similar τ value between two different excitations (450 and 490 nm) especially when the A^-/H_2O complex and free A^- coexist at the water% value below 4% strongly justify our proposition that the emission of the A^-/H_2O complex originated from the excited state of free A^- after breaking of the H-bond in the excited state (Fig. 4 and Fig. S14, ESI†). However, an expected stronger electrostatic interaction of A^- with the water molecule than any of those aprotic solvent molecules may increase the local water concentration surrounded to A^- largely than remaining of the solution even for a small increase of water% in the solution. Presumably, the higher water accumulation around A^- may affect greater solvation induced its higher excited state stability to observe the gradual increase in the τ value with the increase in the water% value. Moreover, the τ value for the A^- species in a pure aqueous medium is ~4.7 ns which is significantly lower than that observed in various aprotic solvents containing 8% water (~5.9 ns) probably due to a significant decrease in non-radiative decay rate from the aprotic solvents to water (Fig. 3, Fig. S14, ESI† and Table 1).

Theoretical studies for H-bonding interaction in A^-/H_2O

To identify the probable H-bonding mode in the A^-/H_2O complex, DFT-based theoretical calculations were performed considering the most probable H-bonding interaction between phenolate-O and one hydrogen atom of water molecules (Fig. 1 and Fig. S15A, ESI†). The ground-state structures in the gas phase for free A^- and A^-/H_2O complex were optimized using the B3LYP 6-31G++(3d,3p) basis set (Fig. S15A, ESI†). To correlate the experimental UV-vis absorption parameters, TD-DFT calculations (B3LYP, 6-31G++(3d,3p) basis function) on the optimized ground-state geometries were performed in the solution phase considering the CPCM solvent model for acetone, MeCN and DMSO, and the calculated values of various absorption parameters are depicted in Table 2 and Fig. S15B (ESI†). The electric charge densities in HOMO/LUMO both for A^- and A^-/H_2O are centered within the diformyl-phenolate unit (Fig. S15B, ESI†). The excitation wavelengths for A^- species in different aprotic

Table 1 Emission lifetime values of A^- in different polar aprotic solvents containing various water% (v/v)[a]

	Lifetime (τ/ns)				
	Water% (v/v)				
Solvent	0.0	1.0	2.0	4.0	8.0
Acetone	3.34 (3.34)	4.03 (4.03)	4.22 (4.22)	4.77 (4.77)	5.71 (5.71)
MeCN	3.83 (3.83)	4.38 (4.38)	4.54 (4.54)	4.97 (4.97)	5.75 (5.75)
DMF	3.85 (3.85)	4.39 (4.39)	4.47 (4.77)	4.87 (4.87)	5.87 (5.87)
DMSO	4.09 (4.09)	4.57 (4.57)	4.60 (4.60)	4.86 (4.86)	5.87 (5.87)
Water[b]	4.75 (4.75)	—	—	—	—

[a] The emission collected at 525 nm for the excitations at 450 nm and 490 nm. The τ values in bracket are for the excitation at 490 nm. [b] τ values in pure water solvent.

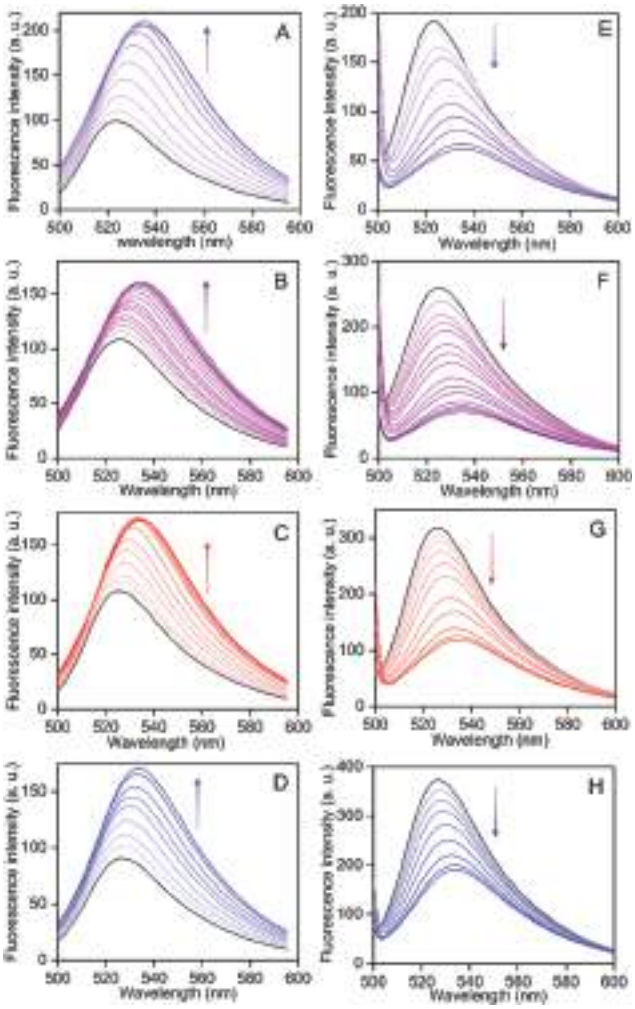

Fig. 4 Excitation wavelength-dependent fluorescence emission spectra of AH (0.5 μM) in the presence of KOH (10 μM) and various water% (v/v) values in different solvents: (A and E) acetone (water%: 0.1, 0.3, 0.6, 1.1, 1.8, 3.0, 4.5, 8.0 and 11.5); (B and F) MeCN (water%: 0.1, 0.2, 0.3, 0.4, 0.6 0.8, 1.0, 1.5, 2.0, 2.5, 3.0, 4.0, 4.7 and 5.5); (C and G) DMF (water%: 0.2, 0.4, 0.8, 1.5, 2.5, 4.0, 6.5, 8.0, 10.0 and 12.0); (D and H) DMSO (water%: 0.5, 1.0, 2.0, 3.5, 5.0, 7.5, 10.0 and 11.4). The spectra in the absence of water are depicted in black. The gradual increase or decrease in intensities with the increase in water% values is indicated by arrows. Excitation wavelengths were 440 nm (A–D) and 485 nm (E–H).

Table 2 Solvent dependent experimental (exp.) and TD-DFT calculated (cal.) wavelengths of UV-vis absorption band (λ_{max}) and molar extinction coefficients (ε) for the deprotonated form of AH (A^-) and its H-bonded complex with water (A^-/H_2O)[a]

	Absorbance parameters							
	A^-				A^-/H_2O			
	λ_{max} (nm)		$\varepsilon \times 10^4$ (M^{-1} cm^{-1})		λ_{max} (nm)		$\varepsilon \times 10^4$ (M^{-1} cm^{-1})	
Solvent	Exp.	Cal.	Exp.	Cal.	Exp.	Cal.	Exp.	Cal.
Acetone	477	458	1.32	0.91	450	444	1.19	0.80
MeCN	478	457	1.34	0.91	445	443	1.06	0.80
DMF	485	—	1.39	—	457	—	1.16	—
DMSO	489	460	1.50	0.95	463	445	1.21	0.90
Water	—	—	—	—	443	443	1.20	0.87

[a] Experimental UV-vis parameters for A^- (absence of water) and A^-/H_2O (presence of highest water% value) obtained according to Fig. 2.

solvents (acetone, DMF and DMSO) were computed to be ~455–460 nm due to the HOMO (43) to LUMO (44) electronic transition (Table 2). However, the A^-/H_2O H-bonded complex exhibited the absorption intensity at ~443–445 nm for HOMO (48) to LUMO (49) transition (Table 2). Although the energy of LUMO is comparable between A^- (−0.075 eV) and A^-/H_2O (−0.077 eV), a considerable decrease in the HOMO energy by 0.006 eV for A^- upon its H-bond interaction with water causes for the spectral blue-shift (Fig. S15B, ESI†). The calculated spectral blue-shift from free A^- species to its water-complex well corresponded with the water-induced experimental blue-shift of the UV-vis absorption (or fluorescence excitation) band of the A^- species in the aprotic solvents (Table 2). In addition, the experimental UV-vis molar extinction coefficient (ε) values also well matched with those values calculated theoretically (Table 2). The results justify the proposed H-bonding mode of the water molecule with A^-.

Detection of water in polar aprotic solvents

Water-induced fluorescence response for A^- remained similar on the nature of base (KOH or TEA) used in the polar aprotic solvents (Fig. S16, ESI†). Thus, the addition of base attributes no other role except for the deprotonation of the phenolic-OH moiety in AH. The conversion from free A^- to H-bonded A^-/H_2O species by the addition of water attributes the blue-shifting of the fluorescence excitation (or UV-vis absorption) band from ~485 to 440 nm for the fluorescence emission at 525 nm (Fig. S12, ESI†), where the excitation band intensity at ~485 and ~440 nm were assigned to the ground-state free A^- and A^-/H_2O species, respectively. In contrast, their emissive properties, *e.g.*, its intensity-wavelength (~530 nm) and lifetime values for different excitation wavelengths at 440 and 485 nm are observed to be identical due to the excited-state H-bond dissociation, as discussed before (Fig. S13, S14, ESI† and Table 2). Consequently, with the increase in water% in the solution (up to 6–12% (v/v)), the more amount of free A^- to A^-/H_2O conversion in the ground state resulted in a gradual increase in the emission intensity at ~530 nm for a fixed wavelength excitation of the A^-/H_2O species at 440 nm (Fig. 4A–D), whereas the emission intensity was found to decrease gradually during the excitation of reduced amount of free A^- species with the 485 nm light (Fig. 4E–H). It is noteworthy to mention here that the base-induced formation of deprotonated A^- species is not possible in relatively nonpolar aprotic solvents (THF) (Fig. S6, ESI†); thus, the operable solvent condition for the detection of moisture should be polar aprotic in nature.

The effect of water-induced changes in the equilibrium concentration of the free A^- and A^-/H_2O complex on emission intensity changes for the two separate excitation (440 and 485 nm) can be combined together by including the effect of both the intensity changes in a single spectrum (Fig. 4 and 5A–D (right spectra)). For each water% value, the emission spectrum for excitation at 440 nm was divided by the maximum intensity value in the absence of water, and the resulting spectrum ($F(\lambda)/F_0$ (λ_{ex} = 440 nm)) was further divided by the extent of emission intensity decrease factor with respect to the zero water condition for excitation at 485 nm (F_{max}/F_0 (λ_{ex} = 485 nm)) to obtain the normalized emission spectrum (($F(\lambda)/F_0$)/(F_{max}/F_0)) (Fig. 5A–D (right spectra)). Such normalization procedure not only is helpful to manifest the water-induced emission response and its detection sensitivity, but also causes the water%-dependent linear emission response (Fig. 5E–H). In addition, such normalization procedure eliminates the AH concentration dependency during the ratiometric detection of water in the solution with heterogeneous distribution of probe molecules (Fig. 5). The maximum normalized intensity value at ~530 nm increased more than 5.5- and 5.7-fold in the presence of 6.0% and 7.5% water in acetone and MeCN, respectively (Fig. 5E and F). However, the extent of increased intensities, maximally up to ~3.5-fold for acetone and 3.3-fold for MeCN, in the presence of various amounts of added water% up to 2% (v/v), maintains a very well behaved linear correlation with a residual of fitting R^2 ~ 0.995–0.997 and slope ~ 1.24 volume%$^{-1}$ (acetone) or 1.20 volume%$^{-1}$ (acetonitrile) (Fig. 5E and F). In comparison, the water%-dependent normalized emission intensity increase was found to be relatively less for the other aprotic solvents (DMF and DMSO) (Fig. 5G and H); maximum up to ~4.3-fold for DMF and 3.8-fold for DMSO. Nevertheless, the linear intensity increasing region expanded up to much higher water% value; ~6% for DMF and ~12% for DMSO medium (R^2 ~ 0.995 and slope 0.34 volume%$^{-1}$ (DMF) or 0.21 volume%$^{-1}$ (DMSO)) than that observed for acetone or MeCN solvent (Fig. 5G and H).

The water amount-dependent linear emission intensity changes can be highly useful for the ratiometric detection of unknown water% in the aprotic solvents. Based on the water-induced minimum extent of detectable unambiguous fluorescence response, the limit of detection (LOD) was evaluated using the eqn. LOD = $3\sigma/k$, where σ and k represent the standard deviation for the emission measurements and the slope value of the linear fitting curve, respectively (Fig. 5E–H). The LOD values for the detection of water% were evaluated to be ~0.01% for acetone and MeCN, whereas it was ~0.04% (v/v) for DMF and DMSO. To check the reversibility in the water detection, fluorescence studies for AH (0.5 μM) in the presence of KOH (10 μM) were performed at a certain water% value (1.8% for acetone; 1.5% for MeCN; 2.5% for DMF and 3.5% for

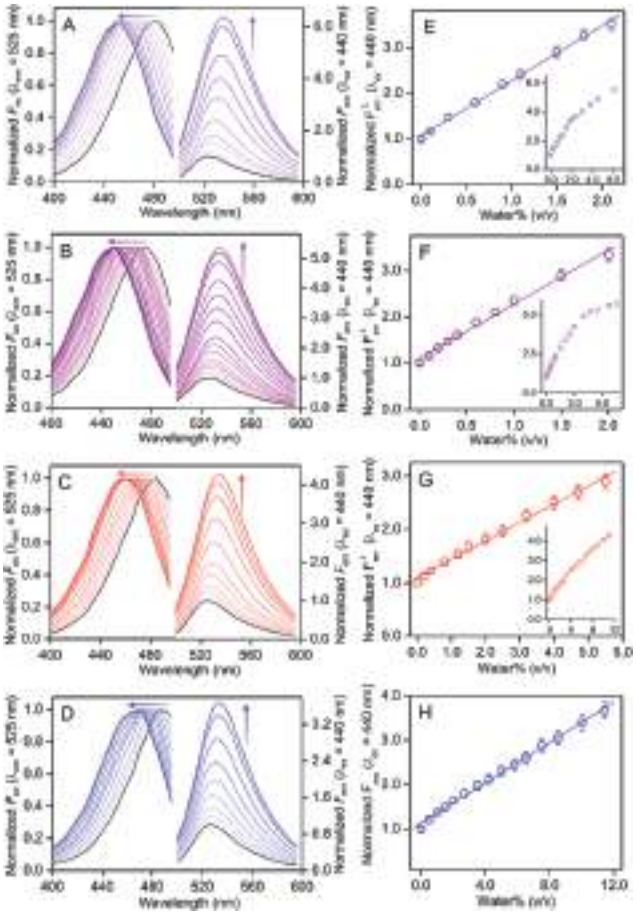

Fig. 5 (A–D) Normalized fluorescence excitation (left side) and emission (right side) spectra of AH (0.5 μM) in the presence of KOH (10 μM) and various water% (v/v) values in different solvents: (A) acetone (water%: 0.1, 0.3, 0.6, 1.1, 1.8, 3.0, 4.5, 8.0 and 11.5); (B) MeCN (water%: 0.1, 0.2, 0.3, 0.4, 0.6 0.8, 1.0, 1.5, 2.0, 2.5, 3.0, 4.0, 4.7 and 5.5); (C) DMF (water%: 0.2, 0.4, 0.8, 1.5, 2.5, 4.0, 6.5, 8.0, 10.0 and 12.0) and (D) DMSO (water%: 0.5, 1.0, 2.0, 3.5, 5.0, 7.5, 10.0 and 11.4). The spectra in the absence of water are depicted in black. (E–H) The normalized intensities are plotted against water% (v/v) and fitted linearly up to certain water% range: (E) acetone; (F) acetonitrile; (G) DMF and (H) DMSO. The variations for other higher water% are shown in the *inset* of E–G. (A–D) Each fluorescence excitation spectrum for the emission at 525 nm is normalized by its maximum intensity value. For normalization of emission spectra, each emission spectrum for the excitation at 440 nm was divided by the maximum intensity value in the absence of water, and the resulting spectrum was further divided by the extent of emission intensity decrease factor with respect to zero water condition for excitation at 485 nm. The gradual blue-shift for the excitation spectra or the increase in the emission intensity with the increase in of water% are depicted in arrows.

DMSO), and followed by the addition of a specific amount of the same solvent without water but containing identical probe concentrations to reach a certain value of water% below that of the respective initial value (0.6% for acetone and MeCN; 0.8% for DMF and 1.0% for DMSO). Fluorescence excitation and emission spectra of final water-diluted solutions were found to be nicely matched with the corresponding known spectra at an identical water% value (Fig. S17, ESI†), showing that the water association with A^- is reversible in nature. In addition to the

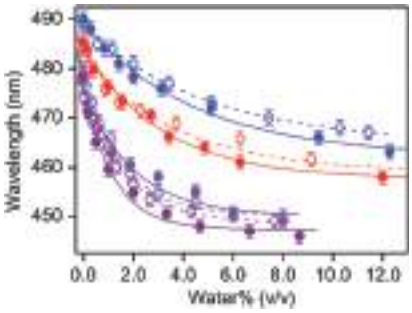

Fig. 6 Water% (v/v)-dependent shift in the fluorescence excitation wavelength (hollow circles, broken lines) for the emission at 525 nm and UV-vis absorption wavelength (solid circles, solid lines) for AH in the presence of KOH in different solvents is plotted: violet, acetone; purple, MeCN; red, DMF; blue, DMSO. The data points are fitted single exponential curves.

emission intensity changes, the wavelength shift of fluorescence excitation or UV-vis absorption band may also be beneficial for the detection of water%. About ~25 nm blue-shift for the addition of ~2% water in acetone and MeCN or ~15 and 20 nm blue-shift for the addition of ~5% water for DMF and DMSO, respectively, was detected (Fig. 6). The extent of blue-shift in the absorption or excitation spectra was plotted against the water% value in different aprotic media (Fig. 6), and the data points were fitted with a single exponential curve. The phenomenon of such a large wavelength shift induced by the presence of a relatively low water amount (<2% (v/v) for acetone and acetonitrile; <4% for DMF and DMSO) can be exploited for the detection of lower water amounts (Fig. 6).

Real-time moisture analysis in polar aprotic solvents

Polar aprotic organic solvents exhibit high moisture affinity, and thus, require special arrangement to preserve them under the moisture-free condition for prolonged period of time. It has been reported that a considerable extent of moisture incorporation in the solvents may happen even for their short-time exposure in an open atmosphere.[19,21] Using the present water detection protocol, the real-time atmospheric moisture incorporations in the aprotic solvents under the open laboratory atmospheric condition were monitored.

The amount of moisture incorporations is highly dependent on the relative atmospheric humidity and temperature.[21] As described in detail in the experimental section, all the solvents were dried meticulously and stored in a closed glass container in a nitrogen atmosphere with 3 Å molecular sieves up to not more than 12 hours. No moisture incorporation during the solvent preservation was confirmed from the unchanged emission response for A^- (Fig. S18, ESI†). We exposed each dried solvent (~40 mL) containing A^- (AH (0.5 μM) + KOH (10 μM)) in a 100 mL beaker with a diameter of ~5 cm for different time intervals up to 2 hours in the open laboratory atmosphere with 75% (±5%) relative humidity at 25 °C (±1 °C). The amount of moisture incorporation was estimated by evaluating the normalized excitation and emission spectra determined from

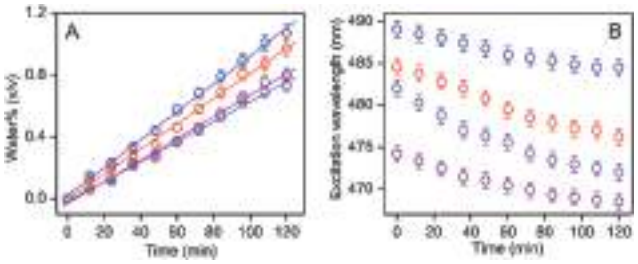

Fig. 7 (A) Plots of water% (v/v) incorporation and (B) the wavelength of fluorescence excitation band for the emission at 525 nm in various aprotic solvents over time upon exposure to an open laboratory atmosphere at 25 °C (±1 °C) and 75% (±5%) relative humidity condition: violet, acetone; purple, MeCN; red, DMF; blue, DMSO.

the time-dependent emission spectra of A^- upon excitation at 440 nm and 485 nm, as described in the previous section (Fig. S19, ESI†). The normalized emission intensity at its intensity maxima at 525–530 nm increased gradually with the increase in exposure time intervals up to 120 min, where the extent of intensity increase depends on the specific solvent system; 1.91-fold for acetone and 1.95-fold for MeCN, 1.40-fold for DMF and 1.37-fold for DMSO for 120 min exposure (Fig. S19, ESI†). The gradual increase in the normalized emission intensity with the time period of atmospheric exposure suggests a greater extent of atmospheric moisture incorporation (Fig. 7A). In addition, the gradual blue-shift in the excitation spectra (from ~474 to 467 nm for acetone; ~482 to 472 nm for MeCN; ~485 to 477 nm for DMF and ~489 to 484 nm for DMSO) with the increase in exposure time intervals also indicates an increase in the moisture content in solvents (Fig. 7B). However, the precise amount of atmospheric moisture incorporation for each solvent system was evaluated by correlating the time-dependent normalized emission intensities at 525–530 nm, according to Fig. 5E–H. It is noteworthy to mention here that the effect of small volume changes, particularly for acetone and MeCN, upon exposure to the open atmosphere, on the relative changes of normalized emission intensities was also considered during the estimation of moisture incorporation from the normalized emission intensity value. With the increase in the exposure time from 12 to 120 min, the amount of moisture intake increased along with maintaining a fairly well linear correlation from ~0.05 to 0.73% (v/v) for acetone, ~0.06 to 0.80% for MeCN, ~0.11 to 0.97% for DMF and ~0.14 to 1.07% for DMSO (Fig. 7A).

To justify the generality of the present methodology in terms of detection accuracy and applicability, we also performed similar atmospheric moisture incorporation studies in the presence of externally added water-spike of 1% before exposing each solvent to the open atmosphere (Fig. S20 and Table S1, ESI†). Notably, the subtracted amount of water-spike from the total recovered water% obtained fluorometrically was found to well match with that evaluated under the condition of without water-spikes (Table S1, ESI†). The results indicate the generality that various extents of contaminated water from different sources can be easily monitored by this method. Based on the atmospheric moisture incorporation capabilities for different aprotic solvents, the relative hygroscopicity scale can be drawn as DMSO > DMF > MeCN > acetone, which is consistent with the earlier reports.[19,21]

Moisture analysis in different food samples

The moisture content in various processed food items is one of the key parameter from legal and economic point of view.[13,55] There are ample possibility to differ the total moisture content from its recommended tolerant limit particularly in diary food items (butter, cheese and ghee (commonly popular in India and south Asian countries)) or coconut oil, obtained from high water content raw materials. Moreover, higher moisture content than its tolerant limit of ~0.3% in pure oil-based ghee and coconut oil are highly susceptible to undergo microbial degradation or water rancidification during their preservation for prolonged time period.[15–17,56–58] Therefore, the quality control of the foods relies heavily on cost-effective convenient moisture detection methods.

The total moisture contents in those food items (butter, cheese, ghee and coconut oil) available in the market were estimated using the present water detection protocol. For the chosen food samples, most of the food components either insoluble or sparingly soluble in the DMSO medium, and thus, the general solvent properties of DMSO are not expected to differ appreciably even in their presence in large excess, making DMSO a preferred solvent over the other aprotic solvents. In addition, the water-induced linear emission response spanning up to the large water-ratio value of ~12% (v/v) for DMSO is an additional advantage for its use as a suitable medium to detect widely different moisture contents in different food items varying from the very low (ghee or coconut oil) to large value (butter or cheese). The moisture content of a food material is defined using the following equation:

$$\%\ \text{Moisture} = (m_w/m_{sample}) \times 100$$

where m_w and m_{sample} represent the mass of water and mass of the sample, respectively.

The water% in various food samples was analysed by mixing different amounts of each food sample in 100 mL DMSO medium according to the protocol described in the Experimental section. The content of free water molecules in ghee or coconut oil is much lower than that in cheese or butter. Therefore, a lower amount of butter (10, 20 and 40 g) or cheese (4.0, 7.5 and 15 g) than ghee or coconut oil (100 g each) was mixed with the DMSO solvent for effective fluorescence studies to estimate the moisture content in those foodstuffs. Fluorescence spectra were recorded with the DMSO phase in the presence of AH (0.5 μM) and KOH (10 μM) (*cf.* experimental). The relative moisture amounts in different food samples obtained by evaluating the normalized fluorescence intensities are listed in Table 3 (Fig. S21, ESI†). The moisture amounts were found to be ~15% for butter and ~48% for cheese irrespective of different quantities of each sample taken (butter sample: 10, 20 and 40 g; cheese sample: 4.0, 7.5 and 15.0 g) in 100 mL DMSO medium (Table 3). However, low moisture

Table 3 Estimated water amounts in commercial food samples

Sample	Amount[a] (g)	Water-spike[b] (%, v/v)	Total water[c] (%, w/w)	A_T–A_0[d] (%, w/w)
Butter	10.0	—	15.0 ± 0.2	—
	20.0	—	14.9 ± 0.2	—
	40.0	—	15.4 ± 0.2	—
Cheese	3.0	—	48.2 ± 0.3	—
	7.5	—	48.5 ± 0.3	—
	15.0	—	47.1 ± 0.3	—
Ghee	100	0	0.32 ± 0.04	—
		0.50	0.79 ± 0.04	0.47
		1.00	1.34 ± 0.06	1.02
		1.50	1.83 ± 0.06	1.51
Coconut oil	100	0	0.40 ± 0.04	—
		0.50	0.87 ± 0.05	0.47
		1.00	1.41 ± 0.06	1.01
		1.50	1.88 ± 0.06	1.48

[a] Mass taken in 100 mL of DMSO solvent. [b] Volume% of water with respect to DMSO volume. [c] Amount of water with respect to 100 g of food sample. [d] Subtracted value of estimated water% without the water-spike from the total estimated water%.

amounts of ~0.3% and 0.4% were estimated for ghee and coconut oil, respectively (Table 3 and Fig. S21(C and D), ESI†). As described earlier, higher moisture contamination in pure oil-based commercial ghee or coconut oils make them susceptible to water rancidity. To validate our method with detecting higher water%, we introduced additional 0.5, 1.0 or 1.5% water-spike in the DMSO medium containing ghee or coconut oil sample (Fig. S21(C and D), ESI†). The recovered moisture amount after subtracting the actual moisture present, *i.e.*, 0.3–0.4% (estimated without water-spike) in the commercial sample, from the estimated total found water% were closely similar to the amount of respective amounts of water-spikes (Table 3). The results strongly indicate that the present moisture detection protocol can be applied to arrest the water rancidity by identifying the contamination of higher moisture% than its permissible limit for those essentially moisture-free food items with great accuracy.

Conclusions

We demonstrated a sensitive fluorometric method for the detection of trace moisture in various common aprotic solvents using a simple aldehydic phenol probe molecule. The phenolate form of the probe participates in the H-bonding interaction with water in the aprotic medium to exhibit a large blue-shift, from ~485 nm to 440 nm, in the absorption or fluorescence excitation spectra, although both H-bonded and free phenolate forms of probe show similar emission characteristics owing to the dissociation of the H-bond in the excited state. The water-induced spectral blue-shift and subsequent emission intensity increase and decrease for excitation at 440 nm and 485 nm, respectively, and they were utilized for the detection of moisture. Both those emission intensities changes for two different excitations were combined in a single spectral profile to enhance the detection sensitivity eliminating the dependency of the probe concentration for the ratiometric detection of moisture even in complex heterogeneous samples. The atmospheric moisture incorporation kinetics was evaluated for various aprotic solvents. Moreover, we estimated the water amount in butter or cheese with a relatively high water content and edible coconut oil or ghee food samples with a low water content. We have also shown that the present water detection protocol is highly effective to check water rancidity in ghee and coconut oil during their manufacture from high-water content raw materials.

Conflicts of interest

The authors declare no competing financial interest.

Acknowledgements

This study is partially supported by UGC and government of West Bengal for financial support under RUSA 2.0 scheme (PPP; No. 5400-F(Y)). SR acknowledge UGC for the SRF fellowship. Authors also acknowledge JU for departmental facilities.

Notes and references

1 H. S. Jung, P. Verwilst, W. Y. Kim and J. S. Kim, *Chem. Soc. Rev.*, 2016, **45**, 1242.
2 N. L. T. Padivitage, J. P. Smuts and D. W. Armstrong, *Specification of drug substances and products: development and validation of analytical methods*, Elsevier, Amsterdam, 2013.
3 T. Kodama, M. Takeuchi, N. Wakiyama and K. Terada, *Int. J. Pharm.*, 2014, **469**, 59.
4 W. E. Lee, Y. J. Jin, L. S. Park and G. Kwak, *Adv. Mater.*, 2012, **24**, 5604.
5 C. Pinheiro, J. C. Lima and A. J. Parola, *Sens. Actuators, B*, 2006, **114**, 978.
6 E. W. Abel, F. G. A. Stone and G. Wilkinson, *Comprehensive Organometallic Chemistry II*, Pergamon, Oxford, 1995.
7 H. W. Roesky, M. G. Walawalkar and R. Murugavel, *Acc. Chem. Res.*, 2001, **34**, 201.
8 S. Das, Y. Sarkar, S. Mukherjee, J. Bandyopadhyay, S. Samantab, P. P. Parui and A. Ray, *Sens. Actuators, B*, 2015, **209**, 545.
9 F. G. Golding, M. Giallorenzo, N. Moreno and V. Chang, *Sens. Actuators, A*, 1995, **47**, 337.
10 R. Liu, X. Xi and C. Liang, *Proc. SPIE-Int. Soc. Opt. Eng.*, 1991, **1572**, 399.
11 A. M. Araujo, L. M. Santos, M. Fortuny, R. L. F. V. Melo, R. C. C. Coutinho and A. F. Santos, *Energy Fuels*, 2008, **22**, 3450.
12 N. S. Foster, J. E. Amonette, T. Autrey and J. T. Ho, *Sens. Actuators, B*, 2001, **77**, 620.
13 J. M. deMan, J. W. Finley, W. J. Hurst and C. Y. Lee, *Principles of Food Chemistry, Food Science Text Series*, 2018, DOI: 10.1007/978-3-319-63607-8.
14 P. Kumar, R. Kaushik, A. Ghosh and D. A. Jose, *Anal. Chem.*, 2016, **88**, 11314.
15 K. Aysegul and J. Issa, *J. Dairy Technol.*, 2008, **61**, 300–306.

16 N. Suwarat and W. Tungjaroenchai, *Int. J. Biosci., Biochem. Bioinf.*, 2013, **3**, 332.
17 E. Lück and G. W. R. Lipinski, Foods, 3. Food Additives, *Ullmann's Encyclopedia of Industrial Chemistry*, 2002, Wiley-VCH, Weinheim, DOI: 10.1002/14356007.a11_561.
18 H. A. Frediani, *Anal. Chem.*, 1952, **24**, 1126.
19 B. Tan, P. Melius and P. Ziegler, *J. Chromatogr. Sci.*, 1982, **20**, 213.
20 J. M. Hogan, R. A. Engel and H. F. Stevenson, *Anal. Chem.*, 1970, **42**, 249.
21 Y. Hui and R. D. Webster, *Anal. Chem.*, 2011, **83**, 976.
22 H. S. Peng, X. H. Li, F. T. You, F. Teng and S. H. Huang, *Microchim. Acta*, 2013, **180**, 807.
23 P. P. Parui, Y. Sarakar, R. Majumder, S. Das, H. Yang, K. Yasuhara and S. Hirota, *Chem. Sci.*, 2019, **10**, 9140.
24 Y. Sarkar, R. Majumder, S. Das, A. Ray and P. P. Parui, *Langmuir*, 2018, **34**, 6271.
25 S. Roy, S. Das, R. Majumder, A. Ray and P. P. Parui, *RSC Adv.*, 2020, **10**, 23245.
26 A. P. de Silva, H. Q. N. Gunaratne, T. Gunnlaugsson, A. J. M. Huxley, C. P. McCoy, J. T. Rademacher and T. E. Rice, *Chem. Rev.*, 1997, **97**, 1515.
27 C. G. Niu, A. L. Guan, G. M. Zeng, Y. G. Liu and Z. W. Li, *Anal. Chim. Acta*, 2006, **577**, 264.
28 Y. Ooyama, M. Sumomogi, T. Nagano, K. Kushimoto, K. Komaguchi, I. Imae and Y. Harima, *Org. Biomol. Chem.*, 2011, **9**, 1314.
29 H. Mishra, V. Misra, M. S. Mehata, T. C. Pant and H. B. Tripathi, *J. Phys. Chem. A*, 2004, **108**, 2346.
30 W. Liu, Y. Wang, W. Jin, G. Shen and R. Yu, *Anal. Chim. Acta*, 1999, **383**, 299.
31 C. Pinheiro, J. C. Lima and A. J. Parola, *Sens. Actuators, B*, 2006, **114**, 978.
32 S. Cha, M. G. Choi, H. R. Jeon and S. K. Chang, *Sens. Actuators, B*, 2011, **157**, 14.
33 W. Chen, Z. Zhang, X. Li, H. Agren and J. Su, *RSC Adv.*, 2015, **5**, 12191.
34 D. W. Cho, *New J. Chem.*, 2014, **38**, 2233.
35 M. Tanioka, S. Kamino, A. Muranaka, Y. Shirasaki, Y. Ooyama, M. Ueda, M. Uchiyama, S. Enomoto and D. Sawada, *Phys. Chem. Chem. Phys.*, 2017, **19**, 1209.
36 D. Yang, X. J. Cao, X. T. Wu, Z. X. Yang and B. X. Zhao, *Anal. Methods*, 2019, **11**, 3079.
37 D. Yang, X. T. Wu, X. J. Cao and B. X. Zhao, *Dyes Pigm.*, 2019, **170**, 1075582.
38 M. G. Choi, M. H. Kim, H. J. Kim, J. E. Park and S. K. Chang, *Bull. Korean Chem. Soc.*, 2007, **28**, 1818.
39 G. Men, G. Zhang, C. Liang, H. Liu, B. Yang, Y. Pan, Z. Wang and S. Jiang, *Analyst*, 2013, **138**, 2847.
40 W. Y. Kim, H. Shi, H. S. Jung, D. Cho, P. Verwilst, J. Y. Lee and J. S. Kim, *Chem. Commun.*, 2016, **52**, 8675.
41 S. A. Poteet and F. M. MacDonnell, *Dalton Trans.*, 2013, **42**, 13305.
42 L. Chen, J. W. Ye, H. P. Wang, M. Pan, S. Y. Yin, Z. W. Wei, L. Y. Zhang, K. Wu, Y. N. Fan and C. Y. Su, *Nat. Commun.*, 2017, **8**, 15985.
43 B. Li, W. Wang, Z. Hong, E. S. M. E. Sayed and D. Yuan, *Chem. Commun.*, 2019, **55**, 6926.
44 R. Kaushik, R. Sakla, N. Kumar, A. Ghosh, V. D. Ghule and D. A. Jose, *Sens. Actuators, B*, 2021, **328**, 129026.
45 T. I. Kim and Y. Kim, *Anal. Chem.*, 2017, **89**, 3768.
46 M. H. Lee, J. S. Kim and J. L. Sessler, *Chem. Soc. Rev.*, 2015, **44**, 4185.
47 R. R. Gagne, C. L. Spiro, T. J. Smith, C. A. Hamann, W. R. Thies and A. K. Schiemke, *J. Am. Chem. Soc.*, 1981, **103**, 4073.
48 International Conference on Harmonization (ICH) of Technical Requirements for Registration of Pharmaceuticals for Human Use, Topic Q2 (R1): Validation of Analytical Procedures: Text and Methodology; http://www.ich.org, 2005.
49 J. V. Morris, M. A. Mahaney and J. R. Huber, *J. Phys. Chem.*, 1976, **80**, 969.
50 M. J. Frisch, *et al.*, *Gaussian 09 Rev. A.1*, Gaussian Inc., Wallingford, CT, 2009.
51 S. Mitra, R. Das and S. Mukherjee, *J. Photochem. Photobiol., A*, 1994, **79**, 49.
52 A. Mandal and S. Mukherjee, *Chem. Phys. Lett.*, 2001, **343**, 265.
53 M. Mukhopadhyay, D. Banerjee and S. Mukherjee, *J. Phys. Chem. A*, 2006, **110**, 12743.
54 H. Shen, L. Zhang and A. Eisenberg, *J. Am. Chem. Soc.*, 1999, **121**, 2728.
55 S. K. Lee, S. Anema and H. Klostermeyer, *Int. J. Food Sci. Technol.*, 2004, **39**, 763.
56 R. L. Bradley, *J. AOAC Int.*, 2001, **84**, 569.
57 M. L. Serunjogi, R. K. Abrahamsen and J. Narvhus, *Int. Dairy J.*, 1998, **8**, 677.
58 A. Kirazci and I. Javidipour, *Int. J. Dairy Technol.*, 2008, **61**, 300.

NJC

ROYAL SOCIETY OF CHEMISTRY

PAPER

Cite this: *New J. Chem.*, 2020, **44**, 4898

An unorthodox metal-free synthesis of dihydro-6*H*-quinoline-5-ones in ethanol/water using a non-nucleophilic base and their cytotoxic studies on human cancer cell line†

Arijit Kundu,[a] Bhaswati Bhattacharyya,[b] Kaliprasanna Dhara,*[c] Subhabrata Paul,[d] Indira Majumder[e] and Rita Kundu[e]

Received 23rd December 2019,
Accepted 17th February 2020

DOI: 10.1039/c9nj06346c

rsc.li/njc

A DBU-catalysed metal-free domino reaction strategy has been developed for the facile synthesis of dihydro-6*H*-quinoline-5-ones. This protocol employs a very expedient route to the synthesis of pyridine frameworks using β-chloro-α,β-unsaturated aldehydes, 1,3-diketones, and ammonium acetate in ethanol : water (1 : 1) solvent under eco-friendly conditions. Diverse types of acyclic and cyclic β-chloro-α,β-unsaturated aldehydes were used to obtain a variety of dihydro-6*H*-quinoline-5-ones. The mechanism of the domino reaction was established by isolating the intermediate compound, which was subjected to the next step of the reaction to obtain the target product. The structure of the intermediate was established from spectral and single crystal XRD studies. Most of the synthesized dihydro-6*H*-quinoline-5-one derivatives were found to be cytotoxic to the HeLa cell lines, showing profound cytotoxicity in MTT assays. The DNA fragmentation assay showed no fragmented DNA in the treated sets, which indicated that the compounds did not induce apoptosis of the HeLa cells. In most of the cases, autophagic cell death was evident from fluorescence microscopy studies, though necrosis was also observed in some cases.

Introduction

In the recent eon of research, the discovery of small molecules with the efficiency to work in complex biological processes to prevent diseases has been one of the major challenges facing researchers.[1] This trend has clearly indicated a paradigm shift of the spotlight from natural product chemistry to combinatorial chemistry.[2] Among numerous nitrogen heterocycles, quinoline is a scaffold of crucial importance with respect to biomedical use. Several quinoline derivatives, isolated from natural resources or prepared synthetically, show a wide variety of biological activities.[3] One such type of important quinoline moiety is dihydroquinoline, which exhibits interesting biological and pharmaceutical activities including antitubercular (**1**), anti-HIV (**2**), anticancer (**3**), apical sodium-dependent bile acid transporter (ASBT) inhibition (**4**), (Fig. 1) *etc.* Compounds, streptonigrin (**5**), ascidiathiazones and lavendamycin, (Fig. 1) showed antibiotic, anticancer, and antiproliferative activities, respectively.[3]

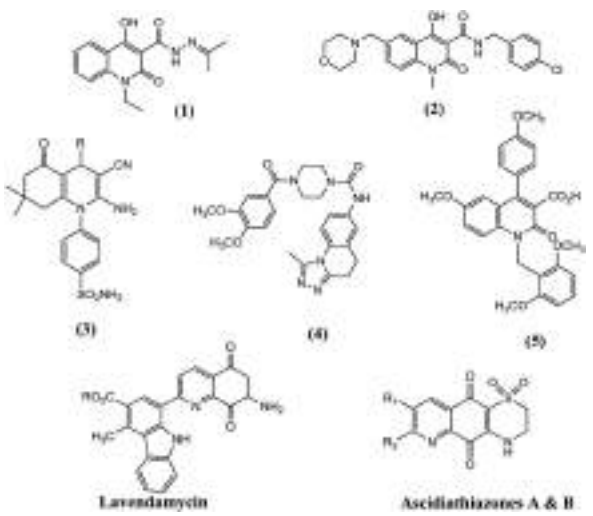

Fig. 1 Some naturally occurring quinoline derivatives.

Numerous skeletal analogues incorporating these crucial moieties have been prepared using synthetic approaches to

[a] *Department of Chemistry, Maulana Azad College, Kolkata-700013, India*
[b] *Department of Chemistry, Government Girls General Degree College, Ekbalpur, Kolkata-700023, India*
[c] *Department of Chemistry, University College of Science and Technology, University of Calcutta, Kolkata-700009, India. E-mail: chemkpd@gmail.com*
[d] *Department of Botany, Presidency University, Kolkata-700019, India*
[e] *Department of Botany, University of Calcutta, Kolkata-700019, India*

† Electronic supplementary information (ESI) available. CCDC 1542885 and 1542887. For ESI and crystallographic data in CIF or other electronic format see DOI: 10.1039/c9nj06346c

accomplish a vast and diverse chemical library.[4] Development of a green technique requires fulfillment of certain criteria such as, use of nontoxic reagents and absence of additives, ambient reaction conditions, atom economy and procedural simplicity. Coupled with this concern, one-pot multicomponent reactions are equally significant as they give rise to complex structures by simultaneous formation of two or more bonds in time-saving procedures.[5] A number of synthetic strategies have been utilized for the preparation of dihydro-6*H*-quinoline-5-one skeletons either by the reaction of β-enaminones with β-dicarbonyls in the presence of $CeCl_3$/NaI in 2-propanol,[6] DBU in butanol,[7] ammonium acetate using microwave,[8] $K_5CoW_{12}O_{40}\cdot 3H_2O$[9] *etc.* or by the reaction between a ketone, 1,3-diketone, and an aldehyde in the presence of a copper incorporated nanorod like mesoporous silica catalyst using molecular O_2[10] or MCM-41 supported HPF_6.[11] One crucial feature of multicomponent reactions is cost efficiency. Besides many other factors, cost efficiency depends on the number of starting materials and reagents used or steps required for the formation of the product. In this regard, development of reaction protocols involving inexpensive starting materials or minimal number of steps to reach the target molecule is more acceptable.

A literature review on the synthetic methodologies for 7,8-dihydroquinolin-5-ones and similar derivatives reveal that most of the synthetic techniques engage either more than one step with costly metal catalysts or a three to four component-strategy. The majority of groups have reported the preparation of dihydro-6*H*-quinoline-5-one derivatives using a two-step procedure entailing β-enaminone intermediates, which could be obtained from the reaction between dimethylformamide, dimethyl acetals and aryl methyl ketones.[6–9] Mukhopadhyay *et al.*[10,11] demonstrated a four-component-reaction strategy for the preparation of dihydro-6*H*-quinoline-5-one derivatives (Scheme 1).

To enrich this library, we focused on the synthesis of different dihydroquinoline derivatives. Here, the synthesis of dihydro-6*H*-quinoline-5-one derivatives was developed by taking the advantages of the skeletal motif of β-chloro-α,β-unsaturated aldehydes. Goroi *et al.*[12] had reported the synthesis of dihydro-6*H*-quinolin-5-ones from similar motifs of β-bromo-α,β-unsaturated aldehydes by using a three-component methodology between 1,3-diketones, and ammonium acetate without any additional catalyst or metal salt at 120 °C, where the methodology involves the elimination of a more labile bromide group. Moreover, flexibility of the methodology with an acyclic analog of β-bromo-α,β-unsaturated aldehydes was not reported. Additionally proof of mechanistic pathway was not established in the approach. In the pursuit of an easier and more green technique at a lower temperature we have adopted a metal-free protocol in an ethanol/water solvent starting from different β-chloro-α,β-unsaturated aldehydes as a source of carbonyl functionalities. To the best of our knowledge this is the first report of the formation of dihydro-6*H*-quinoline-5-ones from β-chloro-α,β-unsaturated aldehydes as a source of carbonyl functionality.

Quinolines and their derivatives are known for their diverse (antimicrobial, anticancer, anti-HIV, anti-inflammatory, antidepressant *etc.*) biological activities and have been studied for centuries. Anticancer drugs with quinoline moieties can induce apoptosis, dysregulate cell cycles and inhibit angiogenesis (Afzal *et al.*, 2015).[13] Koprulu and coworkers (2019)[14] reported the synthesis of methoxy and hydroxy substituted quinoline compounds and their antiproliferative properties against human adenocarcinoma (HT29), human cervical cancer cell line-HeLa and rat glioblastoma (C6). In the present study, the anticancer activity of the synthesized dihydro-6*H*-quinoline-5-one derivatives on cervical cancer cells *in vitro* (HeLa, HPV 18 positive cell line) was explored. As the compounds have a planar structure, they tend to intercalate within the DNA bases, causing DNA damage and inhibiting replicative processes (Okten *et al.*, 2017),[15] leading to cell death. To evaluate the mode of cell death, DNA fragmentation assays were undertaken and the presence of autophagic vacuoles was studied.

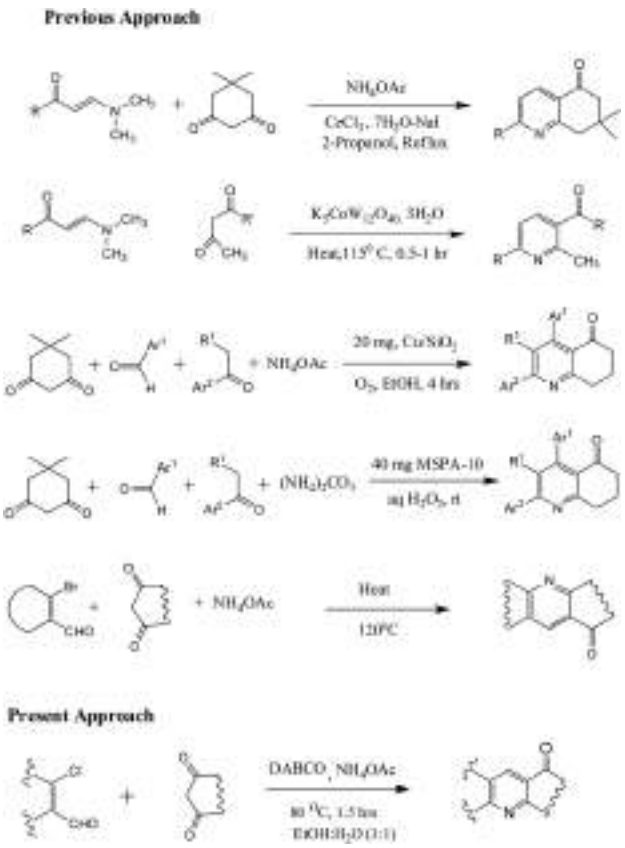

Scheme 1 A comparative study of previous and present work.

Results and discussion

In order to find out the suitable reaction conditions associated with the synthesis of dihydro-6*H*-quinoline-5-one, we optimized the reaction by carrying out extensive screening tests utilizing a representative reaction between 3-chloro-2-methyl-3-phenyl-acrylaldehyde (**1h**) (1 mmol) and dimedone (**2a**) (2.0 mmol) in the presence of NH_4OAc (5 mmol) and different bases by varying solvents to obtain **3h**.

All the results are summarized in Table 1. Initially the reaction was carried out by using potassium carbonate as the

Table 1 Optimization study using **1h** and aldehyde **2a**

S. no.	Base[a]	Solvent[b]	Time (h)	Temp. (°C)	Yield[c,d] (%)
1	K_2CO_3	Water	12	100	10
2	Triethyl amine	Water	8	100	10
3	Triethyl amine	Ethanol/water (1 : 1)	8	100	20
4	Morpholine	Water	8	100	25
5	Morpholine	Ethanol/water (1 : 1)	8	100	45
6	Pyridine	water	6	100	55
7	Pyridine	Ethanol/water (1 : 1)	6	100	75
8	Piperidine	Ethanol/water (1 : 1)	6	100	60
9	α-Picoline	Ethanol/water (1 : 1)	5	100	75
10	β-Picoline	Ethanol/water (1 : 1)	5	100	80
11	γ-Picoline	Ethanol/water (1 : 1)	4.5	100	85
12	Lutidine	Ethanol/water (1 : 1)	4	100	85
13	Bipyridine	Ethanol/water (1 : 1)	3	100	85
14	DABCO	Ethanol/water (1 : 1)	1.5	100	90
15	DBU	Ethanol/water (1 : 1)	2	100	85
16	**DABCO**	**Ethanol/water (1 : 1)**	**1**	**80**	**96**
17	DABCO	Ethanol/water (1 : 1)	2.5	60	90
18	DABCO	Ethanol/water (1 : 1)	2	70	92

[a] All the reactions were carried out with 3 mmol base. [b] 10 ml of solvent was used in each case. [c] All the reactions were carried out with 3-chloro-2-methyl-3-phenyl-acrylaldehyde (1.0 mmol) and dimedone (2.0 mmol). [d] Yield of isolated product.

base in water, but it resulted in low yield of the product even after a long reaction time at 100 °C (Table 1, entry 1). In the pursuit of more fruitful reaction conditions, we performed the same reaction in water and ethanol–water mixture in the presence of triethyl amine as the base (Table 1, entries 2 and 3) and it was observed that there was a slight increase in the yield of the product in the ethanol–water (1 : 1) solvent after a long reaction time. Consequently, we studied the reaction in water and ethanol–water (1 : 1) in the presence of morpholine and pyridine as the bases (Table 1, entries 4–7), where a marginal enhancement in the product yield was noticed when pyridine was used as the base in an ethanol–water (1 : 1) solvent. Henceforth screening tests were done in ethanol–water (1 : 1) solvent to obtain the best reaction conditions by studying with different non-nucleophilic bases and various reaction times (Table 1, entries 8–15). Ultimately the optimum conditions were realized by using DABCO as the base at 80 °C, which afforded 96% yield of the desired product in ethanol–water (1 : 1) solvent (Table 1, entry 16). A study to observe the effect of temperature on the yield of the product was also performed (Table 1, entries 17 and 18), which indicated that any further alteration of the reaction temperature decreased the yield of the product. To show the scope of this protocol, we utilized the new methodology using different 1,3-dicarbonyl systems with various acyclic β-chloro-α,β-unsaturated aldehydes (Table 2) and cyclic β-chloro-α,β-unsaturated aldehydes (Table 3). In all the cases, the reaction proceeded efficiently with good to excellent yields.

The reactions were simultaneously carried out at the 1 mmol scale and no change in the yield of the product was observed when scaled up to the 10 mmol scale. From the point of view of green chemistry, it was interesting to note that the solvent used herein is a mixture of ethanol and water and the base DABCO is completely benign for the environment.

Besides cost efficiency, the methodology involved procedural simplicity, easy work-up and minimization of chemical impurities. The structures of the products were well characterized by using spectral (IR, ^{1}H and ^{13}C NMR) and elemental analysis data. The structural pattern of the products was fully established by X-ray crystallographic analysis of compound **6a** (CCDC 1542885)† (Fig. 2). We herein synthesized twenty-three compounds and of them, seven are new additions to the literature.

A plausible mechanistic pathway was proposed to explain the base-catalyzed formation of dihydro-6*H*-quinoline-5-ones from β-chloro-α,β-unsaturated aldehydes (Fig. 3). The β-chloro-α,β-unsaturated aldehyde initially went through a Knoevenagel condensation with the 1,3-diketone in the presence of a non-nucleophilic base. Subsequently the presence of a vinylic chlorine atom facilitated the incorporation of the second molecule of 1,3-diketone to produce the xanthene-dione intermediate (**8**). The *in situ* product **8** immediately reacted with ammonia, generated from ammonium acetate under the reaction conditions, to form the β-enaminone through ring opening. This β-enaminone ultimately formed the dihydro-6*H*-quinoline-5-one through internal rearrangement involving N–C bond formation and C–C bond cleavage losing one molecule of the 1,3-diketone.

The xanthene-dione intermediate (**8**), proposed in the above-mentioned reaction pathway for the formation of dihydro-6*H*-quinoline-5-one derivatives, had been isolated in the following way. Initially, the reaction between/with (*Z*)-3-chloro-3-phenylacrylaldehyde (**1a**) and dimedone (**2a**) was carried out in the presence of base DABCO in water at room temperature for ten minutes. The intermediate **8** was immediately precipitated, which was

Table 2 Base catalysed dihydro-6*H*-quinoline-5-one derivatives from acyclic β-chloro-α,β-unsaturated aldehydes

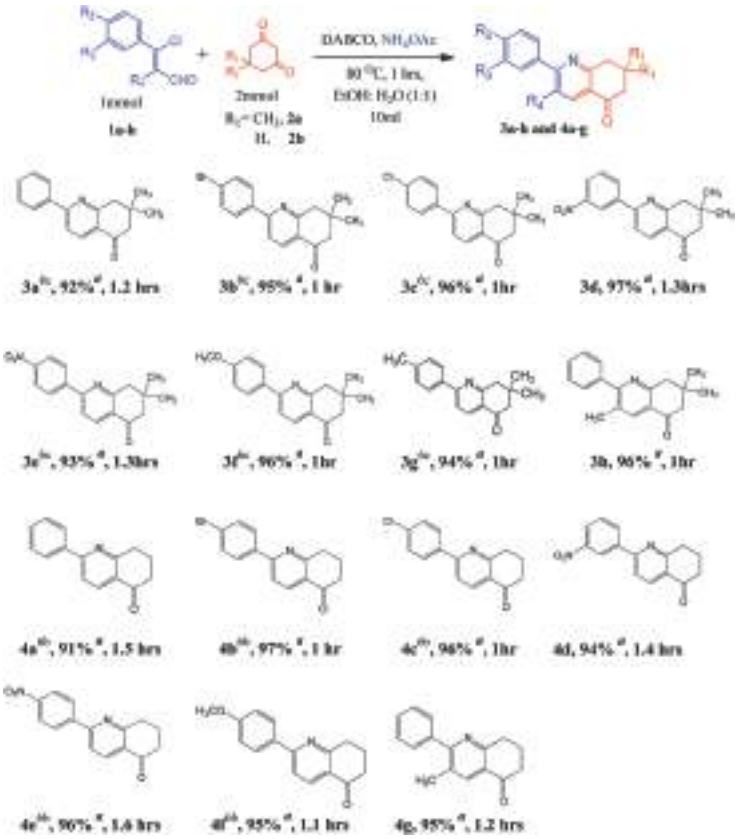

[a] % yield was calculated from the isolated product.

Table 3 Base catalysed dihydro-6*H*-quinoline-5-one derivatives from cyclic β-chloro-α,β-unsaturated aldehydes

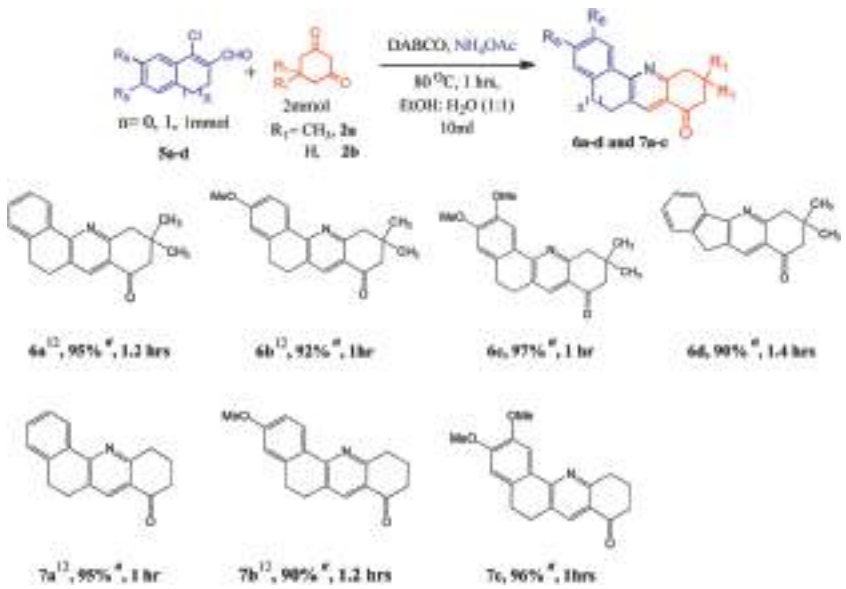

[a] % yield was calculated from the isolated product.

filtered and further reacted in the presence of ammonium acetate in ethanol–water (1 : 1) solvent at 80 °C when **3a** was obtained after 1.2 hours. A schematic diagram of the aforesaid procedure is shown in Fig. 4. The structure of the xanthene-dione intermediate (**8**) was confirmed by spectroscopic and X-ray crystallographic studies (CCDC 1542887)† (Fig. 5).

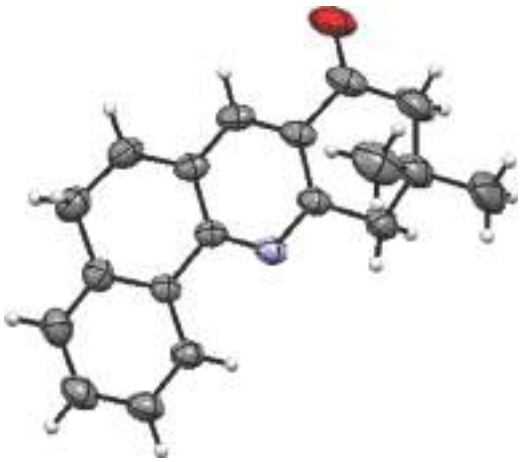

Fig. 2 X-ray crystallographic structure of compound **6a**.

Isolation of intermediate **8** confirmed the proposed mechanistic pathway as shown in the scheme shown in Fig. 3. The role of vinylic chlorine present in the β-chloro-α,β-unsaturated aldehyde for the formation of **8** was thus established.

Being a class of substituted pyridine scaffolds, dihydro-6*H*-quinoline-5-one moieties show high potential towards biological systems. In the present study, we have evaluated the cytotoxic potential of the synthesized dihydro-6*H*-quinoline-5-one scaffolds using MTT cell viability assays on a cervical cancer cell line (HeLa) followed by a DNA fragmentation assay. Morphology of acidic vesicles (vacuoles and lysosomes) and the presence of autophagosomes were observed by fluorescence microscopy after staining with a vital metachromatic dye acridine orange (AO).

Biological study

Cytotoxicity assay. Many of the synthesized quinoline compounds bearing different functional groups exhibit antimetastatic effects. The nature and position of the substituent on the

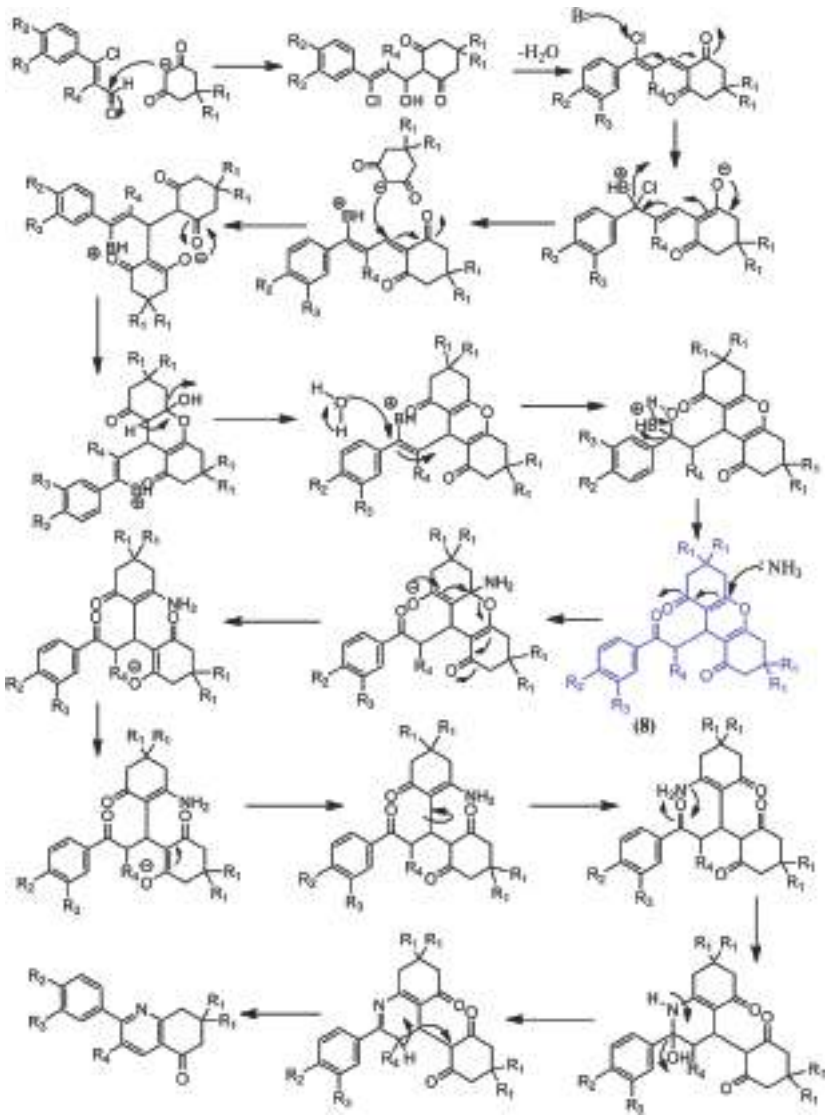

Fig. 3 Plausible mechanistic pathway for the synthesis of dihydro-6*H*-quinoline-5-one derivatives.

Fig. 4 Schematic diagram of the formation of dihydro-6*H*-quinoline-5-one derivative through xanthene-dione intermediate.

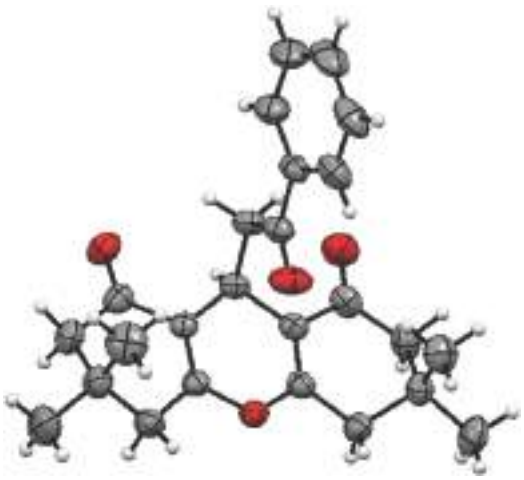

Fig. 5 X-ray crystallographic structure of compound **8**.

quinoline framework show variety in their efficacy in terms of anticancer activity, thus generating structure–activity relationship studies.[16] In our case, the presence of methoxyl groups at different positions with respect to quinoline nitrogen has shown relatively higher cytotoxicity than that of other substituents. We thereby undertook a detailed study with the compounds containing methoxyl groups only. From the MTT assay (Table 4), it was evident that less cytotoxicity was observed in HeLa cells treated with **3f**, **7c**, and **6b** (IC_{50} 120 μm, 100 μm, and 90 μm respectively), whereas cells treated with **4f**, **6c**, and **7b** showed significant cytotoxicity. Among these compounds, it was found that compound **6c** is the most cytotoxic when compared with the others ($IC_{50} \sim 0.95$ μM) (Fig. 6).

DNA fragmentation assay. DNA fragmentation is a hallmark of apoptotic cell death. However, in the treated cells no sign of laddering of DNA (fragments with 180 kb or its multiples) was observed (Fig. 7). Intact genomic DNA was found in all the treated sets, which indicate that apoptosis might not be the mechanism for inducing cell death in the treated ones.

Fluorescence microscopy with acridine orange dye. From the fluorescence microscopy study, it was observed that in the sets treated with compounds **3f**, **4f**, **6b** and **7b** formation of acidic vacuoles (autophagosomes) was evident. Increased amounts of diffused red specks can be easily observed indicating that the cell death pathway was mediated by autophagy, which was induced after 24 hours of chemical treatments, whereas a necrotic cellular morphology was observed in the sets treated with compounds **6c** and **7c** (Fig. 8).

Table 4 Results obtained from an MTT assay of HeLa cells with different dihydro-6*H*-quinoline-5-one derivatives

		Dose								
Compound	% cell viability	0.05 μM	0.1 μM	0.5 μM	0.75 μM	1 μM	25 μM	50 μM	100 μM	250 μM
3f	Average	92	89.67	87	83.67	81.77	75.33	71.67	69.33	3.67
	SD	0.65	0.73	0.5	0.72	0.05	1.6	1.63	1.05	0.4
6b	Average	99.33	92	95.33	95	88.33	88	72.33	45.67	—
	SD	1.25	1.15	0.65	1.15	0.45	0.75	2.08	1.13	—
6c	Average	90.33	90.67	93.33	65.66	47	35.33	20.33	15	—
	SD	2.51	0.23	0.6	0.65	0.43	1.3	0.05	1.5	—
4f	Average	104.69	97.66	101.17	97.26	90.23	82.03	48.44	31.05	—
	SD	3.5	3.1	4.6	4.2	3.5	3.7	0.8	1.8	—
7b	Average	101.7	102.54	100.2	97.07	95.31	26.75	22.07	19.94	—
	SD	7.8	8.14	1.25	2.98	0.8	10.44	0.265	1.01	—
7c	Average	101.37	99.61	100.2	98.44	90.43	81.84	67.77	51.37	—
	SD	1.82	1.2	1.5	0.41	2.12	0.11	2.6	2.62	—
Doxorubicin	IC_{50}	1 μM[17]								

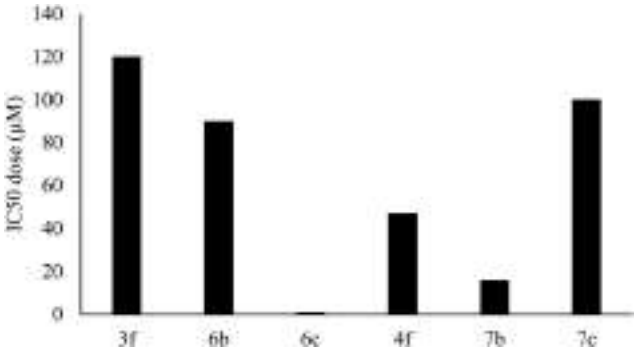

Fig. 6 Bar graph showing IC_{50} doses of the compounds in HeLa cells.

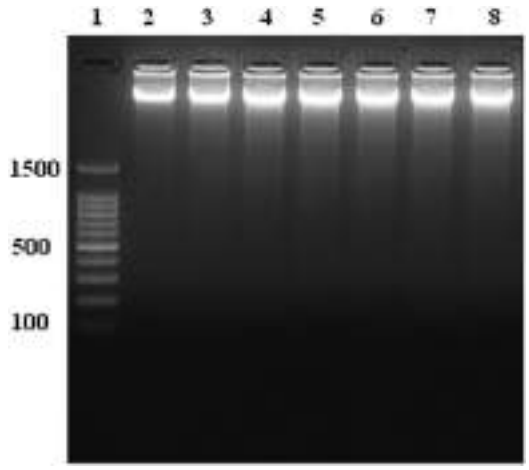

Fig. 7 HeLa cells grown in T25 flask were treated with IC_{50} doses of corresponding treatments for 24 hours. Lane 1: DNA marker (1.5 kb), lane 2: control set, lane 3: compound **3f**, lane 4: compound **6b**, lane 5: compound **6c**, lane 6: compound **4f**, lane 7: compound **7b**, and lane 8: compound **7c**.

Experimental

Procedure for the synthesis of dihydro-6*H*-quinoline-5-one derivatives

2 mmol of a 1,3-diketone compound and 1.2 mmol of β-chloro-α,β-unsaturated aldehydes were stirred in the presence of 5 mmol ammonium acetate in 10 ml ethanol/water (1 : 1) solvent using DABCO as a base at 80 °C for 1–1.6 hours. The reaction was monitored by TLC. After completion of the reaction the whole mixture was extracted with ethyl acetate and the ethyl acetate part was washed with brine three times and evaporated under vacuum. The reaction mixture obtained was subjected to column chromatographic separation using different proportions of a petroleum ether:ethyl acetate mixture. The product was obtained from a 20% ethyl acetate petroleum ether mixture. The products were well characterized by IR, ^{1}H NMR, ^{13}C NMR, elemental analysis and an X-ray crystallographic study.

Synthesis of 3,3,6,6-tetramethyl-9-(2-oxo-2-phenylethyl)-3,4,5,6,7,9-hexahydro-1*H*-xanthene-1,8(2*H*)-dione (8) (proposed intermediate) and its conversion to the 7,7-dimethyl-2-phenyl-7,8-dihydroquinolin-5(6*H*)-one (3a)

A mixture of 3-chloro-3-phenylacrylaldehyde (**1a**) (1 mmol) and dimedone (**2a**) (2 mmol) was stirred in the presence of DABCO in 5 ml water at room temperature for 10 min. The compound 3,3,6,6-tetramethyl-9-(2-oxo-2-phenylethyl)-3,4,5,6,7,9-hexahydro-1*H*-xanthene-1,8(2*H*)-dione was precipitated as a white solid, which was isolated by filtration and washed with water. The isolated xanthene dione was further reacted in the presence of 5 mmol ammonium acetate in 10 ml ethanol/water (1 : 1) solvent at 80 °C for 1.2 hour and the expected 7,7-dimethyl-2-phenyl-7,8-dihydroquinolin-5(6*H*)-one was obtained.

General procedure for *in vitro* evaluation of anticancer activity

Maintenance of cell line. Human cervical cancer cell line, HeLa, a HPV 18 positive cell line was obtained from NCCS, Pune. Cells were maintained in EMEM (Eagle's minimum essential medium), supplemented with 10% FBS, non-essential amino acid and glutamic acid, in a humidified CO_2 (5%) at 37 °C.

Cytotoxicity assay. Cytotoxicity of the chemicals towards HeLa cells was investigated using standard MTT reduction assays.[18] Positively charged tetrazolium dye MTT can penetrate viable cell membranes easily. After reduction by viable cell mitochondrial dehydrogenases and oxidoreductases, the yellow colored MTT dye turns to purple colored crystals. These water insoluble formazan crystals can be solubilized and quantified spectrophotometrically to determine the viability percentage. 1×10^3 cells were seeded in a 96-well plate and were incubated overnight at 37 °C. Cells were then treated with the synthesized compounds in a concentration range of 0.05 μM to 100 μM for 24 hours. Then 100 μg of MTT (Sigma) (5 mg MTT per ml PBS) was added to each well, mixed and then incubated in a 5% CO_2 incubator for another 3–4 hours. Then the media was removed from the wells and the formazan crystals were dissolved with 80 μl of DMSO (Merck). Absorption spectra were recorded using an ELISA microplate reader (BioRad) at 595 nm. The extent of cytotoxicity was determined using the following formula:

$$\%\ \text{inhibition} = [(\text{absorbance of control set} - \text{absorbance of treated set})/\text{absorbance of control set}] \times 100$$

From the absorption spectral data, cell viabilities (in percentage) in treated and control sets were calculated along with standard deviations and bar graphs were made using the standard software (Microsoft Excel).

DNA fragmentation

Apoptotic cell death can be established by DNA fragmentation assays. DNA ladder assays have previously shown fragmented DNA of 180 base pairs and its multiples (which is an apoptotic phenomenon) in Hep-2 cells treated with only AMK OX-12, a 1,3,4-oxadiazole derivative. To assess the cell cytotoxic potential of the synthesized chemicals on the HeLa cell line, cells were seeded in surface-treated 60 mm culture dishes for 24 hours. Treatments were added according to the IC_{50} doses from MTT cell viability assays and incubated for 24 hours. Total DNA was isolated according to Herrmann and his coworkers (1994) after slight modification.[19] 1×10^6 HeLa cells were harvested using a policeman (cell scrapper) and washed with chilled PBS. Then the cells were dissolved in Tris–EDTA (TE) buffer. Equal amounts of

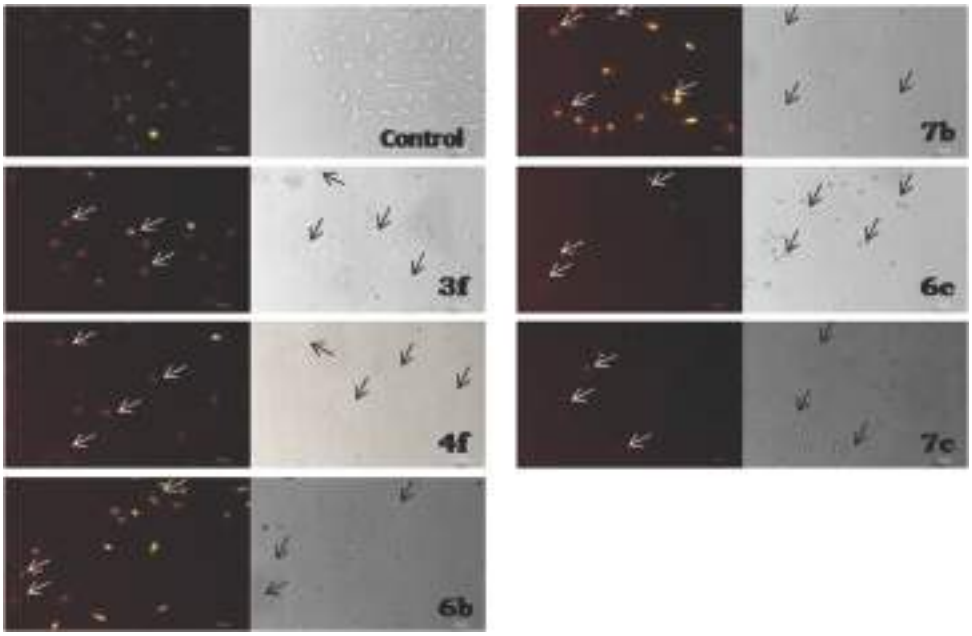

Fig. 8 Fluorescence microscopic study with acridine orange; fluorescence (right) and phase contrast (left) images of treated HeLa cells. Cells were treated with IC_{50} doses of the respective compounds.

2× lysis buffer (200 mM NaCl, 20 mM Tris, 50 mM EDTA, 1% SDS and 2% NP-40) was added, tapped and incubated in ice for 30 minutes. Then a phenol–chloroform–isoamyl alcohol (25 : 24 : 1) mixture was used to eliminate fats and proteins. DNA was collected from the aqueous phase and precipitated with isopropanol and sodium acetate after two rounds of centrifugation. The collected pellet was redissolved in TE buffer and incubated with RNaseA to remove RNA. DNA was finally precipitated with isopropanol and sodium acetate. DNA pellets were washed in 70% ethanol and air dried to evaporate alcohol fully. Then the pellets were dissolved in TE buffer and run on a 1.5% agarose gel and visualized under a UV documentation system.

Fluorescence microscopic study of acidic cellular compartments with acridine orange dye

Acridine orange (AO) is a metachromatic dye. Cell cytoplasm and nucleus are stained as green and the acidic compartments of a cell *viz.*, lysosome and vacuoles are stained orange. Formation of these kinds of acidic compartments in a higher degree represents an increased degree of autophagosome formation, a hallmark of autophagic cell death. In most of the autophagy pathway, the lysosome after fusion with an autophagosome forms an autophagolysosome that can engulf other cellular components leading to completion of the autophagic cell death cascade. Some key proteins are involved for conducting this pathway. Beclin-1, Atg group of proteins are the positive regulatory upstream proteins and LC3B proteins are the key proteins, which act as downstream regulators leading to the formation of an autophagosome.

In this experiment 1×10^4 HeLa cells were seeded on poly-lysine coated 60 mm Petri dishes. On addition of treatments with their respective IC_{50} doses, cells were incubated overnight at 37 °C. Cells were stained with 10 μg ml^{-1} AO and visualized under a fluorescence microscope (Leica).

Conclusion

A green, atom economic metal-free methodology has been developed using a non-nucleophilic base for the syntheses of dihydro-6*H*-quinoline-5-one derivatives from β-chloro-α,β-unsaturated aldehydes with good to excellent yield of the products. Molecular structures of two representative molecules were investigated by means of X-ray diffraction analysis. A mechanistic pathway was established by isolating the xanthenedione intermediate, which was further subjected to the second step of the domino reaction to yield the corresponding dihydro-6*H*-quinoline-5-one derivative. The biological study revealed that dihydro-6*H*-quinoline-5-one derivatives were cytotoxic to HeLa cells and among them, the compound **6c** showed profound cytotoxicity. As the DNA fragmentation assay showed no fragmented DNA in the treated sets, it could be concluded that the dihydro-6*H*-quinoline-5-one compounds did not induce apoptosis to the HeLa cells. In most of the cases autophagic cell death was evident from fluorescence microscopy studies, though necrosis was also observed in a few cases.

Conflicts of interest

There are no conflicts to declare.

Acknowledgements

The authors gratefully acknowledge the Department of Chemistry, University of Calcutta for Crystallographic and NMR studies and

the Department of Botany, University of Calcutta for the biological studies. The authors also thank Maulana Azad College, Kolkata for use of the departmental facilities.

References

1 (*a*) W. R. J. D. Galloway, A. Isidro-Llobet and D. R. Spring, *Nat. Commun.*, 2010, **1**, 80; (*b*) A. Bender *et al.*, in *Diversity Oriented Synthesis: A Challenge for Synthetic Chemists*, ed. S. Jaroch and H. Weinmann, Chemical Genomics, Ernst Schering Research Foundation Workshop, Springer, Berlin, Heidelberg, 2006, vol. 58.

2 (*a*) M. D. Burke and S. L. Schreiber, *Angew. Chem., Int. Ed.*, 2004, **43**, 46; (*b*) S. L. Schreiber, *Nature*, 2009, **457**, 153; (*c*) J. P. Kennedy, *J. Comb. Chem.*, 2008, **10**, 345; (*d*) G. D. Henry, *Tetrahedron*, 2004, **60**, 6043; (*e*) D. S. Tan, *Nat. Chem. Biol.*, 2005, **1**, 74.

3 (*a*) J.-P. Wan and Y.-J. Pan, *Chem. Commun.*, 2009, 2768; (*b*) F. Lieby-Muller, C. Allais and T. R. Constantieux, *Chem. Commun.*, 2008, 4207; (*c*) R. S. Senaiar, D. D. Young and A. Deiters, *Chem. Commun.*, 2006, 1313; (*d*) J. M. Davis, A. Truong and A. D. Hamilton, *Org. Lett.*, 2005, **7**, 5405; (*e*) B. Al-Saleh, M. M. Abdelkhalik, A. M. Eltoukhy and M. H. Elnagdi, *J. Heterocycl. Chem.*, 2002, **39**, 1035; (*f*) F. A. Omran, N. A. Awadi, A. A. E. Khair and M. H. Elnagdi, *Org. Prep. Proced. Int.*, 1997, **29**, 285.

4 (*a*) Y.-K. Sim, H. Lee, J.-W. Park, D.-S. Kim and C.-H. Jun, *Chem. Commun.*, 2012, **48**, 11787; (*b*) D.-S. Kim, J.-W. Park and C.-H. Jun, *Chem. Commun.*, 2012, **48**, 11334; (*c*) H. Jiang, J. Yang, X. Tang, J. Li and W. Wu, *J. Org. Chem.*, 2015, **80**, 8763; (*d*) S. Thi Le, H. Asahara and N. Nishiwaki, *J. Org. Chem.*, 2015, **80**, 8856; (*e*) Y. Bai, L. Tang, H. Huang and G.-J. Deng, *Org. Biomol. Chem.*, 2015, **13**, 4404.

5 L. R. Wen, Z. R. Li, M. Li and H. Cao, *Green Chem.*, 2012, **14**, 707.

6 (*a*) S. Kantevari, D. Addla and B. Sridhar, *Synthesis*, 2010, 3745; (*b*) S. Kantevari, S. R. Patpi, B. Sridhar, P. Yogeeswari and D. Sriram, *Bioorg. Med. Chem. Lett.*, 2011, **21**, 1214; (*c*) S. Kantevari, S. R. Patpi, D. Addla, S. R. Putapatri, B. Sridhar, P. Yogeeswari and D. Sriram, *ACS Comb. Sci.*, 2011, **13**, 427.

7 S. Gowrisankar, J. E. Na, M. J. Lee and J. N. Kim, *Bull. Korean Chem. Soc.*, 2005, **26**, 319.

8 A. S. Devi, S. Kaping and J. N. Vishwakarma, *Heterocycl. Lett.*, 2014, **4**, 203.

9 S. Kantevari, M. V. Chary, S. V. N. Vuppalapati and N. Lingaiah, *J. Heterocycl. Chem.*, 2008, **45**, 1099.

10 S. Ray, B. Banerjee, A. Bhaumik and C. Mukhopadhyay, *Catal. Commun.*, 2015, **58**, 97.

11 S. Ray, M. Brown, A. Bhaumik, A. Dutta and C. Mukhopadhyay, *Green Chem.*, 2013, **15**, 1910.

12 L. Goswami, S. Gogoi, J. Gogoi, R. K. Boruah, R. C. Boruah and P. Gogoi, *ACS Comb. Sci.*, 2016, **18**, 253.

13 O. Afzal, S. Kumar, M. R. Haider, M. R. Ali, R. Kumar, M. Jaggi and S. Bawa, *Eur. J. Med. Chem.*, 2015, **97**, 871.

14 T. K. Köprülü, S. Ökten, Ş. Tekin and O. Çakmak, *J. Biochem. Mol. Toxicol.*, 2019, **33**(3), e22260.

15 S. Okten, O. Cakmak, S. Tekin and T. K. Koprulu, *Lett. Drug Des. Discovery*, 2017, **14**(12), 1415.

16 S. K. Liew, S. Malagobadan, N. M. Arshad and N. H. Nagoor, *Biomolecules*, 2020, **10**(1), 138.

17 R. Arianingrum, I. S. Arty and S. Atun, *AIP Conf. Proc.*, 2017, **1823**(1), 020112.

18 T. Mossman, *J. Immunol. Methods*, 1983, **65**, 55.

19 B. Herrmenn and S. Hummel, *Ancient DNA*, Spinger-Verlag, New York, 1994.

RSC Advances

PAPER

View Article Online
View Journal | View Issue

Cite this: *RSC Adv.*, 2020, **10**, 23245

An aluminium fluorosensor for the early detection of micro-level alcoholate corrosion†

Snigdha Roy,[a] Sanju Das,[ab] Rini Majumder,[a] Ambarish Ray‡*[b] and Partha Pratim Parui *[a]

Received 20th January 2020
Accepted 1st June 2020

DOI: 10.1039/d0ra00619j

rsc.li/rsc-advances

The detection of the dry alcoholate corrosion of aluminium is vital to design a corrosion resistive aluminium alloy for the storage and transportation of biofuel (methanol or ethanol). By synthesizing an Al^{3+} fluorescent probe operable in an alcoholic medium, we quantified the alcoholate corrosion in terms of the fluorometrically estimated soluble alkoxide ($Al(OR)_3$) generation under nitrogen atmosphere. With time, a linear increase in corrosion with specific aluminium dissolution rate constants ~2.0 and 0.9 μg per day per cm^2 were estimated for aluminium and Al-7075 alloy, respectively. During open atmosphere monitoring, the adsorbed moisture converted small extent of $Al(OR)_3$ to the insoluble $Al(OH)_3$ at the alloy surface which retarded the alcoholate corrosion appreciably.

Switching over from conventional fossil fuel to biofuel is of current interest owing to the maximum utilization of eco-friendly non-conventional energy.[1] Commercially produced less polluted biofuels such as methanol and ethanol, mixed with fossil fuels have an acceptable performance capacity for the gasoline engine.[2] Moreover, in comparison to the gasoline, methanol and ethanol have much higher octane rating or compression ratio to resist the knocking for better thermal efficiency.[3] Since most of the fuel tanks/pipes are made of aluminium or its alloys owing to its high strength-to-density ratio, the aluminium corrosion due to the formation of alkoxide (alcoholate or dry corrosion) during storage or even transportation of such bio-alcohols may cause leakage in the fuel tanks and in worst cases enough threat is speculated for fire and explosion.[4] Mechanical overloads, alloy impurities even at elevated temperatures are further contenders for accelerating the alcoholate corrosion.[5] However, a prolong exposure to the moisture retards the alcoholate corrosion by forming a protective layer of hydrated aluminium oxide in the metallic surface but moisture impurity in the fuel may damage the gasoline engine.[6] Hence, a maintenance optimization is crucial in critical engineering disasters by detecting alcoholate corrosion as in its nascent state with minimizing the chance of water contamination.[6,7]

Several electrochemical and mechanical methods have been exploited for decades to propose aluminium alcoholate and other corrosions;[6] yet the early detection of the alcoholate corrosion is still a challenging task due to the lack of sensitive analytical methods.[6,8] Here, the fluorescence technique may act as a better alternative owing to its simplicity and high sensitivity.[9] Till date, a large number of fluorescent probes for Al^{3+} have been exploited in the biological or environmental domain,[10] but has never focused on alcoholate corrosion studies. Based on this requirement, we synthesized a fluorescent probe, namely HMBDC ((6*Z*)-6-(2-hydroxy-3-(hydroxymethyl)-5-methylbenzylideneamine)-2*H*-chromen-2-one), to detect alcoholate corrosion with μg-level detection ability along with its retarding signature in the presence of moisture in a judicious way. Such novel method may lead to an early detection of alcoholate corrosion in a simpler way.

The non-fluorescent phenolic Schiff-base molecule containing a coumarin moiety (HMBDC) was prepared by condensing an equimolar mixture of 6-amino coumarin (6-ACO) and 2-hydroxy-3-(hydroxymethyl)-5-methylbenzaldehyde (HHMB) in dry ethanol (Scheme 1 and Fig. S1†) (*c.f.* ESI† for details). Among various organic solvents, the interaction of HMBDC with Al^{3+} was observed only in the alcoholic medium according to the UV-vis studies (Fig. S2†). In methanol, the absorption intensity at ~353 nm for HMBDC (5 μM) decreased gradually with the continuous addition of $Al(NO_3)_3$ until saturated at ~8-equiv., giving rise to a new peak at ~406 nm, where an isosbestic point at ~384 nm assures the formation of Al^{3+}/HMBDC complex (**1**) (Fig. 1A). Upon optimization of the complex formation affinity in various ethanol/methanol mixed media, highest reactivity with the lowest saturated Al^{3+} concentration (~5 equiv.) compared to that obtained in pure methanol was observed in a 4 : 1 methanol/ethanol-mixed medium (Fig. S3†). Most probably, more effective H-bonding interaction of the dimeric ethanol/methanol[11] with **1** induces greater complex (**1**) stability, although the complex

[a]*Department of Chemistry, Jadavpur University, Kolkata 700032, India. E-mail: parthaparui@yahoo.com; Fax: +91-33-24146223; Tel: +91-9433490492*

[b]*Department of Chemistry, Maulana Azad College, Kolakta 700013, India. E-mail: r_ambarish@yahoo.co.in; Fax: +91-33-22268111; Tel: +91-9836650180*

† Electronic supplementary information (ESI) available. See DOI: 10.1039/d0ra00619j

‡ Department of Chemistry, Barasat Govt. College, Kolkata 700124, India

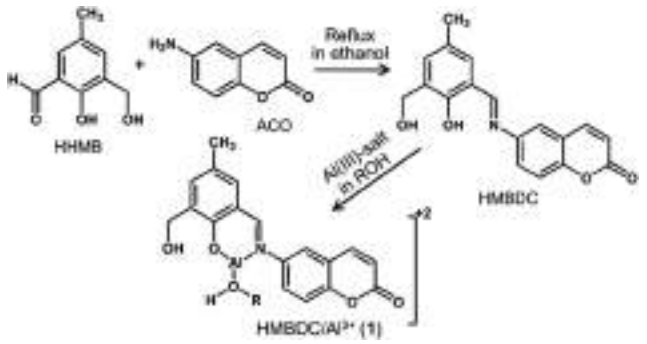

Scheme 1 Synthesis of HMBDC and its complexation with Al^{3+} in an alcohol solvent.

formation reactivity was much less in pure ethanol compared to the methanol medium (Fig. 1 and S2†).

In spite of the stronger H-bonding interactions of **1** with water compared to the methanol or ethanol, a complete dissociation of **1** in the presence of 20% (v/v) water in methanol (Fig. S4†) suggests that, in addition to the solvent assisted H-bonded structural stability of **1**, alcohol molecule may also participate in the coordination with Al^{3+} to form **1**. Indeed, the possible methanol coordination is reflected in the ESI-MS^+ analysis (Fig. S5B†). In addition, the Job's plots in the absorption studies showed that the HMBDC formed 1 : 1 stoichiometric complex with Al^{3+} (Fig. S6†). To elucidate the probable structure of **1**, we carried out the DFT-based theoretical calculation by considering the 1 : 1 stoichiometric Al^{3+}/HMBDC complex with or without methanol coordination. A stable structure of **1** was obtained when the oxygen atom of the methanol molecule coordinates with Al^{3+} and other two coordination sites of Al^{3+} are occupied by the phenolic-oxygen and imine-nitrogen of HMBDC (Scheme 1, Fig. 2 and S7†). Facile coordination of those hard donor sites of HMBDC towards harder Al^{3+} is susceptible towards alcohol assisted stabilization of **1**. The UV-vis absorbance at ~402 nm for **1** computed from the time-dependent DFT (TD-DFT) calculations in methanol medium, where the HOMO (90) → LUMO (92) excitation nicely matched with the experimental absorbance at ~406 nm (Fig. 1 and 2). However, monitoring of the ^{1}H-NMR peak characterized for aldimine proton is a useful strategy to identify the bonding of the imine-N to Al^{3+}.[12] We observed that the aldimine proton peak intensity for HMBDC in CD_3OD was quenched to a great extent with a considerable down-field shift from 8.80 to 8.88 ppm in the presence of Al^{3+} (Fig. S8†); the down-field shift is expected owing to the imine-N and Al^{3+} coordination, but intensity quenching does not follow the previous trend in the aprotic polar medium.[12] The generation of a partial positive charge at the N-centre upon its binding with the Al^{3+} may enhance the acidity of the aldimine proton to become labile for participating in the H/D exchange in a protic medium (CD_3OD), as reported previously for other allied systems.[13] These results strongly suggest the imine-N and Al^{3+} bonding in **1**. On the other hand, Al^{3+} induced large decrease in the IR intensity at ~3300 cm^{-1} for phenolic-OH also supports the phenoxide coordination (Fig. S9†).

The electronic distribution in the molecular orbital diagram (MO) of the HMBDC evaluated from the DFT calculation showed an intra-molecular photo-induced electron transfer (PET) from coumarin to the HHMB moiety, which makes the HMBDC non-fluorescent (Fig. 2). Al^{3+} induced an instantaneous increase in the fluorescence intensity for HMBDC (5 μM) in the alcoholic medium (methanol/ethanol or their mixture) due to the formation of **1** (Fig. 1B and S10†). A gradual fluorescence intensity increase at ~506 nm (λ_{ex} = 406 nm) of ~30-fold for 8 equiv. of

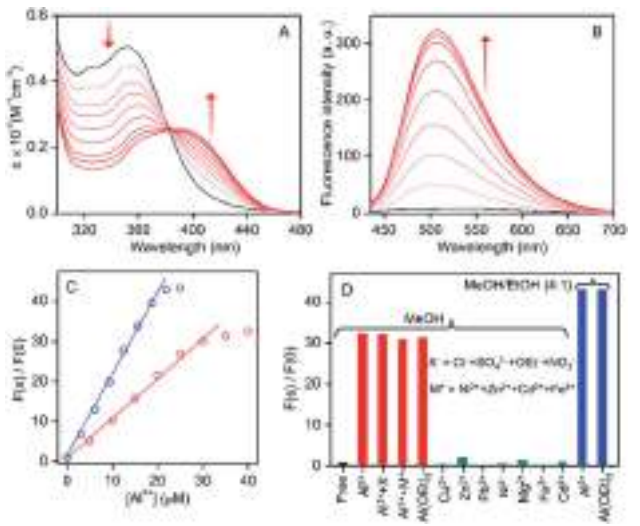

Fig. 1 (A) UV-vis absorption and (B) fluorescence spectra of HMBDC (5 μM) in the presence (red) and absence (black) of increasing concentration of $Al(NO_3)_3$ (0–40 μM) in anhydrous methanol at 25 °C. The intensity changes with increasing Al^{3+} concentrations are indicated by arrows. (C) Al^{3+} concentration dependent relative increase in the fluorescence intensity with respect to its absence in methanol (red) or methanol/ethanol (4 : 1) (blue). (D) Fluorescence intensity ratios in the presence and absence of various ions or mixture of ions in the mixed solvent (25 μM each; blue) or methanol (40 μM each; other colors) or are shown by bar-diagram.

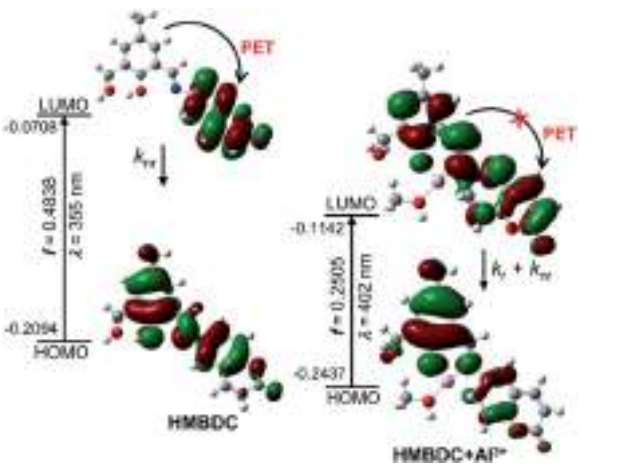

Fig. 2 Frontier molecular orbital profiles including various UV-vis absorption parameters of HMBDC (left panel) and HMBDC/Al^{3+} complex (right panel) based on TD-DFT (B3LYP/6-31G(d)).

Al^{3+} and ~40-fold for 5 equiv. of Al^{3+} was observed in the methanol and 4 : 1 (v/v) methanol/ethanol medium, respectively (Fig. 1 and S10B†). According to the HOMO and LUMO electronic distributions for **1** in the DFT studies, the PET process in HMBDC was highly restricted upon its binding with Al^{3+} in **1**, causing for the large increase in the fluorescence intensity (Fig. 2). However, the better fluorescence response (lower intensity-saturated Al^{3+} concentration and larger intensity increase) in the mixed medium than pure methanol may be associated with greater stability of **1**, as described in the previous section (Fig. S2†). The fluorescence intensity increase remains invariant using other soluble Al(III)-salts (Fig. 1D and S11†), which eliminates the role of counter anions for the increasing intensity. To ascertain the Al^{3+} selectivity, we performed similar fluorescence studies with other potentially interfering cations but failed to produce any noticeable fluorescence (Fig. 1D and S12†). However, a linear intensity increase with the increase in the concentration of Al^{3+} up to 6 equiv. in methanol and 4 equiv. in the 4 : 1 methanol/ethanol mixed medium can be useful for a ratiometric detection of unknown concentration of Al^{3+} (Fig. 1C), where the limit of detection[14] (LOD) of Al^{3+} with HMBDC in the methanol medium was found to be ~0.5 μM (*c.f.* details in ESI†). Most importantly, HMBDC recognized Al^{3+} selectively from the mixture of various other cations, and also in presence of other soluble Al(III) salts, particularly, aluminium alkoxide (ethoxide) with similar accuracy (Fig. 1D and S12†). Therefore, the Al(III) sensing ability for an alcoholate corrosion with an aluminium alloy must not be perturbed due to the interference of other leached cations.

The dry alcoholate corrosion of aluminium or its alloy while forming soluble alkoxide ($Al(OR)_3$) can be detected upon incubation in an anhydrous alcoholic medium. However, under a condition of prolonged incubation, the contamination of trace amounts of moisture may also trigger the conversion of $Al(OR)_3$ to $Al(OH)_3$, followed by the hydrated alumina ($Al_2O_3 \cdot xH_2O$) coating on the metallic surface.[6] The formation of hydrated alumina can also be possible *via* the decomposition of $Al(OR)_3$.[6] To characterize the alcoholate corrosion as an exclusive process to the maximum limit, we minimized those wet-processes by allowing the corrosion under inert conditions. A previously grazed aluminium-sheet (dimension ~3.5 × 1.5 × 0.2 cm^3; surface area ~12.5 cm^2) was incubated for 18 days in 100 mL anhydrous methanol or methanol/ethanol (4 : 1) mixed solvent under nitrogen atmosphere by purging nitrogen every 24 h, where the small change in the solution volume if required was adjusted by injecting an appropriate amount of the nitrogen-saturated anhydrous solvent. The amount of $Al(OR)_3$ (R = -Me, -Et) generated in the medium was estimated by monitoring the HMBDC (5 μM) fluorescence. After 10-fold dilution of the medium with the parent solvent, the amount of $Al(OR)_3$ formed or the alcoholate corrosion was estimated in every 3 days interval according to the amount of Al^{3+} obtained from the time-dependent fluorescence responses (Fig. S13†) as per the linear calibration plots in Fig. 1C multiplied by the dilution factor. A linear increase in the normalized fluorescence intensity from ~3.5 to 16.8 and ~7.3 to 36.1 was observed with an increase in the incubation time period from 3 day to 18 day for methanol and methanol/ethanol (4 : 1) media (Fig. 3A and S13†), respectively, which correspond to the linear increase in the Al^{3+} amount in the medium from ~3.2 to 16.6 μmol for either solvents (Fig. 3C). Indeed, the weight-loss of ~0.47 mg *i.e.*, ~17.5 μmol was found to be closely similar with that of the increase in Al^{3+}, revealing that not only the dry corrosion leads to the generation of Al^{3+} ($Al(OR)_3$) as the only product, but also HMBDC is highly effective for an accurate estimation of the alcoholate corrosion. In addition, the nice correlation between the weight-loss and $Al(OR)_3$ amount also reveals that the decomposition of alkoxide into insoluble alumina is negligibly small during the whole corrosion time-course.

However, under open atmospheric conditions maintained by air purging (average relative humidity ~70%; average temperature 28 °C) in every 24 h interval while maintaining other similar experimental conditions and analysis protocol, the specific corrosion rate (~2.0 μg per day per cm^2) up to 12 days, was found to be closely similar to that detected under the nitrogen atmosphere (Fig. 3C and S13†). The results also indicate that the early stage of the alcoholate corrosion process (at least up to 12 days) for pure aluminium is not affected significantly by the atmospheric moisture content, although the final corrosion amount after 18 days incubation in normal atmosphere was slightly lower (~84%) for the mixed medium compared to that obtained for pure methanol (Fig. 3C). The decrease in the $Al(OR)_3$ amount can be affected by two

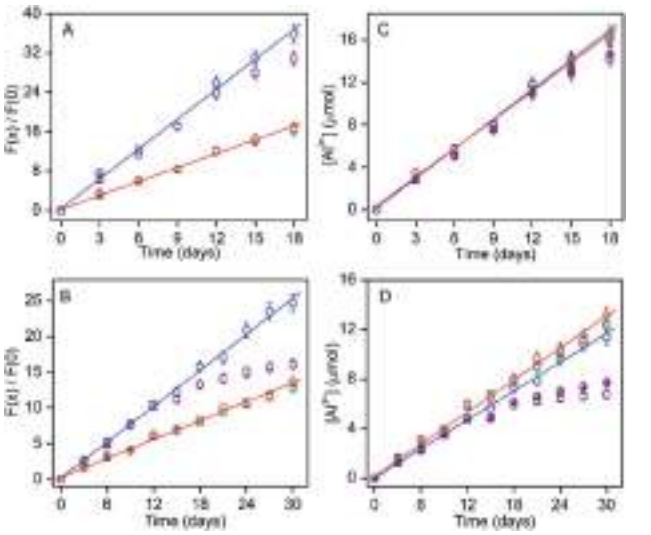

Fig. 3 (A and B) Extent of the fluorescence intensity increase due to corrosion-induced leached Al^{3+} ($F(x)/F(0)$) of HMBDC (5 μM) and (C and D) amount of Al^{3+} in the corrosion medium according to fluorescence response are plotted with various incubation times of pure aluminium sheet or its alloy (Al-7075) in different mediums/atmosphere conditions: nitrogen atmosphere in methanol (red) and methanol/ethanol (4 : 1) (blue); open atmosphere in methanol (green) and methanol/ethanol (4 : 1) (purple). The data at nitrogen conditions are only fitted linearly. (A and B) The fluorescence intensity of HMBDC (5 μM) were monitored after the 10-fold dilution of the corrosion medium with the same solvent. (C and D) The amount of Al^{3+} estimated as the amount obtained from the normalized intensity with comparing the linear plots in Fig. 1C multiplied by the dilution factor 10. The actual amount of alcoholate corrosions for the mixed medium under open atmosphere are depicted by solid circle (purple).

processes: (a) $Al(OR)_3$ to insoluble $Al(OH)_3$ conversion due to the adsorbed moisture; (b) actual retardation of the corrosion rate due to the surface deposition of $Al(OH)_3$. The extent of the conversion of $Al(OR)_3$ to $Al(OH)_3$ in the corrosion medium under the open air condition can be assessed by estimating the fluorescence intensity at every 3 day time interval in the absence of aluminium sheet (from day-3 to day-18) with the addition of same amount of $Al(OEt)_3$ (3.2, 5.7, 8.0, 11.7, 14.2 and 16.4 μmol (final added amount) at day 0 (beginning of day 1), 3, 9, 12 and 15, respectively, in 100 mL mixed medium) as that of the alkoxide amount detected due to the corrosion under nitrogen condition (Fig. S14†). In comparison to the actual added $Al(OEt)_3$, any decrease in the $Al(OEt)_3$ amount upon such incubation should be added with the corrosion induced formation of $Al(OR)_3$ amount under nitrogen condition for respective time interval to obtain the actual alcoholate corrosion. The actual corrosion was found to be slightly higher than that estimated from the corrosion-induced $Al(OR)_3$ formation (Fig. 3C, solid symbol). According to the LOD of Al^{3+}, the detection of the alcoholate corrosion amount as minimum as ~0.1 μg mL^{-1} can be possible by monitoring the fluorescence response of HMBDC.

Alcoholate corrosion in a widely used aluminium alloy, Al-7075 (composition: Al, 90%; Zn, 5.5%; Mg, 2.5%; Cu, 1.5 and Si, 0.5%) was also studied. The previously grazed alloy sheet with same dimension and surface area as that of the pure aluminium sheet was incubated in 100 mL anhydrous methanol or 4 : 1 methanol/ethanol under nitrogen as well as normal atmospheric conditions. The amount of the alcoholate corrosion in every 3 days interval up to 30 days was estimated by evaluating the fluorescence response of HMBDC (Fig. 3B and S15†). In comparison to the pure aluminium sheet, the increase in corrosion from ~1.5 to 4.0 μmol evaluated from the increase in the normalized fluorescence intensity (1.65 to 5.90 in methanol; 2.64 to 10.40 in methanol/ethanol (4 : 1) mixture) with the increase in the incubation time from day-3 to day-12 follows a similar linear relation regardless of the solvent compositions and atmospheric conditions (Fig. 3B and D), while the intrinsic rate of corrosion ~0.95 μg per day per cm^2 was more than 2-fold slower (Fig. 3C and D). The lower rate constant value for the alloy compared to pure aluminium indicates that the contamination of other metals in the alloy resists the early stage alcoholate corrosion process. However, under normal atmospheric condition, the corrosion amount *vs.* time relation deviates from the linearity after 12 days. Importantly, after 30 days of incubation, a large reduction in the $Al(OR)_3$ amount from ~11.38 to 6.64 μmol was estimated for the mixed medium, but the change was only from ~13.20 to ~12.33 μmol for pure methanol (Fig. 3D). By determining the hydration-induced conversion amount of $Al(OR)_3$ to $Al(OH)_3$ according to the procedure, as described before (Fig. S16†), the actual alcoholate corrosion was found to decrease from ~11.38 to 7.70 μmol by changing the condition from nitrogen to open atmosphere after 30 days (Fig. 3D, solid symbol). Our study reveals that in comparison to pure methanol, the formation of $Al(OH)_3$ under open atmospheric condition retards the alcoholate corrosion largely due to the presence of more hygroscopic ethanol.[15] The deposition of $Al_2O_3 \cdot xH_2O$ onto the alloy-surface is responsible for resisting the further alcoholate corrosion[6] (Fig. 3D). In fact, the generation of more surface pits owing to the higher extent of the alcoholate corrosion in methanol over the mixed medium was also detected by naked eye (Fig. S17†). The surface morphology in the SEM studies showed that the alloy surface was little bit smoother after the corrosion in the mixed medium (Fig. S18†), justifying our proposition for the surface deposition of $Al_2O_3 \cdot xH_2O$. On the other hand, cyclic voltammetric studies in the corrosion medium exposed to normal atmospheric conditions identified an irreversible cathodic peak at ~−0.7 V due to the formation of insoluble $Al(OH)_3$ in addition to the conversion from Al to Al^{3+}, but such irreversible peak was not observed for the medium exposed to nitrogen (Fig. S19†). Moreover, the formation of white gelatinous precipitate of $Al(OH)_3$ in the mixed medium was clearly visible by naked eye under normal atmospheric conditions (Fig. S17B†). All those results strongly support that the initiation of the wet-process by forming $Al(OH)_3$ inhibits the alcoholate corrosion rate.

In conclusion, a phenolic Schiff-base consisting of a coumarin unit as a fluorescent sensor for Al^{3+} operable only in the alcoholic medium is synthesized to monitor dry alcoholate corrosion. The photo-induced electron transfer process in the probe molecule exhibits Al^{3+} induced large increase of fluorescence intensity, lifted by its complexation with Al^{3+}, which was further stabilized by the coordination and H-bonding interaction with the solvent molecule. The alcohol specific complex formation and subsequent fluorescence generation was suitably tuned to monitor the alcoholate corrosion by fluorometrically estimating aluminium alkoxide formation with a sensitivity of ~10 μg L^{-1}. However, the simultaneous participation of small extent of the wet-process ($Al(OR)_3$ to $Al(OH)_3$ conversion) and its deposition in metal surface, particularly for the alloy, inhibits the dry alcoholate corrosion. The alloy specific detection of the early stage alcoholate corrosion is in progress to obtain suitable material useful as a biofuel container.

Conflicts of interest

There are no conflicts to declare.

Acknowledgements

This study is partially supported by UGC and government of West Bengal for financial support under RUSA 2.0 scheme (PPP; No: 5400-F(Y)). SR and RM acknowledge UGC for the SRF fellowship. Authors also acknowledge JU and MA College, for departmental facilities. We are thankful to Dr N. R. Singha (GCELT) for TGA studies.

Notes and references

1 (*a*) J. Xuan, D. Y. C. Leung, M. Ni and M. K. H. Leung, *Renew. Sustain. Energy Rev.*, 2009, **13**, 1301; (*b*) F. H. Shinya and Y. KenjiImou, *Bioresour. Technol.*, 2010, **101**, 109.

2 (*a*) L. Matejovsky, J. Macak, M. Pospisil, P. Baros, M. Stas and A. Krausova, *Energy Fuels*, 2017, **31**, 10880; (*b*) R. H. Borgwardt, *Ind. Eng. Chem. Res.*, 1998, **37**, 3760; (*c*) B. Shayan, S. M. Seyedpour, F. Ommi, S. H. Moosavy and

M. Alizadeh, *Int. J. Automot. Mech. Eng.*, 2011, **1**, 3; (*d*) J. H. Lunsford, *Catal. Today*, 2000, **63**, 165.

3 M. B. Çelik, B. Ozdalyan and F. Alkan, *Fuel*, 2011, **90**, 1591.

4 K. Wagner, K. Eppel, T. Troßmann and C. Berger, *Energy Mater. Mater. Sci. Eng. Energy Syst.*, 2008, **3**, 227.

5 K. Eppel, M. Scholz,T. Troßmann and C. Berger, *Proceedings: EUROCORR*, 2009, Nice, p. 9.

6 J. Linder, thesis on, Alcoholate corrosion of aluminium in ethanol blends, Master thesis, KTH Royal Institute of Technology, Div. Surface and Corrosion Science, Stockholm, 2012.

7 (*a*) P. B. L. Fregolente, M. R. Wolf Maciel and L. S. Oliveira, *Braz. J. Chem. Eng.*, 2015, **32**, 895; (*b*) S. K. Thangavelu, A. S. Ahmed and F. N. Ani, *Int. J. Energy Res.*, 2016, **40**, 1704.

8 (*a*) L. Kruger, F. Tuchscheerer, M. Mandel, S. Muller and S. Liebsch, *J. Mater. Sci.*, 2012, **47**, 2798; (*b*) O. Seri and Y. Kido, *Mater. Trans.*, 2009, **50**, 1433; (*c*) Corrosion resistance of aluminium and protective measures where appropriate, First Edition: 2011 © AFSA Compiled and published by the Aluminium Federation of South Africa; (*d*) G. R. Kramer, C. M. Mendez and A. E. Ares, *Mat. Res.*, 2018, **21**, 1.

9 (*a*) S. Das, Y. Sarkar, S. Mukherjee, J. Bandyopadhyay, S. Samanta, P. P. Parui and A. Ray, *Sens. Actuators, B*, 2015, **209**, 545; (*b*) P. P. Parui, A. Ray, S. Das, Y. Sarkar, T. Paul, S. Roy, R. Majumder and J. Bandyopadhyay, *New J. Chem.*, 2019, **43**, 3750; (*c*) P. A. Anna, P. Paul and W. R. David, *Anal. Chem.*, 1997, **69**, 1635.

10 (*a*) A. Gupta and N. Kumar, *RSC Adv.*, 2016, **6**, 106413; (*b*) Q. Jiang, M. Li, J. Song, Y. Yang, X. Xu, H. Xu and S. Wang, *RSC Adv.*, 2019, **9**, 10414; (*c*) H. L. Nguyen, N. Kumar, J.-F. Audibert, R. Ghesami, J.-P. Lefevre, M.-H. Ha-Thi, C. Mongin and I. Leray, *New J. Chem.*, 2019, **43**, 15302.

11 I. A. Finneran, P. B. Carroll, G. J. Mead and G. A. Blake, *Phys. Chem. Chem. Phys.*, 2016, **18**, 22565.

12 S. Sahana, S. Bose, S. K. Mukhopadhyay and P. K. Bharadwaj, *J. Lumin.*, 2016, **169**, 334.

13 (*a*) R. Casasnovas, M. Adrover, J. Ortega-Castro, J. Frau, J. Donoso and F. Muñoz, *J. Phys. Chem. B*, 2012, **116**, 10665; (*b*) B. Setner, M. Wierzbicka, L. Jerzykiewicz, M. Lisowski and Z. Szewczuk, *Org. Biomol. Chem.*, 2018, **16**, 825.

14 V. Thomsen, D. Schatzlein and D. Mercuro, *Spectroscopy*, 2003, **18**, 112.

15 B. Tan, P. Melius and P. Ziegler, *J. Chromatogr. Sci.*, 1982, **20**, 213.

Soft Matter

PAPER

View Article Online
View Journal | View Issue

Cite this: *Soft Matter*, 2020, **16**, 798

Protonation-induced pH increase at the triblock copolymer micelle interface for transient membrane permeability at neutral pH†

Yeasmin Sarkar,[a] Snigdha Roy,[a] Rini Majumder,[a] Sanju Das,[ab] Dixit V. Bhalani,[c] Ambarish Ray,[b] Suresh K. Jewrajka [c] and Partha Pratim Parui *[a]

Achieving controlled membrane permeability using pH-responsive block copolymers is crucial for selective intercellular uptake. We have shown that the pH at the triblock-copolymer micelle interface as compared to its bulk pH can help regulate membrane permeability. The pH-dependent acid/base equilibriums of two different interface-interacting pH probes were determined in order to measure the interfacial pH for a pH-responsive triblock copolymer (TBP) micelle under a wide range of bulk pH (4.5–9.0). According to ^{1}H NMR studies, both pH probes provided interfacial pH at a similar interfacial depth. We revealed that the protonation of the amine moiety at the micelle interface and the subsequent formation of a positive charge caused the interface to become relatively less acidic than that of the bulk as well as an increase in the bulk-to-interfacial pH deviation (ΔpH) from ~0.9 to 1.9 with bulk pH reducing from 8.0 to 4.5. From the ΔpH *vs.* interface and bulk pH plots, the apparent and intrinsic protonations or positive charge formation pK_a values for the micelle were estimated to be ~7.3 and 6.0, respectively. When the TBP micelle interacted with an anionic large unilamellar vesicle (LUV) of a binary lipid (neutral and anionic) system at the bulk pH of 7.0, fluorescence leakage studies revealed that the pH increase at the micelle interface from that of the LUV interface (pH ~ 5.5) made the micelle interface partially protonated/cationic, thereby exhibiting transient membrane permeability. Although the increasing interface protonation causes the interface to become relatively less acidic than the bulk at any bulk pH below 6.5, the pH increase at the micelle interface may not be sufficiently large to maintain the threshold for the amine-protonated condition for effecting transient leakage and therefore, a continuous leakage was observed due to the slow disruption of the lipid bilayer.

Received 18th May 2019,
Accepted 27th November 2019

DOI: 10.1039/c9sm01002e

rsc.li/soft-matter-journal

Introduction

Amphiphilic block copolymers have received enormous interest in the field of medical science because of their interesting solution properties. Polymers comprising hydrophilic and hydrophobic blocks spontaneously self-organize in an aqueous solution to form micelles or vesicles of different shapes and sizes.[1] The generation of membrane permeability by the interaction of a block copolymer system with a cellular membrane is crucial for targeted drug and gene delivery,[2–5] insertion of bioactive peptides,[6–8] intercellular uptake,[9] and antimicrobial activity.[10,11] However, controlling membrane permeability is difficult owing to the large flexibility and high elasticity of the lipid bilayers. Different antimicrobial peptides or block copolymers during their actions have shown to form uncontrolled lipid pores to leach out essential cellular constituents along with exhibiting high cytotoxicity.[12,13]

Formulating a suitable strategy that can not only affect the membrane properties, but also control membrane permeability by maintaining the bilayer structure intact is the ultimate aim to overcome major challenges in applied biochemical research. In the recent past, different stimuli-responsive copolymer systems have been used to generate transient chemical gates in a lipid bilayer by a change in the local physical (*e.g.*, temperature, light, ultrasonic, magnetic, and electrical) or chemical (*e.g.*, pH, polarity, redox, charge, and ionic strength) properties.[13–17] For example, Sebai *et al.* demonstrated UV-light-induced controlled membrane permeabilization in the presence of azobenzene-modified polymers.[15] Different types of graft copolymers, such as octyl-modified poly(acrylic acid),[16] poly(maleic acid) copolymers 4,[18] poly(styrene-*alt*-methacrylic acid) (PS-*alt*-MAA 3),[19] acrylamides,[20] or octadecyl-modified dextran[21] have been utilized to form transient lipid pores at the membrane surface. However, the design and

[a] *Department of Chemistry, Jadavpur University, Kolkata 700032, India. E-mail: parthaparui@yahoo.com; Fax: +91-33-24146223; Tel: +91-9433490492*
[b] *Department of Chemistry, Maulana Azad College, Kolkata 700013, India*
[c] *Membrane Science and Separation Technology Division, CSIR-Central Salt and Marine Chemicals Research Institute, Bhavnagar 364002, India*

† Electronic supplementary information (ESI) available. See DOI: 10.1039/c9sm01002e

development of a pH-responsive amphiphilic block copolymer system with the capacity to generate transient lipid pores can be advantageous using the variations in biological pH from ~7.4 (extracellular environment) to 5.5–6.5 (inside the endosome). It has been shown that the binding of amphiphilic acrylic copolymers at the surface of a lipid membrane generates well-defined pores when they are partly neutralized under the mildly acidic condition.[20] On the other hand, intense research efforts have been directed toward developing a variety of pH-responsive block copolymers. However, their interaction mechanism with lipid membranes is still unexplored. It has been reported that hydrophobic poly(L-histidine) with pendant imidazole groups at neutral pH exhibits hydrophilic and cationic characteristics in acidic environments, which may be used to target tumor tissues and intracellular endocytic vesicles.[4,5,22] Recently, Nutan *et al.* synthesized poly(caprolactone)–poly(ethylene glycol) multiblock copolymers that formed stable micelles under physiological pH, whereas the micelle readily disintegrated due to protonation even under a weakly acidic condition.[23] The pH-dependent protonation of acetal-, ketal-, or amido-residue-containing copolymeric systems,[24–28] as well as the subsequent formation of positive charges, may significantly perturb membrane stability, eventually generating lipid pores even under a mildly acidic condition.

By utilizing an interface-interacting pH probe, we recently observed that pH at the self-assembled interface is different than the bulk pH.[29–31] A change in equilibrium between two different pH-dependent molecular forms of a pH probe at the interface from that of the bulk can be evaluated to estimate the interfacial pH and its deviation from bulk pH (ΔpH). We have shown that the interfacial pH for a charged self-assembled micelle or membrane is substantially different as compared to that for bulk pH. Depending on the self-assembled composition/nature and interfacial charge properties, a large pH deviation of 1.5–3.0 units at the interface than that of the bulk phase has already been reported by us.[29–31] As the pH at the micelle or membrane interface is different from that of the bulk medium,[29–33] a definite pH change and therefore a change in the charge properties at the micelle interface may occur during its interaction with the membrane. Therefore, the local pH at a polymeric micelle interface as well as the micelle-localized membrane surface, rather than the exterior bulk pH, can critically regulate the protonation process of hydrophilic residues at the micelle interface. Changes in the interface protonation or pH can result in the fine-tuning of the interaction between the polymer micelle and membrane bilayer, which can be exploited to control the membrane permeability for an optimal period of time without disrupting the lipid bilayer structure. However, no investigation has ever been reported to identify the correlation between pH and protonation at the polymeric micelle interface and its effect on transient membrane permeability.

Herein, we measured the interfacial pH and ΔpH for a pH-responsive triblock copolymer (TBP),[34] namely, a PDMA-*b*-PMMA-*b*-PDMA [PDMA = poly(2-dimethylaminoethyl)methacrylate; PMMA = poly(methyl methacrylate)] micelle system under a wide range of bulk pH (from 4.5 to 9.0), where PMMA and PDMA form the hydrophobic core and hydrophilic shell, respectively. With an increase in the extent of DMA protonation in the PDMA block with a decrease in bulk pH, the pH at the interface was found to be increasingly basic from ~0.9 to 1.9 as compared to the respective bulk pH due to an equivalent increase in the interfacial cationic charges. From the ΔpH *vs.* interface and bulk pH plots, the apparent and intrinsic protonation/positive charge formation (pK_a) for the PDMA block were estimated to be ~6.0 and 7.3, respectively. When the polymeric micelle interacted with an acidic interface (pH ~ 5.5) of the anionic membrane loaded with dye molecules at bulk pH of ~7.0,[31] an increase in pH at the micelle interface as compared to that at the membrane interface induced PDMA block to become protonated and partially cationic, thereby exhibiting time-limited transient membrane permeability with dye leakage of up to ~48%. However, at any bulk pH below 6.5, the increase in protonation and positive charge formation induce large membrane instability, presumably due to the formation of strong electrostatic interactions; further, an uncontrolled and continuous leaky characteristic was observed until all the dye molecules were released. Our results suggest that the interfacial pH plays a significant role in controlling the protonation of a basic amine group at the micelle interface toward its transient permeability for anionic membranes.

Experimental

General experimental procedures

1,2-Dioleoyl-*sn-glycero*-3-phosphocholine (DOPC), 1,2-dimyristoyl-*sn-glycero*-3-phosphorylglycerol (DMPG) sodium salt, and 1,2-dimyristoyl-*sn-glycero*-3-phosphocholine (DMPC) were procured from Avanti Polar Lipids (USA). The solvents and other reagents (analytical GR grade), unless otherwise mentioned, were purchased from Sigma-Aldrich (USA) and used as received. Milli-Q water (Millipore) (conductivity: 18.2 MΩ cm) was used to prepare the various buffer solutions for the spectroscopic studies. Different 10 mM buffer compositions were used to attain specific pH: citric acid/Na_2HPO_4 for pH 2.5–6.0, HEPES–NaOH for pH 6.0–7.5, Tris–HCl for 7.0–9.0, and sodium carbonate/sodium bicarbonate for 9.0–12.0. The pH of the buffer solution was determined using a SYSTRONICS digital pH meter (model no.: 335); either ~1.0 M NaOH or 1.0 M HCl solution was used for fine-tuning the pH. Sufficient pH probes were added into the buffer solution containing TBP or q-TBP, with the addition of either 0.1 M NaOH or 0.1 M HCl to adjust the desired pH, if required. The dielectric constant of the mixed solvent medium was determined as reported earlier.[35,36] Further, ^{1}H NMR investigation was performed in various media with Bruker 300, 400, or 600 MHz NMR instruments, where tetramethylsilane (0 ppm) was considered to be the internal standard. The average particle sizes for polymeric micelles and lipid vesicles were determined by dynamic light scattering (DLS) measurements with the Zetasizer Nano ZS (Malvern Instruments). Differential scanning calorimetry (DSC) measurements were carried out using a Malvern MicroCal VP-DSC calorimeter. For performing the Langmuir–Blodgett (LB) experiment, a Teflon-bar-barrier-type LB trough (model: LB2007DC; Apex Instruments Co., India) was used. Cryo-transmitted

electron microscopy (TEM) experiments were performed with a FEI Tecnai F20 electron microscope equipped with Gatan K2 Summit direct detection device.

Synthesis of TBPs

A neutral TBP comprising poly(methyl methacrylate) (PMMA) middle block and two poly(2-dimethylaminoethyl) methacrylate (PDMA) terminal blocks (molecular weight, M_n = ~25 kD; dispersity: 1.28) was synthesized by a two-step atom transfer radical polymerization process, as reported earlier (Fig. S1, ESI†).[37] The tertiary amino groups in the PDMA were quaternized by excess butyl bromide to yield the corresponding cationic copolymer (q-TBP) (Fig. S2, ESI†).

Synthesis of pH probes

Here, pH probes, namely, monofunctional phenolic-aldimine appended to the triazole-unit-containing Schiff base molecule (MSB),[29] and a polarity-indicating probe, *i.e.*, 2-((2-(pyridine-2-yl)ethylimino)methyl)-6-(hydroxymethyl)-4-methylphenol (PMP),[38] were prepared according to procedures reported earlier. The purity of each compound was verified from the ^{1}H NMR spectra (Fig. S3 and S4, ESI†). For the synthesis of the bifunctional molecule (DSB), *p*-cresol and 4-amino-4*H*-1,2,4-triazole (analytical grade) were used as received without further purification. Further, 4-methyl-2,6-diformyl phenol (DFC) was synthesized starting from *p*-cresol, as stated elsewhere.[39] A methanolic solution of DFC (0.328 g, 2 mmol) and 4-amino-4*H*-1,2,4-triazole (0.336 g, 4 mmol) was added dropwise under constant stirring; thereafter, 0.1 mL AcOH was added to this mixture. The reaction mixture was refluxed for 3 h and then filtered. The filtrate was then evaporated under reduced pressure to afford the crude product, which was purified by column chromatography followed by rotary evaporation to obtain the pure product and dried over $CaCl_2$ *in vacuo*, affording a yield of ~65.0% with respect to DFC. The structural analyses were performed by ^{1}H NMR measurements (Fig. S5, ESI†). ^{1}H NMR (DMSO-d_6, 300 MHz): chemical shift (ppm) = 2.30 (s, 3H, Ar-CH_3), 7.79 (s, 2H, Ar-H), 9.17 (d, 6H, imine-2H and triazole-4H).

Preparation of polymeric micelle solution

PDMA-*b*-PMMA-*b*-PDMA (TBP) or its *N*-alkylated analogue cationic qPDMA$^+$-*b*-PMMA-*b*-qPDMA$^+$ (q-TBP) (50 mg) was dissolved in DMF (1.5 mL), and the solution was added dropwise in 10 mL water under constant stirring. To obtain the TBP/q-TBP micelle solution, the resulting mixture was dialyzed (MW cutoff: ~1000 Da) against water for 48 h; the water was exchanged in intervals of 6 h. By using the surface tension method, the critical micellar concentration (cmc) was estimated to be ~0.040–0.045 g L^{-1} for TBP and q-TBP at neutral pH (Fig. S6, ESI†). Further, we performed DLS measurements at various pH values (4.5–9.0) in the absence and presence of the probes; micelle sizes were determined to be ~10–11 nm (Fig. S7, ESI†). Similar micelle sizes were also confirmed from the cryo-TEM studies (Fig. S8, ESI†).

Large unilamellar vesicle (LUV) preparation

Different lipid mixtures were solubilized in 1.0 mL chloroform in a round-bottom flask. By using a rotary evaporator, chloroform was removed to form a lipid film on the wall of the flask. Any residual chloroform was removed *in vacuo* for 3 h. The lipid film was hydrated at a particular amount of 10 mM buffer solution in the absence and presence of 80 mM calcein at 40 °C. For the complete dissolution of lipids, the solution was vortexed for 2 min. Five cycles of freeze-and-thaw were carried out from −196 to 50 °C to obtain giant multilamellar vesicles (GMVs). To obtain LUVs, the liposome dispersion was extruded 15 times through a polycarbonate membrane (pore size: 100 nm) with a Mini-Extruder instrument (Avanti Polar Lipids, USA). The free calcein was removed by gel filtration by using Sepharose CL-4B. The dye encapsulation in the LUVs was confirmed from the ~5–6-fold increase in fluorescence intensity by disrupting the LUVs in the presence of 10 mM TX-100. For spectroscopic measurements, the LUV solutions were diluted with a certain amount of buffer solution. The LUV particle sizes (~100 nm) were determined from the DLS and cryo-TEM measurements (Fig. S7 and S8, ESI†).

UV-vis absorption and fluorescence studies

The UV-vis absorption and fluorescence measurements were carried out at 25 °C with a UV-2450 spectrophotometer (Shimadzu, Japan) and a PerkinElmer LS-55 spectrofluorometer (PerkinElmer, USA), respectively, and quartz cells (path length: 10 mm) were used for both these measurements.

A calcein-encapsulated LUV solution was diluted to 50 μM (total lipid) in 10 mM buffer, pH 6.0–7.5, containing a certain concentration of glucose in order to maintain similar osmotic pressures on both the inside and outside of the vesicle measured using a vapor pressure osmometer (VAPRO 5520, Germany) and adjusted to ~200 mM kg^{-1}. To remove the dissolved oxygen from the buffer, nitrogen was purged in the buffer for ~1 h. Further, 20 μL TBP or q-TBP stock solution (final concentration: 0.05 g dm^{-3}) was injected in 2 mL of a solution containing DOPC : DMPC (1 : 1) or DOPC : DMPG (1 : 1) LUV (50 μM, total lipid) in the buffer at 25 °C under constant stirring (speed: ~130 rpm) with a small bar magnet to obtain the time-dependent fluorescence leakage profile. The TBP/q-TBP-induced time curve of the fluorescence leakage ($L(t)$) was estimated by the equation $L(t) = (I_x - I_0)/(I_{max} - I_0)$, where I_0 and I_x represent the fluorescence intensities before and after the addition of TBP/q-TBP at different times, respectively, whereas the intense increase in the TX-100-micelle-induced fluorescence intensity of LUV is denoted by F_{max}.

Results and discussion

Probes to measure interfacial pH

Two different interface-interacting pH-sensing molecules were employed to measure the interfacial pH under a wide range of bulk pH values from 4.5 to 9.0 for triblock polymeric micelle systems (TBP and q-TBP) for various interfacial charges. The pH probe, comprising a MSB[29] and DSB, exhibit pH-dependent equilibrium between the corresponding protonated phenol form (p-MSB or p-DSB) and deprotonated phenolate form (d-MSB or d-DSB) (Fig. 1A). The similar chemical functionalities of MSB and DSB are purposefully chosen to obtain synchronized interfacial

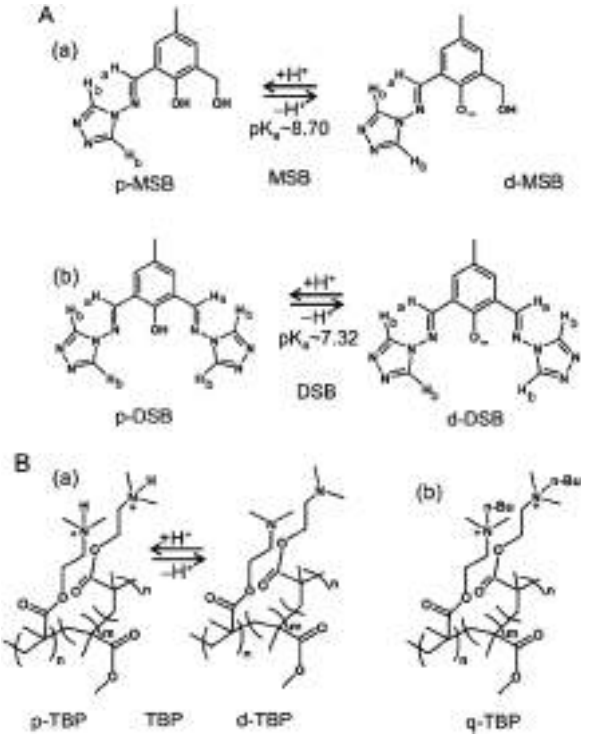

Fig. 1 (A) pH-Dependent equilibriums between the two molecular forms of different pH probe molecules: (a) DSB and (b) MSB (labeled protons in (a and b) were monitored by ^{1}H NMR, as shown in Fig. 2). (B) TBPs: (a) protonated form (p-TBP) and deprotonated form (d-TBP) of PDMA-*b*-PMMA-*b*-PDMA (TBP) and (b) the corresponding *N*-alkylated compound, qPDMA$^+$-*b*-PMMA-*b*-qPDMA$^+$ (q-TBP).

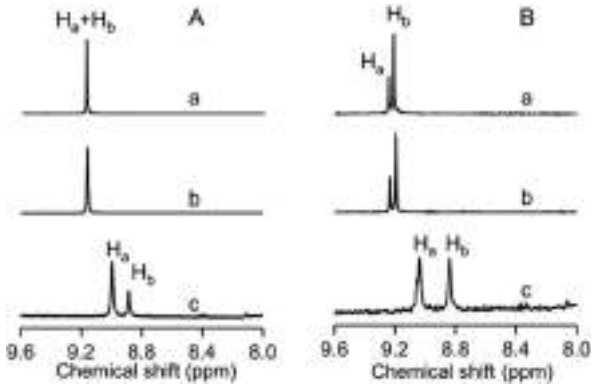

Fig. 2 400 MHz ^{1}H NMR spectra (downfield region) of (A) MSB (2 mM) and (B) DSB (2 mM) in different solvent systems in the presence or absence of TBP/q-TBP at 25 °C: (A, B): (a) DMSO-d_6; (b) DMSO-d_6 and the presence of 1 equiv. NaOH (with respect to MSB or DSB); (A (c)) q-TBP micelle (15 g dm^{-3}) solution in D_2O for pD: ~8.5; (B (c)) TBP micelle (15 g L^{-1}) solution in D_2O for pD: ~6.2. (A and B) Imine and triazole protons for MSB and DSB are labeled as H_a and H_b (as shown in Fig. 1), respectively.

pH values at a similar interfacial depth under a wide range of bulk pH (4.5–9.0). According to the UV-vis absorption studies, mono- to bifunctional substitution caused a large decrease in the phenol-to-phenolate pK_a interconversion from 8.7 to 7.1 (Fig. S9, ESI†), which is useful to measure the interfacial pH at relatively low bulk pH values. Presumably, more extended π-conjugation in the chromophore unit of DSB than that in MSB is responsible for the decrease in protonation pK_a from MSB to DSB.

Interaction between pH probes and TBP and q-TBP micelles

Recently, we reported that phenolic Schiff base molecules containing triazole moieties are highly susceptible to interactions with the water-exposed Stern layer of the micelle interface.[29,38] Here, ^{1}H NMR becomes an effective tool to monitor the probe-localized depth within the self-assembled interface.[40,41] Amphiphilic self-assembly exhibits significant differences in polarities or electrical charge properties along various cross-sectional depths from the water-exposed Stern layer to the inner hydrocarbon region. Since the proton chemical shift is highly dependent on environmental charge characteristics and polarity parameters, the probe-binding location at the interface can be assigned from a change in the chemical shift values induced by the amphiphilic systems. To eliminate the bulk phase contribution in the observed changes, a large ratio of amphiphilic molecules to probe concentrations is used to ensure that almost all the probe molecules interact with the amphiphilic systems.

With ^{1}H NMR studies, the proton chemical shifts in triazole moieties in DSB and MSB were investigated to identify the probe-localized depth within the TBP/q-TBP micelle interface. Two closely spaced proton peaks were observed at 9.24 ppm (imine proton) and 9.17 ppm (triazole proton) for DSB, and their overlapping peaks were observed at 9.17 ppm for MSB shifted upfield by a small amount (~0.07 ppm for DSB-triazole; ~0.10 ppm for MSB-triazole) by changing the solvent from DMSO-d_6 to MeOD$_4$, presumably due to a change in the solvent polarity (Fig. S10, ESI†). However, the chemical shift did not change by the addition of NaOH (1 equiv. with respect to MSB/DSB) in DMSO-d_6 (Fig. 2), suggesting that the chemical shifts in the imine or triazole protons for MSB or DSB were unaffected due to the conversion of the molecular form from phenol to phenolate. Since the interfacial dielectric constant for the TBP or q-TBP micelle (~52) is close to that of DMSO-d_6 (~47) (as shown in the subsequent section), the proton chemical shifts are compared between the D_2O medium containing TBP/q-TBP micelles and DMSO-d_6 medium in the absence of a polymer to determine the probe-localize depth within the interface. When MSB interacted with cationic q-TBP micelles containing 1 equiv. NaOH (with respect to MSB), overlapping peaks for imine and triazole protons observed in DMSO-d_6 were split, and the peak of the triazole proton as compared to that of the imine proton shifted toward the more upfield region by an amount of 0.35 ppm (from 9.17 to ~8.82 ppm; Fig. 2). Almost a similar magnitude of upfield chemical shift of ~0.33 ppm (from 9.17 to 8.84 ppm) for the triazole proton of DSB was also detected in the TBP-containing D_2O medium at pH 6.2 (Fig. 2), where TBP existed as a mixture of protonated (cationic) and deprotonated (neutral) forms and that of DSB as a mixture of protonated (neutral) and deprotonated (anionic) forms, as shown in the subsequent section. These results demonstrate that a strong as well as similar cationic charge field surrounds both MSB and DSB, which can also justify that both MSB and DSB are localized at the outer interfacial region of the micelle

(Stern layer). Therefore, the interfacial pH and its deviation from the bulk phase (ΔpH) at a similar interfacial depth can be obtained from two different pH probes (MSB and DSB).

The difference in the acid/base equilibriums for the probe molecules at the interface and in bulk can be evaluated from the UV-vis absorption spectra. The pH difference from the bulk to the interface and subsequently the interfacial pH under different bulk pH conditions can be measured from the apparent pH shift in the acid/base equilibriums of the probe molecules, while considering the polarity-induced change in the equilibriums between the micelle interface and bulk phase.

PDMA-*b*-PMMA-*b*-PDMA (TBP) and the corresponding amine-quaternized qPDMA$^+$-*b*-PMMA-*b*-qPDMA$^+$ (q-TBP) form a core–shell-type micelle in an aqueous solution (Fig. 1B). The water/oil-separating interface shells comprise hydrophilic neutral PDMA or cationic qPDMA$^+$ blocks, where the amine or *N*-alkylated amine and ester residues are directed to the bulk aqueous phase, and hydrophobic PMMA units constitute the nonpolar micelle core. Here, d-MSB and d-DSB exhibit absorbances in the visible region (d-MSB: ~410 nm; d-DSB: ~440 nm), whereas the corresponding p-MSB and p-DSB do not exhibit these absorbances (Fig. 3). The visible absorption intensities for DSB (5.0 μM) at pH 5.5 or MSB (5.0 μM) at pH 8.0 get progressively enhanced with an increase in the TBP micelle concentration (0.0–1.0 g dm^{-3}) (Fig. S11, ESI†), indicating that the probe molecules not only interact with the interface, but their acid/base equilibrium ratio at the micelle interface is different from that of the bulk phase. Similarly, the UV-vis absorption spectra of the probe molecules in the presence of various concentrations of q-TBP micelles (0.0–1.0 g dm^{-3}) were also monitored (Fig. S12, ESI†). Irrespective of the different pH probes used, the saturations of the absorbance intensity were observed above TBP or q-TBP micelle concentration of 0.9–1.0 g dm^{-3} (Fig. S11 and S12, ESI†), where the intensity saturation indicated that nearly all the probe molecules interacted with the micelle interface. Therefore, further spectral studies were performed under saturated micelle concentrations to determine the acid/base equilibriums for the interface-interacting probe molecules. However, the relatively low cmc value for TBP/q-TBP micelles (~0.04 g dm^{-3}) did not allow us to monitor the interaction of the probe molecule (ε: ~10^{-4} M^{-1} cm^{-1}) with the polymer under the condition of less than cmc concentration by maintaining the aforesaid intensity-saturated high polymer–probe concentration ratio.

Determination of interfacial pH and its deviation from bulk pH (ΔpH) for TBP/q-TBP micelles

It has been reported that the amine moieties in PDMA blocks are highly susceptible to accept a proton even under neutral bulk pH values.[42] However, an accurate estimation of the amine protonation pH or pK_a for PDMA in TBP micelles is not possible by monitoring the bulk-pH-dependent acid/base equilibriums of the probe molecules by performing the usual pH-metric titration because the pH at the micelle interface is different from the bulk pH.[29,31] The interfacial pH values for different

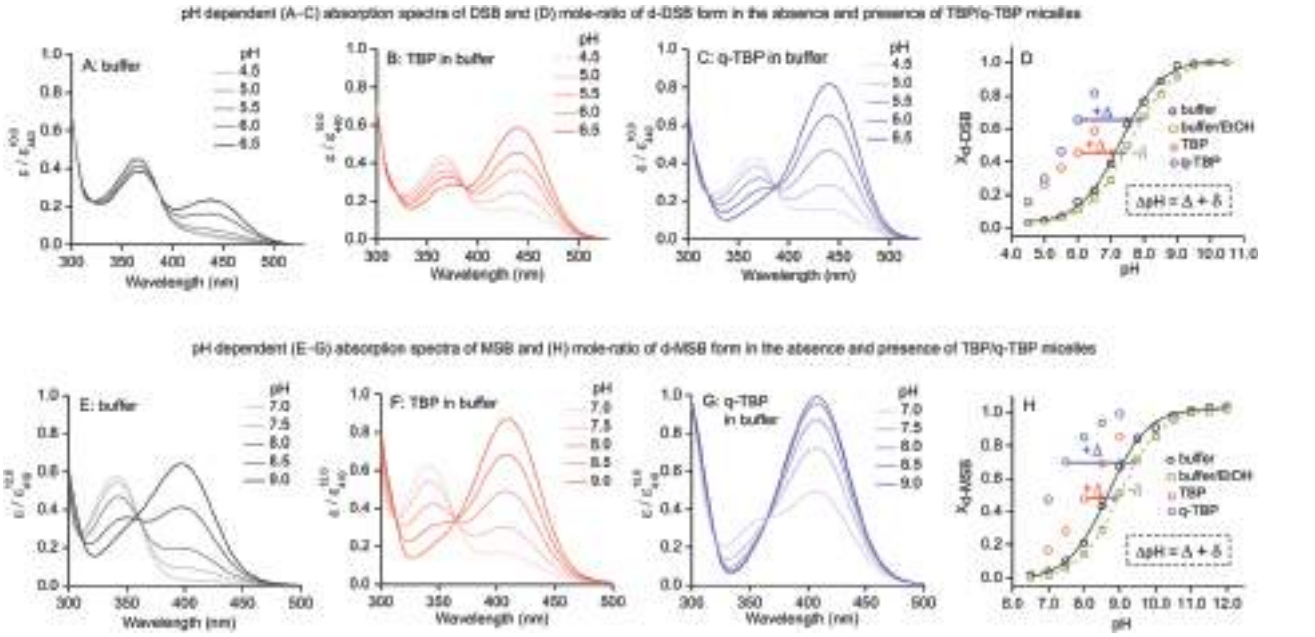

Fig. 3 UV-vis absorption spectra of (A–C) DSB (5.0 μM) and (E–H) MSB (5.0 μM) in the absence and presence of intensity-saturated concentrations of TBP or q-TBP (1.0 g dm^{-3}) at various bulk pH values. Each spectrum is normalized by dividing with the corresponding intensity at intensity-saturated pH value at the maximum absorption wavelength (λ_{max}). (A–C) pH 10.0 and λ_{max}: 440 nm for DSB; (E–G) pH 11.5 and λ_{max}: 410 nm for MSB. (D and H) Bulk-pH-dependent mole fraction (X) of d-DSB and d-MSB in the absence and presence of the intensity-saturated concentration (1.0 g dm^{-3}) of TBP/q-TBP micelles are plotted against different bulk pH values, respectively. The molar ratio plots in 40 wt% ethanol-containing buffer without polymer are also shown. The solid or broken lines represent the least-square fitted curves of the plots with a sigmoidal-Boltzmann equation. (D and H) TPB/q-TBP and apparent pH shift induced by ethanol (40% (w/w)) are depicted by Δ and δ, respectively. The expression for the estimation of pH deviation from the bulk to the interface (ΔpH) are shown by the dashed boxes.

extents of amine protonations for PDMA blocks were measured to estimate the actual amine protonation pH or pK_a for TBP micelles. The UV-vis absorption spectra of DSB and MSB in the absence and presence of intensity-saturated concentrations of TBP micelles were monitored at various ranges of bulk pH values (4.5–10.0 and 6.5–12.0, respectively; Fig. 3 and Fig. S13, ESI†). In addition, the interfacial pH values for cationic q-TBP micelles for all the bulk pH conditions were estimated to elucidate the role of positive interfacial charges on pH deviation from the bulk to the interface (ΔpH) (Fig. 3 and Fig. S14, ESI†). In the presence of TBP-micelle-interacting-saturated concentration ($\sim$1.0 g dm^{-3}), the absorption intensities at 440 nm for DSB (5 μM) and 410 nm for MSB (5 μM) increased progressively with the bulk pH until the intensity saturated at above pH $\sim$10.0 for MSB and pH $\sim$8.0 for DSB. Similarly, the pH-dependent UV-vis spectra for these probe molecules were also measured in the presence of q-TBP micelle-interacting saturated conditions (Fig. S12, ESI†). In the absence of TBP or q-TBP micelles, the pH-saturated intensities were observed at bulk pH $\sim$9.5 and $\sim$11.0 for DSB and MSB, respectively (Fig. S14, ESI†). The pH-saturated intensities in the absence or presence of TBP/q-TBP micelles (1 g dm^{-3}) justified the fact that p-MSB and p-DSB were completely converted into d-MSB and d-DSB, respectively (Fig. 1A). The pH-dependent absorption intensities in the absence or presence of micelle-interacting saturated conditions were normalized by dividing the spectra with the maximum intensity of the corresponding pH-saturated spectra, and d-MSB and d-DSB molar ratios for the respective probe molecules were determined from the corresponding intensities of the normalized spectra (Fig. 3). The bulk-pH-dependent normalized absorption spectra of MSB/DSB (Fig. 3) reveal that the intensities of the deprotonated forms (d-DSB or d-MSB) significantly increase when all the probe molecules were localized at the interface upon the addition of interaction-saturated concentrations of TBP or q-TBP micelles (Fig. 3). As the bulk pH increased from 4.5 to 7.0, the normalized absorbances of DSB increased from 0.16 to 0.59 and from 0.16 to 0.82 for TBP and q-TBP, respectively (Fig. 3(A)–(D)). On further increase in the bulk pH from 8.0 to 9.0, the intensity at 410 nm for MSB increased from 0.16 to 0.86 for TBP and 0.49 to 1.0 for q-TBP (Fig. 3(E)–(H)). The increased deprotonations for DSB and MSB at the micelle interface as compared to that at the bulk phase is correlated with a pH increase at the interface than the bulk pH.

The difference in the protonation/deprotonation equilibriums of the probe molecules between the interface and bulk phase was estimated in order to measure the interfacial pH values for TBP/q-TBP micelles. It is noteworthy that the large ratio of TBP or q-TBP (1 g dm^{-3}) to the probe (5 μM) required to induce intensity saturation suggests that the probe molecules non-specifically interact with the micelle interface. The intensity-saturated TBP/q-TBP micelle concentration (1 g dm^{-3}) induced an apparent pH shift from the pH at the micelle interface to the bulk medium (Δ = the apparent pH difference between red (TBP micelle) or blue (q-TBP micelle) points and the corresponding point on the solid black curve shown in Fig. 3D and H) is related to the difference in the equilibrium molar ratio at the interface and in the bulk. By evaluating Δ from the plots of molar ratios of the deprotonated form of the probe (DSB/MSB) *vs.* bulk pH, interfacial pH under various bulk pH values were obtained (Fig. 3D and H). A positive value of Δ due to an increase in the deprotonation of the probe upon the addition of micelles (Fig. 3(A)–(C) and (E)–(G)) corresponds to a higher pH value at the interface than that at the bulk. However, the protonation/deprotonation equilibriums of the probe molecules is not only affected by the probe-localized environmental pH, but also depends on local polarity (Fig. S15, ESI†). Since the polarity at the interface is lower than that of the bulk phase, Δ should incorporate the contributions of both pH and polarity differences between the interface and bulk. By estimating the difference in pK_a between the buffer and buffer/ethanol mixture with a similar dielectric constant (κ) as that of the micellar interface, the contribution of interface polarity affected the apparent pH shift, which was defined as the polarity correction factor (δ) (the pH difference between the dark yellow and black curves, as shown in Fig. 3D and H), was estimated as Δ. Similar κ values ($\sim$52–53) for TBP and q-TBP micelles were estimated by using a probe for detecting interface polarity (PMP)[39] (Fig. S15, ESI†) and therefore κ is expected to remain unchanged due to a change in the positive interfacial charges upon being subjected to various extents of PDMA protonation in TBP micelles. Notably, the higher extent of PDMA protonation for TBP with a decrease in bulk pH from 6.5 to 4.5 causes an increase in the magnitude of Δ from 0.6 to 1.6 (Fig. 3D). Regardless of the bulk pH, almost a constant value of δ was estimated for MSB and DSB (~ -0.30 and -0.34, respectively) by comparing the respective pH-metric titration curves between the buffer and 40% (w/w) ethanol/buffer mixture with similar dielectric constants as those at the micelle interface (Fig. 3D and H (dark yellow curve)). Therefore, the increase in Δ upon a decrease in bulk pH for TBP micelles directly reflects the higher pH deviation from the bulk to the interface (ΔpH). Notably, Δ for TBP micelles under completely protonated conditions was found to be similar to that of q-TBP micelles (Fig. 3D), revealing that the formation of positive charges makes the interface less acidic (more basic) than the corresponding bulk.

However, the pH at the micelle interface (pH_i) at a certain bulk pH (pH_b) can be quantitatively estimated from the following equations:[29,31]

$$\Delta pH = pH_i - pH_b = \Delta - \delta \quad (1)$$

$$pH_i = pH_b + \Delta - \delta \quad (2)$$

The estimated values of interfacial pH and ΔpH under different bulk pH values calculated as per eqn (1) and (2) are listed in Table 1. For TBP micelles, ΔpH of $\sim$0.9 at pH 8.0 was found to gradually increase with a decrease in bulk pH until reaching saturation (ΔpH $\sim$ 1.9) at pH below 4.5 (Table 1). Interestingly, the magnitude of ΔpH at pH below 4.5 for TBP micelles remained almost constant, which is similar to that of cationic q-TBP micelles (ΔpH: $\sim$1.9) for the entire range of bulk pH under consideration (4.5–9.0) (Table 1).

Table 1 pH deviation from the bulk to the interface (ΔpH) and interfacial pH (pH_i) for TBP micelles for different bulk pH values (pH_b) at 25 °C[a]

	TBP		q-TBP	
pH_b	ΔpH	pH_i	ΔpH	pH_i
4.5	1.89	6.39	1.92	6.42
5.0	1.82	6.82	1.94	6.94
5.5	1.66	7.16	1.94	7.44
6.0	1.42	7.42	1.93	7.93
6.5	1.26	7.76	1.93	8.43
7.0	1.1	7.96	1.94	8.94
7.5	0.98	8.48	1.98	9.49
8.0	0.94	8.94	1.97	9.97
8.5	0.93	9.43	1.91	10.36
9.0	0.92	9.92	1.93	10.93

[a] pH_i and ΔpH under different pH_b values were estimated using different probe molecules: DSB for pH_b 4.5–6.5 and MSB for pH_b 7.0–9.0.

The quaternized amine-containing cationic $qPDMA^+$ unit in q-TBP is not involved in the protonation/deprotonation reaction with the buffer medium and remains cationic at any bulk pH (4.5–9.0), whereas the DMA group in the PDMA blocks for TBP accepts protons at an acidic pH to generate positive interfacial charges. However, when the PDMA unit in TBP becomes completely protonated exhibiting similar surface charge as that of q-TBP micelles, a similar value of Δ (~1.6) or ΔpH (~1.9) could be determined upon the addition of TBP or q-TBP under identical bulk pH (4.5) (Fig. 3D). This result suggests that the protonation of PDMA does not affect the acid/base equilibriums of the probe molecules upon the addition of TBP; in fact, the increased amount of positive interfacial charges and subsequent pH increase at the micelle interface is responsible for this. For a cationic micelle interface, the interfacial charge character may change the distribution of H^+ and OH^- concentrations between the interface and bulk. The cationic charges at the micelle interface may involve electrostatic interactions with the negatively charged OH^- ions, whereas it repels the positively charged H^+ ions (Scheme 1). The concentrations of H^+ and OH^- may decrease and increase at the interface as compared to those in the bulk phase, respectively, and the decrease in H^+ concentration at the interface may increase the pH at the micelle interface, whereas the concentrations of H^+ and OH^- and subsequently the bulk pH do not change due to the large volume of the bulk phase (Scheme 1).

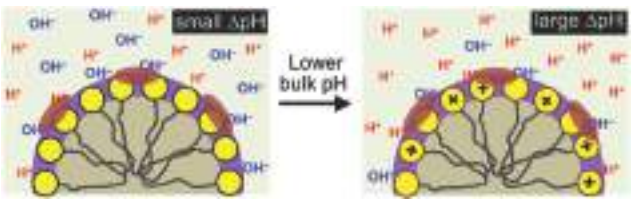

Scheme 1 Schematic representation of the pH-dependent H^+ and OH^- concentrations at the interface of TBP micelles (yellow: hydrophilic PDMA block; violet: Stern layer). Changes in the charge characteristics of the PDMA blocks from neutral (left) to partially cationic (right) and subsequent variations in the interface H^+ and OH^- concentrations and pH deviation from the bulk to the interface (ΔpH) due to pH-dependent protonation of PDMA unit in TBP are shown. The interface-localized probe molecules are depicted in brown color.

Relationship between ΔpH with interface protonation or positive charge formation for TBP micelles

As the increased amine protonation in the PDMA-*block*-dependent higher cationic charge generation at the TBP micelle interface increases the magnitude of ΔpH, the ΔpH values of ~0.9 and 1.9 can be associated with entirely deprotonated (neutral) and entirely protonated (cationic) PDMA blocks, respectively. The ΔpH values were plotted with bulk pH, which exhibited a sigmoidal fit to yield the PDMA protonation curve for TBP micelles at various pH conditions (Fig. 4). The transition midpoint of the fitted curve represents the protonation pK_a. Since the protonation of PDMA was evaluated in terms of bulk pH, the obtained pK_a considered as the apparent pK_a was estimated to be ~6.0 (Fig. 4, blue curve). Alternatively, applying the usual acid/base titration method, a similar value of the apparent protonation pK_a of ~6.2 was determined by measuring the pH of the aqueous micelle solution containing 50 mol% HCl with respect to the total amine groups for the PDMA blocks. The similar apparent pK_a values between those two different procedures strongly justify that the increase in amine protonation to form cationic PDMA is responsible for the increase in ΔpH from ~0.9 to 1.9 (Table 1).

However, as the PDMA protonation reaction occurs at the micelle interface and the pH at the interface is larger to a different extent as compared to the bulk pH, the intrinsic pH or pK_a for the protonation/deprotonation reaction in the PDMA block is expected to be larger than that of the corresponding apparent pH or pK_a. To determine the intrinsic pH/pK_a for the protonation or cation formation of the PDMA block, the change in ΔpH at various interfacial pH values are plotted and fitted with the sigmoidal curve, similar to that done earlier (Fig. 4, red curve). The fitted curve represents the intrinsic PDMA protonation or cation formation curve, and the intrinsic pK_a value was estimated to be ~7.2 by evaluating the transition midpoint of the fitted curve (Fig. 4, red curve). As the bulk pH decreases, the increase in PDMA protonation at the micelle interface may suppress the effective pH decrease at the interface owing to the increasing magnitude of ΔpH. Consequently, the difference between the intrinsic and apparent protonation pH values can be represented by the bulk-pH-dependent ΔpH values (Table 1). Our results show that the estimation of the intrinsic

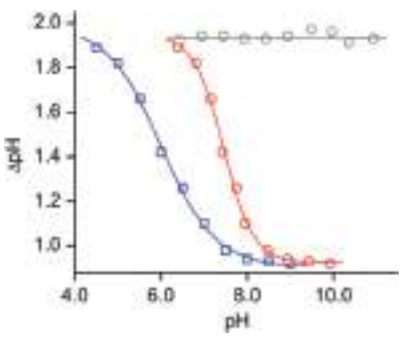

Fig. 4 pH deviations from the bulk to the interface (ΔpH) are plotted against bulk pH (squares, blue) and interfacial pH (circles, red) for TBP, and that against interfacial pH for q-TBP (circles, gray). The lines represent the least-square fitted curves of the plots with sigmoidal-Boltzmann or linear equations.

protonation pH or pK_a for the functional residue localized at the self-assembled interface is practically impossible by the usual acid/base titration using a pH probe, particularly when an appreciable difference in the pH between the interface and bulk exists. However, to determine the validity of our method for the determination of intrinsic protonation pH or pK_a, the DMA protonation reaction characteristics with non-micelle-forming homopolymer of DMA (homo-PDMA) (removing the possibility of apparent pH) were obtained from ^{1}H NMR studies and simple acid/base titration. The ^{1}H NMR spectra of homo-PDMA were recorded in D_2O at pH ~8.2 and ~6.0. The downfield chemical shift from 2.34 to 2.96 for methyl protons (6H, connected to N–), 2.74 to 3.54 for methylene protons (2H, connected to N–), and 4.18 to 4.35 for methylene protons (2H, ester) by decreasing the medium's pH indicated the protonation of amine groups in homo-PDMA (Fig. S16, ESI†). This result also revealed that the intrinsic DMA protonation pK_a for TBP micelles was at least greater than 6.5. In fact, by measuring the pH of the poly-PDMA solution containing 50 mol% HCl with respect to the total DMA residues, the DMA protonation pK_a was estimated to be ~7.3, which is fairly similar to that of the intrinsic protonation pK_a for TBP micelles obtained from the ΔpH *vs.* interfacial pH plot. All these results strongly authenticate our methodology for the estimation of the intrinsic protonation pH or pK_a for self-assembled systems.

Anionic membrane permeability induced by TBP micelles

Cellular membranes contain different types of negative and neutrally charged zwitterionic lipids that produce overall negatively charged membrane surfaces. Further, pH-controlled cationic molecules (cytosolic or foreign) can be electrostatically bound to the negatively charged membrane surface by tuning the membrane functionality.[43–45] We observed that a decrease in pH induced a higher extent of PDMA protonation at the TBP micelle interface, making the micelle interface more cationic and less acidic than the corresponding bulk pH. However, the interfacial pH and positive charges remain unaltered at the analogous cationic q-TBP micelle interface. The TBP and q-TBP micelles induced membrane permeability for anionic DOPC : DMPG (1 : 1) LUVs were investigated with fluorescence leakage studies at different bulk pH values (5.8–7.6). The role of pH-dependent variation in the positive charge quantity at the TBP micelle interface on the properties of membrane permeability can be assured from the difference in fluorescence leakage characters between TBP and q-TBP. Further, we performed fluorescence leakage studies for neutrally charged DOPC : DMPC (1 : 1) LUVs under similar experimental conditions to evaluate the effect of negatively charged membrane interfaces on membrane permeability.

The permeability of LUV membranes by their interaction with TBP/q-TBP micelles was estimated from the extent of fluorescence intensity increase due to the leakage of fluorescent dyes from the inner space of the LUVs to the exterior buffer medium through the lipid pores formed at the membrane surface. A very high concentration of fluorescent dye, namely, calcein (~50 mM), was encapsulated within the inner space of the LUVs to obtain a large extent of self-quenched fluorescence intensity. In the presence of TBP/q-TBP micelles (0.05 g dm^{-3}), a recovery of

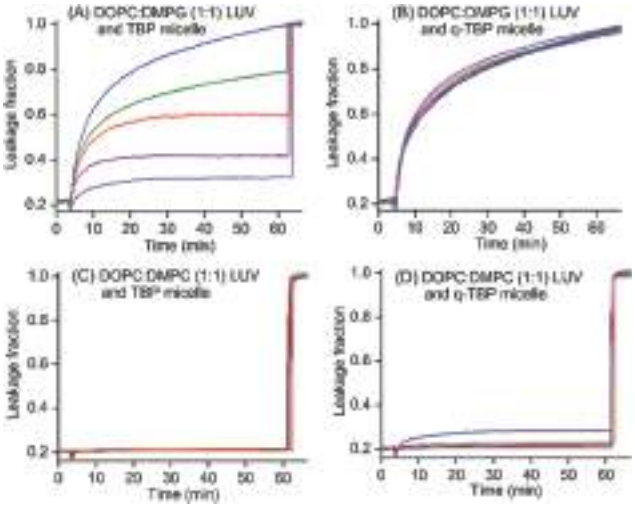

Fig. 5 Time profile of the fluorescence leakage fraction induced by the block copolymer (TBP and q-TBP) micelles for different LUVs encapsulated with calcein at different pH values for 10 mM buffer. (A–D) Bulk pH conditions are as follows. Blue: pH 5.8; green: pH 6.5; red: pH 7.0; purple: pH 7.3; and violet: pH 7.6. Measurement conditions are as follows. Buffer: 10 mM HEPES; pH: 5.8–7.6; LUV diameter: ~100 nm; total lipid concentration: 50 μM; block copolymer concentration: 0.05 g dm^{-3}; temperature: 25 °C. The identical osmotic pressure of the experimental buffer solution similar to the LUV-encapsulated calcein stock solution was adjusted with glucose. The leakage fraction curve is obtained by subtracting the intensity curve without the addition of a polymer from that with the polymer, further divided by the increased intensity amount due to the intense reaction of LUV with the TX-100 surfactant (20 mM). The excitation/fluorescence wavelength was 485/515 nm.

fluorescence intensity was observed, showing the leakage of calcein from the inner space of the LUV to the outer buffer medium due to the dilution of dye molecules (Fig. 5). The amount of dye leakage was estimated from the ratio of the increase in fluorescence intensity induced by the polymeric micelles against that induced by complete leakage accomplished by the addition of TX-100 (10 mM) micelles. The time-dependent micelle-induced leakage fraction ($L(t)$) was determined from the following equation:

$$L(t) = (I_t - I_0)/(I_{max} - I_0) \quad (3)$$

where the background fluorescence before the addition of polymeric micelles is denoted by I_0. Further, I_t and I_{max} represent the fluorescence intensities at time t after the addition of TBP/q-TBP micelles and that due to the complete disruption of LUV by the addition of TX-100 (20 mM), respectively. Depending on the polymeric systems (TBP and q-TBP) and bulk pH, the fluorescence intensity increased *via* a single phase (fast phase) or a double phase (fast phase culminating into a slow phase). An increase in fluorescence intensity *via* the fast phase with the maximum leakage fraction of ~48% or less followed by an intensity saturation within ~20–30 min after the addition of TBP micelles was observed for DOPC : DMPG (1 : 1) LUVs at bulk pH of 7.0 or above (Fig. 5A; red, purple, and violet curves). The saturation of the fluorescence intensity even though more than 52% of the dye was still entrapped within the LUV at pH 7.0 reflected the fact that the leakage process through the formed lipid pores onto the membrane interface is transient in nature. In contrast, the fluorescence

intensity increased in two phases at bulk pH of 6.5 or below (Fig. 5A; blue and green curves): a fast phase similar to that at pH 7.0 or above followed by a continuously increasing slow phase. Although the leakage in the fast phase was completed within ~20–30 min at pH of less than 6.5, the continuous leakage phenomenon may correspond to the slow destruction of the lipid bilayer structure. In fact, the leakage of all the encapsulated dye molecules was observed in ~65 min after the addition of TBP at pH 6.0 (Fig. 5A, blue curve).

The time dependence of the dye leakage was analyzed with the sum of two exponential curves as follows:

$$L(t) = A_f(1 - \exp(-k_f t)) + A_s(1 - \exp(-k_s t)) \quad (4)$$

where k_f and k_s represent the leakage rate constants for the fast and slow phases, respectively. Further, A_f and A_s represent the contribution of each leakage phase. The leakage rate constant for the fast phase (k_f) was determined from the initial slope of the fluorescence increase with respect to time. When leakage occurs in the two phases, the extrapolated fluorescence intensity at zero reaction time for the fitted exponential curve of the slow phase corresponds to the fluorescence intensity change caused by the leakage in the fast phase, A_f. The leakage fraction and rate constant in the fast phase in the presence of TBP micelles were found to increase from ~15% to 73% and from 0.03 to 0.15 min^{-1}, respectively, as the pH of the medium decreased from 7.6 to 5.8 (Fig. 5A and Table 2). For all the pH values (5.8–7.6), the dye leaked through two similar phases for q-TBP micelles, similar to that observed for TBP micelles at pH 5.8: namely, the fast phase followed by a continuous slow phase. Moreover, the leakage fraction (71–76%) and rate constant (0.14–0.16 min^{-1}) of the fast phase for q-TBP micelles were found to remain unchanged regardless of the bulk pH (5.8–7.6) (Fig. 5B).

By using an anionic interface-interacting glucose derivative in the form of a spiro-rhodamine molecule, we recently reported that the interfacial pH for anionic DMPG : DMPC (2 : 1) LUV is ~1.6 units more acidic under various bulk pH values.[31] Using the same pH probe, the ΔpH value for DOPC : DMPG (1 : 1) LUV was estimated to be around −1.5, according to eqn (1) (Fig. S17, ESI†) at various bulk pH values. When the TBP micelles interacted with the DOPC : DMPG (1 : 1) LUV interface at bulk pH (7.0), the local pH surrounding the micelle interface in contact with the LUV interface was expected to be around −1.5 pH units more acidic than that of the bulk medium[31] (Scheme 2). Therefore, PDMA blocks for TBP micelles attached with the DOPC : DMPG (1 : 1) LUV interface may face a decreased pH environment as compared to the surrounding bulk pH (Scheme 2). For the TBP micelle system, by correlating ΔpH *vs.* bulk pH plots with the protonation of PDMA at the TBP micelle interface (Fig. 4 and Table 1), the micelle interface was found to be mostly neutral (around pH 7.0) while exhibiting relatively small ΔpH (~1.0). With a decrease in bulk pH, the comparisons between ΔpH *vs.* bulk and ΔpH *vs.* interfacial pH plots reveal that the effective pH decrease at the TBP micelle interface gradually reduces in comparison to the amount of bulk pH decrease to induce a considerable suppression in PDMA protonation and

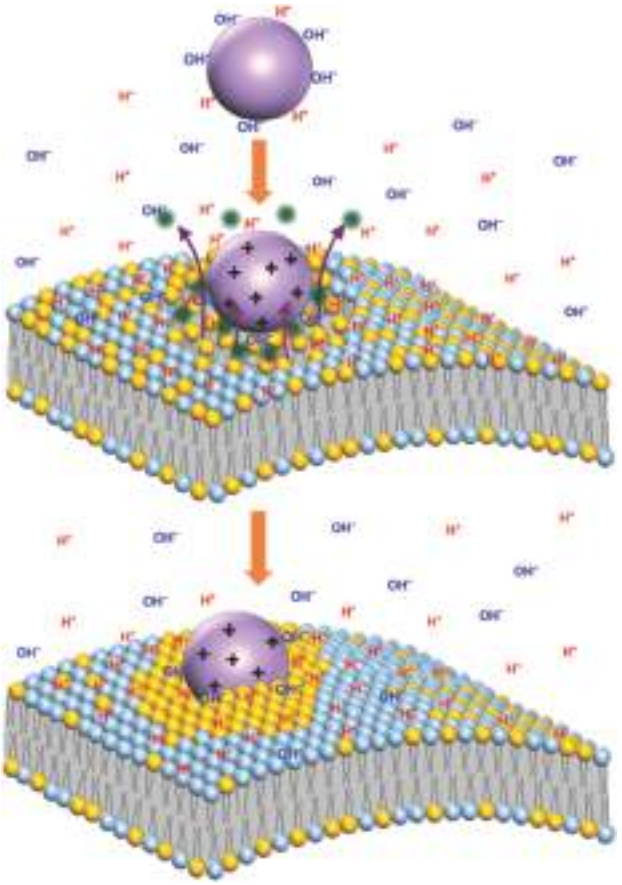

Scheme 2 Schematic representation of H^+ and OH^- concentrations at the interface of TBP micelles (large spheres) and DOPC : DMPG (1 : 1) LUVs (yellow: DMPG; light blue: DOPC) at neutral bulk pH. The cationic charges at the interface of the TBP micelles interacting with the anionic DMPG headgroup at the LUV interface are shown. PDMA-protonation-induced positive charges are formed at the micelle interface when the micelle interacts with the membrane interface. The purple arrows represent the transient permeation of small molecules (green) from the interior of the LUV to the exterior buffer medium (middle panel). Permeation caused by the formation of a lipid–polymer complex (lower panel).

Table 2 Kinetics of the pH-dependent fluorescence leakage for calcein-encapsulated LUVs in the presence of block copolymer (TBP and q-TBP) micelles[a]

		TBP		q-TBP	
LUV	pH	k_f (min^{-1})	A_f (%)	k_f (min^{-1})	A_f (%)
Anionic DOPC/DMPG (1 : 1)	5.8	0.15	73	0.15	71
	6.5	0.13	59	0.16	76
	7.0	0.11	48	0.14	72
	7.3	0.07	29	0.14	70
	7.6	0.03	15	0.15	76
Neutral DOPC/DMPC (1 : 1)	5.8	—	0	0.01	9
	6.5	—	0	—	3
	7.0	—	0	—	0
	7.3	—	0	—	0
	7.6	—	0	—	0

[a] Leakage rate constant and leakage amount for the fast phase are denoted by k_f and A_f, respectively.

positive charge formation at the micelle interface (Fig. 4). On the other hand, the interface protonation or positive charge formation causes an increase in pH at the TBP micelle interface. Therefore, the amount of effective pH at the micelle interfacial region in contact with the DOPC : DMPG (1 : 1) LUV interface can be effectively above the LUV interfacial pH (~5.5), but less than the bulk pH (7.0). Presumably, such pH adjustment at the membrane–contact micelle interface makes the micelle interface partially protonated or cationic to exhibit transient membrane leakage without disrupting the LUV bilayer structure for TBP micelles up to the bulk pH (7.0) (Scheme 2). However, for the increasing protonation of PDMA for TBP micelles as bulk pH reduces from ~6.5, an uncontrolled leaky nature was detected (Fig. 5A). With increasing protonation, the increase in pH at the micelle interface than that at the bulk may not be sufficiently large to maintain the threshold for the partially protonated PDMA condition to eliminate the continuously slow leakage phase. The leakage in the slow phase may be due to the disruption of the LUV membrane structure under bulk pH of 6.5 or below (Fig. 5A; blue and green curves). Therefore, the pH at the TBP micelle to DOPC : DMPG (1 : 1) LUV membrane contact increases from ~5.5 (membrane interfacial pH at bulk pH is 7.0) and plays the most important role to avoid uncontrolled leakage or disruption of the bilayer structure of the LUV membrane by making the PDMA unit only partially protonated or cationic. On the other hand, the total charge quantity for positively charged *N*-alkylated amine residues at the corresponding q-TBP micelle interface remains unperturbed by any change in the surrounding pH within that of the bulk pH (5.8–7.6) and therefore the continuous slow leakage is similar to that at pH 6.0 for TBP micelles was detected at all the studied pH values (5.8–7.6) (Fig. 5). Because all the PDMA blocks in TBP are protonated and cationic at the bulk pH (5.8), the uncontrolled leakage between TBP and q-TBP were comparable for DOPC/DMPG (1 : 1) (Fig. 5A and B).

Further, we performed similar fluorescence leakage studies for neutral DOPC : DMPC (1 : 1) LUVs. For TBP micelles, we found that the DOPC : DMPC (1 : 1) LUV did not leak at all for the pH values under investigation (5.8–7.6) (Fig. 5C). Even in the presence of cationic q-TBP micelles, only a small extent of leakage (~9%) was detected at pH 5.8 (Fig. 5D). Therefore, the replacement of anionic DMPG with neutral lipid DMPC with identical acryl lipid chain, q-TBB, or TBP micelles exhibited almost no fluorescence leakage even at acidic pH (5.8) (Fig. 5D). These results demonstrate that the presence of anionic lipids with an acidic membrane interface in the LUV membrane composition is also important to ensure membrane permeability.

The cationic form of TBP due to the protonation of PDMA blocks can involve electrostatic interactions with negatively charged DOPC : DMPG (1 : 1) LUV interface to alter the homogeneous distribution of lipids. The anionic headgroups of DMPG may accumulate in the surrounding of the cationic micelle interface comprising protonated PDMA blocks in contact with the LUV interface (Scheme 2). This lipid rearrangement probably makes the membrane surface porous to allow the leakage of small molecules (Scheme 2). It has been reported that the loose packing of the lipid molecules during such a rearrangement of the lipid phase in the membrane allows the formation of lipid pores that induce membrane permeability.[13,46,47] As mentioned earlier, the appreciable amount of residual dyes inside the LUV even after the completion of the leakage process at pH 7.0 or above suggests that pore formation is transient in nature (Fig. 5A). We propose that TBP-micelles-induced transient formation of leakage pores may reflect the relaxation process of membrane reorganization, yielding lipids domains enriched with phase-separated DMPG or DOPC (Scheme 2).[48,49] The closing of lipid pores may occur after the completion of lipid rearrangement due to the formation of another thermodynamically stable lipid arrangement (Scheme 2; lower panel). DSC thermograms or surface pressure (π)–area (A) compression isotherms of the LB monolayer for the DOPC/DMPG (1 : 1) lipid mixture in the presence and absence of TBP are compared to justify the formation of phase-separated lipid domain. In the DSC thermogram, a new peak at ~9 °C was formed by the addition of TBP micelles in DOPC/DMPG (1 : 1) LUVs, whereas without TBP, no peak was detected within 5–40 °C (Fig. S18, ESI†). Because the gel–liquid-crystalline temperature (T_m) of DMPG (24 °C) is greater than that of DOPC (−18 °C) (Fig. S18, ESI†), the peak at ~9 °C can be assigned to the gel–liquid-crystalline phase transition of the DMPC-rich domain. In LB monolayer studies, the π–A isotherm of DOPC/DMPG (1 : 1) contains a small plateau region within an area/molecule of 0.88–0.92 nm^2 in a high-pressure region of ~40 mN m^{-1} (Fig. S19, ESI†). By the addition of TBP in the water subphase, the area/molecule shifted toward a higher value with respect to DOPC/DMPG (1 : 1) in the absence of TBP, suggesting the association of TBP with the lipid headgroups. Most significantly, when TBP interacted with the lipid headgroups, the plateau region appeared at a lower pressure (~37.4 mN m^{-1}) with a much larger expansion of its area/molecule from 0.98 to 1.10 nm^2 (Fig. S19, ESI†). It has been reported that such a plateau region can be formed in a high-pressure region (beyond the liquid expansion phase) due to the squeezing out of the molecules from the monolayer.[50,51] With increasing monolayer contraction, because of the large stability of the electrostatic interaction between the negatively charged DMPG headgroup and the cationic form of TBP, neutral DOPC may be squeezed out from the binary lipid monolayer much more effectively with respect to that in the absence of TBP to form DMPG-rich lipid domains, as proposed by us. In addition, to ensure that there is a definite impact of the pH probe molecules on the membrane properties, similar studies were also performed. Because of the same negative charge characteristic of the lipid system and probe molecule (DSB/MSB), almost identical DSC thermograms or π–A compression isotherms between the presence and absence of probe molecules were detected (Fig. S18 and S19, ESI†), which confirms that the surface properties of the lipids remain unchanged upon the addition of the probe.

Upon the generation of increasing positive charges at the TBP micelle interface at bulk pH (6.5 or below), an increased amount of DMPG may participate in the lipid rearrangement process for DOPC : DMPG (1 : 1) LUVs, which may increase the total pore formation area on the LUV membrane surface, yielding an increase in the leakage fraction and rate constant

(Fig. 5, Table 2, and Scheme 2). In addition, the participation of a large number of lipid molecules in phase rearrangement can also significantly destabilize the bilayer membrane structure. The gradual loss of the membrane bilayer structure can be responsible for the appearance of a continuous slow leakage until all the dye molecules get removed from the LUV interior at pH 6.5 or below.

Conclusions

By utilizing two different interface-interacting pH probe molecules, we measured the interfacial pH and its deviation from the bulk pH (ΔpH) for a pH-responsive TBP, *i.e.*, PDMA-*b*-PMMA-*b*-PDMA [PDMA = poly(2-dimethylaminoethyl) methacrylate; PMMA = poly(methyl methacrylate)] micelle system under a wide range of bulk pH (from 4.5 to 9.0). To estimate the interfacial pH and pH deviation from the interface to the bulk (ΔpH), the change in the equilibrium ratio between the two pH-dependent molecular forms for each probe molecule at the micelle interface from the bulk medium were evaluated. As the bulk pH decreased from 8.0 to 4.5, the ΔpH value gradually increased from 0.9 to 1.9 due to the increased protonation of the amine moieties in water-exposed hydrophilic PDMA block at the TBP micelle interface. However, regardless of the variation in bulk pH, almost similar ΔpH (~1.9) for analogous n-alkylated copolymer (q-TBP) micelles revealed that the protonation-induced cationic charge generation at the interface for TBP micelles was responsible for the increase in ΔpH with decreasing bulk pH. From the correlation between ΔpH *vs.* protonation or cation formation pH, intrinsic protonation pK_a was estimated to be ~7.3. When the TBP micelle interface interacted with anionic DMPG-containing membrane interface, the pH increase at the polymer micelle interface from that of the membrane interface pH (~5.5) at the bulk pH (7.0 or above) made the membrane surface partially positive, thereby generating transient membrane permeability up to a certain time period. However, the interfacial pH increase was insufficient at bulk pH below 6.5 to increase the interfacial charges to higher positive values, allowing uncontrolled and continuous leakage until all the dye molecules were released. Considering these results, we introduced a novel view on selective and controlled permeability through various anionic membranes by their interaction with PDMA-containing polymeric systems under physiological pH.

Conflicts of interest

There are no conflicts to declare.

Acknowledgements

This work was supported by Research Projects (DST PURSE and UGC CAS II program). PPP acknowledges UGC and government of WB for financial support under RUSA 2.0 scheme (No: 5400-F(Y)). YS, RM acknowledges UGC for SRF fellowship. We thank Prof. Pabitra K. Paul (JU) and Prof. Debasish Haldar (IISER, kolkata) for LB monolayer and cryo-TEM studies, respectively.

Notes and references

1 F. S. Bates, M. A. Hillmyer, T. P. Lodge, C. M. Bates, K. T. Delaney and G. H. Fredrickson, *Science*, 2012, **336**, 434–440.
2 K. Kataoka, G. S. Kwon, M. Yokoyama, T. Okano and Y. Sakurai, *J. Controlled Release*, 1993, **24**, 119–132.
3 G. S. Kwon and K. Kataoka, *Adv. Drug Delivery Rev.*, 1995, **16**, 295–309.
4 K. Seo, S. W. Chung, Y. Byun and D. Kim, *Int. J. Pharm.*, 2012, **424**, 26–32.
5 D. Kim, Z. G. Gao, E. S. Lee and Y. H. Bae, *Mol. Pharmaceutics*, 2009, **6**, 1353–1362.
6 E. F. Palermo, D. K. Lee, A. Ramamoorthy and K. Kuroda, *J. Phys. Chem. B*, 2011, **115**, 366–375.
7 Y. Teramura, Y. Kaneda, T. Totani and H. Iwata, *Biomaterials*, 2008, **29**, 1345–1355.
8 M. Sikor, J. Sabin, A. Keyvanloo, M. F. Schneider, J. L. Thewalt, A. E. Bailey and B. J. Frisken, *Langmuir*, 2010, **26**, 4095–4102.
9 A. T. Ngo and G. Cosa, *Langmuir*, 2010, **26**, 6746–6754.
10 E. F. Palermo, I. Sovadinova and K. Kuroda, *Biomacromolecules*, 2009, **10**, 3098–3107.
11 L. P. Ding, E. Y. Chi, S. Chemburu, E. Ji, K. S. Schanze, G. P. Lopez and D. G. Whitten, *Langmuir*, 2009, **25**, 13742–13751.
12 W. van't Hof, E. C. I. Veerman, E. J. Helmerhorst and A. V. N. Amerongen, *Biol. Chem.*, 2001, **382**, 597–619.
13 M. Schulz, A. Olubummo and W. H. Binder, *Soft Matter*, 2012, **8**, 4849–4864.
14 W. H. Binder, *Angew. Chem., Int. Ed.*, 2008, **47**, 3092–3095.
15 S. C. Sebai, S. Cribier, A. Karimi, D. Massotte and C. Tribet, *Langmuir*, 2010, **26**, 14135–14141.
16 F. Vial, A. G. Oukhaled, L. Auvray and C. Tribet, *Soft Matter*, 2007, **3**, 75–78.
17 C. Tribet and F. Vial, *Soft Matter*, 2008, **4**, 68–81.
18 S. Osanai and K. Nakamura, *Biomaterials*, 2000, **21**, 867–876.
19 Y. Luan and L. Ramos, *J. Am. Chem. Soc.*, 2007, **129**, 14619–14624.
20 F. Vial, S. Rabhi and C. Tribet, *Langmuir*, 2005, **21**, 853–862.
21 V. Frette, I. Tsafrir, M. A. Guedeau-Boudeville, L. Jullien, D. Kandel and J. Stavans, *Phys. Rev. Lett.*, 1999, **83**, 2465–2468.
22 X. L. Zhang, Y. X. Huang, M. Ghazwani, P. Zhang, J. Li, S. H. Thorne and S. Li, *ACS Macro Lett.*, 2015, **4**, 620–623.
23 B. Nutan, A. K. Singh Chandel and S. K. Jewrajka, *Chem. – Eur. J.*, 2017, **23**, 8166–8170.
24 S. E. Paramonov, E. M. Bachelder, T. T. Beaudette, S. M. Standley, C. C. Lee, J. Dashe and J. M. J. Fréchet, *Bioconjugate Chem.*, 2008, **19**, 911–919.
25 R. Jain, S. M. Standley and J. M. J. Fréchet, *Macromolecules*, 2007, **40**, 452–457.
26 R. A. Shenoi, J. K. Narayanannair, J. L. Hamilton, B. F. L. Lai, S. Horte, R. K. Kainthan, J. P. Varghese, K. G. Rajeev, M. Manoharan and J. N. Kizhakkedathu, *J. Am. Chem. Soc.*, 2012, **134**, 14945–14957.
27 S. Chatterjee and S. Ramakrishnan, *Macromolecules*, 2011, **44**, 4658–4664.

28 B. Liu and S. Thayumanavan, *J. Am. Chem. Soc.*, 2017, **139**, 2306–2317.
29 Y. Sarkar, S. Das, A. Ray, S. K. Jewrajka, S. Hirota and P. P. Parui, *Analyst*, 2016, **141**, 2030–2039.
30 P. P. Parui, Y. Sarakar, R. Majumder, S. Das, H. Yang, K. Yasuhara and S. Hirota, *Chem. Sci.*, 2019, **10**, 9140–9151.
31 Y. Sarkar, R. Majumder, S. Das, A. Ray and P. P. Parui, *Langmuir*, 2018, **34**, 6271–6284.
32 S. Yamaguchi, K. Bhattacharyya and T. Tahara, *J. Phys. Chem. C*, 2011, **115**, 4168–4173.
33 A. Kundu, S. Yamaguchi and T. Tahara, *J. Phys. Chem. Lett.*, 2014, **5**, 762–766.
34 A. Bera, A. K. Singh Chandel, C. Uday Kumar and S. K. Jewrajka, *J. Mater. Chem. B*, 2015, **3**, 8548–8557.
35 G. Akerlof, *J. Am. Chem. Soc.*, 1932, **54**, 4125–4139.
36 F. E. Critchfield, J. A. Gibson and J. L. Hall, *J. Am. Chem. Soc.*, 1953, **75**, 6044–6045.
37 U. Chatterjee, S. K. Jewrajka and B. M. Mandal, *Polymer*, 2005, **46**, 1575–1582.
38 R. Majumder, Y. Sarkar, S. Das, S. K. Jewrajka, A. Ray and P. P. Parui, *Analyst*, 2016, **141**, 3246–3250.
39 S. Das, Y. Sarkar, S. Mukherjee, J. Bandyopadhyay, S. Samanta, P. P. Parui and A. Ray, *Sens. Actuators, B*, 2015, **209**, 545–554.
40 E. Gaidamauskas, D. P. Cleaver, P. B. Chatterjee and D. C. Crans, *Langmuir*, 2010, **26**, 13153–13161.
41 B. B. Lorenz, D. C. Crans and M. D. Johnson, *Eur. J. Inorg. Chem.*, 2014, 4537–4540.
42 P. van de Wetering, N. J. Zuidam, M. J. van Steenbergen, O. A. G. J. van der Houwen, W. J. M. Underberg and W. E. Hennink, *Macromolecules*, 1998, **31**, 8063–8068.
43 Z. Jiang, A. I. Vasil, J. D. Hale, R. E. W. Hancock, M. L. Vasil and R. S. Hodges, *Biopolymers*, 2008, **90**, 369–383.
44 I. Nakase and S. Futaki, *Sci. Rep.*, 2015, **5**, 10112.
45 J. Wang, S. Chou, L. Xu, X. Zhu, N. Dong, A. Shan and Z. Chen, *Sci. Rep.*, 2015, **5**, 15963.
46 J. J. Krebs, H. Hauser and E. Carafoli, *J. Biol. Chem.*, 1979, **254**, 5308–5316.
47 R. M. Epand and R. F. Epand, *Mol. BioSyst.*, 2009, **5**, 580–587.
48 S. A. Safran, T. L. Kuhl and J. N. Israelachvili, *Biophys. J.*, 2001, **81**, 659–666.
49 D. Bochicchio, E. Panizon, L. Monticelli and G. Rossi, *Sci. Rep.*, 2017, **7**, 6357.
50 D. Fischer, A. Curioni and W. Andreoni, *Langmuir*, 2003, **19**, 3567–3571.
51 M. Mahato, P. Pal, B. Tah and G. B. Talapatra, *Colloids Surf., A*, 2012, **414**, 375–383.

Chemical Science

EDGE ARTICLE

View Article Online
View Journal | View Issue

Cite this: *Chem. Sci.*, 2019, **10**, 9140

All publication charges for this article have been paid for by the Royal Society of Chemistry

Received 18th June 2019
Accepted 3rd August 2019

DOI: 10.1039/c9sc02993a

rsc.li/chemical-science

Determination of proton concentration at cardiolipin-containing membrane interfaces and its relation with the peroxidase activity of cytochrome *c*†

Partha Pratim Parui,*[ab] Yeasmin Sarakar,[a] Rini Majumder,[a] Sanju Das,[ac] Hongxu Yang,[b] Kazuma Yasuhara[b] and Shun Hirota*[b]

The activities of biomolecules are affected by the proton concentrations at biological membranes. Here, we succeeded in evaluating the interface proton concentration (−log[H^+] defined as pH′) of cardiolipin (CL)-enriched membrane models of the inner mitochondrial membrane (IMM) using a spiro-rhodamine-glucose molecule (RHG). According to fluorescence microscopy and ^{1}H-NMR studies, RHG interacted with the Stern layer of the membrane. The acid/base equilibrium of RHG between its protonated open form (o-RHG) and deprotonated closed spiro-form (c-RHG) at the membrane interface was monitored with UV-vis absorption and fluorescence spectra. The interface pH′ of 25% cardiolipin (CL)-containing large unilamellar vesicles (LUVs), which possess similar lipid properties to those of the IMM, was estimated to be ∼3.9, when the bulk pH was similar to the mitochondrial intermembrane space pH (6.8). However, for the membranes containing mono-anionic lipids, the interface pH′ was estimated to be ∼5.3 at bulk pH 6.8, indicating that the local negative charges of the lipid headgroups in the lipid membranes are responsible for the deviation of the interface pH′ from the bulk pH. The peroxidase activity of cyt *c* increased 5–7 fold upon lowering the pH to 3.9–4.3 or adding CL-containing (10–25% of total lipids) LUVs compared to that at bulk pH 6.8, indicating that the pH′ decrease at the IMM interface from the bulk pH enhances the peroxidase activity of cyt *c*. The peroxidase activity of cyt *c* at the membrane interface of tetraoleoyl CL (TOCL)-enriched (50% of total lipids) LUVs was higher than that estimated from the interface pH′, while the peroxidase activity was similar to that estimated from the interface pH′ for tetramyristoyl CL (TMCL)-enriched LUVs, supporting the hypothesis that when interacting with TOCL (not TMCL), cyt *c* opens the heme crevice to substrates. The present simple methodology allows us to estimate the interface proton concentrations of complex biological membranes.

Introduction

Biological membranes separate cellular organelles from the exterior of cells. The water-exposed interfaces of bilayer membranes act as barriers keeping ions, proteins, and other molecules where they are needed, and preventing them from diffusing into areas where they should not be.[1] Selective cellular uptake and refusal of various molecules by channels and other proteins at membrane interfaces frequently control biological processes, such as protein and ion transport,[2] cell apoptosis,[3] cell signaling,[4] membrane trafficking,[5] *etc.* Membrane interface H^+ concentration, which is affected by the membrane lipid composition, may also control the biological processes at the membrane interfaces. Although determination of the membrane interface H^+ concentration is indispensable for evaluating the biomolecular activities at the membrane interface, the interface H^+ concentration and its relationship with biological processes are often elusive.

The proton gradient across the inner mitochondrial membrane (IMM) makes the IMM acidic (pH ∼ 6.8) and the matrix alkaline (pH ∼ 7.7) in isolated mitochondria.[6] It has been reported that the pH change and proton gradient at the mitochondrial membrane are induced by physiological processes, such as Ca^{2+} transport,[7] glutamate transport,[8] and glucose starvation or sorbic acid stress.[9] The lateral pH-profile along the p-side of cristae has been measured *in situ* by attaching a ratiometric fluorescent pH-sensitive GFP variant to oxidative phosphorylation complex IV and the dimeric F_0F_1 ATP-synthase in the mitochondrial membrane, showing that the local pH

[a]*Department of Chemistry, Jadavpur University, Kolkata 700032, India. E-mail: parthaparui@yahoo.com; Fax: +91-33-24146223; Tel: +91-9433490492*

[b]*Division of Materials Science, Nara Institute of Science and Technology, Nara 630-0192, Japan*

[c]*Department of Chemistry, Maulana Azad College, Kolkata 700013, India*

† Electronic supplementary information (ESI) available: Additional spectroscopic and data analysis. See DOI: 10.1039/c9sc02993a

($-\log[H^+]$) at F_0F_1 ATP-synthase dimers is 0.3 unit less acidic than that of complex IV.[10]

Self-assemblies of amphiphilic lipids and surfactants have been utilized to investigate the properties of biological membranes[11] and their effects on protein activities,[12] where the deviations in the interface $-\log[H^+]$ (defined as pH′) from the bulk pH have been determined from the shifts in the acid/base pK_a of small organic molecules upon interaction with self-assemblies.[13] For example, the interface pH′ has been estimated from the shift in the acid/base pK_a between the self-assembly interface and bulk by heterodyne-detected electronic sum frequency generation (HD-ESFG) spectroscopy.[14] Various anionic amphiphilic self-assemblies, including inner and outer mitochondrial membranes, interact electrostatically with cationic rhodamine derivatives.[15] Recently, we have introduced an interface pH′ detection method for various amphiphilic self-assemblies by exploiting the acid/base equilibrium of a H^+ concentration probe (RHG), which is a glucose derivative of a spiro-rhodamine molecule.[16]

Cytochrome *c* (cyt *c*) contains 104 amino acid residues and is a positively charged protein at neutral pH. It is bound to the outer interface of the IMM, mainly by electrostatic interactions with anionic cardiolipins (CLs) in the membrane,[17] and triggers apoptosis by its release from mitochondria.[18] The peroxidase activity of cyt *c* increases upon interaction with CL, resulting in CL oxidation and subsequent apoptosis execution *via* cyt *c* permeabilization to the cytosol.[19] Recently, it has been suggested that protein activities are affected by the pH gradient across biological membranes.[20] The peroxidase activity of yeast cyt *c* adsorbed onto kaolinite was enhanced remarkably by decreasing the pH value below 4.[21] In this study, by monitoring the acid/base equilibrium of RHG, we showed that the pH′ at the interfaces of large unilamellar vesicles (LUVs) containing monounsaturated tetraoleoyl CL (TOCL) or saturated tetramyristoyl CL (TMCL) (10–50% CL of total lipids) decreases ~2.5–3.2 units from the neutral bulk pH. The peroxidase activity of cyt *c* was found to increase 5–7 fold at the LUV interface, due to the decrease in the interface pH′, while that at the interface of TOCL-containing LUVs was enhanced more than that estimated from the decrease in the interface pH′, apparently due to a cyt *c* structural change which has been previously reported.[22]

Results and discussion

Interaction of RHG with the membrane interface

RHG shows a pH-dependent equilibrium between a protonated open form (o-RHG) and a deprotonated closed spiro-form (c-RHG), with an interconversion pK_a of ~4.35 (Fig. 1A).[16c] RHG comprises a hydrophobic rhodamine moiety (a cationic moiety for o-RHG) and a hydrophilic glucose moiety; thus, it binds to an anionic membrane. The difference in the o-RHG/c-RHG equilibrium at the membrane interface and in the bulk can be monitored by examining the UV-vis absorption and fluorescence spectra of RHG (Fig. 1A).[16c]

The pH of the intermembrane space is 6.8–6.9,[23] while high concentrations of di-anionic CL are unique for mitochondrial membranes.[24] Giant unilamellar vesicles (GUVs) (diameter, 1–10 μm; Fig. S1†) and LUVs (diameter, ~100 nm) with a lipid composition of 1,2-dioleoyl-*sn*-glycero-3-phosphocholine (DOPC)/1,2-dioleoyl-*sn*-glycero-3-phosphoethanolamine (DOPE)/TOCL = 2 : 1 : 1 were constructed to reproduce the major lipid components of the IMM[24] (zwitterionic phosphatidylcholine (PC), ~40%; zwitterionic phosphatidylethanolamine (PE), ~30%; TOCL, ~25%). The fluorescence of the o-RHG form of RHG (0.3 μM) was observed at the DOPC/DOPE/TOCL (2 : 1 : 1) GUV (total lipid, 500 μM) surface but not in the bulk medium (Fig. 1Ba), indicating that all the RHG molecules interacted with the GUV interface and the interface was more acidic than the bulk. However, for the interaction of RHG with a DOPC/1,2-dioleoyl-*sn*-glycero-3-phosphoglycerol (DOPG) (1 : 2) GUV containing mono-anionic lipids, the RHG fluorescence intensity decreased significantly compared to that for the interaction with the DOPC/DOPE/TOCL (2 : 1 : 1) GUV under the same RHG and total lipid concentrations (Fig. 1Bb), apparently due to the decrease in H^+ concentration and the o-RHG/RHG ratio at the DOPG GUV interface.

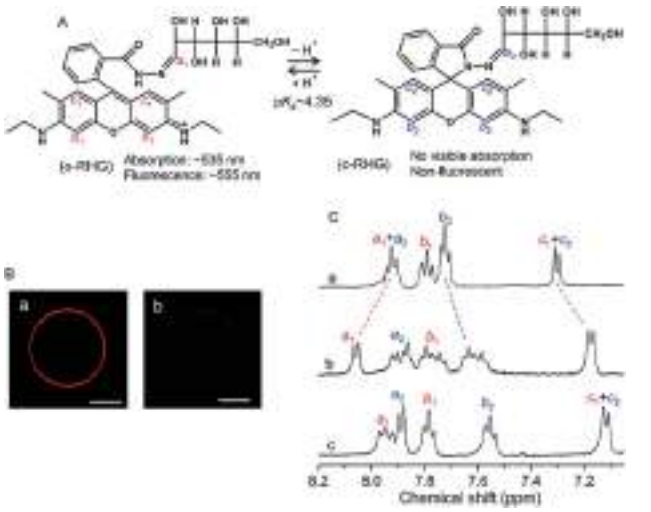

Fig. 1 (A) Equilibrium between the two pH-dependent forms of RHG. (B) Fluorescence microscopy observations of (a) DOPC/DOPE/TOCL (2 : 1 : 1) and (b) DOPC/DOPG (1 : 2) GUVs. GUVs were prepared in 1 mM HEPES buffer, pH 6.5, containing 200 mM sucrose. The total concentration of the lipids was 0.5 mM. RHG was added to GUVs for 0.06% of the total lipid concentration of GUVs. The red colour represents RHG fluorescence. White bars represent 5 μm. (C) ^{1}H NMR (500 MHz) spectra of RHG (1.5 mM) in D_2O medium (a) in the absence of lipids at pH 4.5, (b) in the presence of DOPC/DOPE/TOCL (2 : 1 : 1) LUVs (total lipid, 15 mM) at pH 6.5 and (c) in the presence of DOPG LUVs (total lipid, 15 mM) at pH 5.5. The pD value of the solution was adjusted by addition of 0.01 M CF_3COOH. The protons labeled in (C) correspond to the protons labeled in (A).

We obtained the absorption spectra of RHG in the presence of LUVs by subtracting the absorption spectrum of the LUV solution from that of the solution containing RHG and LUVs, although the LUV solution exhibited light scattering at the excitation (~530 nm) and emission (~560 nm) wavelengths of RHG (Fig. S2†). The absorbances of the DOPC/DOPE/TOCL (2 : 1 : 1) LUV solution (total lipid, 1 mM) were 0.080–0.145 and 0.071–0.130 at 530 and 560 nm, respectively, and those of

the DOPG LUV solution were 0.051–0.097 and 0.045–0.088 at 530 and 560 nm, respectively, at pH 4.0–7.0 (Fig. S2A†). To identify the inner filter effect (IFE) in the RHG fluorescence intensity due to the LUV light scattering, we increased the concentration of DOPC/DOPE/TOCL (2 : 1 : 1) LUVs at pH 4.5 and DOPG LUVs at pH 4.0 from 0.2 to 1 mM (total lipid) under a constant RHG concentration (0.2 μM), where the RHG fluorescence intensity was saturated (against LUV concentration) for all LUV concentrations used. The fluorescence intensity remained identical for the LUV concentrations studied (Fig. S3†), revealing that the IFE due to LUV light scattering was negligibly small, as reported previously.[25] A linear correlation between the RHG concentration (keeping RHG : lipid = 1 : 1000 constant) and fluorescence intensity at 560 nm was observed up to 1.0 μM RHG at pH 5.5 and 6.0 (Fig. S4A†). The fluorescence intensity of the RHG (1 μM) solution was also measured in the presence of DOPC/DOPE/TOCL LUVs (DOPC : DOPE = 2 : 1 : 1) at pH 5.5 and 6.0 under different concentrations of TOCL by changing the LUV concentration. A linear behaviour between the TOCL concentration and fluorescence intensity was observed up to 50 μM TOCL (Fig. S5B†). All these results demonstrate that there was no significant interference from light scattering on the fluorescence intensity. The absorbance and fluorescence intensity of RHG (1.0–2.0 μM) at pH 5.5 gradually increased upon increasing the amount of DOPC/DOPE/TOCL (2 : 1 : 1) or DOPG LUVs (Fig. S5†), indicating that RHG interacted with LUVs and the o-RHG/RHG ratio increased due to the interaction. Thus, LUV-binding saturation conditions with high LUV concentrations were used at all pH for further experiments.

The fluorescence quantum yield of RHG did not change upon varying the TOCL% (5–25% of total lipids) in DOPC/DOPE/TOCL LUVs at acidic pH 3.0, in which all of the c-RHG was converted to the o-RHG form (Fig. S6†). These results indicate that the fluorescence of RHG was not due to formation of a dimer, the formation of which has been reported for 10-*N*-nonyl acridine orange when it interacts with TOCL.[26] To investigate the interaction of RHG with TOCL in more detail, the absorbance of RHG at 535 nm was measured for RHG solutions under various TOCL concentrations obtained by changing the concentration of DOPC/DOPE/TOCL LUVs (DOPC : DOPE = 2 : 1; TOCL, 10 and 25% of total lipids) at pH 6.2. A gradual increase in the absorbance of RHG (2 μM) at 535 nm was observed upon increasing the TOCL concentration, and the absorbance saturated at ~125 and ~160 μM TOCL for LUVs containing 10 and 25% TOCL, respectively (Fig. S7†). Large [TOCL]/[RHG] ratios were required for the absorbance to saturate, suggesting a non-specific binding between RHG and TOCL. These results support the hypothesis that the dimer formation is not responsible for the increase in the fluorescence intensity of RHG.

RHG binding to DOPC/DOPE/TOCL (2 : 1 : 1) LUVs was also investigated at pH 4.5–8.0 (Fig. S8†). The RHG (2 μM) solutions containing LUVs at various pHs from 4.5 to 8.0 were filtered using a 100 K molecular weight cut-off filter. The pH value of the filtrate was adjusted to 2.0, at which all of the RHG is converted to the o-RHG form and exhibits absorbance at 532 nm. For all the pH conditions (4.5–8.0) studied, the absorbance at 532 nm of the filtrate after adjusting the pH to 2.0 was less than 5% that of 2 μM RHG at pH 2.0. These results reveal that the binding of RHG to TOCL was more than 95% at pH 4.5–8.0.

We have previously reported that when RHG is located at the outer interface, the fluorescence of RHG can be selectively quenched by addition of $Cu(ClO_4)_2/Na_2S$ (1 : 2) solution containing a non-permeable Cu^{2+}/S^{2-} quencher.[16c] The amount of RHG localized at the inner interface can be estimated from the residual fluorescence intensity obtained after the addition of the quencher. DOPC/DOPE/TOCL (2 : 1 : 1) LUVs (total lipid, 1 mM) were prepared in 10 mM cacodylate buffer, pH 6.0. The solution containing RHG (1 μM) and DOPC/DOPE/TOCL (2 : 1 : 1) LUVs (total lipid, 1 mM) in 10 mM cacodylate buffer, pH 6.0, was concentrated from 1 mL to ~40 μM using a 100k Da molecular weight cut-off filter to separate unbound RHG from LUVs. Subsequently, we diluted the concentrated LUV solution to 1 mL with 10 mM HEPES buffer, pH 8.0, and the pH of the solution was adjusted to 8.0 with addition of ~3 μL of 0.1 M NaOH. The fluorescence intensity of the pH-adjusted solution decreased to ~9% compared to that of the solution at pH 6.0 before concentration (Fig. S9†). We also concentrated the solution containing RHG (1 μM) and DOPC/DOPE/TOCL (2 : 1 : 1) LUVs (total lipid, 1 mM) in 10 mM cacodylate buffer, pH 6.0, and mixed the concentrated LUV solution with the filtrate. The fluorescence intensity of the mixture was similar to that of the solution before filtration (Fig. S9†). Upon addition of $Cu(ClO_4)_2/Na_2S$ (1 : 2) (total salt, 2 mM) to the mixture, the fluorescence intensity decreased to a similar intensity (~8%) to that observed when changing the pH from 6.0 to 8.0 with the concentration procedure (Fig. S9†). These results demonstrate that not only ~8% RHG was incorporated into the inner LUV lumen during the concentration procedure but also RHG exhibited negligibly small fluorescence intensity in the presence of DOPC/DOPE/TOCL (2 : 1 : 1) LUVs at pH 8.0.

To identify the interface location of the two molecular forms of RHG (o-RHG and c-RHG), we performed ^{1}H-NMR studies in D_2O medium in the presence and absence of LUVs under the pH conditions at which o-RHG and c-RHG coexist: in the presence of DOPC/DOPE/TOCL (2 : 1 : 1) LUVs at pH 6.5, in the presence of DOPG LUVs at pH 5.5, and in the absence of LUVs at pH 4.5 (Fig. 1C). In the absence of LUVs, ^{1}H-NMR chemical shifts of the imine protons (H–C=N: a_1 and a_2) were observed at 7.92 ppm for both o-RHG and c-RHG, and those of the aromatic protons c_1 and c_2 were observed at 7.30 ppm for o-RHG and c-RHG. However, the chemical shift of the aromatic proton b_1 of o-RHG shifted downfield to 7.79 ppm compared to that of the aromatic proton b_2 of c-RHG at 7.72 ppm, presumably due to the nearby positive charge field caused by the protonation of the amine moiety (Fig. 1A and C). The chemical shifts of c_1 of o-RHG and c_2 of c-RHG were both observed at the same chemical shifts of 7.17 and 7.11 ppm in the presence of DOPC/DOPE/TOCL (2 : 1 : 1) LUVs and DOPG LUVs, respectively, and at 7.30 ppm in the absence of LUVs, indicating that the rhodamine unit was located in a strong negative charge field formed at the Stern layer of LUVs for both o-RHG and c-RHG. Similar upfield chemical shifts were observed for the b_2 protons of o-RHG and c-RHG: from 7.72 to 7.60 ppm for DOPC/DOPE/TOCL (2 : 1 : 1)

LUVs and from 7.72 to 7.55 ppm for DOPG LUVs. Interestingly, the chemical shifts of the imine protons (a_1 and a_2) in the presence of LUVs were not the same for o-RHG and c-RHG; they differed relatively significantly for DOPC/DOPE/TOCL (2 : 1 : 1) LUVs (downfield from 7.92 to 8.06 ppm for a_1 and upfield from 7.92 to 7.89 ppm for a_2), suggesting positive and negative charge environments around the imine protons of o-RHG and c-RHG, respectively. When the cationic rhodamine moiety of o-RHG interacts with the anionic headgroup of TOCL as evaluated from the chemical shifts of the c_1 protons, the imine-N—connecting the water-exposed glucose region and the rhodamine unit—may face the positive charge field, due to the increase in proton concentration around the interface compared to the bulk as identified in the microscopic observation (Fig. 1Ba). A relatively small downfield chemical shift from 7.92 to 7.94 for the imine proton of o-RHG was detected upon addition of DOPG LUVs (Fig. 1C), indicating that the difference in the proton concentration between the interface and bulk is relatively small for DOPG LUVs (Fig. 1Bb). However, irrespective of LUV compositions, a similar upfield chemical shift for the imine proton (a_2) of c-RHG was observed at 7.89 ppm, suggesting a negative charge environment around the imine proton. The neutral hydrophobic rhodamine unit of c-RHG may move toward the hydrophobic acyl chain of the lipids, while the hydrophilic glucose region prefers to stay in the water phase, and eventually the imine-N connecting the two units will face a negative charge environment produced by the anionic lipid headgroups of the LUVs. All these results suggest that both o-RHG and c-RHG interact with the Stern layer of the LUVs, and are useful to estimate the interface H^+ concentration.

Red-shifts of 5–7 nm were observed in the wavelengths of absorption and fluorescence intensity maxima of RHG when it interacted with DOPC/DOPE/TOCL (2 : 1 : 1) LUVs at bulk pH 4.0–6.5 (Fig. 2 and S5†), presumably due to the decrease in dielectric constant at the interface compared to that of the bulk solution.[15b,16c] The absorption and fluorescence spectra of RHG (concentration: absorption, 2 μM; fluorescence, 1 μM) were measured in the presence of DOPC, DOPE, or DOPG LUVs (total lipid: absorption, 2 mM; fluorescence, 1 mM) and in the absence of LUVs. When RHG was attached to the DOPG LUVs, the maximum intensity wavelengths of absorption and fluorescence were observed at 539 and 560 nm, respectively, at pH 4.0–5.0, and they were also red-shifted 5–7 nm compared to the corresponding wavelengths in the absence of LUVs (Fig. S10†). However, the wavelengths and intensities of the absorption and fluorescence maxima in the RHG spectra did not change significantly when DOPC or DOPE LUV was used at pH 4.0–5.0, indicating that RHG interacts with DOPG LUV but not with DOPC or DOPE LUV.

There is a debate on the two pK_a values of the phosphate groups of CL. It has been reported that the phosphate groups of CL have strongly disparate ionization behaviours (pK_1 ~ 2–4 and pK_2 ~ 7.5).[27] In contrast, a recent study suggested that both of the phosphates ionize as strong acids with pK_a values ranging between 1 and 1.5.[28] RHG interacts with mono-anionic DOPG LUVs at bulk pHs 4.0–6.5 (Fig. 2 and S5†), but not with neutral DOPE LUVs at similar bulk pHs (4.0–5.0) (Fig. S10†), indicating that RHG may interact with CL even if it is monoionic under the acidic conditions used (pH 4.5). However, the concentration of RHG (1–2 μM) was considerably lower than that of the lipids (1–2 mM), and thus there was presumably no significant effect of RHG on the pK_a of CL.

Estimation of H^+ concentration at the LUV membrane interface

The absorbance and fluorescence intensity of RHG increased gradually upon decreasing the pH from 8.3 to 2.0 in the absence of lipids and in the presence of DOPC/DOPE/TOCL (2 : 1 : 1) or DOPG LUV (RHG : lipid = 1 : 1000) under LUV-binding saturation conditions of RHG (Fig. S11†), indicating that c-RHG converted to o-RHG at low pH. The absorption and fluorescence intensity in the presence of DOPC/DOPE/TOCL (2 : 1 : 1) and DOPG LUVs saturated below pH ~ 4.0 and ~3.5, respectively, while they saturated below pH ~ 2.0 in the absence of LUVs (Fig. S11†). However, the intensities of the saturated absorption and fluorescence spectra increased about 30% upon addition of DOPC/DOPE/TOCL (2 : 1 : 1) LUVs at pH 3.8 or DOPG LUVs at pH 3.5 (Fig. S11†), apparently due to changes in the UV-vis extinction coefficient and fluorescence quantum yield of o-RHG brought about by the change in polarity.[16c] The intensities of the absorption and fluorescence spectra were normalized by dividing the spectra by the maximum absorbance and fluorescence intensities, respectively, of the corresponding pH-saturated spectra, and the o-RHG/RHG ratios were calculated using the normalized spectra. The normalized absorption at 539 nm and fluorescence intensity at 560 nm of RHG increased gradually from 0.044 to 0.44 and 0.065 to 0.45, respectively, upon increasing TOCL from 5 to 25% in DOPC/DOPE/TOCL (DOPC : DOPE = 2 : 1) LUVs at pH 6.5 (Fig. 2A and B), indicating the conversion of c-RHG to o-RHG due to the increase in acidity at the LUV interface.

The interface pH′ values of LUVs were estimated by measuring the difference in the o-RHG/RHG ratio at the interface and in the bulk (Fig. 2C and D). The apparent difference (Δ) between the pH′ at the LUV membrane interface and pH in the bulk medium is related to the difference in the o-RHG/c-RHG equilibrium at the interface and in the bulk. A similar value of Δ = ~0.8 was obtained for DOPG LUVs by the absorption and fluorescence measurements under all bulk pH conditions measured (Fig. 2C and D, black and purple curves). For DOPC/DOPE/TOCL (2 : 1 : 1) LUVs, the value of Δ decreased from ~2.1 to ~1.5 and ~1.2 according to absorption and fluorescence measurements, respectively, upon decreasing the bulk pH from 7.5 to 4.5 (Fig. 2C and D, black and red curves). However, the o-RHG/RHG ratio and thus Δ are affected by the polarity of the medium (Fig. S12†). The polarity contribution (δ) to Δ is estimated from the apparent pH shift caused by the polarity difference between the interface and the bulk. The LUV interface pH′ (pH'_{inf}) is obtained from the bulk pH (pH_{bulk}), Δ, and δ:[16c]

$$pH'_{inf} = pH_{bulk} + \Delta - \delta \quad (1)$$

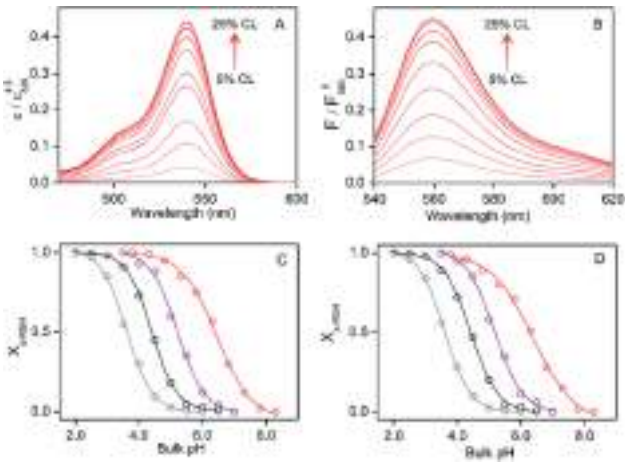

Fig. 2 (A and B) UV-vis absorption and fluorescence spectra of RHG in the presence of DOPC/DOPE/TOCL LUVs at binding saturation concentrations (DOPC : DOPE = 2 : 1; TOCL, 5, 7.5, 10, 12.5, 15, 17.5, 20, 22.5, and 25% of total lipids) at pH 6.5: (A) UV-vis absorption and (B) fluorescence spectra. ε represents the molar extinction coefficient of RHG, and ε^0_{539} represents ε at 539 nm at pH 3.0. F represents the fluorescence intensity, and F^0_{560} represents F at pH 3.0. The intensity changes upon increasing the TOCL ratio in LUVs are shown by arrows. (C and D) Plots of $X_{o\text{-}RHG}$ ([o-RHG]/[RHG]) against bulk pH under LUV-binding saturation conditions (red, DOPC/DOPE/TOCL = 2 : 1 : 1; purple, DOPG): analysed with (C) absorption and (D) fluorescence spectra. The $X_{o\text{-}RHG}$ plots for RHG are also shown (gray, with 58% (w/w) ethanol; black, without ethanol). The solid lines represent the least-squares fitted curves of the plots with sigmoidal-Boltzmann equations. Measurement conditions: RHG, (A and C) 2.0 μM and (B and D) 1.0 μM; total lipid, (A and C) 2 mM and (B and D) 1 mM; buffer: citrate–phosphate buffer, pH 3.5–5.0, 10 mM cacodylate buffer, pH 5.0–6.0, or 10 mM HEPES buffer, pH 6.0–8.5; temperature, 25 °C.

The interface dielectric constants of 45 and 44 were obtained for DOPC/DOPE/TOCL (2 : 1 : 1) and DOPG LUVs, respectively, by utilizing an interface polarity detecting Schiff base molecule (2-((2-(pyridine-2-yl)ethylimino)methyl)-6-(hydroxymethyl)-4-methylphenol (PMP)) (Fig. S13†).[29] The dielectric constant of the buffer solution was adjusted to 44–45 with addition of 58% (w/w) ethanol at pH 2.0–6.5,[30] where the δ value was estimated to be ∼0.7 (Fig. 2C and D, gray and black curves). The pH′ values at DOPC/DOPE/TOCL (2 : 1 : 1) and DOPG LUV interfaces under various bulk pHs were obtained from eqn (1) and are listed in Table 1. When the bulk pH was 7.0, the interface pH′ of the DOPC/DOPE/TOCL (2 : 1 : 1) LUV was ∼4.1, ∼2.9 units more acidic compared to the bulk pH. Considering these results, the interface pH′ of the IMM interface may be reduced to ∼3.9 when that of the mitochondrial intermembrane space is ∼6.8. However, the deviation between the interface pH′ and the bulk pH decreased gradually to ∼2.0 upon decreasing the bulk pH to ∼4.5 (Table 1), presumably due to protonation of one of the phosphate groups of TOCL. For the mono-anionic DOPG LUVs, a ∼1.5 unit decrease in interface pH′ from the bulk pH was detected under all bulk pH conditions investigated (pH 4.0–6.5) (Table 1).

We isolated mitoplasts from horse heart muscle, and tried to estimate the interface pH′ with RHG at pH 6.8. However, the mitoplast solution exhibited very large absorbances (∼1.5) at the excitation (530 nm) and emission (560 nm) wavelengths of RHG even at one order lower lipid concentration (∼0.1 mM) necessary for fluorescence saturation (Fig. S14†), not allowing us to measure the RHG absorption and fluorescence intensity under LUV-binding saturation conditions (lipid concentrations > ∼1 mM). Thus, we made LUVs with lipids extracted from mitochondrial membranes, where the interface pH′ of the LUVs made with extracted mitochondrial lipids was ∼4.5 at bulk pH 6.8 (Fig. S15†).

Table 1 Interface pH′ (pH'_{inf}) values of DOPC/DOPE/TOCL (2 : 1 : 1) and DOPG LUVs at various bulk pHs[a]

	pH'_{inf}			
	DOPC/DOPE/TOCL (2 : 1 : 1)		DOPG	
pH	Abs	FL	Abs	FL
7.50	4.59 ± 0.08	4.60 ± 0.05	—	—
7.00	4.10 ± 0.05	4.13 ± 0.04	—	—
6.50	3.65 ± 0.03	3.75 ± 0.02	4.92 ± 0.06	4.86 ± 0.05
6.00	3.33 ± 0.03	3.41 ± 0.02	4.44 ± 0.04	4.41 ± 0.03
5.50	2.99 ± 0.03	3.09 ± 0.02	3.93 ± 0.02	3.95 ± 0.02
5.00	2.68 ± 0.04	2.81 ± 0.03	3.43 ± 0.02	3.44 ± 0.02
4.50	2.44 ± 0.07	2.49 ± 0.05	2.97 ± 0.04	2.93 ± 0.03
4.00	—	—	2.55 ± 0.07	2.39 ± 0.06

[a] Interface pH′ values were estimated from the absorption (Abs) and fluorescence (FL) spectra of RHG at 25 °C.

A similar amount of c-RHG-to-o-RHG conversion was obtained between DOPC/DOPE/TOCL (2 : 1 : 1) and DOPC/TOCL (3 : 1) LUVs for a wide range of pH (4.0–8.0) (Fig. S16†), showing that DOPE does not influence RHG binding to LUVs at pH 4.0–8.0. We obtained the fluorescence intensity of RHG (1 μM) under fluorescence saturation conditions with high LUV concentrations for all the measurements (total lipid, 1 mM; Fig. S17†). The interface pH′ decreased as the TOCL% in DOPC/DOPE/TOCL LUVs was increased at pH 5.5–7.0 (Fig. S18A†). However, using DOPC/DOPE/TOCL LUVs with constant DOPC and DOPE concentrations but different TOCL concentrations ([DOPC] = 360; [DOPE] = 180 μM; TOCL 60–290 μM) under saturated RHG fluorescence intensity conditions at bulk pH 6.5, the plots of the interface pH′ against the TOCL% in LUVs were similar to those obtained with a constant total lipid concentration (1 mM) (Fig. S18B†). These results indicate that the increase in the negative charges in LUVs causes a decrease in the interface pH′.

It has been reported that the pH′ values at the anionic interfaces of amphiphilic self-assemblies are lower than the bulk pH.[16c] The o-RHG/RHG ratios at the interfaces of DOPC/DOPE/TOCL (DOPC/DOPE = 2 : 1; TOCL = 5–25%) and DOPC/DOPG (DOPG = 8–100%) LUVs increased for higher TOCL% and DOPG% (Fig. 2A and B, and S19†), strongly supporting the hypothesis that the negative charges of the anionic lipids at the interfaces are responsible for the decrease in pH′ at the interfaces compared to the bulk pH. $[H^+]$ values at the LUV

interface, calculated from the interface pH′ (Fig. S18 and S19†), were higher than those in the bulk by ~40- and ~50-fold at pH 6.5 and 7.0, respectively, even for DOPC/DOPE/TOCL (DOPC : DOPE = 2 : 1) LUVs containing 5% TOCL (Fig. 3A). Upon increasing TOCL% from 5 to ~25% in DOPC/DOPE/TOCL LUVs, the ratio of $[H^+]$ between the interface and the bulk increased linearly to ~700 and ~800 at bulk pH 6.5 and 7.0, respectively (Fig. 3A). For DOPC/DOPG LUVs containing 25% mono-anionic DOPG, the $[H^+]$ ratio between the interface and the bulk was ~5 at bulk pH ~ 5.0, and only a ~35-fold increase was detected for DOPG LUVs at 100% DOPG (Fig. 3). For an anionic lipid membrane, the negatively charged headgroups of the lipids at the membrane interface may interact electrostatically with H^+, whereas they repel OH^-. $[H^+]$ and $[OH^-]$ may increase and decrease, respectively, at the interface compared to those in the bulk phase, while $[H^+]$ and $[OH^-]$ remain unchanged in the bulk (Fig. 4). However, a deviation (~2.9) about twice as large between the interface pH′ and bulk pH was observed for DOPC/DOPE/TOCL (2 : 1 : 1) LUV compared to that (~1.5) for DOPG LUV, although the DOPG ratio in DOPG LUV was four times higher than the TOCL ratio in DOPC/DOPE/TOCL LUV, showing that the local negative charges of the lipid headgroup affect the interface pH′ significantly (Fig. 4).

H^+ concentration at the interface of the LUV membrane in the presence of cyt *c*

The effect of cyt *c* binding to TOCL on the interface pH′ was estimated at bulk pH 6.5 and 7.0 in the presence of oxidized horse cyt *c* (0.5–5.0) at a low TOCL concentration (10 μM) in DOPC/DOPE/TOCL (2 : 1 : 1) LUVs to avoid cyt *c* precipitation (Fig. 5 and S20†). A concentration of 0.05 μM was used for RHG to satisfy the fluorescence intensity saturation by LUV binding. The fluorescence intensity decreased a little, but less than 10%, for all the pH conditions studied (pH 2.5 to 5.3) (Fig. S21†). The fluorescence spectra of o-RHG in the presence of cyt *c* were

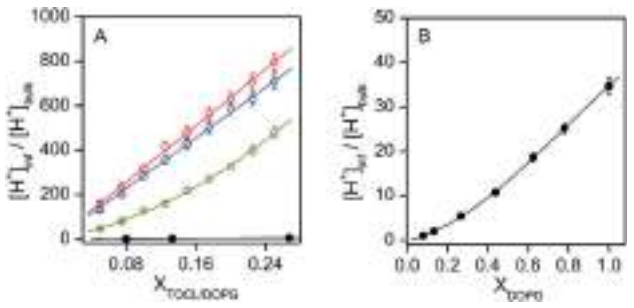

Fig. 3 Ratio between interface $[H^+]$ and bulk $[H^+]$ ($[H^+]_{inf}/[H^+]_{bulk}$) plotted against the molar ratio of charged lipids ($X_{TOCL/DOPG}$ and X_{DOPG}). (A) Plots of $[H^+]_{inf}/[H^+]_{bulk}$ against TOCL ratio ([TOCL]/([DOPC] + [DOPE] + [TOCL])) for DOPC/DOPE/TOCL LUVs (total lipid, 2.0 mM) at various bulk pHs: dark yellow, pH 6.0; blue, pH 6.5; red, pH 7.0. The DOPC : DOPE ratio was kept constant at 2 : 1. The plots of $[H^+]_{inf}/[H^+]_{bulk}$ against DOPG ratio for DOPG/DOPC LUVs at pH 5.0 are also shown (black). (B) Extended plots of $[H^+]_{inf}/[H^+]_{bulk}$ against DOPG ratio for DOPG/DOPC LUVs. The absorption intensities of RHG were saturated under the TOCL and DOPG concentrations used. Measurements were performed at 25 °C.

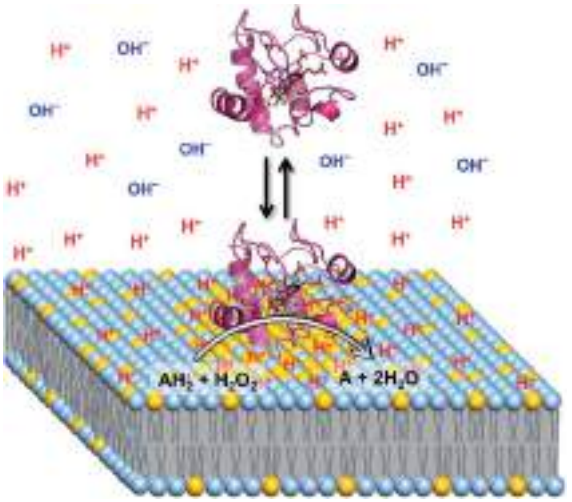

Fig. 4 Schematic representation of H^+ and OH^- concentrations at the interface of a CL-containing LUV (yellow, CL; light blue, DOPC and DOPE) and the bulk medium. The peroxidase reactivity of cyt *c* (violet) is enhanced at the membrane interface due to a higher H^+ concentration than that in the bulk.

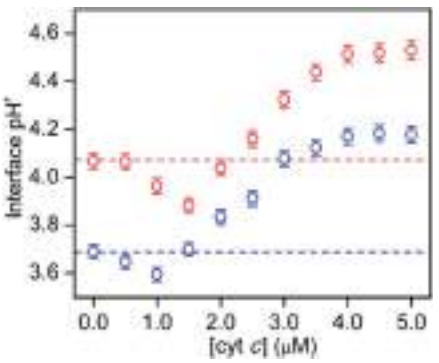

Fig. 5 Interface pH′ (−log$[H^+]$) of DOPC/DOPE/TOCL (2 : 1 : 1) LUVs (total lipid, 0.04 mM) plotted against cyt *c* concentration at 25 °C in 10 mM HEPES at various pHs: blue, pH 6.5; red, pH 7.0. The plots of interface pH′ in the absence of cyt *c* at pH 6.5 and 7.0 are depicted in red and blue broken lines, respectively, for comparison.

calibrated taking into account of the quenching effect by cyt *c* (Fig. S20C and D†), and the interface pH′ at each concentration of cyt *c* was obtained from the calibrated spectra (Fig. 5). By increasing the cyt *c* concentration from 0 to 1.5 μM at pH 7.0, the interface pH′ decreased gradually from 4.07 to 3.86, followed by a gradual increase until it saturated at ~4.51 at cyt *c* concentrations higher than 4.0 μM (Fig. 5). Although a similar trend was observed at pH 6.5, a smaller interface pH′ decrease from 3.69 to 3.59 was detected upon increasing the cyt *c* concentration from 0 to 1.0 μM (Fig. 5). Positively charged cyt *c* interacts electrostatically with negatively charged TOCL, forming TOCL-enriched lipid domains in LUVs (Fig. 4).[31] When the concentration of TOCL is significantly higher than that of cyt *c* (TOCL concentration, 10 μM; cyt *c* concentration, <1.5 μM), the negative charge density at the TOCL-enriched domain may be higher compared to that of a homogeneous distribution

domain, even though the negative charge density of the TOCL-enriched domain can be partially reduced by the positively charged cyt *c*. As a result, the increase in the negative charge density at the interface due to accumulation of TOCL may contribute to the decrease in the interface pH′ upon addition of 0.5 to 1.5 μM cyt *c*. At high cyt *c* concentrations (>1.5 μM), the effect of cyt *c* on the decrease in the negative charge density may supersede that by TOCL clustering, inducing an increase in the interface pH′ (Fig. 5). However, the interface pH′ saturated at ~4.18 and ~4.51 at bulk pH 6.5 and 7.0, respectively, upon addition of cyt *c* with concentrations higher than 4.0 μM, suggesting saturation of cyt *c* binding to LUVs.

Effect of pH′ decrease at the cardiolipin-containing LUV interface on the peroxidase activity of cyt *c*

Recently, theoretical calculations have shown that the charge density 2–3 nm away from the interface of a 100 nm diameter nanoparticle does not alter significantly.[32] Cyt *c* is localized at the IMM interface and its diameter is 2–3 nm. Thus, cyt *c* may experience a pH′ close to ~3.9 at the IMM interface (Fig. 4). It has been reported by NMR studies that only a certain number of cyt *c* molecules may exist in the TOCL-bound state in the presence of TOCL-containing LUVs, while the other cyt *c* molecules exist in the free state, indicating an equilibrium for cyt *c* binding to the TOCL-containing LUVs.[33] However, the H^+ concentration may affect the stability and function of cyt *c* at the IMM. At pH below 3.0, cyt *c* exists in the molten globule and denatured states in the presence of high and low salt concentrations, respectively, according to circular dichroism (CD), differential scanning calorimetry (DSC), and small angle X-ray scattering measurements.[34] The structures of various partially unfolded intermediate states of cyt *c* have been determined during alkaline pH-dependent unfolding using the fluorometric photon counting histogram model.[35] We obtained an approximate folded-to-unfolded transition temperature (T_m) of cyt *c* from the DSC thermogram as in other papers (Fig. S22†),[36] although cyt *c* aggregation was detected in the DSC thermogram at all pH values studied (pH 3.9–6.8) at high temperatures (Fig. S22 and S23†). T_m decreased from 81 °C to 71 °C upon lowering the pH from 6.8 to 3.9, whereas it did not change significantly at pH 5.3 (~80 °C) (Fig. S22†), indicating that the stability of cyt *c* decreases when it is bound to the IMM interface. Upon interaction with mono-anion-containing lipid membranes, cyt *c* may not destabilize significantly, owing to the pH′ at the membrane interface not changing appreciably from the bulk pH†). However, the peroxidase activity of cyt *c* increases when the Met80–heme iron coordination is cleaved or perturbed significantly.[37] A decrease in the 695 nm absorbance, which is related to the Met80–heme iron coordination bond, was observed when decreasing the pH from 6.8 to 3.9 in the presence of H_2O_2 and 2-methoxyphenol, indicating that the Met80–heme iron bond was perturbed under high H^+ concentration environments, such as the IMM interface (Fig. S24†).

The product formation rates for 2,2′-azino-bis(3-ethylbenzothiazoline-6-sulfonic acid) diammonium salt (ABTS) is frequently used as a model substrate in the oxidation reaction of heme proteins;[22d,38] thus the oxidation of ABTS (40 μM) by cyt *c* (5 μM) in the presence of H_2O_2 (0–4 mM) was monitored at 730 nm ($\varepsilon_{730} \sim 14\ mM^{-1}\ cm^{-1}$).[39] The steady-state rate (k_{obs}) increased linearly from 0.09 to 0.65 s^{-1} upon increasing the H_2O_2 concentration from 0.5 to 4 mM at pH 6.8, indicating that ABTS oxidation followed a bimolecular kinetics (Fig. 6). We estimated the effect of interface pH′ on the cyt *c* peroxidase activity for DOPG and DOPC/DOPE/TOCL LUVs (DOPC : DOPE = 2 : 1; CL, 10–50% of total lipid) containing various mol% of a different CL, TOCL or TMCL. The product formation rate of the cyt *c* peroxidase reaction increased in the presence of DOPC/DOPE/TOCL (2 : 1 : 1) LUVs upon increasing the TOCL concentration up to 0.2 mM and did not change further up to

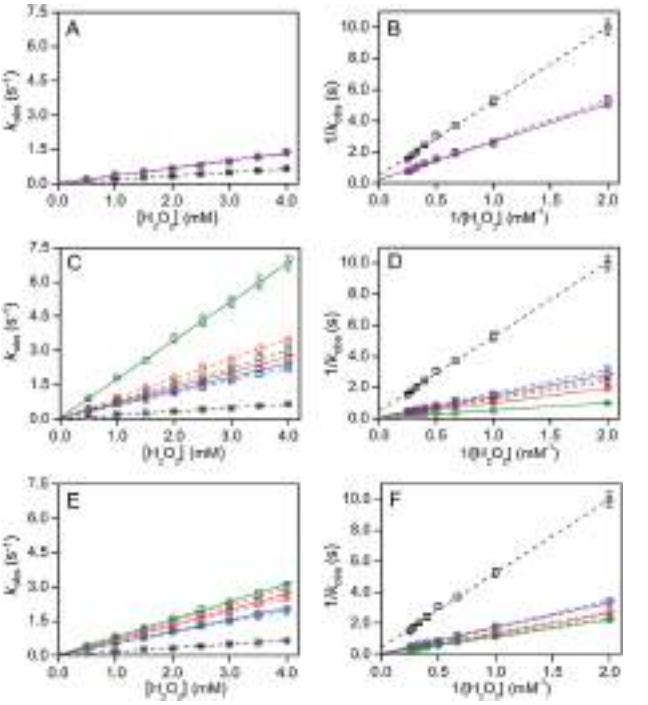

Fig. 6 H_2O_2 concentration-dependent horse cyt *c*-catalysed ABTS oxidation reaction parameters in the presence of DOPC/DOPE/CL LUVs containing different CL% or DOPG LUVs (circles, solid line) and in the absence of LUVs (squares, broken lines). (A, C, and E) Plots of observed reaction rate k_{obs} against H_2O_2 concentration and (B, D, and F) plots of inverse of reaction rate against inverse of H_2O_2 concentration: (A and B) in the presence of DOPG LUVs (lipid, 0.5 mM) at bulk pH 6.8 and in the absence of LUVs at pH 5.3 (purple); (C and D) in the presence of DOPC/DOPE/TOCL LUVs (DOPC : DOPE = 2 : 1, TOCL = 10% (blue), 25% (red) and 50% (green) of total lipids; TOCL = 0.25 mM) at bulk pH 6.8 and in the absence of LUVs at pH 4.3 (blue), 3.9 (red), and 3.6 (green); (E and F) in the presence of DOPC/DOPE/TMCL LUVs (DOPC : DOPE = 2 : 1, TMCL = 10% (blue), 25% (red) and 50% (green) of total lipid; TMCL = 0.25 mM) at bulk pH 6.8 and in the absence of LUVs at pH 4.3 (blue), 3.9 (red), and 3.6 (green). The plots in the absence of LUVs at pH 6.8 are represented in black for comparison in (A–F). The initial reaction rate was obtained by spectrophotometric measurement of ABTS oxidation. The oxidation rate of ABTS in (A, C, and E) agrees with the equation for a bimolecular reaction: $k_{obs} = k_1[\text{cyt } c][H_2O_2] = k_{obs}[\text{cyt } c]$ ($k_{obs} = k_1[H_2O_2]$). Reaction conditions: cyt *c* concentration, 5 μM; H_2O_2 concentration, 0–4 mM; ABTS concentration, 40 μM; 25 °C.

~0.28 mM, followed by a gradual decrease, apparently due to the degradation of cyt *c* (Fig. S25†).[38b] Thus, we used a constant concentration (0.25 mM) for TOCL and TMCL, exhibiting a relatively high cyt *c* peroxidase activity, and measured the cyt *c* peroxidase activity in the presence of LUVs with different CL ratios. DOPG LUVs (total lipid, 0.5 mM) were used as a reference by adjusting the total negative charge to that of DOPC/DOPE/TOCL LUVs (DOPC : DOPE = 2 : 1). A similar pH dependence of the interface pH′ was observed for LUVs containing TMCL (pH′ 4.25, 3.95, and 3.55 for LUVs containing 10, 25, and 50% TMCL, respectively) and those containing TOCL (pH′ ~ 4.32, 3.90, and 3.61 for LUVs containing 10, 25, and 50% TOCL, respectively) (Fig. S26†).

Similar to the Kitz–Wilson double-reciprocal plots,[40] peroxidase activity constants, k_{cat} and K_m, were obtained from the intercept ($1/k_{cat}$) and slope (K_m/k_{cat}) of the plots of the inverse of product formation rate ($1/k_{obs}$) against inverse of H_2O_2 concentration, according to the following equation.

$$1/k_{obs} = 1/k_{cat} + (K_m/k_{cat}) \times 1/[H_2O_2], \quad (2)$$

where k_{cat} represents the turnover number and K_m represents the Michaelis–Menten constant. Due to the suicidal nature of cyt *c* during the catalytic process, the product formation rate was obtained from the initial reaction rate.

In the presence of DOPC/DOPE/TMCL LUVs (DOPC : DOPE = 2 : 1), the cyt *c* peroxidase activity increased 5 to 7 fold upon addition of LUVs depending on the TMCL% in the LUVs (Fig. 6 and Table 2). However, only a ~2 fold increase in peroxidase activity was detected in the presence of DOPG LUVs (Fig. 6A and B). To evaluate the effect of pH decrease at the LUV interface on the peroxidase activity, we measured the peroxidase activity in the absence of LUVs at bulk pH identical to the interface pH′. Interestingly, the kinetic parameters (k_{cat} and K_m) at pH 6.8 in the presence of DOPC/DOPE/TOCL (DOPC : DOPE = 2 : 1, TOCL = 10–25%), DOPC/DOPE/TMCL (DOPC : DOPE = 2 : 1, TMCL = 10–50%), and DOPG LUVs were similar to the corresponding values obtained in the absence of LUVs at pH values corresponding to the interface pH′ (Fig. 6 and Table 2) (Fig. 6C–F and Table 2). However, the k_{cat} in the presence of LUVs containing relatively high TOCL% (>50%) was ~2-fold higher than that estimated by the pH decrease (Fig. 6C and D, and Table 2), indicating that other factors than the interface pH′ affect the peroxidase activity of cyt *c*. Related to this, protein modification of cyt *c* may also affect its peroxidase activity.[41]

It has been reported that the peroxidase activity of cyt *c* increases dramatically upon interaction with TOCL, due to the opening of the protein upon breaking of the Met80–heme iron bond and increase in ligand accessibility to the heme.[22a–d] Additionally, docking studies of cyt *c* with TOCL have shown that C11 of CL can bind to cyt *c* at a position adjacent to the heme.[22f] Full binding of cyt *c* to a membrane requires a cyt *c* : TOCL threshold ratio of 1 : 5 for cyt *c* to gain peroxidase activity.[42] The structure of cyt *c* is perturbed significantly when it interacts strongly with TOCL-containing membranes.[22e] There are three possible TOCL binding sites of cyt *c* containing positive amino acid residues (Lys, His and Asp), and the heme crevice is opened to substrates by the simultaneous binding of two sites, at opposing sides to the heme, to the membrane.[42] A ~50-fold increase in the cyt *c* peroxidase activity has been reported for the reaction of cyt *c* (40 μM) with H_2O_2 (100 μM) and etoposide (700 μM) upon addition of DOPC/TOCL (1 : 1) LUVs (total lipid, 400 μM), due to a change in the protein structure.[22b,43] On the other hand, it has been reported that the peroxidase activity increases ~15-fold for the reaction of cyt *c* (1 μM) with H_2O_2 (100 μM) upon addition of DOPC/TOCL (1 : 1) LUVs (total lipid, 250 μM).[44] Although the peroxidase activity of cyt *c* at the membrane interface of TMCL-enriched LUVs (50% of total lipid) was similar to that estimated from the interface pH′, the cyt *c* peroxidase activity was higher than that estimated from the interface pH′ for TOCL-enriched LUVs (Fig. 6 and Table 2), supporting the hypothesis that cyt *c* opens the heme crevice to substrates when interacting with TOCL. We conclude that the peroxidase activity of cyt *c* increases due to both the pH decrease at the interface and the cyt *c* structural perturbation caused by the interaction with TOCL.

Table 2 Kinetic parameters for ABTS oxidation by the peroxidase reaction of cyt *c* in the presence of DOPC/DOPE/TOCL LUVs containing TOCL or TMCL (TOCL or TMCL = 0.25 mM) and DOPG LUVs (0.5 mM) at pH 6.8, and those in the absence of LUVs at bulk pH corresponding to the interface pH′. Measurements were performed at 25 °C

LUV	Bulk pH	Interface pH′	k_{cat} (s^{-1})	K_m (μM)
None	6.80		2.0 ± 0.1	10.0 ± 0.4
DOPG	6.80	5.30	4.7 ± 0.2	11.8 ± 0.5
None	5.30		5.5 ± 0.2	12.3 ± 0.5
10% TOCL[a]	6.80	4.32	11.3 ± 0.4	12.7 ± 0.5
None	4.32	—	11.2 ± 0.4	14.0 ± 0.6
25% TOCL[a]	6.80	3.90	15.5 ± 0.5	13.5 ± 0.5
None	3.90	—	14.4 ± 0.5	13.2 ± 0.6
50% TOCL[a]	6.80	3.61	31.9 ± 1.0	14.0 ± 0.5
None	3.61		15.9 ± 0.5	14.1 ± 0.5
10% TMCL[b]	6.80	4.25	10.3 ± 0.4	12.1 ± 0.5
None	4.25		11.1 ± 0.4	11.9 ± 0.5
25% TMCL[b]	6.80	3.95	13.7 ± 0.5	13.5 ± 0.5
None	3.95		12.9 ± 0.5	13.3 ± 0.5
50% TMCL[b]	6.80	3.55	15.7 ± 0.5	13.9 ± 0.6
None	3.65		15.5 ± 0.5	13.7 ± 0.5

[a] DOPC/DOPE/TOCL LUVs (DOPC : DOPE = 2 : 1, TOCL = 10, 25, and 50% of total lipids). [b] DOPC/DOPE/TMCL LUVs (DOPC : DOPE = 2 : 1, TMCL = 10, 25, and 50% of total lipids).

Conclusions

We demonstrate that RHG, an interface H^+ concentration-sensing probe, can be used to measure the proton concentration ($-\log[H^+]$, defined as pH′) at lipid membrane interfaces by monitoring the change in its acid/base equilibrium between the Stern layer and the bulk. The interface pH′ for CL-enriched membrane models of the IMM is evaluated to be ~3.9, while the mitochondrial intermembrane space pH is ~6.8. The large decrease in pH at the interfaces of the IMM model membranes compared to the bulk pH may enhance the peroxidase activity of

cyt *c* by a factor of 5–7 fold. However, the peroxidase activity of cyt *c* increased not only because of the decrease in the interface pH′ but also due to the structural perturbation of cyt *c* when interacting with TOCL, whereas there was no additional increase in the peroxidase activity from that estimated from the interface pH′ when interacting with TMCL. Considering these results, we added information on interface pH′ to the peroxidase activity of cyt *c* at negatively charged membranes. These results also show that the inherent simplicity of our method for H^+ concentration detection can be widely applied to various biological membrane interfaces.

Experimental

Materials and general procedures

DOPC, DOPG, and DOPE were purchased from NOF Co. (Tokyo, Japan). TOCL and TMCL were purchased from Avanti Polar Lipids (Alabaster, AL, USA). Horse cyt *c*, ABTS, and 2-methoxyphenol were purchased from Sigma-Aldrich (St. Louis, MO, USA). Cyt *c* was purified by gel filtration chromatography (Superdex 75, GE Healthcare, Sweden) before performing spectroscopic measurements. Different buffer compositions were used to obtain specific medium pH: pH 1.5–5.0, sodium citrate–phosphate buffer (a mixture of sodium phosphate and sodium citrate solutions); pH 5.0–6.0, sodium cacodylate buffer; pH 6.0–8.3, HEPES buffer. The pH value was adjusted by addition of 1.0 M NaOH or 1.0 M HCl, if necessary.

Syntheses of a spiro-rhodamine-glucose molecule and a Schiff-base molecule

A spiro-rhodamine-glucose molecule (RHG)[45] and a Schiff-base molecule (PMP)[46] were prepared according to earlier procedures. Briefly, spiro-rhodamine 6G hydrazide was prepared by the reaction of rhodamine 6G hydrochloride with hydrazine in ethanol. The condensation reaction between rhodamine 6G hydrazide and glucose was performed in the presence of *p*-toluene sulfonic acid. The product was purified by silica gel column chromatography followed by rotary evaporation. Stock aqueous RHG solutions were used for all absorption and fluorescence experiments. The purity of RHG was confirmed by the ^{1}H NMR spectrum in DMSO-d_6 (Fig. S27†). PMP was synthesized by the condensation reaction between 2-hydroxy-3-(hydroxymethyl)-5-methylbenzaldehyde and 2-(2-aminoethyl)-pyridine.

Purification of mitochondria and mitochondrial lipids

Horse heart meat chunks (200 g) were placed in 0.6 L of 10 mM sodium phosphate buffer, pH 8.0, containing 250 mM sucrose and 0.1 mM EDTA, and blended with a food processor (TK430, TESCOM) for 2 min. The blended sample was centrifuged at 900*g* for 10 min, and the supernatant was filtered with 2 layers of gauze to remove the fat. After adjusting the pH of the solution to 7.4 with 3 M NaOH, the solution was centrifuged at 7000*g* for 10 min. The precipitate was suspended in 25 mL of 10 mM sodium phosphate buffer, pH 7.4, containing 150 mM NaCl. The suspended solution (25 mL) was homogenized twice with a tissue grinder (WHEATON) and centrifuged at 7600*g* for 10 min. The supernatant was removed with a pipette, and the brown precipitate was suspended in 25 mL of 10 mM Tris–HCl buffer, pH 7.4, containing 70 mM sucrose and 210 mM mannitol. The suspended solution was homogenized twice with the tissue grinder and centrifuged at 7600*g* for 10 min. The supernatant was removed with a pipette, and the brown precipitate was suspended in 4 mL of 5 mM sodium phosphate buffer, pH 7.4, containing 10 mM KCl, 2 mM $MgCl_2$, 70 mM sucrose, 0.2 mM EDTA, and 210 mM mannitol, obtaining mitochondria. To extract lipids from mitochondria, a mixture of chloroform (20 mL), methanol (40 mL), and pure water (12 mL) was added to the mitochondrial solution, and mixed for 2 min. Additional chloroform (20 mL) was added to the solution mixture, and the solution was mixed for 30 s. Subsequently, pure water (20 mL) was added to the sample solution, and the solution was mixed for another 30 s (the final proportion of chloroform, methanol, and water was 2 : 2 : 1.8).[47] The sample was filtered through filter paper on a Buchner funnel and transferred to a separatory funnel. After allowing a few minutes for complete separation and clarification of the solutions, the chloroform layer containing the mitochondrial lipids was collected.

Preparation of LUVs

Lipid components of DOPG, DOPC, DOPE, DOPC/DOPG (DOPG, 8–95%), DOPC/CL (3 : 1), DOPC/DOPE/CL (DOPC : DOPE = 2 : 1; CL (TOCL/TMCL), 5–50% of total lipids), or lipids separated from mitochondria were dissolved in chloroform in a flask. The chloroform solvent was removed with a rotary evaporator at 40 °C, forming a thin lipid film on the wall of the flask. Residual chloroform in the thin lipid film was completely removed by drying *in vacuo* for 3 h. The lipids were hydrated by addition of a buffer with desired pH (2.0–8.3) at 40 °C. The lipid solution was mixed with a vortex mixer for ~2 min for complete dissolution of the lipids. Seven cycles of freeze-and-thaw were performed at −196 and 50 °C to obtain multilamellar vesicles (MLVs). MLVs were extruded 15 times through two stacked polycarbonate membrane filters (pore size, 100 nm) equipped in a Liposo Fast mini extruder (Avestin, USA) to adjust the diameter of LUVs to 100 nm.

Formation and microscopic observation of GUVs

A DOPC/DOPG (1 : 2) or DOPC/DOPE/TOCL (2 : 1 : 1) mixture was dissolved in chloroform in a cylindrical container. A thin lipid film was prepared on the wall of the container as descried above. The lipid film was hydrated with 1 mM HEPES buffer, pH 6.5, containing 200 mM sucrose by placing the buffer gently on the lipid film at 30 °C and incubating overnight, resulting in the formation of GUVs (≥1 μm in diameter).

RHG (0.3 μM) was added to GUVs (total lipid, 500 μM) in 1 mM HEPES buffer, pH 6.5. The solution containing RHG and GUVs was incubated for at least 30 min to obtain uniform fluorescence intensities among different GUV surfaces. GUVs were imaged at room temperature using an Olympus IX 71 microscope (Olympus, Center Valley, PA, USA). An Olympus

60×/1.4 NA Plan Apo oil immersion lens was used as an objective lens. Excitation light was obtained using an Hg lamp with a U-MWIY2 filter set (Olympus; excitation wavelength, 545–580 nm). Microscopic images were recorded using an Orca-Flash2.8 Scientific CMOS Camera (Hamamatsu, Japan).

^{1}H-NMR measurements

^{1}H-NMR spectra were measured in DMSO-d_6 and D_2O in the presence and absence of DOPC/DOPE/TOCL (2 : 1 : 1) or DOPG LUVs (total lipids, 15 mM) with a 300 MHz or 500 MHz NMR spectrophotometer (Bruker, USA) using tetramethylsilane (δ = 0) as a standard. The pD of the D_2O medium in the presence and absence of LUVs was adjusted to 4.5–6.5 by addition of 0.01 M CF_3COOH.

Absorption and fluorescence measurements

The UV-vis optical absorption and fluorescence measurements were performed with a UV-2450 spectrophotometer (Shimadzu, Japan). Fluorescence measurements were performed with a PerkinElmer LS-55 spectrofluorimeter (PerkinElmer, USA) or a Fluoromax-4 spectrophotometer (HORIBA, USA). RHG (0.05–2.0 μM) was mixed with LUVs (total lipids, 0–2.0 mM), and the UV-vis absorption spectra (RHG, 2 μM) and fluorescence spectra (RHG, 0.05–1.0 μM) were measured at 25 °C in the presence and absence of cyt *c* (0.5–5.0 μM) with and without DOPC/DOPE/CL LUVs (DOPC : DOPE = 2 : 1; CL (TOCL/TMCL), 5–50%). The spectra were also measured for DOPC/TOCL (3 : 1) LUVs and LUVs of mitochondrial lipids at pH 3.0–8.3, DOPC and DOPE LUVs at pH 3.5–5.0, DOPC/DOPG and DOPG LUVs (DOPG, 8–100%) at pH 2.0–7.0, and buffers containing ethanol (35–58% (w/w)) at pH 1.5–6.0. The fluorescence spectrum of RHG was corrected by subtracting the background intensity. The UV-vis absorption/fluorescence spectra were normalized by dividing them by the intensities of the corresponding spectra at 532/554 nm in the buffer medium and 539/560 nm in the buffer containing LUVs or ethanol, where the intensities were saturated by lowering the pH. The saturated spectra used for the calculations were measured at pH 3.0 for DOPC/DOPE/CL LUVs (DOPC : DOPE = 2 : 1; CL (TOCL/TMCL), 5–50%) and LUVs of mitochondrial lipids, pH 2.0 for DOPC, DOPE, DOPG and DOPC/DOPG LUVs, and pH 1.5 for buffers containing ethanol. The plots of normalized intensities *vs.* bulk pH were fitted with sigmoidal-Boltzmann equations. The bulk and interface H^+ concentrations were calculated from the bulk pH and interface pH′ values, respectively.

The UV-vis absorption spectra of PMP were measured in the presence and absence of DOPC/DOPE/CL (2 : 1 : 1), DOPC/DOPE (2 : 1), DOPC, or DOPG LUVs (total lipid, 3 mM) and LUVs of lipids from the mitochondrial membranes in 10 mM HEPES buffer, pH 6.5. The dielectric constant (*D*) at the LUV interface was estimated using the following relation as reported previously.[29]

$$\varepsilon_{420}{}^{D}/\varepsilon_{420}{}^{8.0} = 0.42 \times D - 1.8 \quad (3)$$

The extinction coefficient at 420 nm for the buffer containing LUVs ($\varepsilon_{420}{}^{D}$) was divided by that for THF ($\varepsilon_{420}{}^{8.0}$), where *D* of THF is 8.0.

The UV-vis absorption spectra of cyt *c* (10–20 μM) in the 600–800 nm region were measured in the presence of H_2O_2 and 2-methoxyphenol (5 μM) at pH 3.9, 5.3, and 6.8 in citrate–phosphate buffer (a mixture of 10 mM sodium phosphate and 10 mM sodium citrate solutions), 10 mM cacodylate buffer, and 10 mM HEPES buffer, respectively, at 25 °C.

Determination of the fluorescence quantum yield

The fluorescence quantum yields of RHG (1 μM) in the presence of DOPC/DOPE/TOCL LUVs (total lipid, 1 mM) containing various TOCL% (5–25% of total lipids) were determined by adapting the procedure described previously.[48] In brief, 9,10-diphenylanthracene in ethanol was used as the reference fluorophore with fluorescence quantum yield (ϕ_r) = 0.95. The fluorescence quantum yield of RHG (ϕ_s) in the presence of LUVs was measured by using the following equation:

$$\phi_s = (A_r F_s n_s / A_s F_r n_r) \times \phi_s \quad (4)$$

where *A* is the absorbance at the excitation wavelength, *F* is the integrated emission area, and *n* is the refractive index of the solvent used. Subscripts refer to the ethanol (r) and LUV (s) media.

Binding assay of RHG to LUVs

After mixing RHG (2.0 μM) with DOPC/DOPE/TOCL (2 : 1 : 1) LUVs (total lipid, 2 mM) at pH 4.5–8.0, unbound RHG molecules were collected with a centrifugal filter (Amicon Ultra, Millipore; cut-off, 100k MW). The amount of RHG in the filtrate was calculated from the concentration of unbound RHG estimated by measuring the UV-vis absorption spectrum after adjusting the pH to 2.0.

DSC measurements

DSC thermograms of oxidized horse cyt *c* (100 μM) at pH 3.9, 5.3, and 6.8 in citrate–phosphate buffer (a mixture of 10 mM sodium phosphate and 10 mM sodium citrate solutions), 10 mM cacodylate buffer, and 10 mM HEPES buffer, respectively, were measured with a VP-DSC calorimeter (MicroCal, GE Healthcare) at a scan rate of 1 °C min^{-1}.

Peroxidase activity measurements

The catalytic steady-state kinetics of ABTS oxidation was investigated with a UV-2450 spectrophotometer (Shimadzu) at 25 °C. The oxidation of ABTS (40 μM) with H_2O_2 (0–4 mM) was catalyzed by oxidized horse cyt *c* (5 μM) at pH 3.6–4.3, 5.3, and 6.8 in citrate–phosphate buffer (a mixture of 10 mM sodium phosphate and 10 mM sodium citrate solutions), 10 mM cacodylate buffer, and 10 mM HEPES buffer, respectively. The steady-state reaction rates were obtained by monitoring the absorbance at 730 nm using a molar absorption coefficient of 14 mM^{-1} cm^{-1} for ABTS oxidation.[39] The reaction rate was

determined from the initial reaction. Each experiment was repeated at least three times.

Conflicts of interest

The authors declare no competing financial interest.

Acknowledgements

We thank Mr Leigh McDowell, NAIST, for his advice on manuscript preparation. This work was partially supported by Grants-in-Aid from JSPS for Scientific Research (Category B, no. JP18H02088 (SH) and Innovative Areas, no. JP16H00839 (SH)). PPP acknowledges UGC and the Government of West Bengal for financial support under the RUSA 2.0 scheme (no. 5400-F(Y)), and DST for a Special Grant to the Department of Chemistry, JU in the International Year of Chemistry 2011.

Notes and references

1 (*a*) O. S. Andersen and R. E. Koeppe, *Annu. Rev. Biophys. Biomol. Struct.*, 2007, **36**, 107–130; (*b*) A. Finkelstein, *J. Gen. Physiol.*, 1976, **68**, 127–135.

2 J. Kim, J. H. Jeon, H. J. Kim, H. Lim and I. K. Oh, *ACS Nano*, 2014, **8**, 2986–2997.

3 R. T. Uren, G. Dewson, C. Bonzon, T. Lithgow, D. D. Newmeyer and R. M. Kluck, *J. Biol. Chem.*, 2005, **280**, 2266–2274.

4 (*a*) F. Ramirez and D. B. Rifkin, *Matrix Biol.*, 2003, **22**, 101–107; (*b*) H. K. Kim, H. Wei, A. Kulkarni, R. M. Pogranichniy and D. H. Thompson, *Biomacromolecules*, 2012, **13**, 636–644.

5 L. J. Earp, S. E. Delos, H. E. Park and J. M. White, in *Membrane Trafficking in Viral Replication*, ed. M. Marsh, Springer-Verlag, Heidelberg, 2005, vol. 285, pp. 25–66.

6 J. Santo-Domingo and N. Demaurex, *J. Gen. Physiol.*, 2012, **139**, 415–423.

7 D. Poburko, J. Santo-Domingo and N. Demaurex, *J. Biol. Chem.*, 2011, **286**, 11672–11684.

8 G. Azarias, H. Perreten, S. Lengacher, D. Poburko, N. Demaurex, P. J. Magistretti and J. Y. Chatton, *J. Neurosci.*, 2011, **31**, 3550–3559.

9 R. Orij, J. Postmus, A. Ter Beek, S. Brul and G. J. Smits, *Microbiology*, 2009, **155**, 268–278.

10 B. Rieger, W. Junge and K. B. Busch, *Nat. Commun.*, 2014, **5**, 3103.

11 (*a*) E. London and D. A. Brown, *Biochim. Biophys. Acta*, 2000, **1508**, 182–195; (*b*) K. Kuroda and G. A. Caputo, *Wiley Interdiscip. Rev.: Nanomed. Nanobiotechnol.*, 2013, **5**, 49–66.

12 (*a*) A. Küchler, M. Yoshimoto, S. Luginbühl, F. Mavelli and P. Walde, *Nat. Nanotechnol.*, 2016, **11**, 409–420; (*b*) T. Ravula, C. Barnaba, M. Mahajan, G. M. Anantharamaiah, S. C. Im, L. Waskell and A. Ramamoorthy, *Chem. Commun.*, 2017, **53**, 12798–12801.

13 (*a*) C. Rottman and D. Avnir, *J. Am. Chem. Soc.*, 2001, **123**, 5730–5734; (*b*) H. Chakraborty, R. Banerjee and M. Sarkar, *Biophys. Chem.*, 2003, **104**, 315–325; (*c*) A. Chakrabarty, A. Mallick, B. Haldar, P. Purkayastha, P. Das and N. Chattopadhyay, *Langmuir*, 2007, **23**, 4842–4848.

14 (*a*) S. Yamaguchi, K. Bhattacharyya and T. Tahara, *J. Phys. Chem. C*, 2011, **115**, 4168–4173; (*b*) A. Kundu, S. Yamaguchi and T. Tahara, *J. Phys. Chem. Lett.*, 2014, **5**, 762–766.

15 (*a*) A. R. Gear, *J. Biol. Chem.*, 1974, **249**, 3628–3637; (*b*) R. C. Scaduto and L. W. Grotyohann, *Biophys. J.*, 1999, **76**, 469–477; (*c*) M. Beija, C. A. M. Afonso and J. M. G. Martinho, *Chem. Soc. Rev.*, 2009, **38**, 2410–2433.

16 (*a*) Y. Sarkar, S. Das, A. Ray, S. K. Jewrajka, S. Hirota and P. P. Parui, *Analyst*, 2016, **141**, 2030–2039; (*b*) R. Majumder, Y. Sarkar, S. Das, A. Ray and P. P. Parui, *New J. Chem.*, 2017, **41**, 8536–8545; (*c*) Y. Sarkar, R. Majumder, S. Das, A. Ray and P. P. Parui, *Langmuir*, 2018, **34**, 6271–6284.

17 E. Kalanxhi and C. J. Wallace, *Biochem. J.*, 2007, **407**, 179–187.

18 (*a*) M. Ott, J. D. Robertson, V. Gogvadze, B. Zhivotovsky and S. Orrenius, *Proc. Natl. Acad. Sci. U. S. A.*, 2002, **99**, 1259–1263; (*b*) M. Huttemann, P. Pecina, M. Rainbolt, T. H. Sanderson, V. E. Kagan, L. Samavati, J. W. Doan and I. Lee, *Mitochondrion*, 2011, **11**, 369–381.

19 (*a*) X. Liu, C. N. Kim, J. Yang, R. Jemmerson and X. Wang, *Cell*, 1996, **86**, 147–157; (*b*) X. Saelens, N. Festjens, L. Vande Walle, M. van Gurp, G. van Loo and P. Vandenabeele, *Oncogene*, 2004, **23**, 2861–2874.

20 P. R. Magalhaes, A. S. Oliveira, S. R. Campos, C. M. Soares and A. M. Baptista, *J. Chem. Inf. Model.*, 2017, **57**, 256–266.

21 A. Ranieri, F. Bernini, C. A. Bortolotti, A. Bonifacio, V. Sergo and E. Castellini, *Langmuir*, 2011, **27**, 10683–10690.

22 (*a*) Y. A. Vladimirov, E. V. Proskurnina, D. Y. Izmailov, A. A. Novikov, A. V. Brusnichkin, A. N. Osipov and V. E. Kagan, *Biochemistry (Moscow).*, 2006, **71**, 998–1005; (*b*) N. A. Belikova, Y. A. Vladimirov, A. N. Osipov, A. A. Kapralov, V. A. Tyurin, M. V. Potapovich, L. V. Basova, J. Peterson, I. V. Kurnikov and V. E. Kagan, *Biochemistry*, 2006, **45**, 4998–5009; (*c*) S. Hirota, Y. Hattori, S. Nagao, M. Taketa, H. Komori, H. Kamikubo, Z. Wang, I. Takahashi, S. Negi, Y. Sugiura, M. Kataoka and Y. Higuchi, *Proc. Natl. Acad. Sci. U. S. A.*, 2010, **107**, 12854–12859; (*d*) Z. Wang, T. Matsuo, S. Nagao and S. Hirota, *Org. Biomol. Chem.*, 2011, **9**, 4766–4769; (*e*) J. Hanske, J. R. Toffey, A. M. Morenz, A. J. Bonilla, K. H. Schiavoni and E. V. Pletneva, *Proc. Natl. Acad. Sci. U. S. A.*, 2012, **109**, 125–130; (*f*) L. J. McClelland, H. B. Steele, F. G. Whitby, T. C. Mou, D. Holley, J. B. Ross, S. R. Sprang and B. E. Bowler, *J. Am. Chem. Soc.*, 2016, **138**, 16770–16778.

23 (*a*) A. M. Porcelli, A. Ghelli, C. Zanna, P. Pinton, R. Rizzuto and M. Rugolo, *Biochem. Biophys. Res. Commun.*, 2005, **326**, 799–804; (*b*) J. R. Casey, S. Grinstein and J. Orlowski, *Nat. Rev. Mol. Cell Biol.*, 2010, **11**, 50–61.

24 J. J. Krebs, H. Hauser and E. Carafoli, *J. Biol. Chem.*, 1979, **254**, 5308–5316.

25 J. X. Xu, B. C. N. Vithanage, S. A. Athukorale and D. M. Zhang, *Analyst*, 2018, **143**, 3382–3389.

26 E. Mileykovskaya, W. Dowhan, R. L. Birke, D. H. Zheng, L. Lutterodt and T. H. Haines, *FEBS Lett.*, 2001, **507**, 187–190.

27 G. Olofsson and E. Sparr, *PLoS One*, 2013, **8**, e73040.
28 M. Sathappa and N. N. Alder, *Biochim. Biophys. Acta*, 2016, **1858**, 1362–1372.
29 R. Majumder, Y. Sarkar, S. Das, S. K. Jewrajka, A. Ray and P. P. Parui, *Analyst*, 2016, **141**, 3246–3250.
30 G. Akerlof, *J. Am. Chem. Soc.*, 1932, **54**, 4125–4139.
31 P. A. Beales, C. L. Bergstrom, N. Geerts, J. T. Groves and T. K. Vanderlick, *Langmuir*, 2011, **27**, 6107–6115.
32 S. Atalay, M. Barisik, A. Beskok and S. Z. Qian, *J. Phys. Chem. C*, 2014, **118**, 10927–10935.
33 H. Kobayashi, S. Nagao and S. Hirota, *Angew. Chem., Int. Ed.*, 2016, **55**, 14019–14022.
34 (*a*) Y. Kuroda, S. Kidokoro and A. Wada, *J. Mol. Biol.*, 1992, **223**, 1139–1153; (*b*) S. Cinelli, F. Spinozzi, R. Itri, S. Finet, F. Carsughi, G. Onori and P. Mariani, *Biophys. J.*, 2001, **81**, 3522–3533.
35 T. D. Perroud, M. P. Bokoch and R. N. Zare, *Proc. Natl. Acad. Sci. U. S. A.*, 2005, **102**, 17570–17575.
36 (*a*) J. Bagel'ova, M. Antalik and M. Bona, *Biochem. J.*, 1994, **297**(1), 99–101; (*b*) L. Wang, E. V. Rivera, M. G. Benavides-Garcia and B. T. Nall, *J. Mol. Biol.*, 2005, **353**, 719–729.
37 S. Papadopoulos, K. D. Jurgens and G. Gros, *Biophys. J.*, 2000, **79**, 2084–2094.
38 (*a*) L. Wan, M. B. Twitchett, L. D. Eltis, A. G. Mauk and M. Smith, *Proc. Natl. Acad. Sci. U. S. A.*, 1998, **95**, 12825–12831; (*b*) R. Radi, L. Thomson, H. Rubbo and E. Prodanov, *Arch. Biochem. Biophys.*, 1991, **288**, 112–117.
39 T. Matsui, S. Ozaki, E. Liong, G. N. Phillips and Y. Watanabe, *J. Biol. Chem.*, 1999, **274**, 2838–2844.
40 (*a*) R. Kitz and I. B. Wilson, *J. Biol. Chem.*, 1962, **237**, 3245–3249; (*b*) S. Prasad, N. C. Maiti, S. Mazumdar and S. Mitra, *Biochim. Biophys. Acta*, 2002, **1596**, 63–75.
41 (*a*) Y. R. Chen, L. J. Deterding, B. E. Sturgeon, K. B. Tomer and R. P. Mason, *J. Biol. Chem.*, 2002, **277**, 29781–29791; (*b*) A. D. Nugraheni, C. Ren, Y. Matsumoto, S. Nagao, M. Yamanaka and S. Hirota, *J. Inorg. Biochem.*, 2018, **182**, 200–207.
42 D. Mohammadyani, N. Yanamala, A. K. Samhan-Arias, A. A. Kapralov, G. Stepanov, N. Nuar, J. Planas-Iglesias, N. Sanghera, V. E. Kagan and J. Klein-Seetharaman, *Biochim. Biophys. Acta*, 2018, **1860**, 1057–1068.
43 L. V. Basova, I. V. Kurnikov, L. Wang, V. B. Ritov, N. A. Belikova, Vlasova, II, A. A. Pacheco, D. E. Winnica, J. Peterson, H. Bayir, D. H. Waldeck and V. E. Kagan, *Biochemistry*, 2007, **46**, 3423–3434.
44 M. Abe, R. Niibayashi, S. Koubori, I. Moriyama and H. Miyoshi, *Biochemistry*, 2011, **50**, 8383–8391.
45 W. Huang, P. Zhou, W. Yan, C. He, L. Xiong, F. Li and C. Duan, *J. Environ. Monit.*, 2009, **11**, 330–335.
46 R. Majumder, Y. Sarkar, S. Das, S. K. Jewrajka, A. Ray and P. P. Parui, *Analyst*, 2016, **141**, 3246–3250.
47 E. G. Bligh and W. J. Dyer, *Can. J. Biochem. Physiol.*, 1959, **37**, 911–917.
48 J. V. Morris, M. A. Mahaney and J. R. Huber, *J. Phys. Chem.*, 1976, **80**, 969–974.

NJC

PAPER

View Article Online
View Journal | View Issue

Cite this: *New J. Chem.*, 2019, **43**, 3750

Glutathione-selective "off–on" fluorescence response by a probe-displaced modified ligand for its detection in biological domains†

Partha Pratim Parui, *[a] Ambarish Ray, *[b] Sanju Das,[ab] Yeasmin Sarkar,[a] Tanaya Paul,[c] Snigdha Roy,[a] Rini Majumder[a] and Jaya Bandyopadhyay[c]

Received 14th November 2018,
Accepted 25th January 2019

DOI: 10.1039/c8nj05784b

rsc.li/njc

The detection of a specific biothiol in a mixture of biothiols is a challenging task because of their similarity in structure and reactivity. To discriminate between glutathione (GSH) and cysteine (Cys)/homocysteine (Hcy) at physiological pH, the fluorometric "off–on" displacement approach was adopted, utilizing a Cu(II)-complex of a Schiff-base ligand (**L_1**) containing a phenolic aldimine group attached to a triazole moiety along with a dangling benzylic alcohol branch. The weakly fluorescent **L_1** (quantum yield (ϕ_F) ~ 0.006) formed a non-fluorescent 1 : 1 Cu(II)/**L_1** stoichiometric complex (**1**) and remained as a dimeric $[Cu–L_1]_2^{2+}$ species in an aqueous medium. The Cu(II)-centre in **1** is highly susceptible to interactions with the –SH moiety of biothiol to participate in demetallation reactions. Unlike other solvents, the GSH-induced decomplexation of **1** generates strong fluorescence intensity in an aqueous medium, indicating the liberation of the modified **L_1** (**L_1**′). Experimental evidence suggests that the benzylic alcohol moiety of **L_1** is itself oxidized to the formyl group during the course of the GSH interaction with **1**. However, Cys/Hcy liberates **L_1** by the partial decomplexation of **1** (~40%) in the usual displacement pathway to exhibit an intensity increase of less than 5% in comparison to GSH under similar experimental conditions. Unlike **L_1**, there was an acidity increase by about 2.5 pH units for the phenolic-OH of **L_1**′ (pK_a ~ 7.0) with ~65% phenol to fluorophoric phenolate conversion at pH 7.3, attributed to a large GSH-induced increase in the fluorescence intensity (ϕ_F = 0.18). It is proposed that GSH induced a comparatively rapid attack at the Cu(II) center in **1**, favouring the possibility for radical generation resulting in ligand modification of **L_1**′ along with decomplexation. This is the first report of a biothiol-selective ligand modification exhibiting an "off–on" fluorescence response in the displacement strategy. For biogenic GSH detection and its effect on different biothiol quenchers, *in vivo* fluorescence imaging was carried out in the multicellular domain on *Caenorhabditis elegans* (*C. elegans*), as well as in living human neuroblastoma SH-SY5Y cells. GSH depletion in the presence of a pain killer drug, acetaminophen, was also monitored for *C. elegans*.

Introduction

Biological thiols, including glutathione (GSH), cysteine (Cys), and homocysteine (Hcy), are essential for controlling many fundamental biochemical processes.[1–3] A number of studies have shown that different biothiols and their biological functions are highly interrelated.[2–4] A high GSH concentration in cells (1–10 mM) acts as a vital endogenous antioxidant to protect the cells from undesired toxins and free radicals.[5] The change in GSH level can lead to leukocyte loss, AIDS, heart problems, neurological disorders and other ailments.[6–9] The excessive use of certain drugs including apparently safe painkillers may deplete the normal GSH levels in liver and kidney cells resulting in severe multi-organ damage.[10] Therefore, a precise estimation of *in vivo* GSH concentration is very important. However, the accurate detection of GSH in the presence of Cys/Hcy is highly challenging due to their close similarity in chemical reactivity.[11] In addition, the inter-convertibility equilibrium among the biothiols in cells makes the detection of GSH more complicated under *in vivo* conditions.[12]

For selective biothiol detection, the fluorescence technique is highly advantageous due to its high sensitivity, rapid sensing ability, low-detection limit and suitability for bio-imaging.[13–15] To date, a number of small organic fluorescent probes have been designed for the detection of GSH by excluding Cys and Hcy.[16–22]

[a] *Department of Chemistry, Jadavpur University, Kolkata 700032, India. E-mail: parthaparui@yahoo.com; Fax: +91-33-24146223; Tel: +91-9433490492*
[b] *Department of Chemistry, Maulana Azad College, Kolakta 700013, India. E-mail: r_ambarish@yahoo.co.in; Fax: +91-33-22268111; Tel: +91-9836650180*
[c] *Department of Biotechnology, Maulana Abul Kalam Azad University of Technology, Kolkata 700064, India*

† Electronic supplementary information (ESI) available. See DOI: 10.1039/c8nj05784b

Among them, Yoon and co-workers reported sulfonamide group-attached cyanine-based near-infrared fluorescent molecules for the detection of *in vivo* GSH concentration.[16] The probe was also exploited to determine the reduction of GSH levels in mouse tissue by injecting a large amount of pain killer, acetaminophen (APAP). Other GSH induced fluorescence ''off–on'' behavior for rhodamine/BODIPY/coumarin-based probes with effective cell imaging facilities were reported by different research groups.[20–22] However, in most cases, the requirement for a toxic organic medium to solubilize the giant organic probe molecule in a buffer can be a major concern for GSH detection in biological systems. In this regard, nontoxic ionic metal complexes that are soluble in a pure aqueous medium are more purposeful. Commonly, a suitable fluorophoric ligand is chosen for complexation to generate the cationic probe in its 'off-mode' fluorescence sensing, which on interaction with the –SH moiety of the specific biothiol undergoes subsequent decomplexation to liberate the fluorescent ligand in its 'on-mode' of sensing. This approach to detection is known as the ''co-ordination complex-based displacement approach''.[23]

Using a similar route, we recently reported a number of fluorescent probes by choosing cationic Cu(II) chromophores in aqueous medium.[24–26] The difference in decomplexation ability among different biothiols was exploited to detect specific biothiols. However, the magnitude of decomplexation for apparently less reactive biothiols may considerably increase in high concentration. Therefore, the detection of specific biothiols in the heterogeneous distribution of different biothiols under *in vivo* conditions is not always straightforward and convincing. Herein, we report a unique displacement strategy, in which the specific biothiol detection exclusively depends on the modification from non-fluorescent to highly fluorophoric ligand transformation during the demetalization process. A dimeric Cu(II) complex (**1**) of a non-fluorescent Schiff base ligand ($\mathbf{L_1}$) containing a phenolic aldimine group attached to a triazole moiety with a dangling benzylic alcohol branch was synthesized and exploited for fluorometric GSH detection *via* the ''off–on'' mode of sensing. A large GSH-induced fluorescence intensity enhancement was observed due to the liberation of a partially modified ligand ($\mathbf{L_1}'$) generated by the oxidation of the benzyl alcoholic moiety of $\mathbf{L_1}$ into formyl during the demetalization process. In contrast, Cys/Hcy under similar experimental conditions liberated unchanged $\mathbf{L_1}$ during decomplexation to exhibit a negligibly small amount of fluorescence intensity as compared to that of GSH. This unique GSH detection method, by discriminating other biothoils (Cys/Hcy), was well explored in bio-imaging for the multi-cellular organism, *Caenorhabditis elegans* (*C. elegans*) as well as human SH-SY5Y (neuroblastoma) living cells. GSH depletion by the addition of excessive pain killer, APAP, was also monitored.

Experimental

General methods

Most of the reagents were procured from Sigma-Aldrich (USA) and used as received. All measurements were carried out using Mili-Q Millipore® water with conductivity 18.2 MΩ cm. Different buffer compositions were used to obtain specific medium pH: HEPES–NaOH for pH 6.0–7.5, Tris–HCl for pH 7.5–9.0. The concentration of generated hydrogen peroxide in the buffer solution was estimated with the MAK165 kit (Sigma-Aldrich (USA)), where the H_2O_2 concentration was evaluated from the standard curve according to the manufacturer kit protocol. The solvents saturated with oxygen were achieved by purging oxygen for ~15 min. The ESI-MS$^+$, NMR and IR spectra were recorded on a Waters Qtof Micro YA263 mass spectrometer, Bruker 300 MHz NMR Spectrophotometer and Perkin-Elmer Spectrum-2 spectrophotometer equipped with Zn–Se ATR, respectively. EPR experiments were performed using a JEOL JES-FA-200 instrument at liquid nitrogen temperature (77 K) in water/MeCN 1 : 1 mixture. CHN analysis, pH measurement and bio-imaging studies were carried out in a Perkin-Elmer 240-elemental analyzer, Systronics digital pH meter and Leica DM-3000 fluorescence microscope (excitation ~480 nm) fitted with a Leica DFC-450 C Camera (Leica FireWire V1.39.0), respectively.

Synthesis of ligands ($\mathbf{L_1}$ and $\mathbf{L_1}'$)

The ligand ($\mathbf{L_1}$) was synthesized as previously reported, with a better yield using slight modification.[27] Briefly, 2 mmol (0.168 g) of 4-amino-4*H*-1,2,4-triazole (Tz) was dissolved in 20 mL of methanol and added dropwise to an equimolar amount (2 mmol, 0.332 g) of 2-hydroxy-3-(hydroxymethyl)-5-methylbenzaldehyde (HHMB) with constant stirring. After adding 0.1 mL of acetic acid, the yellow solution was refluxed for 4 h, followed by cooling and filtration. The filtrate became a yellow solid mass after rotary evaporation, which was dried and further purified from acetonitrile–water. Yield: ~71% as compared to the starting aldehyde. M.P. 187 °C. CHN analysis; calcd (obsd.): $C_{11}H_{12}N_4O_2$: C, 56.89 (56.18); H, 5.21 (5.27); N, 24.12 (24.35)%; selected IR in cm^{-1} (KBr): 3300–3200 (br), 3094 (w), 2920 (w), 2881 (w), 1622 (s), 1596 (s), 1512 (s). The structural analyses were performed by NMR and ESI-MS$^+$ measurements (see details in ESI:† S1A, B and S3A).

The synthesis of the starting material, 2,6-diformyl-*p*-cresol (DFC) for obtaining $\mathbf{L_1}'$ is described elsewhere.[28] Briefly, equimolar proportions of DFC (2 mmol, 0.328 g) and Tz (2 mmol, 0.168 g) along with 0.1 mL acetic acid were mixed in anhydrous methanol with constant stirring, refluxed for 4 h and then filtered. A deep yellow colored crude solid was obtained from the filtrate under reduced pressure. The impurities were removed by a column chromatographic technique using petroleum ether–ethylacetate (8 : 2, v/v) eluent and the desired product was collected, recrystallized and dried over $CaCl_2$ under vacuum; yield: 35.4% with respect to DFC. M.P. 192 °C. CHN analysis; calcd (obsd.): $C_{11}H_{10}N_4O_2$; C, 57.39 (57.42); H, 4.38 (4.25); N, 24.34 (24.51)%; selected IR in cm^{-1} (KBr): 3400–3320 (br), 3130 (m), 1651 (s), 1507 (s), 1310 (s), 1163 (s), 1056(s) (Fig. S10B, ESI†). ^{1}H NMR (DMSO-d$_6$, 300 MHz): δ = 2.33 (s, 3H, ArCH$_3$), 7.76 (s, 1 H, ArH), 7.89 (s, 1 H, ArH), 9.18 (d, 3H, imine-H, and Tz-2H), 10.19 (d, 1H, aldehydic-H) 11.13 (s, 1H, ArOH) ppm. ^{13}C NMR (DMSO-d$_6$, 75 MHz): 20.57, 58.40, 117.11, 128.72, 129.08, 130.78, 132.88, 139.25, 153.39, 158.74 ppm (see details in ESI:† S2A and B). ESI-MS$^+$ for $\mathbf{L_1}'$ in water: *m*/*z* calcd (obsd.) for $[\mathbf{L_1}' + H]^+$: 231.235 (231.088) (Fig. S3B, ESI†).

Generation of probe 1

The *in situ* complex (probe **1**) in water was generated by gradually adding 10 mL of 1 mM aqueous $Cu(ClO_4)_2$ solution (10 μmol, 3.7 mg) to an equimolar amount of $\mathbf{L_1}$ (10 μmol, 2.3 mg) with continuous stirring for 30 min, followed by filtration. The formation of **1** was verified by UV-Vis absorption studies. Mass spectral analysis of the filtrate confirmed the existence of the dinuclear entity $[Cu\text{–}\mathbf{L_1}\cdot 2H_2O]_2^{2+}$ (**1**): *m*/*z* calcd (obsd.) for $[C_{22}H_{26}N_8O_6Cu_2 + ClO_4]^+$: 725.038 (725.109) (Fig. S3C, ESI†). The composition of the *in situ* complex (**1**) remained unchanged in 20 mM HEPES–NaOH buffer at pH 7.3, consistent with the ESI-MS^+. Selected IR in cm^{-1} (Zn–Se ATR): 3400–3200 (br), 3052 (s), 2978 (s), 1422 (s), 1263 (s).

UV-Vis absorption and fluorescence measurements

UV-Vis absorption and fluorescence investigations were performed in solution at 25 °C with a UV-2450 (Shimadzu, Japan) and LS-55 (Perkin Elmer, USA), respectively. Absorption and fluorescence spectra were monitored with a quartz cuvette with a path length of 10 mm. Fluorescence spectra were obtained for different excitation wavelengths (340–440 nm). To obtain the time profile of absorption and fluorescence changes, stock solutions of different reactants were injected in the measuring solution under continuous stirring with a small bar magnet at speed of ~130 rpm. The solutions were filtered using a 0.45 mm filter (Millex, Millipore) before measurements. The reproducibility of time-course and spectral data were verified by triplicate measurements.

The fluorescence quantum yields of $\mathbf{L_1}$ and $\mathbf{L_1}'$ were estimated by as reported elsewhere.[29] The ethanolic solution of 9,10-diphenylanthracene was considered as the reference fluorophore with a quantum yield (ϕ_F^r) = 0.95. The ϕ_F of the unknown sample was determined from the equation below:

$$\phi_F^s = [A_r F_s n_s^2 / A_s F_r n_r^2]\cdot\phi_F^r \quad (1)$$

where, the absorbance and fluorescence are represented by *A* and *F*, respectively. The refraction index is denoted by *n*. The reference (r) or sample (s) compounds are represented by subscripts. By using the above eqn (1), $\phi_F \sim 0.006$ and 0.18 for $\mathbf{L_1}$ and $\mathbf{L_1}'$ were obtained, respectively, in 20 mM HEPES–NaOH buffer medium at pH 7.3. However, the ϕ_F of $\mathbf{L_1}'$ changed to ~0.27 at pH ~ 9.0. The GSH detection limit was evaluated from the equation below:[30]

$$\text{Detection limit} = K \times S_{bi} \times S \quad (2)$$

Here, $K = 3$, as per the IUPAC convention. S_{bi} is the experimental standard deviation for the blank, and *S* is the slope of the fluorescence increase with respect to GSH concentration. The GSH detection limit was estimated as ~40 nM in 20 mM HEPES–NaOH buffer medium at pH 7.3.

Theoretical calculations

The most probable geometry of **1** was determined using calculations based on density functional theory (DFT) by the Gaussian 09 program.[31] The B3LYP function, the 6-31G+(d,p) basis set for H, C, N, O atoms and LANL2DZ effective core potentials basis set for the Cu atom, were chosen for the calculations. The energetic minima for different structures were assigned from the positive vibrational frequencies. The low-lying excited states using the optimized geometries of the ground states (S_0) were calculated by time-dependent DFT (TD-DFT) considering the B3LYP function.[32,33] The UV-Vis spectra were obtained from TD-DFT calculations.

Bio-imaging studies for multicellular *C. elegans* and human cell line

Strains of *C. elegans* (wild-type N2) and *Escherichia coli* bacteria (OP50) were collected from the worm laboratory, Department of Biotechnology, Maulana Abul Kalam Azad University of Technology, Kolkata 700064, India. Detailed experimental techniques are described elsewhere.[25] Suitably washed worms were exposed to solution **1** (maximum up to 40 μM) in the absence or presence of different pretreated analytes (*N*-ethylmaleimide (NEM) + Cys/GSH/APAP) individually in M9 buffer at pH 7.0 at 37 °C.

For cell line imaging purposes, the human SH-SY5Y cell line was chosen, grown according to standard protocol.[34] Cells were exposed to solution **1** (maximum up to 30 μM with respect to $\mathbf{L_1}$) in the absence or presence of pretreated L-buthionine sulfoximine (BSO) and BSO + *N*-acetylcysteine (NAC).

Toxicity studies

Toxicity studies were conducted by monitoring the survival assays in wild-type (N2) *C. elegans* according to the procedure described elsewhere.[35] Experimental reproducibility was cross-checked in triplicate, with 100 worms ($n = 100$) in each set. Percentage worm survival on exposure to different analytes was statistically calculated. For cell lines, cell viability was measured using the MTT assay as per the standard protocol of keeping controlled culture in normal medium.[36]

Results and discussion

Synthesis and characterization of probe 1

The Schiff-base molecule ($\mathbf{L_1}$) consisting of a phenolic aldimine group attached to a triazole moiety on one end and a benzylic alcohol branch on the other end was designed for complexation with Cu(II). The complex formation reaction between $\mathbf{L_1}$ and Cu(II) was investigated in 20 mM HEPES–NaOH buffer, pH 7.3. In UV-Vis absorption studies, $\mathbf{L_1}$ exhibited absorbances at ~340 nm and a weak intensity centered at 408 nm, due to the nonionic phenol and the anionic phenolate species, respectively, in pH 7.3 buffer (Fig. 1).[37] By increasing the concentration of $Cu(ClO_4)_2$ (0–40 μM or 8 equiv.) in the buffer containing $\mathbf{L_1}$ (5 μM), the absorption intensities at ~340 nm of $\mathbf{L_1}$ were shown to gradually decrease with the concomitant generation of a new absorbances at a close proximity to the phenolate form of $\mathbf{L_1}$ at ~405 nm until the intensity saturation was identified in the presence of 40 μM $Cu(ClO_4)_2$. The isosbestic absorbance at ~370 nm confirmed the generation of the $\mathbf{L_1}$/Cu(II) complex (probe **1**) (Fig. 1). The absorbance at 405 nm for **1** was found to remain unaffected by a change in buffer pH from 6.0 to 9.0, and

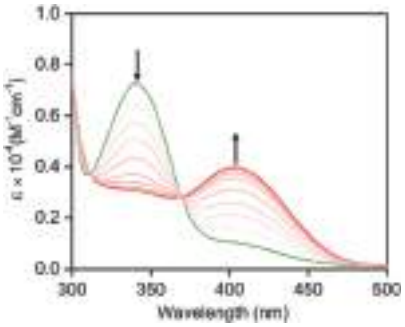

Fig. 1 UV-Vis absorption spectra of $\mathbf{L_1}$ (5 μM) with increasing concentration of $Cu(ClO_4)_2$ (0–40 μM) in 20 mM HEPES–NaOH buffer, pH 7.3 at 25 °C. The spectrum in the absence of $Cu(ClO_4)_2$ is shown in green. The gradual increase or decrease in absorption intensity for different concentrations of $Cu(ClO_4)_2$ is indicated by the arrows.

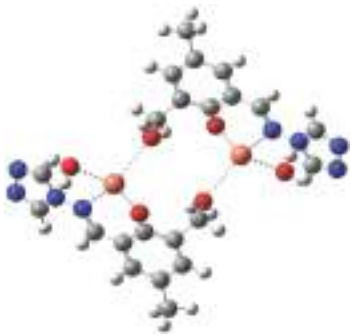

Fig. 2 DFT-optimized structure of **1**; color index: C, gray; N, blue; O, red; H, white and Cu, brown.

the pH-stability of the probe can be useful for pH variation studies (Fig. S4, ESI†). Moreover, in time-dependent studies, the rapid complex formation reaction was confirmed by the Cu^{2+}-induced instantaneous generation of absorption intensity at 405 nm (Fig. S5, ESI†). The complex formation with other transition metal ions (Fe^{2+}, Co^{2+}, Ni^{2+}, Mn^{2+}) was also estimated from UV-Vis absorption studies, where only ~25% of $\mathbf{L_1}$ was found to participate in complexation with Ni^{2+} among those metal ions (8 equiv. each) (Fig. S6, ESI†).

To identify the stoichiometric ratio between Cu(II) and $\mathbf{L_1}$ for **1**, the amount of complex formation was evaluated by estimating the absorbance at 405 nm for different $\mathbf{L_1}$ to Cu(II) mol% (0.1–0.9) according to Job's method (Fig. S7, ESI†). The maximum absorption intensity at an equal mole-ratio between $\mathbf{L_1}$ and Cu(II) suggests a 1 : 1 $\mathbf{L_1}$/Cu(II) stoichiometric ratio in **1**. Formation of the aforementioned complex was also confirmed by the ESI-MS^+ studies. The *m*/*z* peak at 233.216 (calcd *m*/*z*: 233.251) corresponding to $\mathbf{L_1}$ was found to disappear completely with the formation of a new peak at 725.109 by the addition of Cu(II), indicating that the cationic chromophore of the complex **1** exists as a dimeric $[Cu\text{–}\mathbf{L_1}]_2^{2+}$ species (calcd *m*/*z*: 725.038 for $[C_{22}H_{26}N_8O_6Cu_2 + ClO_4]^+$) in the buffer solution (Fig. S3A and C, ESI†). To determine the structure of the dimeric $[Cu\text{–}\mathbf{L_1}]_2^{2+}$ species, DFT-based theoretical calculation was performed. The dimeric Cu(II)-complex is formed by the intermolecular coordination of benzylic-OH.[38,39] Most probably, the monomeric unit is susceptible to dimerizing by coordinating the benzylic-OH from the adjacent monomer due to the lack of enough suitable coordinating sites in $\mathbf{L_1}$. Accordingly, the most probable geometries for $[Cu\text{–}\mathbf{L_1}]_2^{2+}$ in the ground state were optimized to monitor various absorption characteristics between the ground and excited singlet states (Fig. 2). Furthermore, the time-dependent DFT (TD-DFT) calculation was performed on the optimized ground state geometry of $[Cu\text{–}\mathbf{L_1}]_2^{2+}$ to evaluate the oscillator strengths for the vertical electronic transitions. The HOMO (144)→LUMO (145) electronic transition at 418 nm and its extinction coefficient (ε) of $\sim 0.42 \times 10^4$ M^{-1} cm^{-1} closely correspond to the experimental UV-Vis absorption coefficient ($\varepsilon \sim 0.39 \times 10^4$) at 405 nm (Fig. S8, ESI†). These results strongly justify that the chromophore of **1** maintains a dimeric structure in aqueous medium (Fig. 2).

Decomplexation of 1 with different biothiols

The decomplexation reactivity of **1** by the addition of increasing amounts of different biothiols (Cys, Hcy and GSH) in 20 mM of HEPES–NaOH buffer, pH 7.3, containing **1** (5 μM with respect to $\mathbf{L_1}$) were investigated with UV-Vis absorption studies (Fig. 3). By increasing Cys or Hcy concentrations, the UV-Vis absorbances at ~405 nm for **1** (5 μM with respect to $\mathbf{L_1}$) decreased proportionately with the intensity at ~340 nm by maintaining an isosbestic absorbance at ~370 nm, and an intensity saturation was observed in the presence of ~50 equiv. (250 μM) of Cys/Hcy (Fig. 3A and B). The spectrum of **1** in the presence of the intensity saturated amount of Cys/Hcy was almost similar to that of $\mathbf{L_1}$, indicating

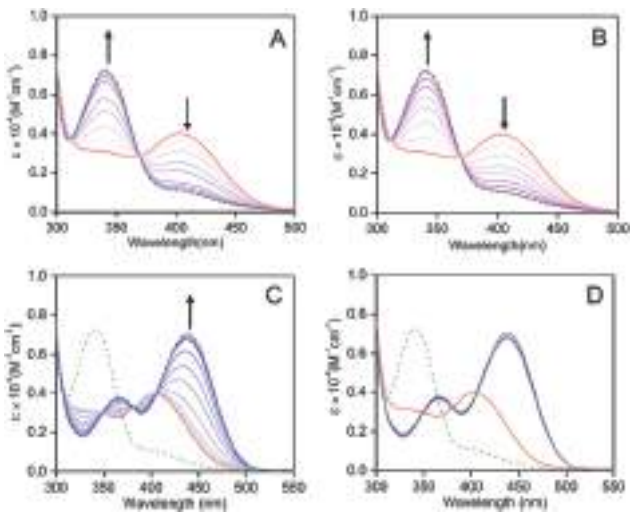

Fig. 3 (A–C) UV-Vis absorption spectra of **1** (5 μM with respect to $\mathbf{L_1}$) with increasing concentration of different biothiols in 20 mM of pH 7.3 HEPES–NaOH buffer at 25 °C: A, Cys (0–250 μM); B, Hcy (0–250 μM) and C, GSH (0–100 μM). (D) The spectra of **1** in the presence of the intensity saturated concentrations of mixed biothiols GSH + Cys (violet), GSH + Hcy (purple) and GSH + Cys + Hcy (dark cyan) (for Cys/Hcy: 250 μM; GSH: 100 μM). The gradual increase or decrease in the absorption intensity for different concentrations of biothiols is indicated by the arrows. The spectra in the absence of biothiols are depicted by red. The spectrum for $\mathbf{L_1}$ (broken line in green) is shown for comparison.

the regeneration of $\mathbf{L_1}$ due to Cys or Hcy-induced decomplexation of **1** (Fig. 3A and B). Recently, we showed that the –SH moiety of biothiols is highly susceptible to interacting with and reducing the Cu(II) center into Cu(I) for various Cu(II)-complexes, triggering the decomplexation process.[25,26] The unstable displaced Cu(I) may be instantaneously converted into Cu(II) by aerial oxidation in aqueous medium. Consequently, the *in situ* regeneration and decomplexation of **1** may occur in a repetitive cyclic pathway in aqueous buffer until the major portion of Cys is converted into cysteine (the oxidized form of Cys), which probably justifies the requirement of the relatively high biothiol concentration (~50 equiv.) to obtain complete demetalization of **1**.

In comparison to Cys or Hcy, a different absorption profile was obtained for the GSH-induced decomplexation of **1**. By the addition of increasing GSH concentration, the absorbances at ~440 nm and ~365 nm steadily increased with the proportionate decrease in the intensity at ~327 nm and ~390 nm by maintaining isosbestic absorption at ~348 nm, ~380 nm and 405 nm, respectively (Fig. 3C), indicating the decomplexation of **1**. Interestingly, the saturation of the absorption intensity due to the decomplexation of **1** was detected at a 2.5-fold lower concentration of GSH (100 μM, 20 equiv.) than Cys/Hcy. In addition, time-course UV-Vis absorption studies show that the decomplexation reaction was rapidly saturated for GSH in ~10 s with a rate constant (k) of ~0.4 s^{-1} as compared to Cys/Hcy in 40 s with k ~ 0.1 s^{-1} in the presence of the respective intensity-saturated biothiols (Fig. S9, ESI†). However, the different absorption characteristics of **1** in the presence of intensity saturated concentration between Cys/Hcy and GSH suggest that the ligand ($\mathbf{L_1}'$) liberated by the GSH-induced decomplexation of **1** is somehow different from that of $\mathbf{L_1}$ (Fig. 3 and Scheme 1). Presumably, the decreased *in situ* complexation affinity between $\mathbf{L_1}'$ and Cu(II) after the decomplexation of **1** affects relatively lower values for the minimum required concentration of GSH as compared to Cys/Hcy to achieve complete demetalization of **1**. To identify $\mathbf{L_1}'$, the reaction mixture for each biothiol (Cys, Hcy and GSH)-induced decomplexation of **1** in water medium was analyzed by FT-IR and ESI-MS^+ studies. In the FT-IR spectrum, the characteristic aldehydic peak at ~1691 cm^{-1} (ν_{CO}) during GSH-induced demetalation renders the assurance of $\mathbf{L_1}'$ generation, while such a signature was completely absent for Cys or Hcy-induced analogous reactions (Fig. S10, ESI†). On the other hand, the m/z peak at 231.305 (calcd m/z: 231.235) corresponding to the molecular formula $C_{11}H_{10}N_4O_2$ ($\mathbf{L_1}'$) was detected in the ESI-MS^+ studies, although the major m/z peak at 233.581 for Cys or Hcy was well-matched with that of $\mathbf{L_1}$ (Fig. S3, ESI†). The results suggest that the benzylic alcohol moiety of $\mathbf{L_1}$ is susceptible to self-oxidation to give one formyl group during the GSH-induced decomplexation of **1** (Scheme 1). There has been some evidence that the ligand containing the benzylic alcohol moiety in the Cu(II)-complexes is converted into the self-oxidized formyl end-product after decomplexation in a free radical pathway.[40]

We synthesized $\mathbf{L_1}'$ due to our repeated failure to isolate $\mathbf{L_1}'$ from the reaction mixture. The synthesized $\mathbf{L_1}'$ exhibited similar UV-Vis absorption intensities at 440 nm and 365 nm at pH 7.3 (Fig. S11, ESI†), and the m/z value at 231.088 was similar to that for **1** in the presence of GSH (Fig. S3B, ESI†). Also, the FT-IR peak position at ~1690 cm^{-1} for the aldehydic C═O moiety of the synthesized $\mathbf{L_1}'$ was almost identical to that obtained for **1** with GSH (Fig. S10, ESI†). All these results strongly justify the aforesaid proposition for the formation of the modified-ligand ($\mathbf{L_1}'$) and unchanged ligand ($\mathbf{L_1}$) by GSH and Cys/Hcy-induced decomplexation of **1**, respectively. The liberated $\mathbf{L_1}'$ may exist in a pH-dependent inter-conversion equilibrium between the deprotonated phenolate form (absorbances at 440 nm) and the protonated phenol form (absorbances at 365 nm) with a pK_a ~ 7.0,

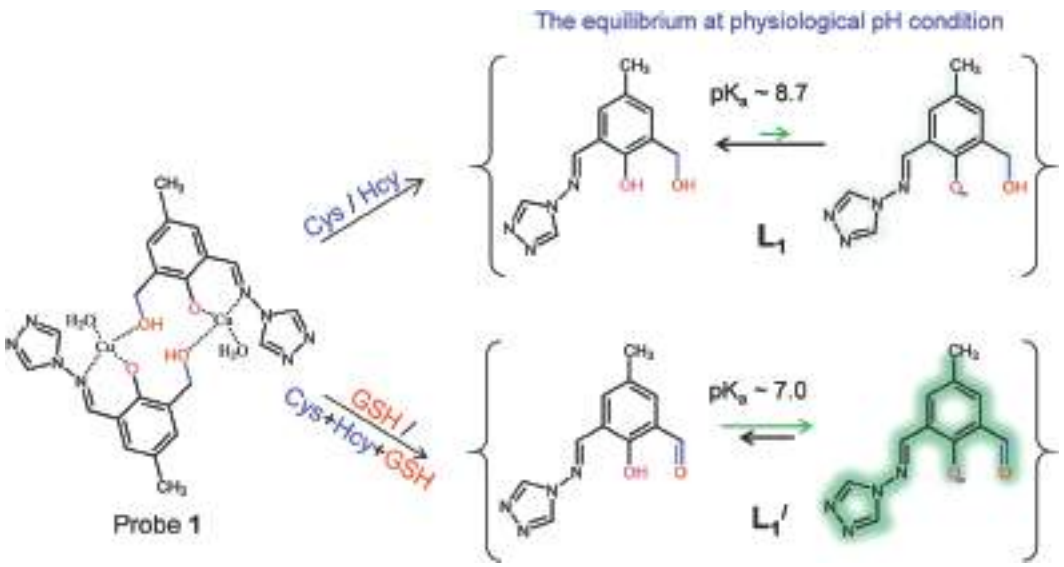

Scheme 1 Schematic representation of the biothiol selective generation of different ligands ($\mathbf{L_1}$ or $\mathbf{L_1}'$) due to the decomplexation of **1**. The acid/base equilibriums between the phenol form and phenolate form of $\mathbf{L_1}$ and $\mathbf{L_1}'$ in pure buffer medium, pH 7.3 are shown in brackets, where the phenolate forms of $\mathbf{L_1}$ and $\mathbf{L_1}'$ are weakly and strongly fluorescent, respectively.

according to the pH-metric UV-Vis absorption studies of the synthesized $\mathbf{L_1}'$ (Fig. S11, ESI†). On the other hand, the acid/base pK_a of $\mathbf{L_1}$ is ~8.7 as reported previously,[37] suggesting that the liberated $\mathbf{L_1}$ exists as mostly the protonated phenol form (absorbances at 340 nm). The co-existence of phenol and phenolate forms of $\mathbf{L_1}'$ in pH 7.3 causes the absorption spectrum of GSH-induced liberated $\mathbf{L_1}'$ to be quite different from that of Cys/Hcy-induced liberated $\mathbf{L_1}$ (Fig. 3A–C).

GSH selective "turn-on" fluorescence for 1

For fluorometric biothiol detection, fluorescence studies of **1** (5 μM with respect to $\mathbf{L_1}$) were performed in the absence and presence of different biothiols (Cys, Hcy and GSH) and their mixtures. **1** exhibited almost no fluorescence intensity for different excitation wavelengths from 300 to 450 nm in 20 mM HEPES–NaOH buffer at pH 7.3, making **1** useful for the "turn-off" fluorescence sensing mode (Fig. 4). Cys, Hcy and GSH (20 equiv.) were separately added to the pH 7.3 buffer containing **1** (5 μM with respect to $\mathbf{L_1}$), in its "turn-off" mode, and fluorescence intensity increases were estimated due to the biothiol-induced generation of free ligands; $\mathbf{L_1}$ for Cys/Hcy and $\mathbf{L_1}'$ for GSH. By exciting the GSH-induced liberation of free $\mathbf{L_1}'$ with 440 nm light, a gradual increase in the fluorescence intensity at 550 nm up to ~550 fold (ϕ_F ~ 0.18) was observed until the intensity was saturated in the presence of ~100 μM GSH (20 equiv. with respect $\mathbf{L_1}$ in **1**) (Fig. 4A). It is worth mentioning that GSH induced a rapid increase in fluorescence saturation within 10–30 s for various concentrations of GSH (Fig. S12, ESI†). Therefore, all the fluorescence intensities were measured 1 min after the addition of GSH. However, the intensity did not increase for the excitation of $\mathbf{L_1}'$ with 365 nm light (Fig. S13, ESI†).

By comparing $\varepsilon_{440} \sim 1.01 \times 10^4\ M^{-1}\ cm^{-1}$ or $\phi_F \sim 0.27$ for the phenolate form of $\mathbf{L_1}'$, according to the pH titration of the synthesized $\mathbf{L_1}'$ with that of **1** in the presence of saturated GSH concentration at pH 7.3 ($\varepsilon_{440} \sim 0.71 \times 10^4\ M^{-1}\ cm^{-1}$ or $\phi_F \sim 0.18$), the liberated $\mathbf{L_1}'$ after decomplexation existed as ~65% phenolate in the buffer medium, and the phenolate species is responsible for the GSH-induced large fluorescence increment (Scheme 1, Fig. 3C, 4A and Fig. S13, ESI†). Interestingly, a small amount of fluorescence generation was detected up to 7 equiv. of GSH with respect to **1** (Fig. 4A), apparently due to the rapid *in situ* conversion of Cu(II) from unstable Cu(I) by GSH-induced demetalation and the subsequent formation of the non-fluorescent Cu(II)–$\mathbf{L_1}'$ complex.[25] Although the increase in fluorescence intensity appeared troublesome up to ~7 equiv. of GSH (~35 μM), a linear fluorescence response with increasing GSH concentration for **1** was detected within 10–20 equiv. (Fig. 4B). Since the cellular GSH concentration is higher (1–10 mM),[25] the linear calibration curve can be beneficial for the ratiometric measurement of the *in vivo* GSH concentration by choosing the right concentration of **1**.

The extent of fluorescence enhancement for **1** (5 μM with respect to $\mathbf{L_1}$) was also monitored in the presence of similar amounts of other biothiols, Cys or Hcy (0–100 μM). From a UV-Vis study, it has already been observed that only ~40% of **1** was involved in decomplexation to generate an equivalent amount of free $\mathbf{L_1}$ by the addition of 100 μM Cys/Hcy (Fig. S14, ESI†). However, the partial liberation of $\mathbf{L_1}$ did not contribute to the generation of even a trace amount of fluorescence intensity by the excitation of the protonated phenol form of $\mathbf{L_1}$ at 340 nm, whereas Cys/Hcy induced only a small fluorescence enhancement, below 5%, as compared to that observed for GSH on excitation at 440 nm by maintaining identical conditions to that of GSH-induced fluorescence intensity enhancement (Fig. 5 and Scheme 1). The addition of Cys/Hcy induced the partial decomplexation of **1**, and the small extent of proton

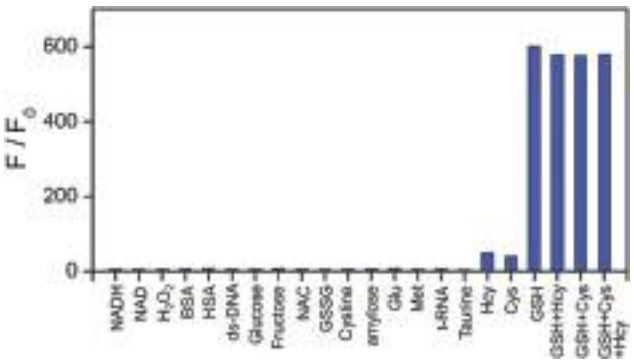

Fig. 5 The extent of the 550 nm fluorescence intensity increase (F/F_0) for **1** with the addition of intensity-saturated concentrations (20 equiv.) of Cys Hcy, GSH and other physiologically relevant molecules in 20 mM HEPES–NaOH buffer at pH 7.3 is shown by bar-diagram.

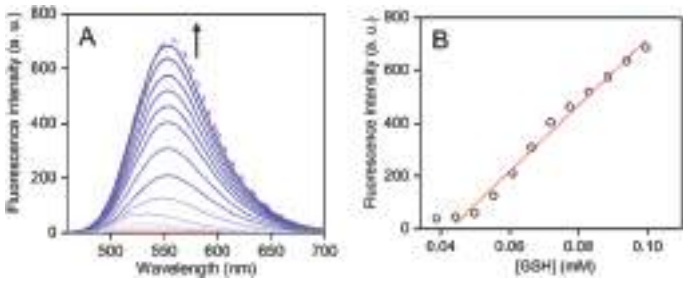

Fig. 4 (A) Fluorescence changes in **1** (5 μM with respect to $\mathbf{L_1}$) with increasing concentration of GSH (0–100 μM) in 20 mM HEPES–NaOH buffer at pH 7.3 at 25 °C. The increase in fluorescence intensity with the concentration of GSH is depicted by the arrow. The broken pink line represents the synthesized modified ligand ($\mathbf{L_1}'$) (5 μM). (B) The increase in fluorescence intensities with increasing GSH concentrations is plotted. The data points in the range 5–100 μM are fitted with a linear equation.

dissociation of $\mathbf{L_1}$ at pH 7.3 ($pK_a \sim 8.7$) to form the weakly fluorescent phenolate species ($\phi_F \sim 0.04$) contributed to the small increase in fluorescence intensity.

To determine the interference of Cys/Hcy in the detection of GSH, fluorometric studies of **1** (5 μM with respect to $\mathbf{L_1}$) under identical buffer medium at pH 7.3 were performed in the presence of biothiol mixtures (GSH + Cys, GSH + Hcy and GSH + Cys + Hcy), where the concentration of each biothiol in the mixture was adjusted to the same as that of intensity-saturated GSH concentration (100 μM, 20 equiv.). The fluorescence intensity increase was ~550-fold for all biothiol combinations, which was similar to that of GSH (20 equiv.) (Fig. 5), indicating that the GSH detection ability of **1** remained unperturbed even in the presence of Cys and Hcy. In comparison to Cys/Hcy, the approximately 4-times higher rate constant of the GSH interaction for the decomplexation of **1** precludes the possible participation of Cys and Hcy-induced decomplexation (Fig. S9, ESI†). The much smaller GSH requirement (20 equiv. with respect to **1**) as compared to that of Cys or Hcy (50 equiv.) to obtain complete decomplexation of **1** is also consistent with the observation of a higher GSH-induced decomplexation reaction rate (Fig. S14, ESI†). As a result, the UV-Vis absorption spectra for different biothiol combinations simply followed the GSH-induced decomplexation trend to generate $\mathbf{L_1}'$ instead of $\mathbf{L_1}$ (Fig. 3D).

The higher selectivity and sensitivity of GSH to **1** is explained pictorially in Scheme 1. On the basis of the higher decomplexation rate constant for GSH as compared to Cys/Hcy (Fig. S9, ESI†), we propose that biothiols like Cys or Hcy exert comparatively less steric congestion, and the electron deficient triazole moiety probably retards their attack on the Cu(II) center in **1**, while such retardation is less significant for tripeptide GSH due to its more negative charge at neutral pH of around 7.3.[41] In contrast to Cys/Hcy, GSH-induced rapid attack favours the ligand modification to $\mathbf{L_1}'$ along with decomplexation (Scheme 1). It has been reported that GSH interaction with Cu(II) generates reduced Cu(I) with the formation of the Cu(I)/GSH complex as an intermediate.[42] It has also been reported that aerial oxidation of the Cu(I) to Cu(II), along with the generation of the superoxide anion (O_2^{-}) are responsible to form H_2O_2 in the reaction medium.[42] Indeed, the *in situ* formation of H_2O_2 (~1.5 μM) was identified during the GSH (100 μM)-induced decomplexation of **1** (10 μM) in 20 mM HEPES–NaOH buffer solution at pH 7.3 by following the standard protocol as described in the H_2O_2 detection kit (MAK165). On the other hand, the GSH-induced instantaneous abolition of the EPR signal of Cu(II) in the EPR spectra also suggests a rapid conversion from Cu(II) to Cu(I) during GSH-induced decomplexation (Fig. S15, ESI†). The *in situ* generated H_2O_2 during the decomplexation of **1** may be responsible for benzylic-OH oxidation to the corresponding formyl group *via* the free radical pathway.[42]

Interestingly, no fluorescence increase for **1** was detected by the addition of similar amounts of GSH (20 equiv.) to different organic solvents like methanol, tetrahydrofuran (THF), acetonitrile (ACN), dimethylformamide (DMF), dimethyl sulfoxide (DMSO) *etc.*, due to the formation of non-fluorescent $\mathbf{L_1}$ by following the usual decomplexation of **1** (Fig. S16, ESI†). To identify the role of dissolved oxygen in solution for ligand modification during GSH interaction, the decomplexation of **1** was separately monitored by UV-Vis absorption spectra in all the non-aqueous solvents, in presence of saturated oxygen concentration. According to UV-Vis absorption studies, the same ligand ($\mathbf{L_1}$) was liberated either in the absence or presence of dissolved oxygen in a non-aqueous medium (Fig. S17, ESI†). The results strongly support our proposition that an aqueous solvent system under atmospheric oxygenated conditions is essential for the oxidation of $\mathbf{L_1}$ into $\mathbf{L_1}'$ during the decomplexation of **1** (Scheme 1). The decomplexation of **1** and subsequent fluorescence generation did not take place in the presence of other anions *viz.* OAc^-, CN^-, S^{2-}, N^{3-}, $H_2PO_4^-$ and HPO_4^{2-} under identical experimental conditions (Fig. S18A, ESI†). Moreover, the GSH-induced fluorescence intensity enhancement remained unperturbed in the presence of other interfering biomolecules (NAD, NADH, GSSG, cystine, H_2O_2, taurine, ds-DNA, glucose, *etc.*) and different biologically important metal ions (K^+, Na^+, Mg^{2+}, Ca^{2+} and $Fe^{2+/3+}$ and Zn^{2+}) present in living systems (Fig. 5 and Fig. S18B, ESI†). Also, no significant fluorescence increase was detected by exposing **1** (5 μM with respect to $\mathbf{L_1}$) to pH 7.3 buffer medium containing various amino acids (20 equiv.) (Fig. S18C, ESI†). The results reveal that **1** is highly suitable for the monitoring of GSH under *in vivo* conditions. In addition, various fluorescence sensing parameters for other reported probes towards the selective detection of GSH under *in vitro* as well as *in vivo* conditions were compared with our results to justify the importance of the present probe selection (Table 1).[14–16,19,22,25,43–47]

Table 1 Comparison of various fluorescence sensing parameters for previously reported probes with the present probe for GSH detection[a]

Solvent	LOD[b] (μM)	Response[c] (min)	Bio-imaging
Water/DMSO (99 : 1)[14]	0.60/0.33	60	SCC7 cell
Water/ACN (7 : 3)[15]	0.12	10	HeLa cell
Water/DMSO (9 : 1)[16]	5.00	15	HeLa/RAW 264.7 cell
Water[19]	0.06	30	HeLa cell
Water/DMSO (1 : 1)[22]	0.03	7	A549 cell
Water[25]	0.05	3.5	*C. elegans*
Water/ACN (2 : 1)[43]	0.43	0.5	HeLa cell
Water/ACN (1 : 3)[44]	1.07	—	HeLa cell
Water[45]	0.04	—	Hela/U2OS cell
Water/DMSO (99 : 1)[46]	24.16	3	HeLa cell
Water/DMF (99 : 1)[47]	0.17	0.1	HeLa/RAW 264.7 cell
Water (this work)	0.04	0.2	*C. elegans*/SH-SY5Y cells

[a] Different literature references are indicated by superscripts in the solvent column. [b] Limit of detection. [c] *In vitro* fluorescence sensing response time.

Bio-imaging studies

The nematode, *Caenorhabditis elegans* (*C. elegans*), was chosen for bio-imaging purposes because of its basic functional similarity to more advanced animals including humans.[48] In addition, the transparent body system of *C. elegans* is highly suitable for monitoring the distribution of essential molecules/ions within its whole-body by the fluorescence imaging method in a simple and cost-effective way. Well-defined organs, such as the pharynx, intestines, gonads (proximal, distal) and uterus are generally exploited for bio-imaging purposes. For the detection of *in vivo*

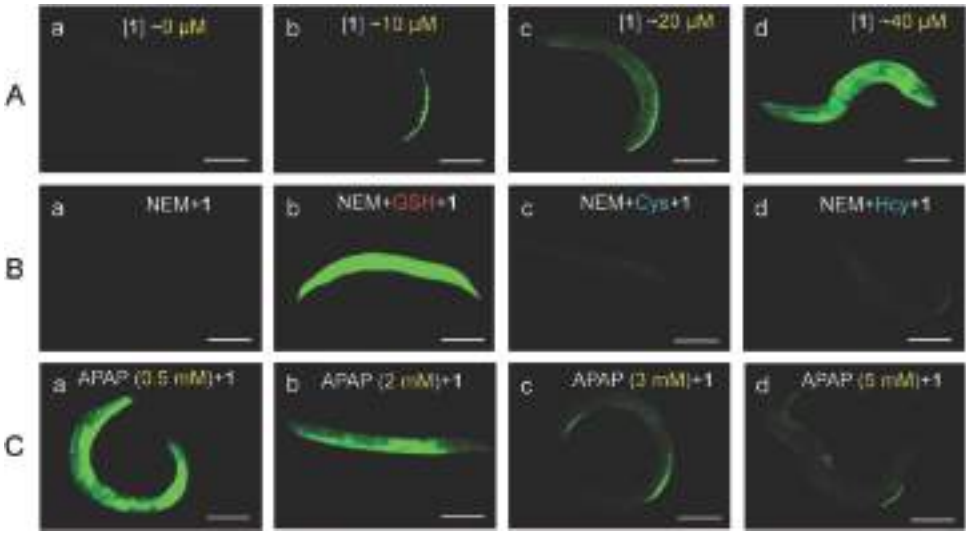

Fig. 6 (A: upper panel) **1** concentrations (0–40 μM) dependent fluorescence imaging studies for *C. elegans*. Fluorescence was monitored at 30 min after the addition of **1**. (B: middle panel) Fluorescence images in presence of 1 mM NEM. The NEM-treated living *C. elegans* were pretreated with 2 mM different biothiols individually followed by further exposure to **1** for 30 min. (C: lower panel) Fluorescence imaging with exposure of APAP (0.5–5 mM) treated living *C. elegans* to **1** (40 μM) after 30 min. (A–C) White scale bars represents 40 μm.

GSH, L4/young adult nematodes were exposed to various concentrations of **1** (0–40 μM with respect to $\mathbf{L_1}$) or synthesized $\mathbf{L_1}'$ (40 μM) for the control experiment in a nematode growth media (NGM) plate at room temperature for various time periods without affecting the survival assay of living *C. elegans* (Fig. S19, ESI†). Fluorescence intensity was mostly observed in the peripheral region of the nematodes for concentrations of **1** up to ~10 μM (Fig. 6A(a and b)). On gradually increasing the concentration of **1** under similar experimental conditions, the fluorescence intensity was found to spread throughout the whole body of *C. elegans*, where the intensity saturation was observed for 40 μM of **1** (Fig. 6A). The liberation of fluorescent $\mathbf{L_1}'$ by decomplexation of **1** is responsible for the fluorescence intensity increase since an almost identical fluorescence increase was observed for the synthesized $\mathbf{L_1}'$ in the control experiment (Fig. S20, ESI†).

To investigate the GSH selectivity of the probe and its reflection in bio-imaging, *N*-ethylmaleimide (NEM), a well-known biothiol-blocking agent, was added (up to 1 mM) prior to incubation with **1** (40 μM); more than 90% of the worms remained alive after treatment with NEM and **1** (Fig. S19, ESI†). The fluorescence intensity in the NEM-treated worms was greatly attenuated (Fig. 6B(a)). Strong fluorescence intensity was found to reappear when NEM-treated living nematodes were further exposed to externally added GSH (2 mM) before the addition of **1** under the same conditions (Fig. 6B(b)). However, no noticeable fluorescence was observed for Cys/Hcy (2 mM) exposure under identical measurement conditions (Fig. 6B(c and d)), showing the remarkable selectivity of **1** to detect GSH *in vivo* judging by the fluorescence response.

The safest painkiller drug acetaminophen (APAP) causes serious liver injury after an overdose in humans. During excretion, APAP may be converted into *N*-acetyliminoquinone, which can generally be detoxified due to its high reactivity with hepatic GSH.[49] An overdose of APAP may generate the highly active metabolite, *N*-acetyl-*p*-benzoquinoneimine, which directly combines with GSH and appears to be responsible for initiating liver damage.[50] Very little is known about APAP distribution in other organs and its impact on GSH. Depletion of GSH levels in the presence of various concentrations of APAP (maximum up to 5 mM) was monitored by **1**. *C. elegans* were pretreated with APAP, followed by the addition of **1** (40 μM), without affecting the survival conditions as mentioned before (Fig. S19, ESI†). The fluorescence measurements in different nematode organs were performed ~30 min after sequentially treating the nematodes with APAP and **1**. Only a small decrease in fluorescence intensity was detected up to APAP concentration of ~0.5 mM (Fig. 6C(a)). However, a large decrease in fluorescence intensity, particularly in the intestines, was observed in the presence of 5.0 mM APAP (Fig. 6C). The decreased reactivity of **1** clearly indicates a significant decrease *in vivo* GSH concentration influenced by APAP. The results also justify the use of **1** as a GSH probe for multi-cellular organisms.

It has been well investigated that GSH acts as an essential protector of neural cells to overcome various oxidative stresses and plays a crucial role in destroying free radical-generated neurotoxins in Perkinson's disease (PD).[51] To clarify the role of GSH as an intracellular antioxidant, we performed bio-imaging studies of probe **1** on human neuroblastoma SH-SY5Y cells by exposing it to a potent GSH synthase inhibitor, L-buthionine-SR-sulfoximine (BSO)[52] in the presence or absence of a GSH source, *N*-acetyl-L-cysteine (NAC)[53] with consideration of the cell viability (Fig. S21, ESI†).[36] Probe **1** (30 μM) was incubated in SH-SY5Y cells at 37 °C for 30 min and green fluorescence was observed inside the cell (Fig. 7A). In the control measurement, a large amount of fluorescence quenching was identified after BSO (0.5 mM)-pretreated cells were exposed to **1** (30 μM with respect to $\mathbf{L_1}$) for 30 min (Fig. 7B), which diminished completely within 2 h (Fig. 7C). Interestingly, an appreciable amount of green

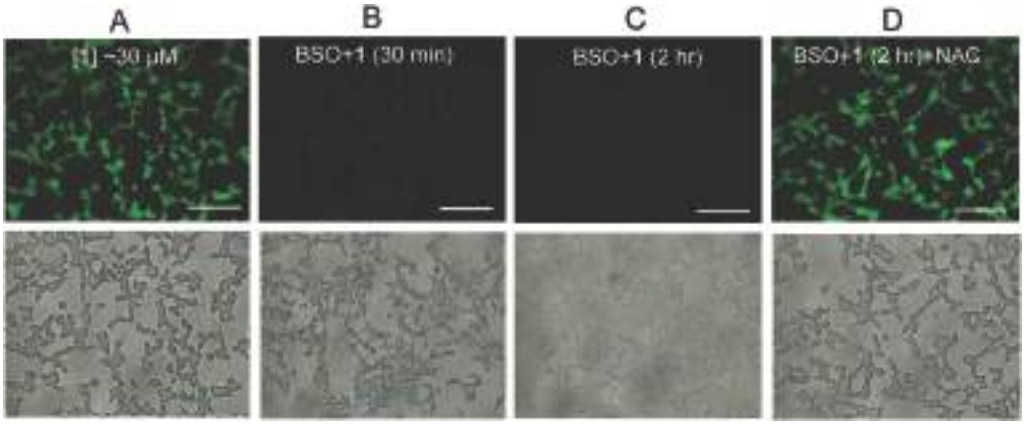

Fig. 7 Fluorescence images (upper panel) and corresponding bright field images (lower panel) of SH-SY5Y cells were captured after incubation with (A) **1** (30 μM) and (B) BSO (0.5 mM) treated cells exposed to **1** (30 μM). (C) A portion of BSO (0.5 mM) + **1** (30 μM) treated cells was further exposed in presence of NAC (5 mM) for 2 h at 37 °C. (A–D) White scale bars represent 40 μm.

fluorescence was regained when the BSO-induced cells were further treated with 5 mM of the water-soluble GSH precursor, NAC, within 2 h (Fig. 7D). Since **1** remains non-fluorescent with the *in vitro* addition of NAC (Fig. 5), the fluorescence intensity increase was definitely due to the increasing concentration of GSH in cells. These significant findings may be explored in the future for GSH-related PD and related diseases.

Conclusions

We demonstrated a novel decomplexation strategy in a pure aqueous medium for the selective detection of glutathione (GSH) in both the absence and presence of other biothiols, cysteine (Cys) and homocysteine (Hcy), by monitoring the "off–on" fluorescence response. A weakly fluorescent phenolic Schiff base molecule ($\mathbf{L_1}$) forms a non-fluorescence dimeric Cu(II)-complex that shows a great affinity for participating in the decomplexation reaction by the interaction of the –SH moiety of biothiols with Cu(II). Among the different biothiols, only strong GSH-induced fluorescence intensity was detected by liberating the modified-$\mathbf{L_1}$ ($\mathbf{L_1}'$) during the decomplexation process. The ligand modification due to the oxidation of the benzylic alcohol moiety to the corresponding formyl is attributed to the large GSH-induced fluorescence enhancement. In contrast, Cys or Hcy-induced partial decomplexation exhibited less than 5% intensity increase as compared to GSH, which was due to the liberation of the unmodified-ligand ($\mathbf{L_1}$) by following the usual decomplexation reaction. The difference in the decomplexation ability of GSH and Cys/Hcy was used to determine biological GSH in living *Caenorhabditis elegans* and human neuroblastoma SH-SY5Y cells. Fluorescence bioimaging was also performed to monitor GSH depletion induced by the common pain killer, acetaminophen, in living *C. elegans*. The simplicity of our GSH detection method may be tuned for more advanced biological domains.

Conflicts of interest

There are no conflicts to declare.

Acknowledgements

Authors acknowledge Jadavpur University and Maulana Azad College, Kolkata, for departmental facilities. PPP acknowledges DST, India for Special Grant to the Department of Chemistry, JU in the International Year of Chemistry 2011. This work was also supported by Research Project UGC (ERO) (PSW-196/13-14) (AR), (PSW-197/13-14) (SD). RM and YS acknowledge UGC for JRF fellowship.

Notes and references

1 Z. A. Wood, E. Schroder, J. R. Harris and L. B. Poole, *Trends Biochem. Sci.*, 2003, **28**, 32.
2 H. J. Forman, H. Q. Zhang and A. Rinna, *Mol. Aspects Med.*, 2009, **30**, 1.
3 S. Y. Zhang, C. N. Ong and H. M. Shen, *Cancer Lett.*, 2004, **208**, 143.
4 T. P. Dalton, H. G. Shertzer and A. Puga, *Annu. Rev. Pharmacol. Toxicol.*, 1999, **39**, 67.
5 A. Meister and M. E. Anderson, *Annu. Rev. Biochem.*, 1983, **52**, 711.
6 L. A. Herzenberg, S. C. De Rosa, J. G. Dubs, M. Roederer, M. T. Anderson, S. W. Ela, S. C. Deresinski and L. A. Herzenberg, *Proc. Natl. Acad. Sci. U. S. A.*, 1997, **94**, 1967.
7 D. M. Townsend, K. D. Tew and H. Tapiero, *Biomed. Pharmacother.*, 2003, **57**, 145.
8 J. M. Estrela, A. Ortega and E. Obrador, *Crit. Rev. Clin. Lab. Sci.*, 2006, **43**, 143.
9 J. Sian, D. T. Dexter, A. J. Lees, P. S. Daniel, P. Jenner and C. D. Marsden, *Ann. Neurol.*, 1994, **36**, 356.
10 C. Saito, C. Zwingmann and H. Jaeschke, *Hepatology*, 2010, **51**, 246.
11 G. Xu, Y. Tang and W. Lin, *New J. Chem.*, 2018, **42**, 12615.
12 Y. Tian, B. Zhu, W. Yang, J. Jing and X. Zhang, *Sens. Actuators, B*, 2018, **262**, 345.
13 L. Y. Niu, Y. Z. Chen, H. R. Zheng, L. Z. Wu, C. H. Tung and Q. Z. Yang, *Chem. Soc. Rev.*, 2015, **44**, 6143.

14 D. Lee, K. Jeong, X. Luo, G. Kim, Y. Yang, X. Chen, S. Kim and J. Yoon, *J. Mater. Chem. B*, 2018, **6**, 2541.
15 X. Hou, Z. Li, B. Li, C. Liu and Z. Xu, *Sens. Actuators, B*, 2018, **260**, 295.
16 J. Yin, Y. Kwon, D. Kim, D. Lee, G. Kim, Y. Hu, J. H. Ryn and J. Yoon, *J. Am. Chem. Soc.*, 2014, **136**, 5351.
17 S. Lee, J. Li, X. Zhou, J. Yin and J. Yoon, *Coord. Chem. Rev.*, 2018, **366**, 29.
18 C. H. Liu, F. P. Qi, F. B. Wen, L. P. Long, A. J. Liu and R. Yang, *Methods Appl. Fluoresc.*, 2018, **6**, 24001.
19 J. Li, Y. Kwon, K. S. Chung, C. S. Lim, D. Lee, Y. Yue, J. Yoon, G. Kim, S. J. Nam, Y. W. Chung, H. M. Kim, C. Yin, J. H. Ryu and J. Yoon, *Theranostics*, 2018, **8**, 1411.
20 X. F. Hou, X. L. Guo, B. Chen, C. H. Liu, F. Guo, J. Zhao and J. H. Wang, *Sens. Actuators, B*, 2015, **209**, 838.
21 L. Y. Niu, Y. S. Guan, Y. Z. Chen, L. Z. Wu, C. H. Tung and Q. Z. Yang, *J. Am. Chem. Soc.*, 2012, **134**, 18928.
22 X. Li, F. Huo, Y. Yue, Y. Zhang and C. Yin, *Sens. Actuators, B*, 2017, **253**, 42.
23 X. Lou, D. Ou, Q. Li and Z. Li, *Chem. Commun.*, 2012, **48**, 8462.
24 S. Das, S. Biswas, S. Mukherjee, J. Bandyopadhyay, S. Samanta, I. Bhowmick, D. K. Hazra, A. Ray and P. P. Parui, *RSC Adv.*, 2014, **4**, 9656.
25 S. Das, Y. Sarkar, S. Mukherjee, J. Bandyopadhyay, S. Samanta, A. Ray and P. P. Parui, *Sens. Actuators, B*, 2015, **209**, 545.
26 S. Das, Y. Sarkar, R. Majumder, S. Mukherjee, J. Bandyopadhyay, A. Ray and P. P. Parui, *New J. Chem.*, 2017, **41**, 1488.
27 Y. Sarkar, S. Das, R. Datta, S. Chattopadhyay, A. Ray and P. P. Parui, *RSC Adv.*, 2015, **5**, 51875.
28 R. R. Gagne, C. L. Spiro, T. J. Smith, C. A. Hamann, W. R. Thies and A. K. Schiemke, *J. Am. Chem. Soc.*, 1981, **103**, 4073.
29 J. V. Morris, M. A. Mahaney and J. R. Huber, *J. Phys. Chem.*, 1976, **80**, 969.
30 V. Thomsen, D. Schatzlein and D. Mercuro, *Spectroscopy*, 2003, **18**, 112.
31 M. J. Frisch, *et al. Gaussian 09, Revision B.01*, Gaussian, Inc., Wallingford, CT, 2009.
32 S. Miertus, E. Scrocco and J. Tomasi, *Chem. Phys.*, 1981, **55**, 117.
33 V. Barone, M. Cossi and J. Tomasi, *J. Comput. Chem.*, 1998, **19**, 404.
34 J. L. Biedler, L. Helson and B. A. Spengler, *Cancer Res.*, 1973, **33**, 2643.
35 J. Bandyopadhyay, H. O. Song, G. Singaravelu, J. L. Sun, B. J. Park, J. Ahnn and J. H. Cho, *Biochem. Biophys. Res. Commun.*, 2009, **390**, 136.
36 T. Mossman, *J. Immunol. Methods*, 1983, **65**, 55.
37 Y. Sarkar, S. Das, A. Ray, S. K. Jewrajka, S. Hirota and P. P. Parui, *Analyst*, 2016, **141**, 2030.
38 A. Chakraborty, J. Goura, P. Kalita, A. Swain, G. Rajaraman and V. Chandrasekhar, *Dalton Trans.*, 2018, **47**, 8841.
39 M. Hubrich, M. Peukert, W. Seichter and E. Weber, *Polyhedron*, 2010, **29**, 1854.
40 H. Korpi, *Copper di-imine complex: structure and catalytic activity in the oxidation of alcohols by dioxygen*, Academic dissertation, University of Helsinki, 2005, pp. 1–59, ISBN-952-10-2707-X, http://ethesis.Helsinki.fi.
41 H. S. Jung, T. Pradhan, J. H. Han, K. J. Heo, J. H. Lee, C. Kang and J. S. Kim, *Biomaterials*, 2012, **33**, 8495.
42 H. Speisky, M. Gomez, F. B. Bravo, C. L. Alarcon, C. Jullian, C. O. Azar and M. E. Aliaga, *Bioorg. Med. Chem.*, 2009, **17**, 1803.
43 Y. Li, W. Liu, P. Zhang, H. Zhang, J. Wu, J. Ge and P. Wang, *Biosens. Bioelectron.*, 2017, **90**, 117.
44 X. L. Liu, L. Y. Niu, Y. Z. Chen, Y. Yang and Q. Z. Yang, *Biosens. Bioelectron.*, 2017, **90**, 403.
45 C. Zhan, G. Zhang and D. Zhang, *ACS Appl. Mater. Interfaces*, 2018, **10**, 12141.
46 S. Qi, W. Liu, P. Zhang, J. Wu, H. Zhang, H. Ren, J. Ge and P. Wang, *Sens. Actuators, B*, 2018, **270**, 459.
47 L. Chen, J. S. Park, D. Wu, C. H. Kim and J. Yoon, *Sens. Actuators, B*, 2018, **262**, 306.
48 M. C. K. Leung, P. L. Williams, A. Benedetto, C. Au, K. J. Helmcke, M. Aachner and J. N. Meyer, *Toxicol. Sci*, 2008, **106**, 5.
49 M. Moore, H. Thor, G. Moore, S. Nelsons, P. Moldeus and S. Orrenius, *J. Biol. Chem.*, 1985, **260**, 13035.
50 E. Albano, M. Rundgren, P. J. Harvison, S. D. Nelson and P. Moldeus, *Mol. Pharmacol.*, 1985, **28**, 306.
51 M. Smeyne, *Free Radical Biol. Med.*, 2013, **62**, 13.
52 A. Tagde, H. Singh, M. H. Kang and C. P. Reynolds, *Blood Cancer J.*, 2014, **4**, 229.
53 K. R. Atkuri, J. J. Mantovani, L. A. Herzenberg and L. A. Herzenberg, *Curr. Opin. Pharmacol.*, 2007, **7**, 355.